Advances in Petroleum Engineering

FORMATION TESTING

LOW MOBILITY PRESSURE TRANSIENT ANALYSIS

Wilson C. Chin
Yanmin Zhou, Yongren Feng and Qiang Yu

Scrivener Publishing

WILEY

Formation Testing

Scrivener Publishing
100 Cummings Center, Suite 541J
Beverly, MA 01915-6106

Publishers at Scrivener
Martin Scrivener(martin@scrivenerpublishing.com)
Phillip Carmical (pcarmical@scrivenerpublishing.com)

Formation Testing

Low Mobility Pressure Transient Analysis

Wilson C. Chin , Ph.D., M.I.T.

Stratamagnetic Software, LLC, Houston

and

Yanmin Zhou, Yongren Feng and Qiang Yu

China Oilfield Services LTD, Beijing

WILEY

Co-published by John Wiley & Sons, Inc. Hoboken, New Jersey, and Scrivener Publishing LLC, Salem, Massachusetts.
Published simultaneously in Canada.

Cover design by Kris Hackerott

Library of Congress Cataloging-in-Publication Data:

ISBN 978-1-118-92594-2

Printed in the United States of America

10 9 8 7 6 5 4 3 2 1

Contents

Preface

Just two years ago, the authors published *Formation Testing Pressure Transient and Contamination Analysis* with Scrivener Publishing, focusing on advanced forward models and inverse solutions pertinent to modern interpretation and job planning. Many of the new models were exact analytical solutions. For example, the flagship module FT-00 solved a general formulation allowing for anisotropic media, skin effects and flowline storage pressure distortions; inverse models complementing this solution were able to provide horizontal and vertical permeabilities at any dip angle for both linear liquid and nonlinear gas flows. We could have stopped with these very satisfying results, but the "bug" that haunts researchers is a terrible beast which never sleeps.

Our results required steady-state pressure drop data at both source and observation probes, a limitation that restricted their applicability to medium-to-high mobility applications. For modern low-mobility reservoirs, this could mean hour-long wait times or more, implying low efficiencies, high costs and increasing risks of lost tools. So the authors asked, "Are there physical processes that take advantage of low mobilities – providing spherical permeability predictions within seconds?" Later, this took an even more ambitious focus. "Is it possible to predict both horizontal and vertical permeability, also within seconds, using only standard dual-probe tools?"

It is well known that fast transient drawdown-buildup methods employing single probes could, at best, provide only the "spherical permeability" $k_h^{2/3}k_v^{1/3}$. Because the two perms can vary by a factor of ten in anisotropic media, spherical predictions are limited in usefulness – a serious issue since both are crucial to hydraulic fracturing, borehole stability, and so on. A second equation was required to uniquely provide two numbers – ideally, one that could be rapidly evaluated from early time data. We successfully followed one important clue. In resistivity logging, where time delays and

amplitude decays between transmitter and receiver coils are used to determine formation resistivity, the quantity "$\sin^2 \delta / R_h + \cos^2 \delta / R_v$" always appeared, where δ is the dip angle. In fact, the more conductive (diffusive) the medium, the better the well log. Finding an estimate for "$\sin^2 \delta / k_h + \cos^2 \delta / k_v$" would surely help predict the relative values of horizontal and vertical permeability for a known $k_h^{2/3} k_v^{1/3}$. This observation motivated us to develop formation testing analogies to electromagnetic logging – our key results are reported in Chapters 3 and 4.

The authors are pleased to present these important new results, and the present book, which completely explains the ideas, methods, equations and algorithms, also provides detailed calculations and applications examples. At the present time, we are developing sophisticated test fixtures to validate our methods and calibrate new tools. This is surely an exciting time for formation tester development and for petroleum exploration well logging.

It is important to emphasize that the approaches developed here did not materialize overnight – they required a long-term commitment to understanding the fundamental physics, developing analogies between seemingly different disciplines like fluid dynamics and electromagnetics, and an obsession with solving important problems that ultimately benefit everyone in society. The authors recognize that creative work requires continuing motivation and investment in people – so our endeavors will continue, whether or not oil prices drop further – we won't be the ones turning out the lights anytime soon.

Wilson C. Chin, Ph.D., M.I.T.
Houston, Texas
Email: wilsonchin@aol.com
Phone: (832) 483-6899

Acknowledgements

The lead author gratefully acknowledges the insights, experiences and friendships he acquired during his early exposure to formation testing at Halliburton Energy Services in the 1990s; and in particular, the contributions of his colleague and friend Mark Proett, now with Saudi Aramco, who shaped his initial thinking and approach to pressure transient and contamination analysis.

In 2004, the United States Department of Energy, through its Small Business Innovation Research (SBIR) program, awarded approximately two hundred grants in support of high-risk efforts in all areas of energy, e.g., nuclear fusion, plasma physics, batteries, green energy, and so on. Four were allocated to fossil fuels – and, of these, two would support the lead author's projects, entitled "*Formation Tester Permeability Prediction in Tight Gas Sands*" and "*Formation Tester Immiscible Flow Response in Horizontally Layered Media*." The insights acquired in these researches no doubt fueled further innovations. For these past opportunities, the lead author is very appreciative.

All of the authors are indebted to China National Offshore Oil Corporation (CNOOC) and its subsidiary China Oilfield Services Limited (COSL) for its support and encouragement throughout our work in formation testing. Without the open access that we were granted to its tools, plans, staff and insights, we would not have been able to focus on the problems that really mattered. The authors appreciate the company's permission to publish significant portions of an internal report documenting our new low mobility inverse methods.

Phillip Carmical, Acquisitions Editor and Publisher, has been extremely supportive of this book project and others in progress. His philosophy, to explain scientific principles the way they must be told, with equations and algorithms, is refreshing in an environment often shrouded in secrecy and commercialism. The authors are optimistic that their story-telling will

advance the technology and explain why "black boxes" aren't so mysterious after all. Finally, the authors thank Xiaoying "Jenny" Zhuang for her hard work and commitment to ably working both sides of the language barrier (the lead author neither speaks nor reads Chinese, while the CNOOC/COSL team is newly conversant in English). Without Jenny's interpretation skills and willingness to learn the technology, progress would have slowed and this formation testing monograph – the second in two years – may not have seen publication.

1
Basic Ideas, Interpretation Issues and Modeling Hierarchies

In this opening chapter, we informally introduce some of the subjects covered in the present manuscript, a sequel to the book Formation Testing Pressure Transient and Contamination Analysis published by the present authors with John Wiley & Sons as recently as 2014. While that work contained many new materials not previously available, the present provides even more interpretation methods, algorithms and extensions resulting from the rapid pace of research advances achieved over the intervening two years. The content offered in this publication is intended to not only stimulate innovation in pressure transient analysis, but encourage early and confident acceptance of new approaches certain to make exploration more efficient and cost-effective.

1.1 Background and Approaches

What are formation testers? Simply said, they are borehole logging instruments which, when pressed against the sandface, extract or "sample" formation fluids for detailed examination at the surface, e.g., as illustrated in Figure 1.1. By-products of the sampling process are flowline pressure transient histories associated with pumping actions, which can be interrogated for valuable information related to formation properties like mobility, permeability, anisotropy and pore pressure. The earliest methods, more than five decades old, are based on well known formulas like "$k_s = CQ\mu/(2\pi r_p \Delta P)$" and gave only spherical permeabilities (subscripted by "s"). These approaches required long wait times for steady-state pressure drops ΔP to develop. Later, more flexible approaches using Horner-type approaches were developed; while decreasing wait times, they unfortunately required additional rock and fluid information, i.e., porosity and compressibility, introducing inconvenience and potential error.

The above formula, which again required steady conditions, was excellent for high mobility formations where pressure equilibrium could be achieved in minutes or seconds. However, it does not apply in the presence of larger flow line volumes when mobilities are low. Pressures normally indicative of the downhole flow environment are initially forced to compress or expand the fluid cushion residing in the line so that formation characteristics are obscured or hidden – an analogy can be made to gauging the power of a boxer's punch with the boxer wearing heavily padded gloves. When flowline volume effects are large, bearing in mind that "large" is relative and depends on unknown fluid compressibility and mobility, measured pressures are distorted and cannot be used to calculate properties like mobility, permeability or viscosity – the Darcy component of pressure cannot be identified (the foregoing problem is akin to "wellbore storage" issues in well testing). In response to this, petroleum engineers simply waited for flowline effects to dissipate or subside, which in low mobility applications may require many hours. Not only did this increase logging time and expense, but the risk of stuck tools rose substantially. Flowline storage problems had been accepted as inevitable until a series of interesting breakthroughs achieved in the 1990s.

Figure 1.1. CNOOC/COSL single and dual-probe formation testers.

In graduate school, students are taught that boundary value problems governing physical phenomena consist of partial differential equations constrained by boundary and initial conditions. Solve the relevant formulation and the problem is fully understood. But the real problem is practical: many important formulations cannot be solved in closed analytical form, so that any physical insights and convenient formulas that would have been useful remain hidden in numerical data. And computational solutions are only partly reliable:

"artificial viscosities" arising from truncation and round-off errors contribute to uncertainties in permeability. Mark Proett, the author's colleague and friend at Halliburton (now with Saudi Aramco), developed a "boundary condition only" analytical approach valid at early times when storage and flow effects were equally strong (a similar approach developed for isotropic media at Baker-Hughes evolved to become the company's "formation rate analysis").

Proett's approach is discussed in United States Patent No. 5,602,334, "Wireline Formation Testing for Low Permeability Formations Utilizing Pressure Transients," awarded to M.A. Proett and M.C. Waid in February 1997. From its Abstract, "An improved formation testing method for measuring initial sandface pressure and formation permeability in tight zone formations exhibiting formation permeabilities on the order of 1.0-0.001 millidarcies based on pressure transients which occur shortly after the tester enters its pressure buildup cycle and substantially before reaching final buildup pressure. The method makes an estimate of formation permeability based on fluid decompression transients which occur in the formation tester flowlines which occur shortly after the tester begins its buildup cycle. The method further estimates initial sandface pressure based on the change in pressure over time shortly after beginning the buildup phase. The method of the present invention thereby permits accurate estimates of formation permeability and initial sandface pressure to be made relatively early in the buildup cycle, thus substantially reducing the time required to make the pressure and permeability measurements."

Proett's heuristic model, surprisingly, was extremely successful in predicting spherical mobility and (steady) pore pressure in low mobility environments from highly transient data. In retrospect, this is not altogether surprising. Many problems in mathematical physics *can* be studied, at least for initial times, without solving the complete formulation. As a case in point, consider classical mass-spring-damper systems: if a small mass is struck quickly, its *initial* motion is completely determined by auxiliary conditions, but only subsequently does the differential equation matter. Similarly, in formation testing, the differential equation would need to be solved if additional information is required.

Motivated by this need, the lead author solved the complete anisotropic formulation in the mid-1990s, with both flowline storage and skin effects in closed analytical form, and demonstrated how Proett's constant rate solution provided the leading term of an asymptotic, low mobility expansion whose application could be further extended. This "exact solution" forms the basis for Halliburton's drawdown-buildup GeoTap™ model used in real-time mobility and pore pressure prediction in "formation testing while drilling" (FTWD) or Measurement While Drilling (MWD) tools. Typical predictions require less than one minute of test time, thus enabling higher density and more economical well logging.

We emphasize that the method, which assumes a single-probe tool, provides pore pressure and *spherical* permeability predictions using early time data – it does not, however, give horizontal and vertical mobility or permeability individually – these can differ substantially in different directions, and as we will show, their determination requires dual-probe formation testing tools. The success of the physics-based approach motivated a second question. While the new drawdown-buildup interpretation method focused on flowline storage and flow as the dominant physical interaction, rather than avoiding storage but having to endure long wait times, is it possible to take advantage of pressure diffusion in such a way that test times can be significantly reduced?

This at first seems counter-intuitive because high mobilities imply rapid pressure equilibrium – thus low values would seem to lead to long test times. However, this conclusion is only the case *if* one restricts attention to constant rate pressure drawdown processes (which are used to derive classical formulas like "$k_s = CQ\mu/(2\pi r_p\ \Delta P)$)." In fact, there *are* pumping actions for which the opposite is true – by focusing on mechanisms that depend strongly on diffusion, it *is* possible to develop fast algorithms for permeability and pore prediction. This book provides a detailed development of new ideas and algorithms in support of this objective and illustrates their use with numerical examples. An interesting comparison of old and new methods is given in Chapter 5.

Many of the formation testing ideas introduced in this book were motivated by electromagnetic logging. *Yes*, resistivity prediction in high conductivity diffusive formations. In electromagnetic well logging, a transmitter broadcasts constant frequency AC waves, whose amplitude decay and phase (that is, time) delay are recorded at neighboring coil receivers. These measurements are interpreted using Maxwell's equations as the host math model and anisotropic resistivities can be estimated – in fact, the greater the diffusion, the higher the signal-to-noise ratio and the better the predictions.

The lead author introduced his "phase delay" approach to formation tester mobility prediction by developing an analogy to electromagnetic logging as follows (e.g., refer to United States Patent No. 5,672,819, "Formation Evaluation Using Phase Shift Periodic Pressure Pulse Testing," awarded to W.C. Chin and M.A. Proett in September 1997). The tester pump was taken as the "transmitter" while a second observation probe assumed the role of the "receiver." When the pump piston oscillates sinusoidally, it creates an AC wave whose pressure amplitude and time delay can be measured at the observation probe. These measurements are interpreted using Darcy's equations to give mobility estimates, thus completing the analogy to electromagnetic logging.

Experiments performed at Halliburton were successful. Interestingly, time delays, in contrast to those observed in resistivity logging, are large and could be ascertained visually from strip charts, thus reducing demands on computational and electronic resources. And mechanical requirements were not demanding – pump frequencies on the order of 1 Hz were sufficient. But many questions

remained unanswered at the time. Once a pressure signal leaves the pumping probe, its fate is completely determined by the formation – the "receiver," so to say, "sees what it sees." But what happens if what it sees is poor in quality? And what if the pump piston cannot execute pure sinusoidal waves as required by theory, but only limited numbers of wave cycles that are, say, rectangular in shape? It turns out, however, that the form of the created wave can be controlled by varying flowline volume, thus providing a means for customization and quality control (e.g., see Chapter 9, Example 7), and that deviations from pure sinusoids are a secondary concern (refer to Chapter 5).

At the time the work was first performed, there was little incentive to commercialize the phase delay approach at Halliburton. The invention applied only to *isotropic* media – the required theoretical extensions to anisotropic formations, in which the effects of dip angle would figure prominently, were not available. To determine isotropic permeability, the single-probe early-time drawdown method was more cost-effective, simpler and additionally provided pore pressure. The phase delay approach, while elegant and interesting, required dual-probe tools and could not give pore pressure estimates. Now, some two decades later, the needed generalization to anisotropic media with dip has been completed, together with more powerful extensions to low-mobility, early-time, drawdown-buildup methods. The combination of the two, as we will demonstrate in this book, allow both horizontal and vertical permeabilities – not "spherical permeabilities" alone – to be predicted from early time data in very low mobility formations. These methods are discussed for the first time in print and patent applications have been appropriately filed. Before presenting details, it is necessary to emphasize the limitations of idealized mathematical models and the physical implications of their consequences.

1.2 Modeling Hierarchies

Few innovations to pressure transient interpretation appeared until the 1990s with Halliburton sponsored research. These initial efforts, summarized in "Advanced Permeability and Anisotropy Measurements While Testing and Sampling in Real-Time Using a Dual Probe Formation Tester," SPE Paper 64650, presented at the *Seventh International Oil & Gas Conference and Exhibition* in Beijing by Proett, Chin and Mandal in November 2000, introduced several avenues of research which saw subsequent development. The first was the low-mobility, early-time drawdown buildup method discussed earlier; the second, a completely analytical solution to the full boundary value problem developed by the lead author; and the third, the phase delay method, also due to the lead author, although restricted then to isotropic media. Difficulties with the analytical solution, which manifested themselves only years later, would motivate further work supported by the United States Department of Energy.

In the two decades since the “exact solution” appeared, some two dozen papers bearing this citation have been authored. And given the wide dissemination of these publications, appearing in journals and conferences associated with the Society of Petrophysicists and Well Log Analysts (SPWLA), the Society of Petroleum Engineers (SPE) and other organizations, it is important to clarify now what is meant by “exact” and the significance (or lack of) in that designation. To understand this further, we need to understand the difference between real-world tools and their mathematical idealizations.

Figure 1.2. Single-probe formation tester (enlarged view).

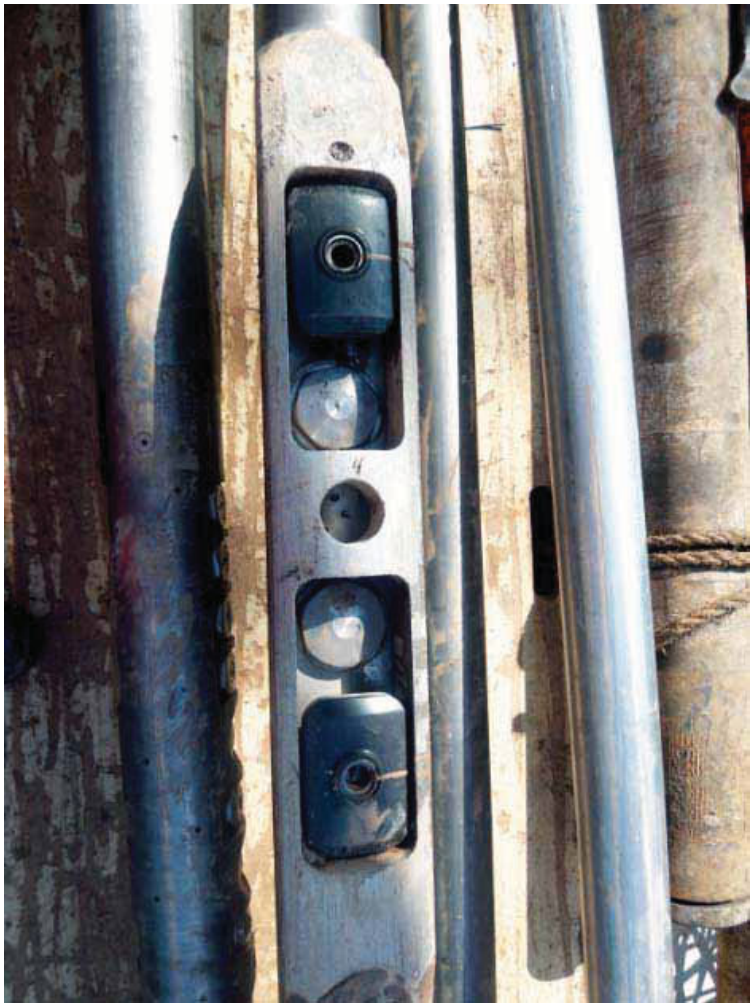

Figure 1.3. Dual-probe formation tester (enlarged view).

Now, Figures 1.2 and 1.3 for single and dual-probe testers provide exploded views showing what single and dual probe formation testers *really* look like. When lowered into the hole and pressed against the sandface, the Darcy flow schematics given in Figure 1.4 applies. In these diagrams, the areas to the right of the red dashed line are taken as the flow domains; the left sides containing the pad and borehole are ignored. Since the resulting domains possess right-left symmetry, the flow due to a "source" (or a "sink") is considered for modeling purposes.

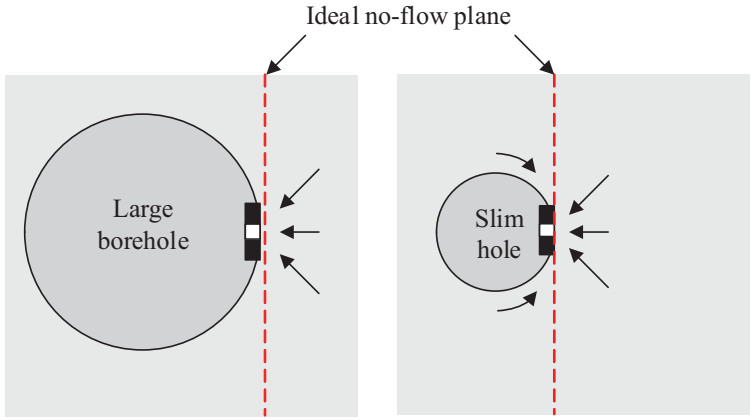

Figure 1.4. Piston pad pressed against the sandface.

Different source models exist which are not "created equal" by any means. Originally, decades ago, "point sources" were assumed at which fluid literally vanished and pressures became infinite; flowline storage and skin effects could not be modeled. The work of Proett, Chin and Mandal (2000) introduced spherical and ellipsoidal sources with nonzero dimensions as shown in Figure 1.5. Although the hardware associated with a flowline does not appear in this figure, flowline volume is accounted for by a term in the boundary condition formulation, as are skin effects, e.g., see Chin *et al* (2014). An "exact" closed form analytical solution for Darcy pressure, expressed in terms of complex complementary error functions, was given in the original publications.

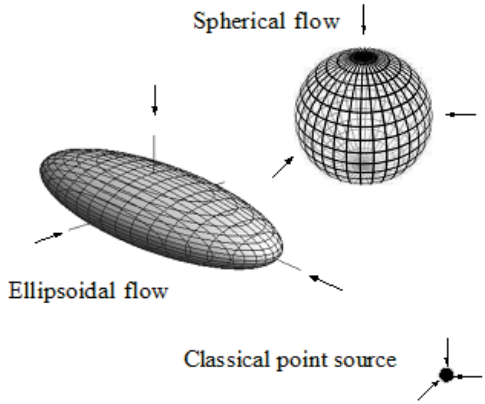

Figure 1.5. Idealized spherical flow for isotropic formations, ellipsoidal flow for transversely isotropic (anisotropic) media.

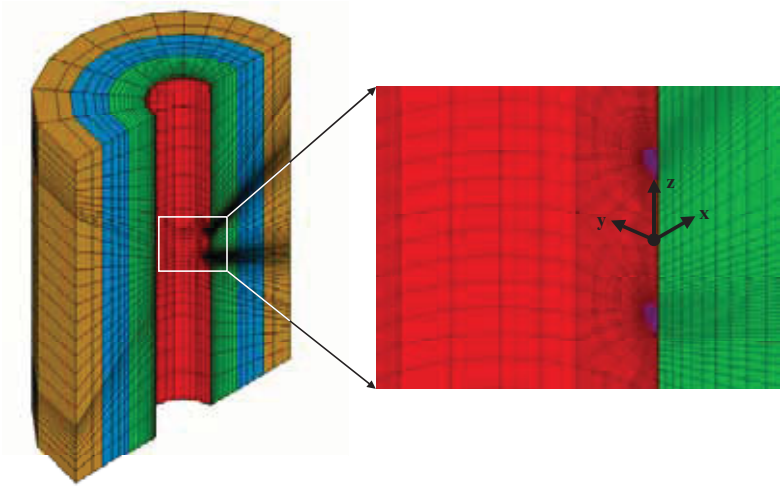

Figure 1.6. Near-Wellbore, Finite-Element Simulator (NEWS™) from Halliburton Energy Services.*

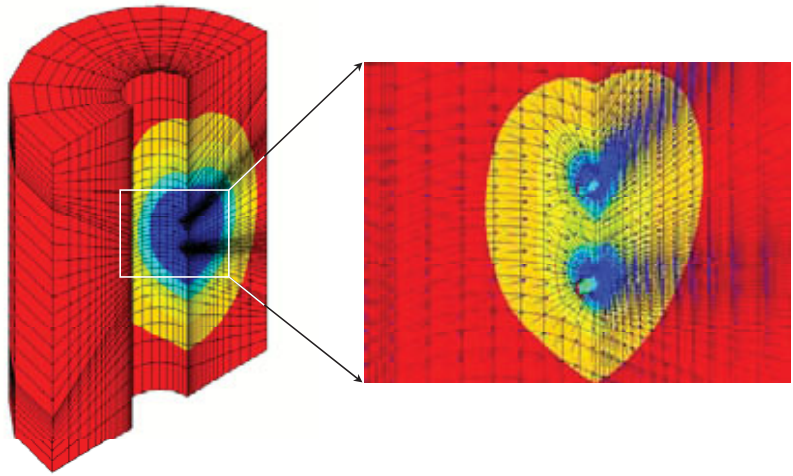

Figure 1.7. Dual-probe, pretest, simulation-pressure contours, 100-md isotropic formation (to the left are 1-psi color bands, and to the right are 10-psi color bands).*

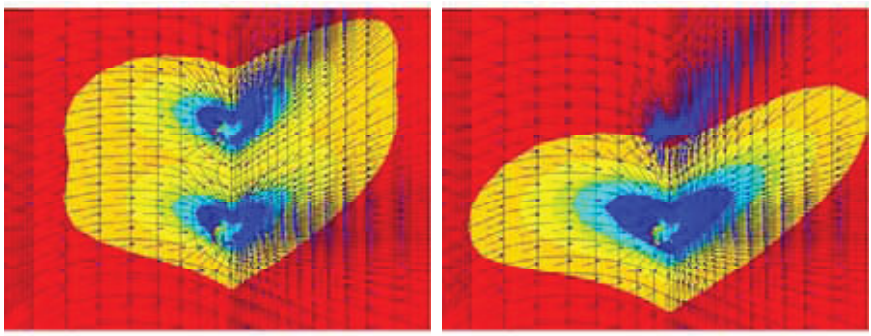

Figure 1.8. Pressure contours for the first drawdown with two probes and the second drawdown with one source probe, 100 md horizontal permeability, 0.1 k_v/k_h, and 10 psi color contour bands. *

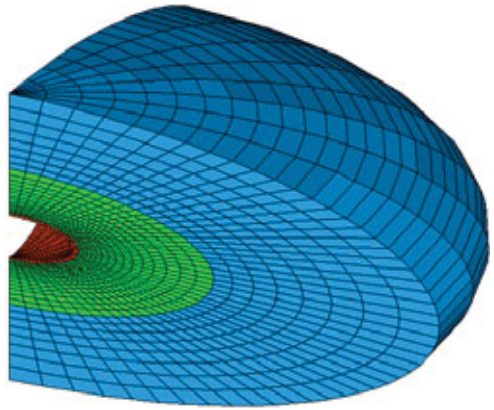

Figure 1.9. Ellipsoidal anisotropic flow, skin layer, three-dimensional finite element, boundary conforming mesh. **

* From "New Wireline Formation Testing Tool with Advanced Sampling Technology," by M.A. Proett, G.N. Gilbert, W.C. Chin and M.L. Monroe, SPE Paper 56711 presented at the 1999 SPE Annual Technical Conference and Exhibition held in Houston, Texas, October 3-6, 1999.

** From "Advanced Dual Probe Formation Tester with Transient, Harmonic, and Pulsed Time-Delay Testing Methods Determines Permeability, Skin, and Anisotropy," by M.A. Proett, W.C. Chin and B. Mandal, SPE Paper 64650 presented at the SPE International Oil and Gas Conference and Exhibition in China held in Beijing, China, November 7-10, 2000.

So how "exact" is exact? Although fluids no longer vanished at a point and pressures were no longer infinite, the finite-radius models in Figure 1.5 bore significant physical limitations. For example, by assuming right-left symmetry about the red dashed line in Figure 1.4, flow perpendicular to the red line cannot be modeled; thus, it is not possible to consider the effects of fluid invasion or dynamic mudcake growth. In addition, borehole size and formation tester pad geometries cannot be studied. Although far from ideal, it is clear that the need for usable math models drives the assumptions behind those in Figure 1.5, but it is now clear why formulas like "$k_s = CQ\mu/(2\pi r_p \Delta P)$" contain "calibration constants" C that conveniently lump all non-ideal effects into one single coefficient. We emphasize at this point that different size pads will have different constants; furthermore, steady-state models are calibrated differently from transient models, and high-mobility calibrations will differ from those for low-mobility. Hence, the development of interpretation models, in which permeabilities are predicted from pressure transient data, is far from trivial.

Just how are calibration constants determined? Quite simply, one needs to have truly "exact solutions" in a physical sense. These can be obtained computationally using three-dimensional simulations or experimentally in test fixtures developed for formation testing applications. Examples of numerical solutions from the lead author's prior work are shown in Figures 1.6 – 1.9. Effects include mudcake modeling, cylindrical borehole radius effects, pad geometry influence, and so on. Despite the apparent geometric generality, such models are not exact in a true sense. All numerical models, whether they are finite difference or finite element in nature, approximate derivatives using Taylor series and neglect higher-order terms. This omission, together with computer round-off errors, results in "artificial viscosity" which effectively changes the assumed input permeabilities. In other words, forward simulation results will typically not correspond to the permeabilities entered into the input box; inverse permeability predictions, for this reason, will not be correct if they are obtained by repeatedly running a forward simulator.

Fully three-dimensional simulators such as those cited in Figures 1.6 – 1.9 are not ideal for other reasons. First, they are difficult to set up; and second, they require significant computation times, often hours. As such, they are typically not used for inverse methods or engineering trend analysis. An intermediate compromise between these methods and the spherical or ellipsoidal source methods in Figure 1.5 is the axisymmetric "ring source" sketched in Figure 1.10. While the red vertical line of symmetry in Figures 1.4 and 1.5 disallows flow across it, thus making the modeling of fluid invasion, mudcake growth and borehole mud pressure impossible, the annular ring at the top of Figure 1.10, when hosted by cylindrical coordinates as suggested at the lower sketch, does allow the specification of additional physical effects.

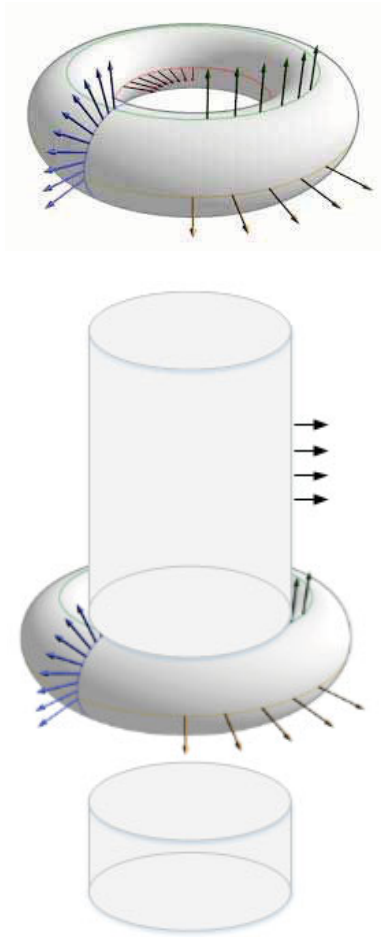

Figure 1.10. Axisymmetric ring source.

Such models allow us to address the effects of "supercharging." In many modern low-mobility applications, mudcakes do not form rapidly because filtration is inhibited by formation resistance. Consequently, the effects of high mud pressure are "felt" by the formation, and predicted pore pressures based on idealized inverse models such as those assuming Figure 1.5 are not correct. Thus, their properties must be well understood, and the development of multiphase flow models with time-varying invasion, as discussed later in this book, helps in this endeavor. But ring source models, still, are approximate; while they do allow borehole effects, pad geometries are however neglected and "calibration constants" are still required.

1.3 Experimental Methods and Tool Calibration

Mathematical models, we now understand, are far from perfect and their practical use requires calibration. The simplest, that is, "$k_s = CQ\mu/(2\pi r_p\ \Delta P)$" cited earlier, assumes steady-state conditions when transient flowline effects have completely dissipated. This formula for spherical permeability extends an earlier result for an isotropic drawdown permeability $k_d = Cq\mu/(2\pi r_p \Delta P)$ where ΔP is the drawdown pressure, C is a flow shape factor (known colloquially as a "fudge factor"), q is the volume flow rate, μ is the liquid viscosity, and r_p is an "effective probe radius."

For convenience, the "$C/(2\pi r_p)$" is usually represented as a single number, say $k_d = 5{,}660\ q\mu/\Delta P$. Here k_d, q, μ and ΔP are expressed in md, cc/s, cp and psi. The constant 5,660 applies to the "standard" RFT probe (that is, "Repeat Formation Tester™ tool offered by Schlumberger). When the "large diameter" or the "fast-acting" probe is used, the constant should be 2,395; for the "large-area packer," the constant becomes 1,107 (e.g., see Schlumberger's Log Interpretation Principles/Applications (1989) for details). These values are calibration constants accounting for non-spherical effects like borehole wall curvature and pad geometry. We emphasize that they apply to the steady spherical model only. If early time transient models are used, in particular, those where flowline effects are significant in low mobility applications, the "Schlumberger constants" cited above do not apply and need to be determined on a case-by-case basis. In fact, calibration challenges grow when anisotropic formations are targeted – the constants may vary dip angle and simple logging solutions may prove difficult. But short of a complete three-dimensional inverse solution (unlikely to be developed), the marriage of convenience formed by simple models and practical calibration is likely to survive indefinitely.

The need for experimental single and multiphase calibration for "formation testing while drilling" (FTWD) interpretation models was first recognized by Halliburton during its development of GeoTap™. In its approach, the calibration constant for the spherical flow models due to Proett and Chin was simply absorbed into the definition for an "effective probe radius R_{eff}" where, in our present notation, $R_{eff} = GF \times R_w$ where GF is a "geometric factor" and R_w is the true nozzle (or spherical well) radius. Details are provided in "Results of Laboratory Experiments to Simulate the Downhole Environment of Formation Testing While Drilling," by H. Lee (University of Texas at Austin), M. Proett (Halliburton Energy Services), P. Weintraub (Halliburton Energy Services), J. Fogal (NuTech Energy) and C. Torres-Verdín (University of Texas at Austin), SPWLA 45th Annual Logging Symposium, held in Noordwijk, The Netherlands, June 6–9, 2004, with graphics and photographs from a complementary SPWLA 2004 poster presentation. The poster and photographs are reprinted with permission from the Society of Petrophysicists and Well Log Analysts.

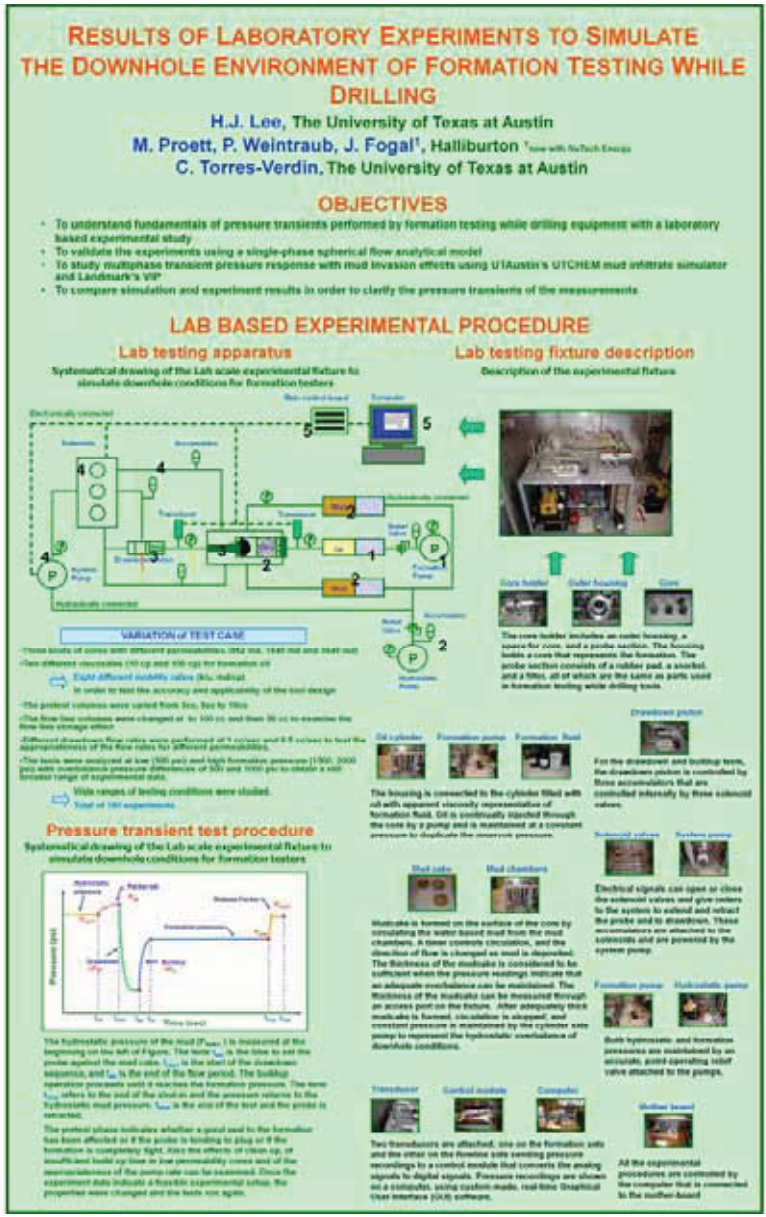

Figure 1.11a. Laboratory calibration facility (reprinted with permission from the Society of Petrophysicists and Well Log Analysts (SPWLA)).

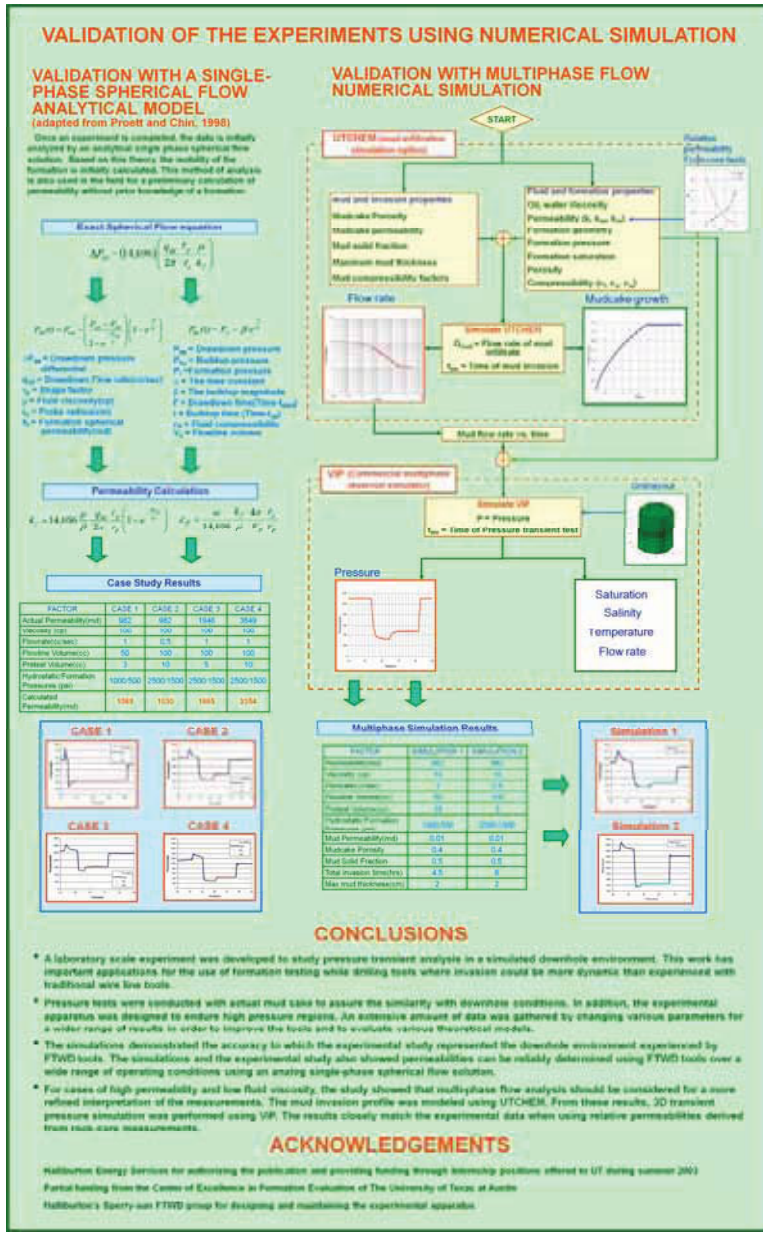

Figure 1.11b. Laboratory calibration facility (reprinted with permission from the Society of Petrophysicists and Well Log Analysts (SPWLA)).

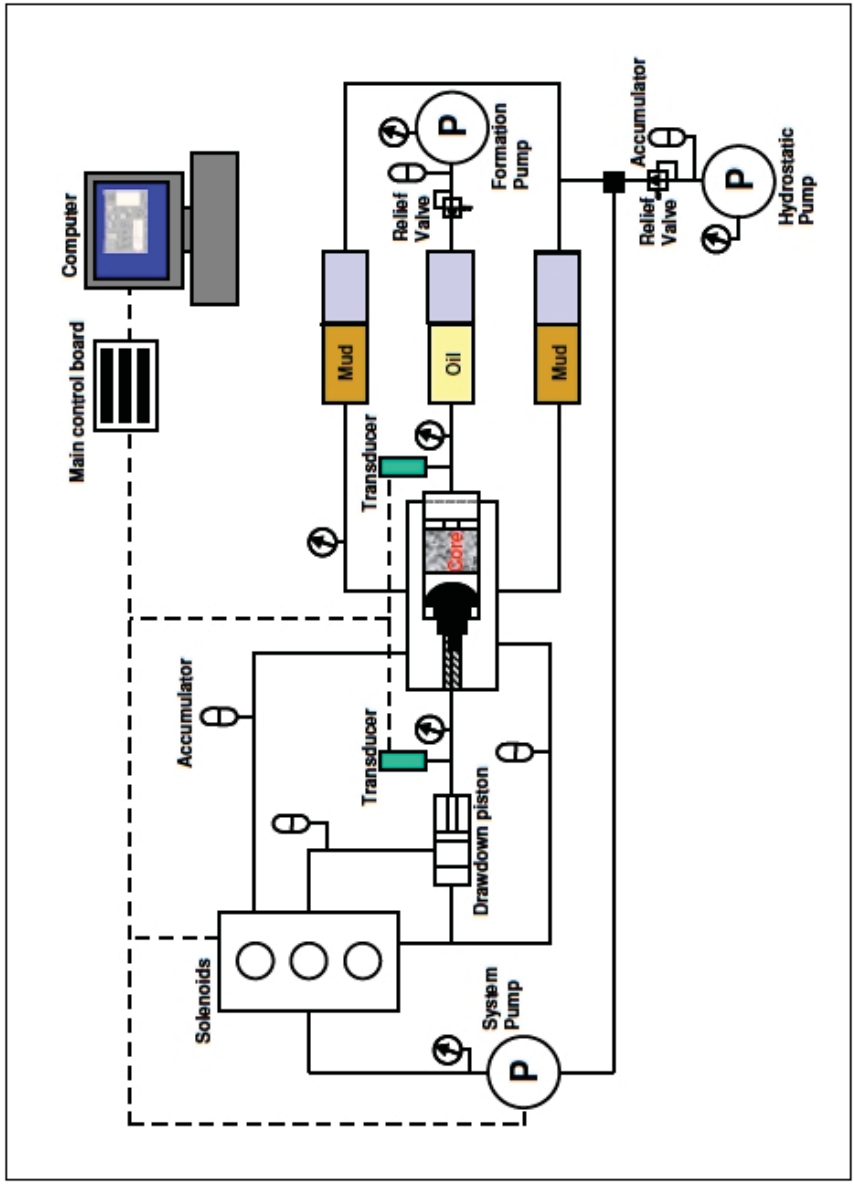

Figure 1.12. Experimental fixture for formation tester operation under downhole conditions with mud and fluid invasion (reprinted with permission from the Society of Petrophysicists and Well Log Analysts).

Figure 1.13a. Formation testing lab experimental fixture.

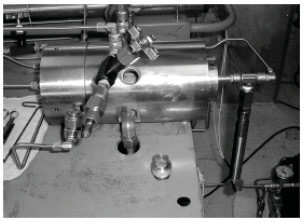

Figure 1.13b. Core holder (includes housing, core, probe section, rubber pad, snorkel and filter).

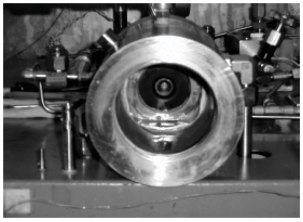

Figure 1.13c. Outer housing, core end view.

Figure 1.13d. Core samples (note curvature).

From "Results of Laboratory Experiments to Simulate the Downhole Environment of Formation Testing While Drilling," by H. Lee, M. Proett , P. Weintraub, J. Fogal and C. Torres-Verdín, SPWLA 45th Annual Logging Symposium, The Netherlands, June 2004, with graphics and photographs from a complementary SPWLA 2004 poster. Reprinted with permission from the Society of Petrophysicists and Well Log Analysts.

Figure 1.13e. Cylinder with oil with viscosity of formation fluid.

Figure 1.13f. Pump injects oil at constant pressure to simulate reservoir.

Figure 1.13g. Piston for drawdown-buildup controlled by accumulators activated by solenoid valves.

Figure 1.13h. Mudcake formed on core surface by circulating water-based mud (thickness is monitored and controlled).

From "Results of Laboratory Experiments to Simulate the Downhole Environment of Formation Testing While Drilling," by H. Lee, M. Proett , P. Weintraub, J. Fogal and C. Torres-Verdín, SPWLA 45th Annual Logging Symposium, The Netherlands, June 2004, with graphics and photographs from a complementary SPWLA 2004 poster. Reprinted with permission from the Society of Petrophysicists and Well Log Analysts.

Figure 1.13i. Mud chambers.

Figure 1.13j. Solenoid valves control drawdown-buildup piston.

Figure 1.13k. System pump (accumulators are attached to solenoids and powered by system pump).

Figure 1.13l. Hydrostatic pump (hydrostatic and formation pressures maintained by accurate, point-operating relief valve attached to formation and hydrostatic pumps).

From "Results of Laboratory Experiments to Simulate the Downhole Environment of Formation Testing While Drilling," by H. Lee, M. Proett , P. Weintraub, J. Fogal and C. Torres-Verdín, SPWLA 45th Annual Logging Symposium, The Netherlands, June 2004, with graphics and photographs from a complementary SPWLA 2004 poster. Reprinted with permission from the Society of Petrophysicists and Well Log Analysts.

Figure 1.13m. Pressure transducer (two used, one on formation side and other on flowline side).

Figure 1.13n. Control module.

Figure 1.13o. Computer with graphical user interface.

Figure 1.13p. Mother board (experiment controlled by computer connected to mother board).

From "Results of Laboratory Experiments to Simulate the Downhole Environment of Formation Testing While Drilling," by H. Lee, M. Proett , P. Weintraub, J. Fogal and C. Torres-Verdín, SPWLA 45th Annual Logging Symposium, The Netherlands, June 2004, with graphics and photographs from a complementary SPWLA 2004 poster. Reprinted with permission from the Society of Petrophysicists and Well Log Analysts.

The Halliburton test fixtures shown in Pages 14-20 illustrate the substantial effort required in calibrating formation tester tools together with the early-time, low-mobility predictive methods used. In general, the constants so obtained will differ from those for steady-state formulas like "$k_s = CQ\mu/(2\pi r_p \Delta P)$." A good discussion on such methods is offered in "Concept of Geometric Factor and Its Practical Application to Estimate Horizontal and Vertical Permeabilities," by Sheng, Georgi and Burge, SPE Reservoir Evaluation and Engineering Journal, December 2006, pp. 698-707. Again, we emphasize that the early-time permeability prediction formulas assume single-phase flow under ideal spherical conditions – the latter condition means that the mudcake is presumed to seal perfectly and fluid invasion does not occur.

Of course, in many low-mobility applications, cake formation is slowed by reduced filtration and the dynamics of mudcake growth are important – this is particularly so in studying "supercharging" where the pressure near the sandface is a combination of borehole and reservoir values. In this case, how much of the pressure measured by the formation tester "belongs" to reservoir effects is crucial and must be studied by multiphase simulators such as those presented in Chapters 6, 7 and 8. These, too, must be calibrated, with laboratory based experimental results. These had been reported in "Formation Evaluation Using Repeated MWD Logging Measurements," by Chin, Suresh, Holbrook, Affleck and Robertson, presented at the *SPWLA 27th Annual Logging Symposium*, Houston, TX, June 9-13, 1986, and subsequent math models were derived in the lead author's book Formation Invasion, *with Applications to Measurement-While-Drilling, Time Lapse Analysis and Formation Damage* (Gulf Publishing, 1995). These works drew upon experimental results from linear and radial flow test vessels placed within Catscan imaging machines. Under constant pressure drop conditions, both invasion front and mudcake thickness were monitored versus time, and analytical models were constructed using "moving boundary" methods which allowed dynamic boundary motion. Examples of the work are shown below.

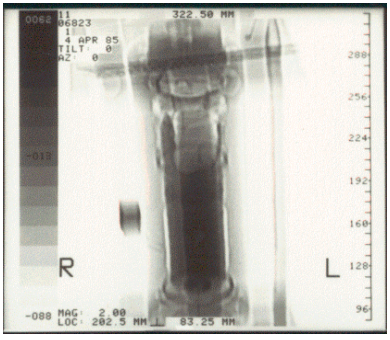

Figure 1.14a. Catscan, linear test vessel with core sample.

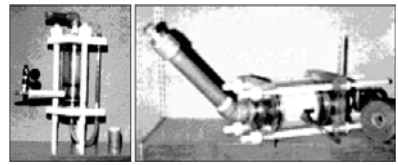

Figure 1.14b. Radial flow test vessel.

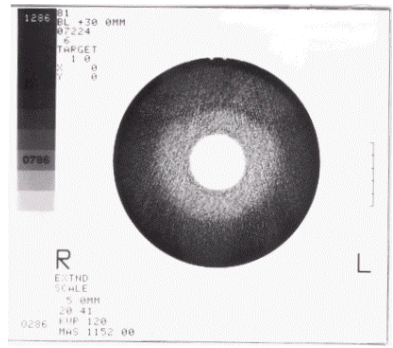

Figure 1.14c. Catscan, invasion in radial core sample.

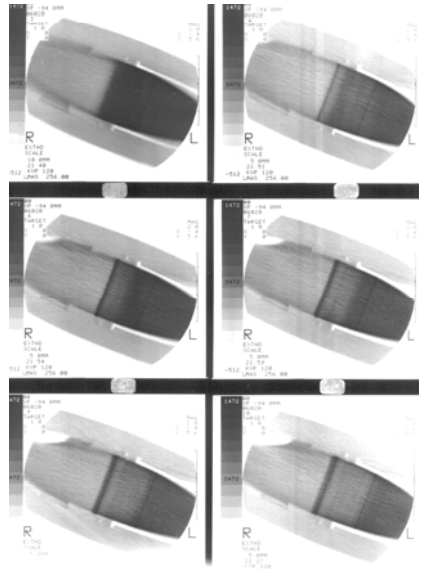

Figure 1.14d. Linear flow Catscans, thin dark mudcake at center of core and invasion front at density contrast (flow, left to right).

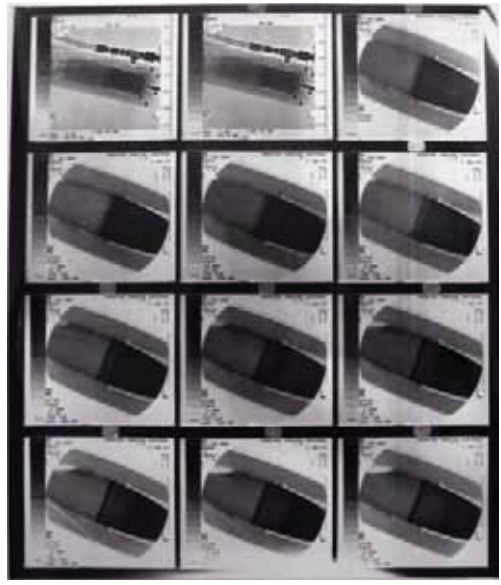

Figure 1.14e. Linear flow Catscans, standard optical contrast.

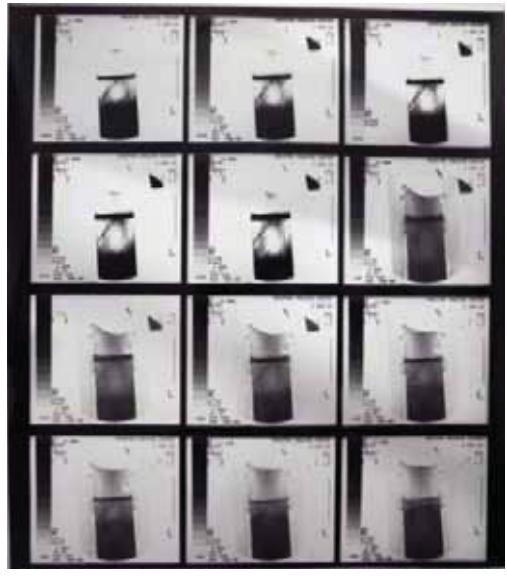

Figure 1.14f. Linear flow Catscans, enhanced contrast.

1.4 References

Chin, W.C., Formation Invasion, *with Applications to Measurement-While-Drilling, Time Lapse Analysis and Formation Damage*, Gulf Publishing, Houston, 1995.

Chin, W.C. and Proett, M.A., "Formation Evaluation Using Phase Shift Periodic Pressure Pulse Testing," United States Patent No. 5,672,819, awarded September 30, 1997.

Chin, W.C., Suresh, A., Holbrook, P., Affleck, L., and Robertson, H., "Formation Evaluation Using Repeated MWD Logging Measurements," *SPWLA 27th Annual Logging Symposium*, Houston, TX, June 9-13, 1986.

Chin, W.C., Zhou, Y., Feng, Y., Yu, Q. and Zhao, L., Formation Testing: Pressure Transient and Contamination Analysis, John Wiley & Sons, Hoboken, New Jersey, 2014.

Proett, M.A., Chin, W.C. and Mandal, B., "Advanced Dual Probe Formation Tester with Transient, Harmonic, and Pulsed Time-Delay Testing Methods Determines Permeability, Skin, and Anisotropy," SPE Paper 64650, *SPE International Oil and Gas Conference and Exhibition*, Beijing, China, November 7-10, 2000.

Proett, M.A., Gilbert, G.N., Chin, W.C., and Monroe, M.L., "New Wireline Formation Testing Tool with Advanced Sampling Technology," SPE Paper 56711 *SPE Annual Technical Conference and Exhibition*, Houston, Texas, October 3-6, 1999.

Proett, M.A. and Waid, M.C., "Wireline Formation Testing for Low Permeability Formations Utilizing Pressure Transients," United States Patent No. 5,602,334, awarded February 11, 1997.

Sheng, J.J., Georgi, D.T. and Burge, J., "Concept of Geometric Factor and Its Practical Application to Estimate Horizontal and Vertical Permeabilities," SPE Reservoir Evaluation and Engineering Journal, December 2006, pp. 698-707.

Staff, Fundamentals of Formation Testing, Schlumberger Marketing Communications, Houston, 2006.

2
Single-Phase Flow
Forward and Inverse Algorithms

Because the authors' prior book Formation Testing: Pressure Transient and Contamination from John Wiley & Sons is relatively new, appearing only in 2014, it is fitting to provide a concise summary of the methods and algorithms introduced there so that the contributions of the present book can be viewed and quickly understood in context. The work provided in this chapter sets the stage for the advanced drawdown-buildup and phase delay models discussed in Chapters 3 and 4.

2.1 Overview

We describe a comprehensive set of integrated formation testing forward and inverse analysis tools developed for wireline and "formation testing while drilling" (FTWD) applications in hardware design and pressure transient interpretation. The methods, based on rigorous Darcy flow formulations, are solved analytically in closed form whenever possible and cross-checked in different limits to ensure physical consistency and accuracy.

The transient problem for formation tester liquid pressure response in anisotropic media with flowline storage and skin at arbitrary dip, earlier solved in exact, closed analytical form assuming ellipsoidal sources (using complex complementary error functions), is used to derive exact solutions to several inverse problems where permeabilities are sought when dip angle and source and observation probe pressure drops are given.

First, the zero-skin forward solution is evaluated in the steady-state limit for constant rate pumping. Explicit inverse formulas are derived for all horizontal and vertical permeabilities and dip angles. With pressure drops computed at various dip angles from the forward simulation, derived formulas are used to predict both assumed permeabilities, demonstrating their utility in field interpretation. Neglect of dip angle can lead to significant errors in anisotropy prediction. Moreover, multi-valued inverse solutions exist: for a given set of pressure drops, three permeability pairs are found which require resolution from additional logging data.

Second, the "with-skin" forward solution is evaluated at steady-state for constant rate pumping to develop formulas relating source and observation probe pressure drop, vertical and horizontal permeabilities and skin factor. An algorithm giving possible solutions for both permeabilities and skin at any dip angle when both pressure drops are known is derived. Because only two pressure data points are assumed, additional logging information is needed to render a unique determination.

Third, short-duration "pulse interactions" at the observation probe are used to determine anisotropy (analogous to the pulses emanating from acoustic tools). These are strongest and most advantageous at low permeabilities where diffusion predominates. Short pulses, high in frequency content, provide detailed information. Multi-pulse wave-trains with different flow rates, pulse durations and separations enable multiple fast test suites at the rigsite without requiring new hardware. They are accurate, economical and reduce tool sticking risks in tight zones.

Fourth, "phase delay" approaches for permeability prediction analogous to electromagnetic logging methods are described. Sinusoidal pressure transients are created at the pumping probe. Their amplitudes and phases are measured at one or more observation probes. These are interpreted using Darcy analysis models. As with pulse interaction methods, phase delay approaches allow short-duration tests that are economical, safe and characterized by high signal-to-noise ratios.

Fifth, a full 3D horizontal well model for single-probe, dual-probe, dual-packer and elongated pad tools with real mandrels in layered media is given, with computations showing effects of azimuth and bed boundary on pressure response and their implications on permeability prediction. While *source models* require dual-probe data for inverse application, *full 3D models* can be used with single-probe FTWD tools (measuring azimuthal pressures) to provide clues related to permeability, anisotropy and bed thickness.

Finally, real-time FTWD pore pressure and mobility prediction is discussed. Such problems, key to drilling safety and rapid economic evaluation, involve transient data distorted by flowline storage effects. Accurate predictions are possible using a minimum of pressure data. We develop rational polynomial expansion methods that do not require exponential, real or complex complementary error functions, and moreover, do not use regression or least-squares smoothing filters that introduce diffusive assumptions beyond those implicit in Darcy's laws. Rapid analysis frees microprocessor resources for other important control and interpretation functions needed during drilling.

2.2 Basic Model Summaries

In formation tester pressure transient analysis, two general types of practical field applications arise, namely, "forward modeling," in which source and observation probe responses are sought when fluid, formation and tool parameters are specified, and "inverse modeling," in which k_h and k_v permeabilities (and possibly pore pressure) are required when all other parameters are given.

Forward models have been developed to a high degree of sophistication. Almost twenty years ago, Proett and Chin (1996) published the first full three-dimensional finite element analysis assuming realistic borehole environments with pad, probe, mandrel, flowline storage and bedding plane effects. These are reviewed in Formation Testing Pressure Transient and Contamination Analysis (Chin *et al*, 2014), which also cites extensions to include coupled dynamic mudcake growth and supercharge corrections.

Chin and Proett (2005) provided finite difference models that included multiphase miscible and immiscible effects. In downhole sampling, the time required to pump until clean in-situ fluids are obtained is important. This time scale differs from that used for pressure transient interpretation. Figures 2.1a,b illustrate capabilities that have been used to design new tools and interpret transient data obtained in complicated environments. Figure 2.1c shows Catscan experiments in which dynamic cake growth is measured in cores with different permeabilities. This is important to supercharge and contamination corrections.

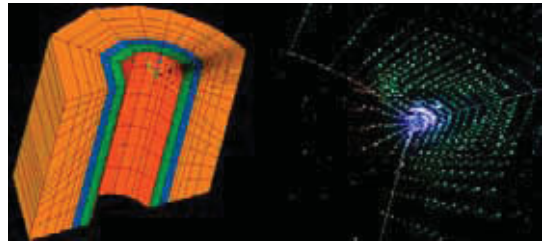

Figure 2.1a. Finite element model, flow vectors near probe.

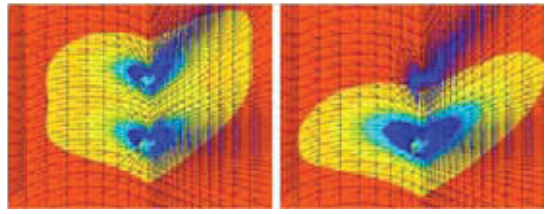

Figure 2.1b. Pressures for drawdown with two probes (left) and one (right).

While fully three-dimensional models are important in their own right, they do require complicated inputs, numerical simulation expertise, not to mention sophisticated and expensive computing environments that host high-overhead software and long calculations. Thus, fast methods that retain the basic elements of the physics are desirable, particularly for field office use and real-time downhole analysis. A number of simpler formulations are possible. These range from elementary point source models, which unfortunately "blow up" at the "r = 0" origin, to finite radius models, which apply flowline storage and skin boundary conditions at spherical source surfaces (ellipsoidal in transversely isotropic flow).

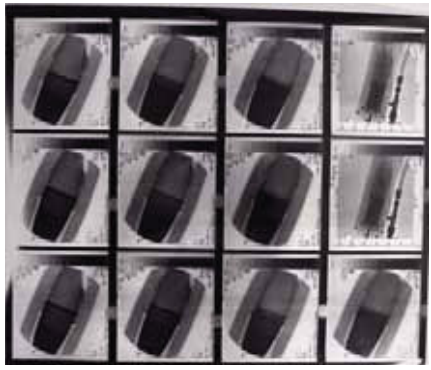

Figure 2.1c. Catscan results (flow from top to bottom, darkening lines at center indicate cake growth in time).

This chapter also introduces new physical concepts in pressure transient interpretation using innovative math models first described in Chin *et al* (2014). So that the ideas are clearly explained, math details are omitted in favor of examples, although shorter summaries are offered. For readers interested in analytical and numerical details, reference to the book is necessary. Several new capabilities and modules are available and, for convenience, are referred to by a "FT-" designation with "FT" referring to formation testing.

2.2.1 Module FT-00

This deals with exact transient liquid response in homogeneous anisotropic media. It solves for the unsteady Darcy pressure field about an ellipsoidal source surface immersed in a transversely isotropic infinite homogeneous medium allowing full skin effect and flowline storage boundary conditions. This "nonzero radius source" model is more powerful than limited point source approximations because it handles nearfield boundary conditions without becoming singular at the origin as do point source models. We emphasize that cylindrical borehole effects and drilling fluid invasion are not directly incorporated.

The earlier exact analytical solution, posed in terms of the complex complementary error function erfc(z), applied to a single drawdown or buildup and was limited to zero dip angles. To be effectively used for job planning and inverse applications, such as those considered here, improvements were needed.

(1) The erfc function in most scientific software libraries does not converge for certain ranges of complex arguments, and unfortunately, those associated with flowline storage effects on the order of those encountered in real formation testing tools (storage distorts pressure transients and its understanding is important to pressure and mobility interpretation). A new, fast and accurate subroutine is used which converges for a much wider range of complex arguments. Split-second response with fourteen digit accuracy guarantees robust and stable numerical performance.

(2) While the original work formally applied to pressures at all points, that is, all observation points in addition to source points, in reality, the former could not be computed because products of very large and very small numbers were involved. This equivalently meant that time superpositions of different flowrates (necessary to model multirate pumping) could not be computed accurately. Here, instead of dealing with erfc directly, a function of erfc, namely "$\exp(-z^2)$ erfc(- i z)" where z = x + iy, is considered, which avoids the foregoing complications. Thus, pressures can be computed at any observation location, and also, multirate pumping applications can be modeled. With this extended capability available, the original theory was extended to include all nonzero dip angles.

(3) The model applies to liquids only and not to nonlinearly responding gases (gas pumping introduces thermodynamics and high compressibilities). Work in this area is described later under FT-06, 07.

(4) The model applies to an ellipsoidal source immersed in a transversely isotropic homogeneous medium (reducing to a spherical source in isotropic media). This means that there is no cylindrical borehole and there are no layers or barriers. By "skin effect," we imply conventional damage mechanisms that would be found on the surface of the assumed ellipsoidal source. This is physically related to the formation damage seen in drilling mud invasion through cylindrical holes.

(5) Module FT-00 is discussed here because it is used to provide exact pressure data needed for inverse pore pressure and permeability prediction interpretation. Just as important, this high level formulation provides the foundation for our first inverse module FT-01 (solving for permeability and anisotropy exactly) when steady dual probe pressure data is available. FT-01 is based on rigorous math. The equations for FT-00 are evaluated in analytical closed form for asymptotically large times to develop formulas for pressure response that are independent of porosity, fluid compressibility and flowline volume. These formulas are inverted to

derive governing algebraic equations for k_h, k_v and k_h/k_v which can be solved exactly in terms of source and observation probe pressure drops. Thus, solutions to the inverse problem, which in the literature often imply running forward simulators repeatedly, is actually solved explicitly and exactly using non-iterative methods. FT-01 assumes the availability of steady-state dual probe pressure data. This is often not the case with low permeability formations. For such problems, a short-time "pulse interaction" method is developed which importantly uses FT-00 as the primary history matching tool. The pulse interaction method, as will be explained, is most effective in tight formations because high levels of diffusion cause individual pump pulses to interact strongly. This interaction is strongly dependent on formation anisotropy. The pulse interaction method is later complemented by "phase delay" and "rapid drawdown-buildup" analyses. These methods taken together cover a broad range of applications.

2.2.2 Module FT-01

We offer additional details related to the new steady-state inverse method. Although the pressure response in a liquid is linear and superposition applies, the asymptotic evaluation of that expression at large time yields nontrivial dependencies in permeability that lead to different (but mathematically consistent and correct) equations for k_h, k_v and the anisotropy k_h/k_v. In fact, cubic equations of the form $k_h^3 + (\ )\ k_h + (\ ) = 0$, $k_v^{3/2} + (\ )\ k_v + (\ ) = 0$ and $(k_h/k_v) + (\ )\ (k_h/k_v)^{1/3} + (\ ) = 0$ are obtained where ( ) represents various lumped parameters depending on pressure drops, fluid and formation properties. Because k_h generally exceeds k_v, its solution is more reliable with less noise contamination.

As is known from algebra, the polynomial k_h equation may have three real roots, or it may have one real and two complex conjugate roots. Only positive real solutions for k_h are physically meaningful – if several real positive roots are found, other logging data will be needed for a unique determination. On the other hand, negative permeabilities are not meaningful. Small imaginary parts, however, do not rule out the usefulness of roots (with positive real parts) since these typically arise from the use of unequilibrated pressure data or data inconsistent with Darcy's equations, e.g., pad slippage, transducer calibration and thermal effects.

2.2.3 Module FT-03

FT-00 and FT-01 derive from the same high-level mathematical source formulation, and the forward and inverse solutions used here are "exact" in the sense that they follow from closed form analytical solutions. However, this does not mean that they are exact in a physical sense. Source solutions possess spherical symmetries (ellipsoidal in anisotropic media) that, while elegant

theoretically, are not representative of real tools – that is, pad nozzles mounted on solid mandrels. Consider a real tester, say a single-probe FTWD tool, logging a horizontal well in transversely isotropic media. A top-mounted pressure transducer will "see" essentially k_v while one that is side-mounted will see basically k_h (actually, complicated functions of the two apply at any specific azimuthal angle). It is clear that pressure drops obtained at two different angles can be used to determine the k_h and k_v provided a 3D model is available to perform the required history matching.

This capability presently exists: as a drillstring torques and un-torques, it winds and unwinds, taking it through a range of twist angles. We emphasize that, in contrast to conventional dual-probe interpretation methods assuming axially displaced pressure measurements, it is possible to determine k_h and k_v with a single-probe tool provided a 3D algorithm is used for azimuthal interpretation. Module FT-03 provides this capability, allowing convenient representation for pad and packer sources, arbitrary azimuthal and axial placement for multiple probes and modeling of bed effects.

Other FT modules will be discussed separately addressing, e.g., nonlinear gas responses and thermodynamic effects, highly transient (as opposed to constant or piecewise-constant multirate) pumping, two phase flow, and so on. We digress temporarily from our basic model overview and introduce new permeability prediction methods by way of examples before continuing. We begin by presenting the capabilities of the new forward simulator FT-00.

2.2.4 Forward model application, Module FT-00

We summarize the required input parameters by reproducing the software screen shown in Figure 2.2a. Several blocks are apparent, namely, "Fluid and Formation Parameters," "Tool Properties," and "Pumping Schedule." Figure 2.2a shows input parameters for a multi-rate pump schedule with mixed production and injection with both long and short time durations. This supports constant rate pumping, pulse interaction and phase delay modeling. Simulations are extremely fast and typically require at most seconds. The pump schedule used appears in Figure 2.2b. Source and observation probe transient pressure responses are given in Figures 2.2c,d. Observe the rapid equilibration in source pressure and close correlation between it and flow rate (that is, compare Figures 2.2b and 2.2c). At the observation probe, as is evident from Figure 2.2d, slower equilibration and smearing due to diffusion are found. In general, the lower the permeability, the greater the diffusion. This diffusion is both bad and good. It is "bad" when steady pressure drops are required for input into steady flow models for permeability prediction. However, it is "good" when specially designed transient interpretation approaches are available. For low permeability formations, the dynamical interaction between short duration pressure pulses is strong and highly dependent on anisotropy. Also, phase delays are more apparent and therefore useful in low mobility applications.

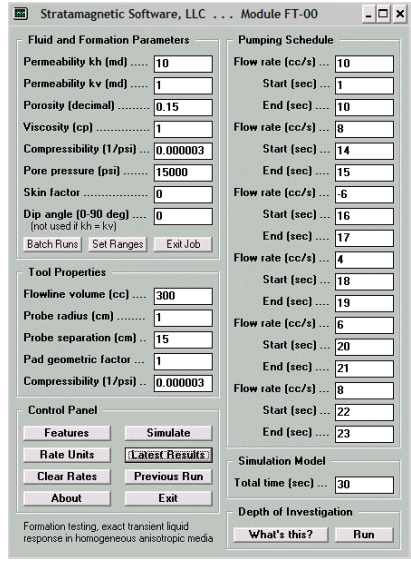

Figure 2.2a. Forward simulation assumptions.

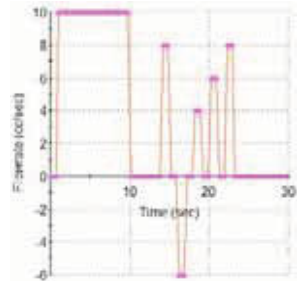

Figure 2.2b. Pumpout schedule, volume flow rate.

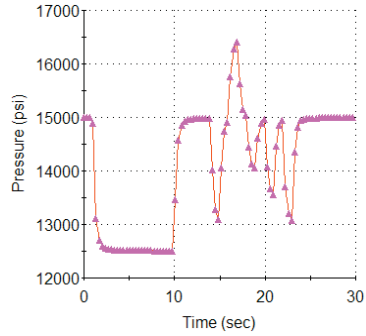

Figure 2.2c. Source probe pressure.

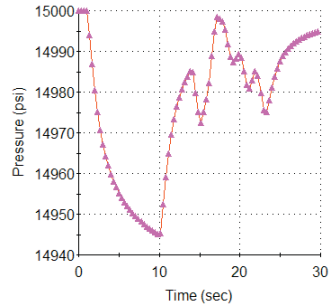

Figure 2.2d. Observation probe pressure.

2.2.5 Inverse model application, Module FT-01

In the following run, the fluid, formation and tool parameters of Figure 2.2a are retained, except that the dip angle is changed from 0 to 45 deg and a constant 10 cc/s pump rate is assumed for all time. Source (left) and observation probe (right) pressure transient responses appear in Figure 2.3a – again, observe how diffusion slows the equilibration to steady-state just 15 cm from the source.

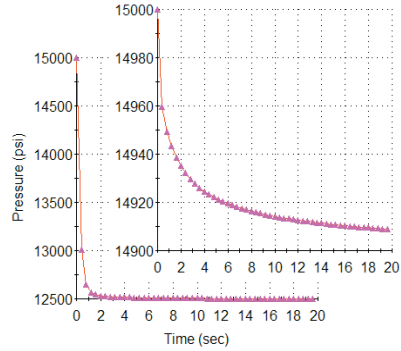

Figure 2.3a. Source (bottom) and observation probe (top) pressure responses.

Time (s)	Δp_{source} (psi)	Δp_{observ} (psi)
0.100E+02	-0.24948E+04	-0.85789E+02
0.200E+02	-0.25001E+04	-0.91263E+02
0.500E+02	-0.25045E+04	-0.96208E+02
0.100E+05	-0.25116E+04	-0.10421E+03

The computed Δp's (probe *minus* a dynamically unimportant pore pressure) are shown above. We now consider the inverse problem and assume that pressure pair data (above table) are obtained from a dual probe tool. The input screen in Figure 2.2a assumes that the skin coefficient is S = 0; thus, the assumptions in the software screen for FT-01 in Figure 2.3b consistently assume zero skin.

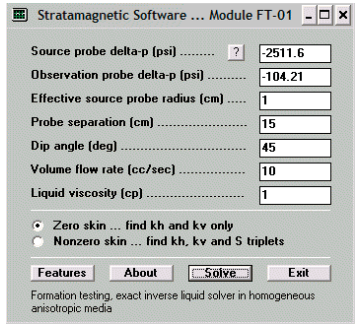

Figure 2.3b. Inverse steady-state solver.

First consider our 10,000 sec (three hour) data. Exact calculation shows three possible solutions, namely,

```
Tentative permeabilities (md) ...

Complex KH root # 1:  -10.97 +   0.00 i, KV:   0.83
Complex KH root # 2:   10.07 +   0.00 i, KV:   0.99
Complex KH root # 3:    0.91 +   0.00 i, KV: 121.96
```

In this case, two of the roots are easily ruled out; the first k_h is negative, while the third k_h is substantially less than k_v. The remaining k_h and k_v results, at 10.07 md and 0.99 md, are almost identical to the assumed 10 md and 1 md in the forward simulation creating the data. The method reproduces assumed permeability data exactly in this calculation with non-vanishing dip.

This success is a nontrivial event. FT-00 solves a fully transient model (via a complex complementary error function formulation with flowline storage and dip angle) while FT-01 solves an analytically derived polynomial equation valid only at steady-state. Agreement and consistency between the two approaches ensures correct mathematics, physics and software logic. This large time validation case thus provides a demanding test of both models.

In field applications, one might use unsteady data that is not consistent with the math model due to cost considerations and risks of tool sticking. Using ten-second pressure data in this case gives k_h = 12.49 md and k_v = 0.65 md. Twenty-second data yields 11.68 and 0.74, while fifty-second data leads to 11.02 and 0.83 – all acceptable, relative to the 10 md and 1 md assumed in FT-00. This accuracy is possible because the formation is relatively permeable. However, in low-mobility applications, steady conditions are almost never realized and methods like FT-01 cannot be used. If in the screen of Figure 2.3b we had checked "nonzero skin," a different less restrictive math model with increased degrees of freedom is used. In the present calculation, the algorithm would return a list of possible solutions, that is, (k_h, k_v, S) triplets, together with the corresponding spherical permeability k_s listed at the far right of the table below (the zero skin solution obtained above is highlighted in red).

kh (md)	kv (md)	S	ks (md)
7.00	8.00	0.62	7.32
7.00	9.00	0.63	7.61
7.00	10.00	0.64	7.88
8.00	5.00	0.52	6.84
8.00	6.00	0.56	7.27
8.00	7.00	0.59	7.65
9.00	3.00	0.36	6.24
9.00	4.00	0.44	6.87
10.00	1.00	0.01	4.64
10.00	2.00	0.21	5.85

2.2.6 Effects of dip angle

The effects of dip angle are well known physically. For example, at zero dip, the tester "sees" k_h from all directions, while at 90 deg, it "sees" k_h from left and right, but k_v from top and bottom (actually, a complicated function of both applies at each azimuthal angle). Since $k_h > k_v$, the measured pressure drop in a vertical well is less than that for one that is horizontal or deviated. As an example, first consider the forward simulation in Figure 2.4a with zero dip angle and a pump rate fixed at 10 cc/s for all time. We vary dip from 0 to 90 deg with other parameters unchanged. Source pressure responses for all runs are identical since they depend on spherical permeability k_s only, as shown in Figure 2.4b. But, as expected, transient observation probe responses (numbered by dip angle) vary in both magnitude and shape as seen from Figure 2.4c. For the k_h = 10 md, k_v = 1 md example here, pressure drops vary over a 200 psi range as dip angles increase. Again, these results are exact.

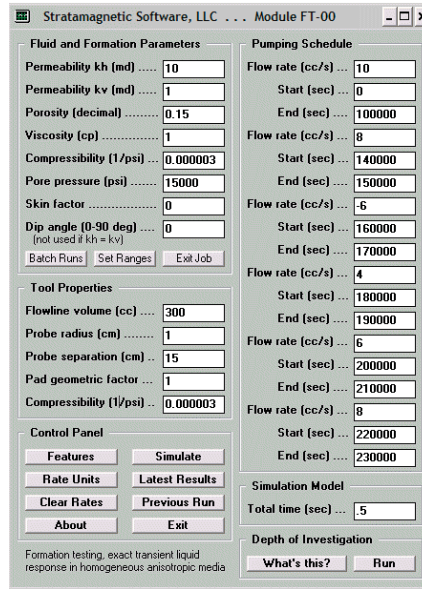

Figure 2.4a. Constant rate pumping example.

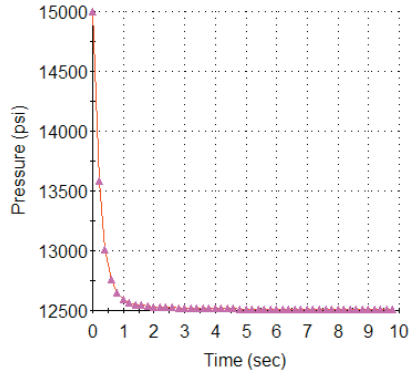

Figure 2.4b. Source probe response.

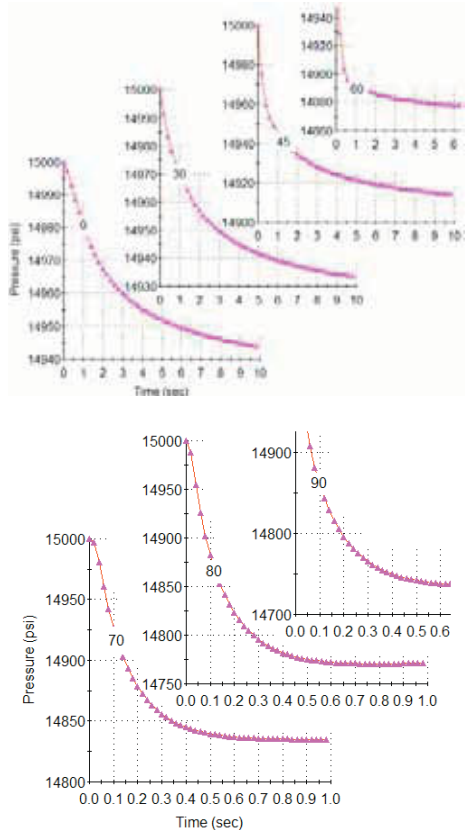

Figure 2.4c. Observation probe response versus dip angle.

We can view the foregoing conclusions from the inverse perspective. Suppose a deviated well were drilled at 45 degrees dip. The 45 degree dip, zero skin forward simulation gives large time (100,000 sec) pressure drops of 2,512 psi at the source and 104.6 psi at the distant probe; the corresponding inverse calculation gives a consistently accurate k_h = 10.02 md and k_v = 1.00 md (in agreement with permeabilities assumed in the forward FT-00 simulation).

But what if, for this measured pressure pair, the exact FT-01 inverse solver were not available? If the conventional industry-standard formula (implicitly assuming zero dip) were used, one would instead calculate k_h = 7.43 md and k_v = 1.81 md with a k_v/k_h of 0.244 versus an exact value of 0.1. Such errors imply grave production and economic consequences. In the table below, inverse calculations for permeability using FT-01 are performed with the above pressures through a range of dips to show the significance of hole deviation.

Dip	kh	kv	kv/kh
0	7.43	1.81	0.244
30	8.35	1.44	0.172
45	10.02	1.00	0.100
60	14.13	0.50	0.035
70	20.88	0.23	0.011
80	41.89	0.06	0.001
90	424.89	0.00	0.000

2.2.7 Inverse "pulse interaction" approach using FT-00

The above inverse approach requires fully equilibrated steady pressure drop data at source and observation probes. In a high permeability environment, this is not severe; as seen earlier, 20 sec data may well suffice under certain conditions if data integrity is not an issue. In "tight" formations, however, steady observation probe responses may not be possible for hours or days. Even if rig costs were not a concern, the risks of tool sticking are – thus, one seeks permeability prediction methods that respond to earlier time dynamic data. Now, the use of steady formulas for permeability interpretation is an artificial limitation used only to render the mathematics tractable. As noted, steady conditions are usually achievable in higher permeability formations so that such models are sometimes useful.

But in low permeability zones, field experience and exact calculations (using FT-00) show that *source probe* responses equilibrate very rapidly. Since they depend only on the spherical permeability k_s (and not k_h or k_v individually), the value of k_s inferred from the source probe pressure drop is an accurate one for interpretation purposes. The conventional steady flow permeability formula $k_s = Q\mu/\{4\pi R_w(P_0 - P_s)\}$ can be used which, again, only constrains the relationship between k_h and k_v (here, Q is volume flow rate, μ is viscosity, R_w is effective probe radius, and "$P_0 - P_s$" is the source probe pressure drop). However, in order to individually quantify k_h and k_v, additional information is required. Unlike the method underlying FT-01, we will not draw upon steady-state pressure data obtained at the observation probe.

In the illustrative example below, a k_s of 4.642 md (corresponding to our earlier k_h = 10 md, k_v = 1 md and S = 0 case) is fixed throughout and simulations are performed with different combinations of k_h and k_v. Again, source probe results for the three runs are identical, but observation probe pressure transients are discernible from each other. Figures 2.5a and 2.5b are clearly different – the former is highly smeared while the pulses in the latter remain distinct; peak pressure drops (from printed FT-00 output not shown) are 19 psi for Figure 2.5a and 159 psi for Figure 2.5b. Again, these differences are seen from early time transient behavior.

Observation probe pressure transient waveform shapes in Figures 2.5b and 2.5c are similar, at least on a normalized basis. However, they are very different in magnitude. From printed FT-00 output, peak pressure drops are 159 psi and 787 psi, respectively. Clear differences in observation probe characteristics suggest that permeability contrasts can be effectively examined using short duration pulse interference rather than long time steady-state drawdown. The dynamical interactions are strongly dependent on anisotropy.

Under what circumstances is our "pulse interaction method" expected to perform well? Interestingly, the lower the permeability, the better the accuracy – a counter-intuitive situation at odds with our experience with steady-state methods. The explanation is simple: at low mobilities, diffusion predominates, so that dynamical interactions between short pulses with high frequency content are strongest; thus, high signal-to-noise ratios are achieved for history matching.

Interference effects are most pronounced at low perms when diffusion is dominant, precisely the field condition associated with long wait times, high rig costs and increased risk of tool sticking. In contrast, large time pressure responses associated with constant rate drawdown methods only produce small pressure drops which may not be accurately measured. We emphasize that, at earlier times, the effects of porosity, compressibility and flowline volume do appear, so that calculations using different pulse types with varied durations, amplitudes and time separations is advisable.

Additional research is presently directed at optimizing the pulse sequence used, e.g., evaluating different combinations of pulse amplitude, width, separation and number. It is important to emphasize that no new hardware is required for pulse interaction analysis. Our FT-00 may be used in infinite homogeneous media, but in applications where bedding plane effects are important, the FT-03 simulator discussed later applies. Because we are evaluating flow differences associated with diffusion itself, it is important that the host math model does not introduce numerical diffusion effects related to truncation errors. These effects, referred to as "artificial viscosity," are most prominent with finite difference and finite element simulators, even when second, up to fourth order, schemes are employed. For this reason, exact analytical models such as FT-00 should be used to interpret pulse interactions.

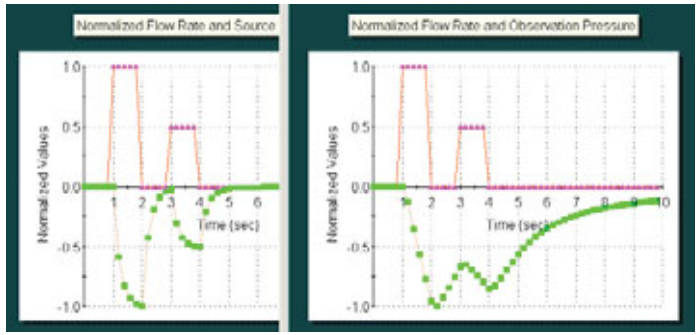

Figure 2.5a. $k_h = 10$ md, $k_v = 1$ md (that is, $k_h > k_v$).

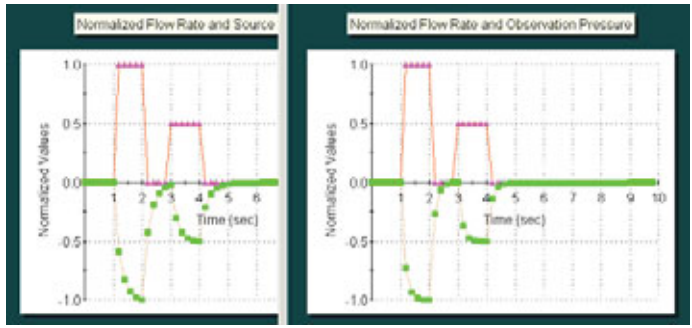

Figure 2.5b. $k_h = k_v = 4.642$ md (that is, isotropic).

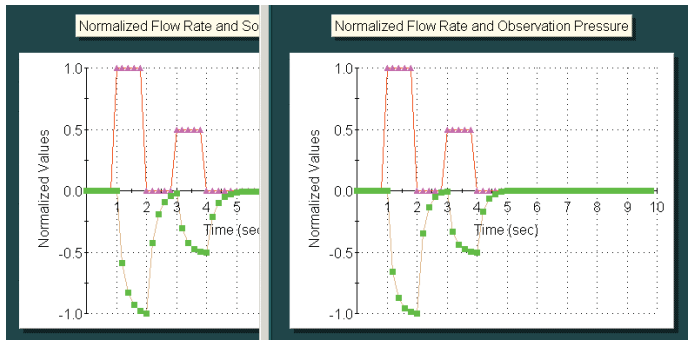

Figure 2.5c. $k_h = 1$ md, $k_v = 100.0$ md (that is, $k_h < k_v$).

In this discussion, we focused on a zero skin example; space limitations preclude similar discussions on nonzero skin results. However, the basic ideas and results for pulse interaction methods remain unchanged.

2.2.8 Computational notes

We observe that short time data contain porosity, compressibility and flowline effects. The exact solution in FT-00 is expressed in terms of the complex complementary error function erfc(z) where z = x + iy is a complex number (x and y are related to fluid, formation and tool parameters and here do not represent the spatial coordinates). In typical function evaluations, e.g., those offered in scientific program libraries, solutions are only possible for a small range of small imaginary values for small real values of the argument near zero, which unfortunately limits the usefulness of our exact solutions (for large real arguments near forty, solutions for all imaginary values are possible). This limitation is most serious for tool applications with flowline volumes such as those typically encountered in logging.

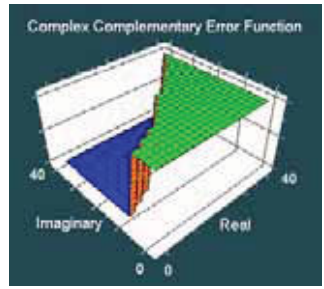

Figure 2.6a. Standard erfc(z) evaluation for x > 0, y > 0.

Figure 2.6a shows Quadrant 1 z ranges where x > 0, y > 0 for which erfc(x + *i*y) can and cannot be computed by standard (IMSL) algorithms. The lower left (blue) zone shows where solutions cannot be computed due to numerical overflow, while the elevated right (green) zone highlights where solutions can be found. The blue zone contains parameters where flowline volume effects are important. Improvements are now given.

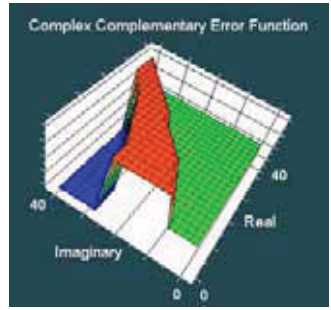

Figure 2.6b. Improved erfc function evaluation.

For our approach to be useful, more robust numerical evaluations are now possible to enable a much broader range of arguments for successful calculation, as shown in Figure 2.6b. The far left (blue) zone still represents solutions that cannot be computed; fortunately, the corresponding arguments do not represent parameters often used in practical formation testing. The far right (green) domain indicates solutions possible using conventional approaches, while the new and sizable middle (red) zone depicts an increased range of newly available computations for erfc(z). Accuracy and speed are emphasized in the method, e.g., hundreds of evaluations per second on typical personal computers.

2.2.9 Source model limitations and more complete model

The word "exact" often used in the literature (including the author's publications) conveys a sense of confidence and accuracy that may not be deserved. As discussed in Chapter 1, "exact" refers to closed form analytical solutions for forward and inverse models – a significant endeavor – but which applies only to approximate source formulations of the tester. While the source model used, which applies boundary conditions on an ellipsoidal surface (with nonzero minor and major radii, and which does not "blow up" as in point source models) is useful in this regard, the model nevertheless is approximate in a physical sense.

In other words, the model "sees" a type of spherical symmetry when, in fact, real formation tester nozzles mounted on real mandrels "see" largely ahead and are shielded from behind by solid material. Thus, a real tool in an anisotropic formation will measure different pressure responses as the transducer is rotated azimuthally about the tool axis. A full three-dimensional model accounting for actual tool geometry plus bedding plane effects could be used as a history matching tool to determine k_h and k_v from pressure data collected at different angles. Such data is possible in field practice. Since the drillstring torques and un-torques during operation, it winds and unwinds, offering the opportunity to record pressures at different azimuths.

Whereas earlier examples emphasized the use of dual probe tools, the above ideas apply to single-probe tools such as those in simple wireline and FTWD applications. The basic idea is simple: two pressure measurements are need to provide two permeabilities. These can be taken from axially or azimuthally displaced probes, or both, as in three-probe tools. This leads to the question, "How can we construct a simulator capable of addressing these inverse and job planning needs?"

Module FT-03 solves the transient Darcy partial differential equation for transversely isotropic media on a boundary-conforming curvilinear mesh in the cross-plane intersecting the tool. The model is fully three-dimensional. High resolution is provided about the borehole using "glove tight, wrap-around" inner meshes while those in the farfield conform to bed boundaries. An algebraically expanding mesh with an origin centered at the pad nozzle or oval pad, or at the

center of a packer, provides good resolution axially. The computational domain appears in Figure 2.7a. The transient equation is solved by finite difference, forward time marching using an Alternating-Direction-Implicit (ADI) scheme for fast speed and numerical stability.

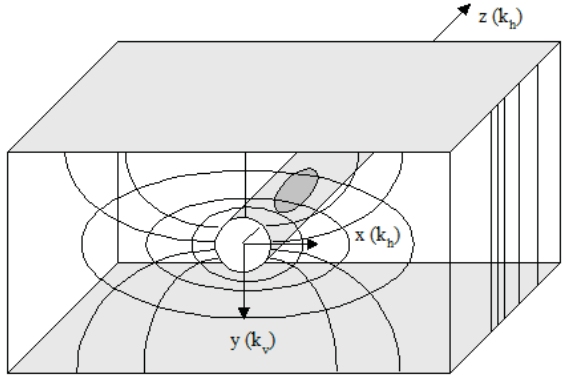

Figure 2.7a. Three-dimensional computational mesh.

We focus on key simulation results and consider the diagrams in Figure 2.7b. The left two show a horizontally oriented borehole in a homogeneous transversely isotropic formation, while the right one shows the same hole bounded by upper and lower planes (along which pressure or no-flow conditions may be prescribed). Again, A "sees" essentially k_h, B sees primarily k_v, while the general point C sees a complicated function of the two. If pressure measurements at any two of A, B or C are available, one can determine both permeabilities by history-matching using a three-dimensional simulator such as FT-03.

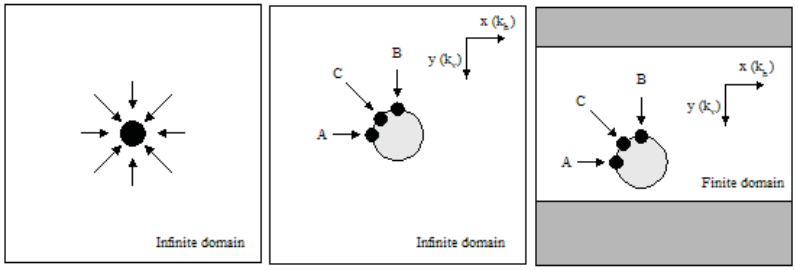

Figure 2.7b. Borehole orientation.

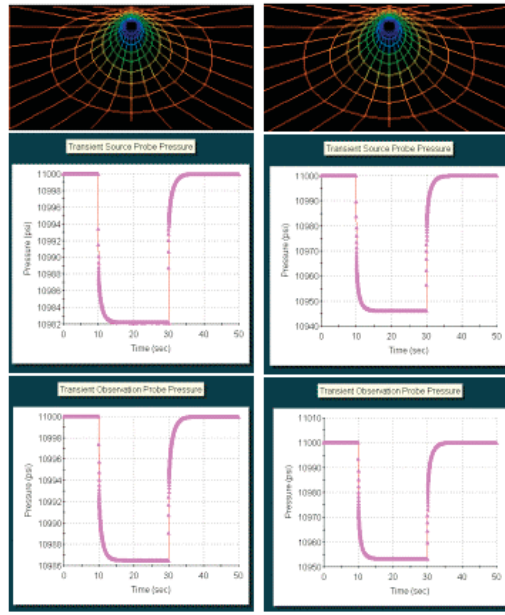

Figure 2.7c. Azimuthal pressure response in layered media.

For our purposes, we refer to Figure 2.7c for a low perm run with typical field parameters. The source probe Δp at A is 18 psi (because the k_h it "sees" is high) while that at B is 54 psi (the k_v it sees is low). This sizable difference is detected at the source probe and can be used to estimate anisotropy. We emphasize that a single-probe tool can be used to determine k_h and k_v provided azimuthal measurements are taken. Figure 2.7c shows observation probe results, assuming that source and observation probes are in line axially (this is not required in general simulations). The effects of bedding plane proximity and centralization are subtle and general conclusions cannot be made. However, the simulator accounts for these as they affect azimuthal transducer placement.

2.2.10 Phase delay analysis, Module FT-04

The pulse interaction method, most effective at low perms, is closely related to our dynamical model for "phase delay" analysis. In electromagnetic logging, wave amplitude differences and phase delays between transmitters and receivers are used to infer resistivity anisotropy using Maxwell's equations. A simple formation testing analogy exists. If the pump piston is operated periodically and pressure amplitude differences and time delays are recorded between source and observation probes, then k_h and k_v can be obtained from history matching using a three-dimensional Darcy simulator. Permeability

formulas as functions of amplitude and phase delay are given in Chin et al (2014) for simple formations. In general, the lower the permeability, the higher the diffusion and the lengthier the phase delay. Larger delays mean more accurate time measurement and hence better predictions.

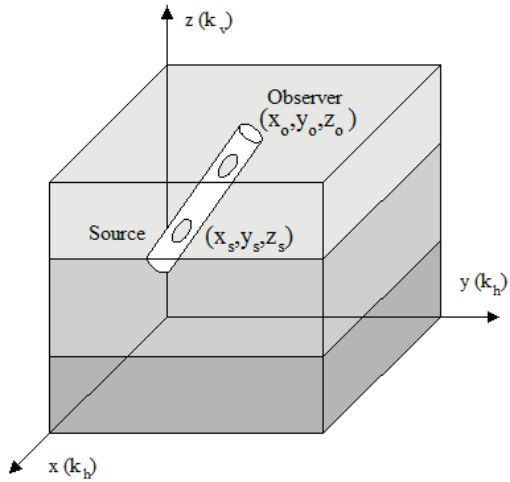

Figure 2.8a. Layered anisotropic media with dipping tool.

The model has since been extended significantly to layered anisotropic media for dipping tool applications, as shown in Figure 2.8a. This complication means that simple formulas are not available and the interpretation must be pursued numerically.

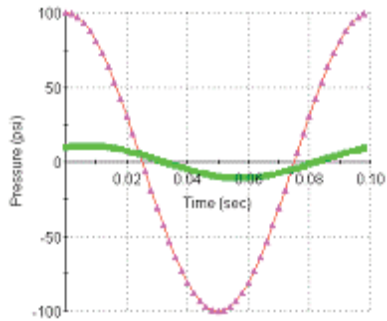

Figure 2.8b. Pressure response.

Figure 2.8b shows typical transient pressure responses calculated at source (red) and observation (green) probes using the FT-04 simulator of Figure 8a. The large amplitude decreases are typical of low permeability rocks, but small

pressure levels at the observation probe may be difficult to measure accurately. On the other hand, time delays are easier and more precise. Phase delays can be calculated using any number of models, e.g., our idealized source model FT-00, the "real tool" simulator FT-03, or the "source in layered media" model in FT-04. We will develop the subject of phase delays in great detail in Chapter 4.

2.2.11 Drawdown-buildup, Module FT-PTA-DDBU

In deep offshore wells where pressure limits separating borehole invasion and fracture are narrow, accurate real-time pore pressure and mobility prediction are essential to safety. Exact models like FT-00 provide forward analyses, calculating transient pressures when fluid, formation and tool properties are given. FTWD and "pressure-while-drilling" (PWD) require fast inverse methods that provide pore pressure for safety objectives and gradient analysis for fluid identification, plus mobility analysis for economic and production planning. These predictions are needed in real-time during drilling. Equations that support FTWD objectives can be derived from the exact, closed form, analytical solution underlying FT-00. Because "while drilling" data are typically early time (due to cost and stuck tool considerations), are often obtained in low mobility applications, or both, derived formulas used must account for highly transient behavior and flowline storage effects, which can distort and mask mobility trends residing in drawdown and buildup data.

Existing methods use exponential, real or complex complementary error functions, complicated integrals, and so on, combined with regression methods for interpretation. For instance, "least squares" fits are often employed, and while reasonable, they introduce arbitrary smoothing assumptions beyond those in Darcy's diffusion laws. It is essential that models invoke no additional flow approximations. Our inverse solution is derived using rational polynomial expansions that reduce the computational overhead associated with transcendental functions. This allows more data processing to be completed in a given time frame, thus freeing valuable microprocessor resources for other important interpretation and downhole control functions. Closed form analytical solutions are derived and used, and numerical regression and chi-square methods are never employed.

Two key models developed for "drawdown only" and "drawdown-buildup" applications were originally reported in Chin *et al* (2014). Both methods apply to transient pressure data distorted by flowline storage effects, and subset models (which run substantially faster for mobility prediction) are also available when steady-state pressures can be found for higher mobility or long test time applications. That prior work is briefly summarized below and much more general extensions are developed in Chapter 3 for problems with multiple drawdowns. Details of the mathematical derivations are also given.

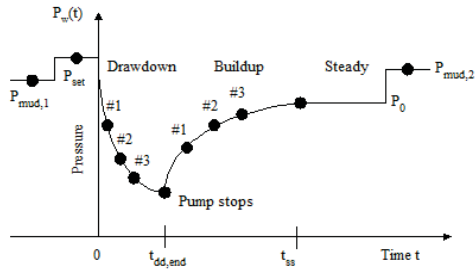

Figure 2.9a. Nomenclature for pressure transient analysis.

Unlike conventional models, ours only require three pressure-time data points along either drawdown or buildup curve, e.g., as shown in Figure 9a, plus auxiliary data related to test setup. For brevity only, we present examples using buildup data, noting that detailed write-ups are available upon request.

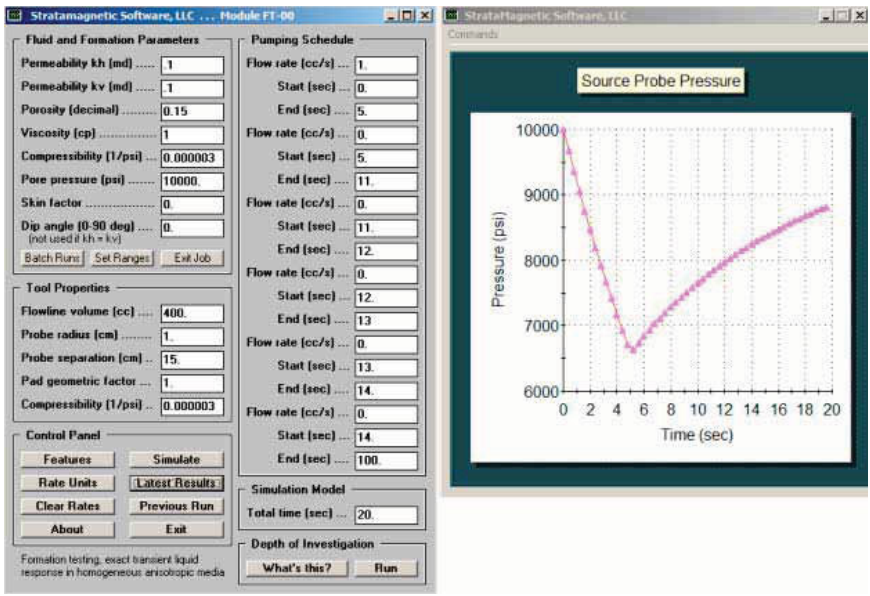

Figure 2.9b. Exact FT-00 forward simulation results from single pre-test (note large flowline volume assumed).

In Figure 2.9b, we use our exact FT-00 forward solver to create the source probe pressure transient data shown. From the input screen, the pore pressure is 10,000 psi while the mobility is 0.1 md/cp.

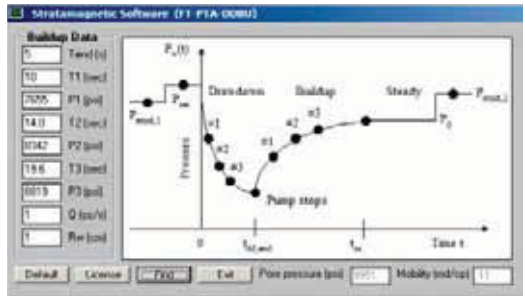

Figure 2.9c. Predicted pore pressure and mobility.

Figure 2.9c displays inputs for FT-PTA-DDBU with pressures taken at 10, 15 and 20 sec. Rapid calculation gives 9,951 psi and 0.11 md/cp, close to exact values in Figure 2.9b. Sensitivity analyses using other time data points yield only small variations. In Figure 2.9d, we create pressure data for two pre-tests having different flow rates.

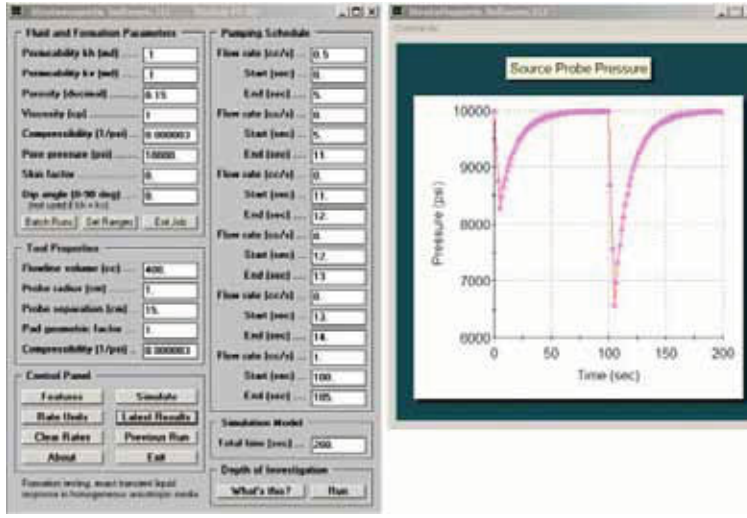

Figure 2.9d. Exact FT-00 forward simulation pressures for two sequential pre-tests used for input to inverse model (next page).

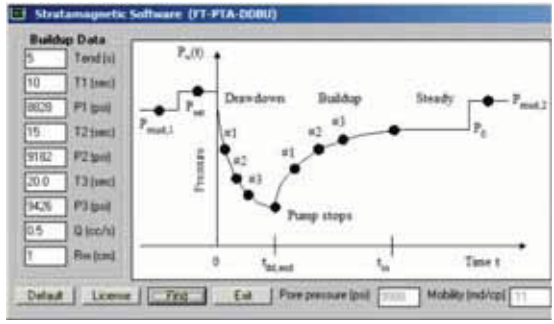

Figure 2.9e. Predictions (first pre-test).

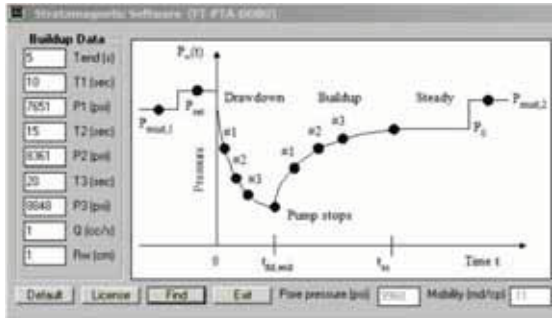

Figure 2.9f. Predictions (second pre-test).

Figures 2.9e and 2.9f offer predictions of 9,988 psi and 0.11 md/cp, and 9,960 and 0.11 md/cp, using first and second pre-test data, values very close to assumed numbers on the prior page. Again, the solutions execute rapidly, are analytical and easily programmed, e.g., ten-fifteen lines of source code depending on the host compiler language. Also, because no iterations are involved, downhole computer microprocessor resources are utilized efficiently and available for other interpretation and control functions. Algorithms have been completed and validated for "drawdown only" as well as buildup test cycles – multiple drawdowns followed by buildup are considered in Chapter 3.

2.2.12 Real pumping, Module FT-06

In real-world applications, flow-rate versus time functions are never constant or piece-wise constant. Flow rates invariably ramp-up and down, with such effects being more dramatic with gas pumping. These features must be modeled numerically and analytical methods are not possible. Figure 2.10a shows the interface for a liquid-gas simulator which supports flow-rate functions that may be, for instance, trapezoidal as in Figure 2.10b unlike the piecewise rectangular functions of Figure 2b. Source and observation probe pressures are also given.

Figure 2.10a. FT-06 liquid-gas simulator inputs.

Figure 2.10b. FT-06 pump rate and pressure solutions.

2.2.13 Closing remarks

We have introduced new ideas in formation tester pressure modeling and permeability interpretation. The forward and inverse methods apply to all service company tools, e.g., wireline or "while drilling," in single, dual-probe or packer operation modes. The methods described have been cross-checked and validated in different physical limits to ensure accuracy and consistency. Specific attention was focused on attractive user interface design (with automated color and line graphics) so that convenient field use with minimal training is possible.

2.2.14 References

Chin, W.C. and Proett, M., "Formation Tester Immiscible and Miscible Flow Modeling for Job Planning Applications," *46th Annual SPWLA Meeting*, New Orleans, LA, June 2005.

Chin, W.C., Zhou, Y., Feng, Y., Yu, Q. and Zhao, L., Formation Testing: Pressure Transient and Contamination Analysis, John Wiley & Sons, Hoboken, New Jersey, 2014.

Proett, M.A. and Chin, W.C., "Supercharge Pressure Compensation with New Wireline Formation Testing Method," 37th Annual SPWLA Symposium, New Orleans, Louisiana, June 16-19, 1996.

3
Advanced Drawdown and Buildup Interpretation in Low Mobility Environments

In conventional "repeat formation tester" (that is, Schlumberger RFT™) applications, permeabilities are predicted using steady-state spherical flow models for drawdown pressure. These assume higher mobilities which allow rapid equilibration. When mobilities are small, however, the formulas are not valid and detailed history matching with transient Darcy flow simulators is required. In our approach, fast, rigorous methods are developed using rapidly changing early-time drawdown or buildup data which satisfactorily predict mobility and pore pressure. Use of early data is crucial operationally because of reduced cost, logging time and risk of stuck tools. We emphasize that, unlike inverse models that repeatedly run forward models in "brute force" manner using guessed values for permeability, ours provide direct solutions for both permeability and pore pressure. Large flowline volumes are permitted as are unequally spaced points in time. Moreover, because the algorithm is compact and fast, it is easily adapted for downhole microprocessor use to support real-time applications. The technique is illustrated with data from a well known industry example.

3.1 Basic Steady Flow Model

The use of formation testers in permeability or mobility prediction is well established and numerous methods are available for different tool designs and operational procedures. The flow into the RFT™, sketched in Figure 3.1, is typically assumed to be rapidly established and "substantially steady-state" (e.g., see Dussan, Auzerais and Kenyon (1994)), as indicated by the bottom arrow (ours) in the familiar diagram of Figure 3.2.

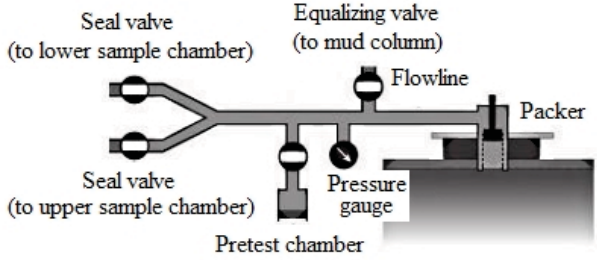

Figure 3.1. Repeat formation tester (RFT™).

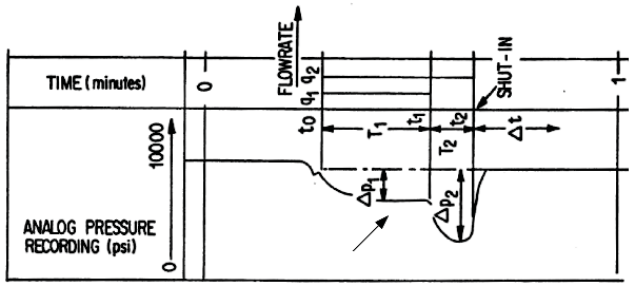

Figure 3.2a. Test procedure from U.S. Patent 5,279,153
(note flat pressure responses assuming quick equilibration)

If ΔP is the steady drawdown pressure, C is a flow shape factor, q is the volume flow rate, μ is the liquid viscosity, and r_p is an "effective probe radius," then the drawdown permeability can be calculated from the simple relation given by $k_d = C q\mu/(2\pi r_p \Delta P)$. For convenience, the "$C/(2\pi r_p)$" is usually represented as a single number, say $k_d = 5{,}660\ q\mu/\Delta P$. Here k_d, q, μ and ΔP are expressed in md, cc/s, cp and psi. The constant 5,660 applies to the "standard" RFT probe. When the "large diameter" or the "fast-acting" probe is used, the constant should be 2,395; for the "large-area packer," the constant becomes 1,107 (see Log Interpretation Principles/Applications (1989) for details – the notation used in this paragraph is retained for consistency with the existing literature and differs slightly with ours below). These values are calibration constants accounting for non-spherical effects like borehole wall curvature and pad geometry. These models have limitations, and to understand them, we develop a general approach. Interestingly, Figure 3.2a illustrates a "double drawdown" – Bowles (2004), in the context of dual packers, notes that double-drawdown tests are effective in removing the need to repeat formation tests. As we show in Section 3.4, Figure 3.2a data are analyzed by twice application of "$k_d = C q\mu/(2\pi r_p \Delta P)$" since the equilibrated pressure traces are independent. For low mobilities, this is not possible; we develop multiple-drawdown methods in Section 3.3 and show how permeabilities are predicted from resulting buildups.

3.2 Transient Spherical Flow Models

We consider the transient, compressible, Darcy flow of a liquid in a homogeneous, isotropic medium, and study the spherically symmetric flow produced into an idealized "spherical well" of radius R_w from an infinite reservoir. Unlike point sources in older studies, our pressures are never singular at the center since unrealistic "r = 0" locations are excluded. Our model simulates the transient dynamics of wireline or MWD testers, where R_w is the spherical probe radius. When we speak of "spherical wells," we do not imply that flowline storage effects are absent. In fact, a term "VC" describing the volume and fluid compressibility product is retained in a boundary condition applied at the spherical radius. We summarize results for isotropic flow with storage, and importantly, implications of the exact, closed form, analytical solution in Chin *et al* (2014). In their book, the authors also provide the exact solution for anisotropic flow with skin effects; our shorter summary is intended to introduce a novel inverse procedure for transient pressure drawdown and buildup data.

3.2.1 Forward or direct analysis

We first study the problem in which pressure responses are sought when fluid, formation and tool data are given. Let P(r,t) represent the transient fluid pressure, where r and t are radial and time coordinates. Also, let P_0 denote the constant initial and farfield pore pressure of the quiescent reservoir, while ϕ, k, μ and c, respectively, refer to rock porosity, isotropic permeability, liquid viscosity and compressibility. Again, R_w is the spherical well radius, and we denote by V the internal flowline volume associated with the formation tester hardware. In engineering applications, a geometric factor $G > 0$, determined through three-dimensional finite element flow analysis or laboratory experiment, is used to correct the spherical radius to GR_w for non-ideal pad, probe and borehole curvature effects.

This use of an "effective probe radius" $r_p = GR_w$ is equivalent to the empirical constant "C" above. Its value may vary among manufacturers and particular models, depending on the details of the mechanical design and possibly fluid flow parameters; ideally, for the sake of discussion, $G = 1$ is often assumed. The value of G may be determined by applying formulas derived here to simple experiments or field trials, as we will show later. In addition, a compressibility C (not to be confused with the calibration constant "C" above) is associated with the fluid inside the flowline, which is not necessarily equal to c in the formation. For example, C and c may differ by a ten-fold factor due to phase segregation effects.

For the single-phase Darcy flow problem, we denote by Q(t) the total volume flowrate produced by the spherical well, due to sandface production *plus* flowline volume storage effects. The initial-boundary value problem without skin effects is completely specified by the mathematical model

$$\partial^2 P(r,t)/\partial r^2 + 2/r\ \partial P/\partial r = (\phi\mu c/k)\ \partial P/\partial t \tag{3.1}$$

$$P(r,t=0) = P_0 \tag{3.2}$$

$$P(r=\infty,t) = P_0 \tag{3.3}$$

$$(4\pi R_w^2 k/\mu)\ \partial P(R_w,t)/\partial r - VC\ \partial P/\partial t = Q(t) \tag{3.4}$$

The "$4\pi R_w^2 k/\mu\ \partial P(R_w,t)/\partial r$" represents the contribution to Q(t) from flow through the sandface, arising as the product of the Darcy fluid velocity $k/\mu\ \partial P/\partial r$ and the spherical surface area $4\pi R_w^2$, while "$VC\ \partial P/\partial t$" represents the contribution associated with fluid expansion and decompression in the flowline.

3.2.2 Dimensionless formulation

In conventional pressure transient analyses, free parameters (typically related to storage) are retained in normalized formulations and varied to produce families of "type curves" for interpretation purposes. However, a more powerful approach enables analytical simplifications that render type curve modeling unnecessary – general exact solutions are obtained once and for all. To determine the governing dimensionless laws in their most fundamental form, we introduce nondimensional *italicized* variables *r*, *t*, and *p*, respectively normalized by the dimensional physical quantities r^*, t^*, and p^*, that is,

$$r = r/r^* \tag{3.5}$$

$$t = t/t^* \tag{3.6}$$

$$p(r,t) = \{P(r,t) - P_0\}/p^* \tag{3.7}$$

whose values are to be determined. It is also convenient to assume the total production (or injection) volume flow rate Q(t) in the form

$$Q(t) = Q_0\ F(t) \tag{3.8}$$

where Q_0 is a positive (or negative) reference flow rate, and the dimensionless function F(*t*) is given. For continuous constant rate drawdown or buildup, F(*t*) is unity; for piecewise-constant multi-rate pumping, F(*t*) is represented by a sequence of step functions. If we now choose

$$r^* = VC/(4\pi R_w^2\ \phi c) > 0 \tag{3.9}$$

$$t^* = V^2C^2\mu/(16\pi^2 R_w^4\ k\phi c) > 0 \tag{3.10}$$

$$p^* = VCQ_0\mu/(16\pi^2 R_w^4\ k\phi c) \tag{3.11}$$

the mathematical boundary value problem can be reduced to its simplest possible form, namely,

$$\partial^2 p(r,t)/\partial r^2 + 2/r\ \partial p/\partial r = \partial p/\partial t \tag{3.12}$$

$$p(r,0) = 0 \tag{3.13}$$

$$p(\infty,t) = 0 \tag{3.14}$$

$$\partial p(r_w,t)/\partial r - \partial p/\partial t = \mathrm{F}(t) \tag{3.15}$$

which is free of explicit parameters (e.g., type curve constants in conventional storage boundary conditions), except for the single dimensionless radius

$$r_w = 4\pi \mathrm{R_w}^3\ \phi \mathrm{c}/(\mathrm{VC}) \Rightarrow 4\pi(G\mathrm{R_w})^3\ \phi \mathrm{c}/(\mathrm{VC}) > 0 \tag{3.16}$$

which appears only in the argument of Equation 3.15. This dimensionless radius depends on the volume related parameters c, C, ϕ and $\mathrm{R_w}$ only, and not transport properties like permeability and viscosity.

3.2.3 Exact solutions for direct problem

In order to solve Equations 3.12 to 3.16, we introduce the Laplace transform

$$\boldsymbol{p}(r,\mathrm{s}) = \int_0^\infty \exp(-\mathrm{s}t)\ p(r,t)\ \mathrm{d}t \tag{3.17}$$

where $\mathrm{s} > 0$ is required in order that the integral exist. Detailed results appear in Chin *et al* (2014) and are not duplicated here. An exact solution for $\boldsymbol{p}$ can be found taking the form

$$\boldsymbol{p}(r,\mathrm{s}) = -\ \{\mathbf{F}(\mathrm{s}) r_w^{\,2} \exp(r_w \mathrm{s}^{1/2})\}\ \{r^{-1}\exp(-r\mathrm{s}^{1/2})/\{r_w \mathrm{s} + r_w \mathrm{s}^{1/2} + 1\} \tag{3.18}$$

which applies to *all* values of r. At the spherical source $r = r_w$, the above equation reduces to $\boldsymbol{p}(r_w,\mathrm{s}) = -\ \mathbf{F}(\mathrm{s})/(\mathrm{s} + \mathrm{s}^{1/2} + r_w^{-1})$.

Constant rate pumping. We give exact, closed-form, analytical solutions for simple transient build-up or drawdown, which can be used to construct more general flowrate solutions using superposition methods. Accordingly, consider $\mathrm{Q}(\mathrm{t}) = \mathrm{Q}_0\ \mathrm{F}(t) = \mathrm{Q}_0$ constant, taking $\mathrm{F}(t) = 1$, with $\mathrm{Q}_0 > 0$ for production and $\mathrm{Q}_0 < 0$ for injection. At the source, it follows that $\mathbf{F}(\mathrm{s}) = 1/\mathrm{s}$ and

$$\boldsymbol{p}(r_w,\mathrm{s}) = -\ 1/\{\mathrm{s}\ (\mathrm{s} + \mathrm{s}^{1/2} + r_w^{-1})\} \tag{3.19}$$

Recourse to numerical inversion is possible, but such algorithms are highly sensitive to discretizations in s-space and inaccurate. Fortunately, analytical solutions are possible. First we observe that Equation 3.19 can be re-expressed in simpler terms using partial fraction expansions as

$$\boldsymbol{p}(r_w,s) = -1/\{s\,(\beta_1 + s^{1/2})(\beta_2 + s^{1/2})\}$$
$$= \{1/(\beta_1 - \beta_2)\}\{1/(s\,(\beta_1 + s^{1/2})) - 1/(s\,(\beta_2 + s^{1/2}))\} \qquad (3.20)$$

where the *complex* constants β_1 and β_2 satisfy $\beta_1 = +1/2 - 1/2\,\sqrt{(1 - 4\,r_w^{-1})}$ and $\beta_2 = +1/2 + 1/2\,\sqrt{(1 - 4\,r_w^{-1})}$. If we now apply the transform-inverse relationship $1/(s\,(\beta + s^{1/2})) \Leftrightarrow \beta^{-1}\,\mathrm{erfc}(0) - \beta^{-1}\exp(\beta^2 t)\,\mathrm{erfc}(\beta\sqrt{t})$ and use the fact that $\mathrm{erfc}(0) = 1$, we obtain the *exact real* dimensionless transient source pressure as

$$p_{exact}(r_w,t) = \{1/(\beta_1 - \beta_2)\}\{\beta_1^{-1} - \beta_1^{-1}\exp(\beta_1^2 t)\,\mathrm{erfc}(\beta_1\sqrt{t})$$
$$-\beta_2^{-1} + \beta_2^{-1}\exp(\beta_2^2 t)\,\mathrm{erfc}(\beta_2\sqrt{t})\} \qquad (3.21)$$

valid for all time and all ranges of dimensionless variables. This applies only at the source, but solutions for $r > r_w$ at a distant probe or any observation point are offered in Chin *et al* (2014). The "erfc" in Equation 3.21 refers to the "complex complementary error function" with complex arguments. Upon evaluation, both source and observation point pressures always form real numbers as required.

In field operations, separate early, intermediate and late-time formulas are used to predict permeability or related quantities from pressure transient behavior. Until now, this practice is widespread because of mathematical difficulties in finding single exact solutions. Unfortunately, these time regimes are ambiguously defined – "how early is early" or "how late is late" depends on fluid and formation properties themselves, which are, of course, unknown. The availability of the single mathematical expression (developed here) valid for all time is important because it reduces interpretation uncertainties. This can be used to develop novel inverse procedures as we will later show.

3.2.4 Special limit solutions

Before considering the inverse problem, we demonstrate how the foregoing solution reduces to familiar expressions in special limits. To show that it reduces to known conventional results at small times, we introduce power series approximations for the exponential and complementary error functions, that is, $e^x = 1 + x + 1/2\,x^2 + 1/6\,x^3 + \ldots$ and $\mathrm{erfc}(x) = 1 - 2x/\sqrt{\pi} + 2x^3/(3\sqrt{\pi}) + \ldots$ in the exact solution. This procedure yields the familiar expansion

$$p(r_w,t)_{\textit{early-time from exact}} = -t + 4t^{3/2}/(3\sqrt{\pi})$$
$$+ (1-r_w)t^2/(2r_w) + 8(r_w-2)t^{5/2}/(15r_w\sqrt{\pi}) + \ldots \qquad (3.22)$$

Observe that Equation 3.22 provides a formal power series solution in t valid for small times. If we retain the first "$p(r_w,t) = -t$" term only and return to dimensional variables, we obtain the often used relationship

$$P(R_w,t)_{early\text{-}time\ from\ exact} = P_0 - Q_0\, t/(VC) \tag{3.23}$$

This "very-early-time" solution reproduces the well known linear variation of pressure with time; the proportionality factor depends on volume flow rate and flowline storage effects only. In field practice, the pressure response at very early time is used to predict the flowline compressibility C; the volume V is known from hardware specifications, and may vary from tool to tool, depending on the logging application. Dynamical or transport effects due to viscosity and permeability are captured by retaining additional terms in Equation 3.22, but these transport properties only become significant at later times. Large values of the product VC mask permeability effects at early times – thus, an interpretation model allowing more accurate formation evaluation is invaluable.

For large times, we can approximate the complementary error function in using the asymptotic series expansion given by erfc (x) = $\exp(-x^2)$ $\{1 - 1/(2x^2) + ...\}/\{x\sqrt{\pi}\}$. Then, our exact solution reduces to

$$p(r_w,t)_{late\text{-}time\ from\ exact} = -r_w + r_w^2/\sqrt{(\pi t)} \tag{3.24}$$

$$+ (2\text{-}r_w)r_w^3/(2t^{3/2}\sqrt{\pi}) + 3r_w^4(r_w\text{-}1)(r_w\text{-}3)/(4t^{5/2}\sqrt{\pi}) + ...$$

In the late time limit, we retain the leading "$p(r_w,t) = -r_w + r_w^2/\sqrt{(\pi t)}$ " terms only and return to dimensional variables to obtain

$$P(R_w,t)_{late\text{-}time\ from\ exact} = P_0 - Q_0\,\mu/(4\pi R_w k)$$

$$+ \{Q_0\,\mu/(4\pi k)\}\sqrt{\{\phi\mu c/(\pi kt)\}} \tag{3.25}$$

This late time solution is independent of flowline storage, but depends not only on μ and k, but ϕ and c. Equation 3.25 also reproduces the algebraic "inverse-square-root" timewise decline in pressure. This large-time transient behavior forms the basis for Horner-type models which, while popular, require "ϕc" estimates which are subject to error (see Chapter 5 for a more detailed discussion). At very large times, a steady-state spherical response is found from

$$P(R_w,t)_{late\text{-}time\ from\ exact} = P_0 - Q_0\,\mu/(4\pi R_w k) \tag{3.26a}$$

which is essentially the conventional high mobility model, that is,

$$k_d = Cq\mu/(2\pi r_p \Delta P) \tag{3.26b}$$

or

$$k_d = 5{,}660\ q\mu/\Delta P \tag{3.26c}$$

but without the geometric correction. If the value of $P(R_w)$ is known from drawdown or buildup measurements, then this simple source-point formula can be used to estimate the value of the isotropic permeability k.

Other solutions can be analogously recovered. For example, we can approximate the Laplace transform at r_w by taking

$$\boldsymbol{p}(r_w,s) = -1/\{s\,(s + s^{1/2} + r_w^{-1})\} \approx -1/\{s\,(s + r_w^{-1})\} \tag{3.27}$$

in which case we obtain the exponential approximation

$$p_{exp}(r_w,t) = r_w(-1 + e^{-t/rw}) \tag{3.28}$$

This has been used successfully by Halliburton in early-time transient interpretation for tight zones, noting that flowline distortions are most severe in this limit (see Chin *et al* (2014) for references). The exponential model forms the basis for the company's GeoTap™ early-time pressure interpretation products. On the other hand, we could have assumed

$$\boldsymbol{p}(r_w,s) = -1/\{s\,(s + s^{1/2} + r_w^{-1})\} \approx -1/\{s\,(s^{1/2} + r_w^{-1})\} \tag{3.29}$$

in which case

$$p_{exp\text{-}erfc}(r_w,t) = -r_w + r_w \exp(t/r_w^2)\mathrm{erfc}(t^{1/2}/r_w) \tag{3.30}$$

which also satisfies initial conditions. Large-time expansions provide solutions similar to those in Equation 3.25. Of course, Equation 3.21 provides a single expression valid for all space and time although, admittedly, the foregoing approximations involve simpler computations.

3.2.5 New inverse approach for mobility and pore pressure prediction

Inverse or "indirect" problems predict mobility or "k/μ" from pressure measurements. We had indicated how the steady-state spherical flow equation has been used together with repeat formation testers. In many low mobility applications, however, equilibrated pressure values are not available – excessive logging times are costly and may result in lost tools. Thus, one naturally inquires if early-time methods can be developed which not only determine mobility, but *also* predict steady-state pore pressure, from highly transient drawdown or buildup data. The required procedure is straightforward. The pressure expression in Equation 3.21 (or any of its approximations) is first re-expressed in physical dimensional variables and then used to create drawdown and buildup solutions using superposition methods. For instance, a single drawdown-buildup sums a "positive rate" pressure solution to one for a "negative rate" shifted forward in time; double drawdown-buildups repeat this superposition, therefore, adding a total of four distinct solutions. The buildup solution begins when the second pumping cycle stops.

The physical solution in dimensional form contains three explicit parameters related to the background hydrostatic pressure, an amplitude proportional to pumping rate, and lastly, a parameter related to mobility. The pressure solution is evaluated at three points in time, thus defining "three equations in three unknowns" which are solved by nonlinear iterative methods. This approach yields both mobility and pore pressure, noting that highly

transient (as well as steady) pressure inputs are permissible. In our implementation, unequal time separations between logging points are permitted and pressure variations may be highly transient. Also, "late time parameters" such as porosity are unimportant at early times and calculations are insensitive to any assumed values. Our approach contrasts with conventional approaches which require steady pressures which predict mobility only. In the next sections, we demonstrate how the method predicts both mobility and pore pressure accurately over a wide range of flowline volumes – a consideration important to modern tight zone applications utilizing increasingly large sampling chambers.

3.3 Multiple-Drawdown Pressure Analysis (Patent Pending)

This section deals with the use of formation testing pressure transient data to obtain isotropic or anisotropic "mobility" and, where applicable, the "pore pressure." Mobility is defined as "permeability/viscosity." If fluid viscosity is known from a separate measurement, then permeability can also be calculated. In petroleum engineering, we generally have horizontal mobility and permeability, and similarly, vertical mobility and permeability, where these directions are taken parallel and perpendicular to the bedding plane. Henceforth, we will only focus on mobility, but it is clear that the conclusions refer to permeability as well. Mobility is a measure of resistance to fluid flow, that is, it is a quantity that is directly related to the economic viability of an oil and gas reservoir. A "double-drawdown pressure transient analysis" method for formation testers is described (extendable to multiple drawdowns). The writing is based on work of the lead author who invented most of the prior art. The new approach improves on the prior art and adds extensive capabilities.

3.3.1 Background on existing models

This section explains the differences between several Halliburton early-time models that have been published. It is essential to understand these so that the contributions of this chapter, which are used together with phase delay methods in Chapter 4 to predict *both* horizontal and vertical permeability, can be appreciated. U.S. Patent No. 7,059,179 awarded to Proett and Chin provided a means to obtain permeabilities from a general math solution and considered the complicated situation when anisotropy *and* skin effects *both* exist.

It is important that the "with skin" solution is fundamentally different from the "no skin" solution in this chapter – the latter does not appear by "setting skin to zero." This may be confusing but the math is explained in Chin *et al* (2014). Essentially, the skin coefficient multiplies a high-order derivative term in the formulation – this term alters the structure of the solution. It is analogous to setting mass to zero in the mass-spring-damper model – it is invalid because the second-order time derivative in "F = ma" would be incorrectly disregarded.

The equations cited in U.S. Patent No. 7,059,179 involved "complex complementary error functions" that are extremely complicated and in retrospect could not be simplified. In the decade since the patent was awarded in 2006, no progress has been made in making the method practical for petroleum engineering applications.

In the earlier work of Proett, Chin and Chen, namely U.S. Patent 5,703,286, the authors use the "no skin" limit of the general solution but consider *isotropic* applications only. Even so, the mathematical expressions contain exponentials and complex complementary error functions and are still impractical. However, Chin importantly later showed that it is possible to simplify the general result in a way that is useful to low mobility reservoir applications. Essentially, in low mobility applications, where formation tester flowline volume effects are likely to significantly distort pressure transient readings, a very simple "exponential" model applies. This is the well known model used successfully commercially by Halliburton in its GeoTap™ "formation testing while drilling" (FTWD) product line. It is for a MWD/LWD single-probe tool in which pressures are measured at the source probe while withdrawing fluid at a constant rate and then pumping is stopped. The model was adapted to this so-called single "drawdown-buildup test" and used to predict mobility and permeability. Halliburton curve fits experimental data to this drawdown-buildup test, a procedure which we do not need or use.

3.3.2 Extension to anisotropic, no-skin applications

The method of U.S. Patent 5,703,286 again assumes isotropic media. To the authors' knowledge, the basic theory has not been extended to anisotropic, no-skin applications. This limit is important in real-time formation evaluation for two reasons: skin effects are unknown initially, but further, the skin model typically used is a crude one. An extension was made in an internal company memo "FTWD-Processing-Algorithms-V56a" (Chin, 2012) and Chin *et al* (2014) in which the Halliburton isotropic approach is extended to anisotropic media without skin. We will quote and use the anisotropic solution below.

Let us describe the steps needed to produce results applicable to anisotropic early-time data in low spherical mobility applications when flowline storage distortion effects can be important. The method applies to data taken at the source (pumping) probe, and can be used for wireline or MWD tools with multiple probes. The mathematical steps are as follows.

- The isotropic formulation of U.S. Patent 5,703,286 is first extended to anisotropic media and solved analytically using Laplace transforms in the no-skin limit.
- Two asymptotic early time solutions, namely Equations 3.31 and 3.32, are obtained in which low mobility effects are balanced by flowline storage effects. Early time solutions are commercially important because they reduce the waiting times needed to collect data.

- The first asymptotic solution obtained is an "anisotropic exponential extension" of Halliburton's isotropic exponential model. The new exponential solution is similar in mathematical structure to the isotropic method of U.S. Patent 5,703,286 and now takes the more general form in below where P_w is the measured pressure, P_0 is the pore pressure, μ is viscosity, Q_0 is volume flow rate, R_w is effective nozzle radius, V is flowline volume, C is fluid compressibility, and k_h and k_v are horizontal and vertical permeabilities, that is

$$P_w(t) = P_0 + \{\mu Q_0/(4\pi R_w k_h^{2/3} k_v^{1/3})\} \times [- 1 + \exp (- 4\pi R_w k_h^{2/3} k_v^{1/3} t)/(\mu VC)] \quad (3.31)$$

- The second asymptotic expansion, our preferred embodiment, is a conventional "rational polynomial expansion," that is, a polynomial series expansion which provides equivalent solutions to the above but at much faster speeds. This takes the form

$$P_w(t) = \sum a_n t^n \quad (3.32)$$

where the coefficients a_n are chosen to satisfy the identical boundary value problem. This "rational polynomial" replaces the terms in the square-brackets of Equation 3.31. The two solutions are only slightly different.

- The two no-skin solutions, for brevity, will be referred to as "the fundamental anisotropic solution" for constant rate pumping. The interpretation objective is to predict both P_0 and the spherical permeability $k_s = k_h^{2/3} k_v^{1/3}$ by regression fitting to either. It is important that we formally prove Equation 3.31 for use in Chapter 4, whereas some authors simply replace (without justification) an isotropic permeability with $k_h^{2/3} k_v^{1/3}$.

3.3.2.1 Method 1 - Drawdown-alone test

There are different test procedures that are employed in field operations. The first is a simple "drawdown-alone" method, in which reservoir fluid is withdrawn by formation tester pumping at a constant rate without stopping. If and when steady conditions are achieved, the formula $\Delta P_s = - Q\mu / (4\pi k_s R_w)$ conventionally used in the industry can be employed to predict spherical mobility or permeability; this is a standard procedure that has been used for decades and its use applies to standard RFT formation testers.

If steady conditions are not possible, the fundamental anisotropic solution is used to match measured transient data to at least three data points [t, $P_w(t)$] using a numerical regression method. The test parameters that provide the best curve-fitting are used to calculate the spherical mobility k_s and the pore pressure P_0. We emphasize that the measured data may be highly transient and are collected at early times, typically in the first fifteen seconds of drawdown.

In Halliburton's isotropic method, a curve is first fitted to all the data, typically ten points, and the properties of this curve are analyzed. This curve fit uses subjective criteria outside of fluid dynamics. We believe this approach is less accurate than direct consideration of the data.

3.3.2.2 Method 2 - Single-drawdown-single-buildup test

In this test, the pump piston is used to withdraw fluid from the formation at a constant volume flow rate, for a fixed duration of time, and then stops. During fluid withdrawal, the measured pressure decreases in time – this is known as the "drawdown." When pumping stops, the pressure increases in time – this is the "buildup." The procedure described consists of a single drawdown followed by a single buildup. For the drawdown cycle, the Method 1 applies. For the buildup cycle, we construct a solution using our fundamental anisotropic solution by applying the "method of superposition" to construct solutions valid for drawdown and buildup. The first part of the pressure solution assumes a volume flow rate Q acting for a given amount of time. To this solution, we add the pressure solution with flowrate "- Q" once pumping stops (this models a total flowrate of zero).

U.S. Patent 6,932,167 provides an example of superposition using the isotropic exponential solution (ours uses the anisotropic exponential and rational polynomial solutions). The patent also describes a curve-fitting regression analysis used to predict the isotropic mobility or permeability. We do not use the Halliburton procedure since we believe that curve-fitting adds a level of uncertainty that is unwarranted. Subjective visual judgements or those made arbitrarily by mathematical rules not based on the flow equations introduce uncertain error. Instead, we use at least three data points [t, $P_w(t)$] from actual drawdown or buildup data, together with a regression analysis, to predict spherical mobility and pore pressure – again, from buildup data that has not necessarily reached steady state. Typically, data can be used from the first fifteen-to-thirty seconds of the test.

3.3.2.3 Method 3 - Double-drawdown-single-buildup test

In certain "fluid sampling" applications, the source probe (pumping piston) withdraws fluid at a volume flow rate Q_1 for a given time duration, followed by a more rapid withdrawal Q_2 for a second time duration, and finally, followed by stoppage of pumping. Thus, we have two pressure drawdowns (that is, two different decreases in time) followed by a buildup (pressure increase). For the first drawdown, Method 1 can be used to predict spherical mobility and pore pressure. These quantities can also be predicted from the buildup curve, but not using Method 2, since we how have an additional drawdown. A new solution must be constructed to represent the buildup. This is developed by linear superposition again. The first solution is the pressure solution for a flowrate Q_1 acting for the first time duration. The second solution is the pressure solution

for flowrate Q_2, which applies for the second drawdown duration. The third and final solution, applicable to the buildup curve, assumes a net flow rate of zero and acts for the remainder of time. Again, the superposition process is adopted from in mathematics. Triple-superpositions are used to construct this buildup solution. As before, we use at least three data points [t, $P_w(t)$] from buildup data, together with a regression analysis, to predict both spherical mobility and pore pressure.

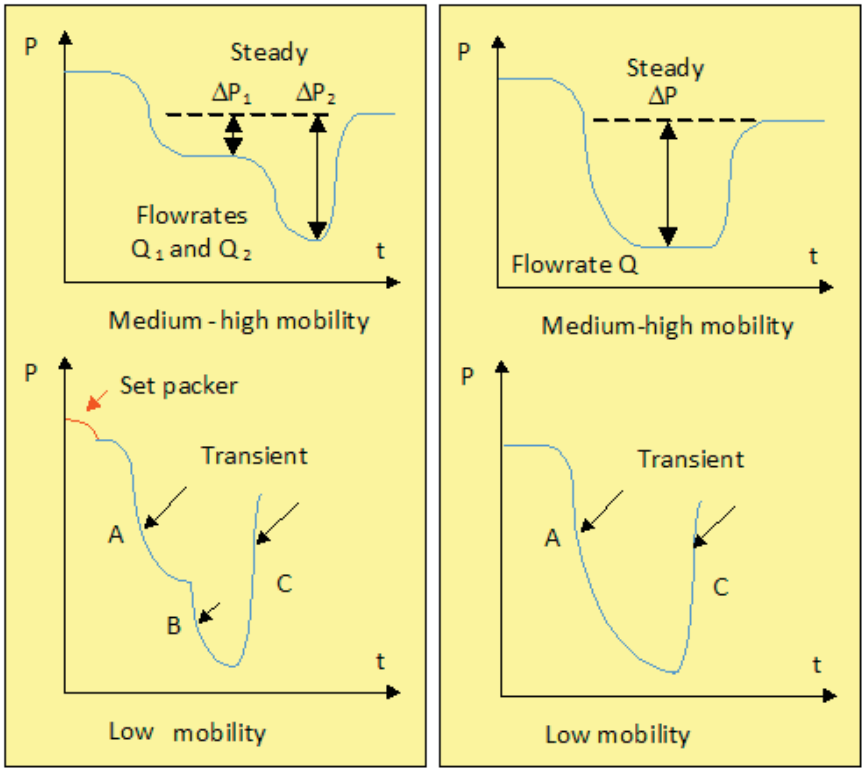

Figure 3.2b. New method for multiple drawdowns.

The new method applies to double-drawdown (left) and single-drawdown (right) of Figure 3.2b both in low mobility anisotropic applications. Use of "rational polynomial" solutions plus a "three data point" approach permits fast calculation speeds useful in surface operations, but particularly important in downhole microprocessor environments where computing resources are limited. Our approach can be extended to any number of drawdowns by using multiple superpositions of the "fundamental anisotropic solution."

3.4 Forward Analysis with Illustrative Calibration

We now consider a well known example from Page 10-9 of Schlumberger's Log Interpretation Principles/Applications. Data from drawdown analyses of two pretests (with 10 cc each) show that

ΔP_1 = 2,050 psi
T_1 = 15.4 sec
q_1 = 10/15.4 = 0.65 cc/sec

and

ΔP_2 = 4,470 psi
T_2 = 6.1 sec
q_2 = 10/6.1 = 1.64 cc/sec

where the upper case T's are defined in our Figure 3.2a (these parameters are used later in our FT-00 screen of Figure 3.3a). The well was drilled using mud with a viscosity of μ = 0.25 cp. Using Equation 3.26b shows that

$$k_{d1} = 5660 \times 0.65 \times 0.25/2050 = 0.45 \text{ md}$$

and

$$k_{d2} = 5660 \times 1.64 \times 0.25/4470 = 0.52 \text{ md}$$

In this example, the two values of permeability agree quite well. This consistency indicates that, for the tests conducted, steady-state pressures were found in both cases – reference to the log in Figure 10-19 of the above publication does, in fact, show a "flat part" or horizontal asymptote adjacent to the bottom arrow (ours) of our Figure 3.2a.

We now pursue a simple exercise to show that the Schlumberger data above are consistent with our exact solver FT-00 for a properly selected geometric factor. For illustrative purposes, we will assume below that the underlying formation has a permeability of about k_d = 0.5 md as suggested by the average of 0.45 and 0.52 md above. As discussed in Chin *et al* (2014), the *exact* solution in Equation 3.21 has been incorporated in forward analysis software algorithm FT-00 which supports a general pump-out schedule using linear superposition methods. Shown in Figure 3.3a is the self-explanatory menu for the most general case, namely, transversely isotropic flow with flowline storage and skin – note that we have inputted the flow rates 0.65 and 1.64 cc/sec, the viscosity 0.25 cp, and two permeabilities of 0.5 md.

Entering the appropriate fluid, formation and tool parameters produces, within a fraction of a second on Intel i5 machines, complete solutions for source and, if applicable, multiple observation probes. Clicking on "Simulate" produces the "double bump" source probe drawdown response in Figure 3.3b for the pumping schedule shown (again, note how steady-state asymptotes appear for both tests). By trial and error, we have selected a geometric factor *G* of 0.38

which adjusts computed pressure drops seen from Figure 3.3b to the 2050 (≈ 20,000 – 18,000) and 4470 (≈ 20,000 – 15,100) psi values indicated in the Schlumberger data – only a single *G* value is required for this fit. Figure 3.3b does verify that the selected simulation parameters do in fact lead to rapidly equilibrating pressures. Note that exact agreement is not possible because of the approximate 0.5 md assumed; also, we indicate that the time 21.5 = 15.4 + 6.1. Our "0.38" is analogous to the "5660" used in the above calculations. So far, we have only shown that our transient FT-00 formulation and the steady spherical model are consistent in the large-time limit. We emphasize, however, that our FT-00 model is exact and can be used to create transient "synthetic data" valid for any point in time. This data is useful, as we will show, for evaluating inverse methods.

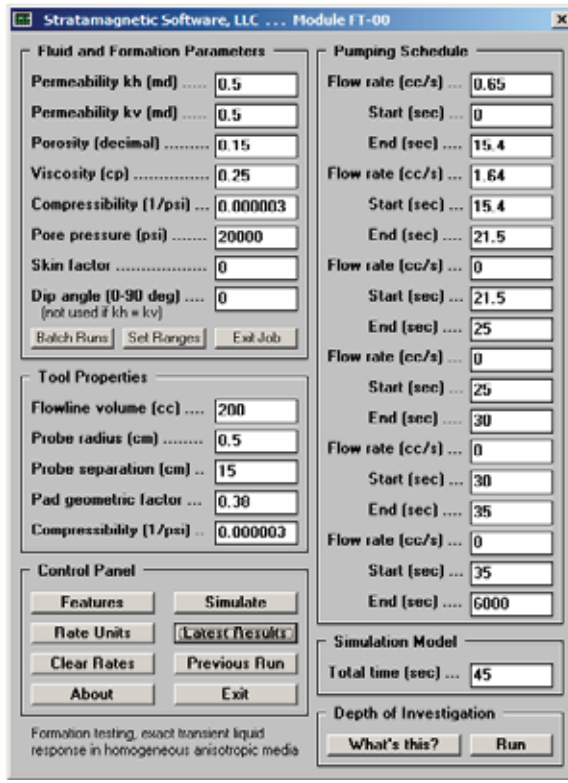

Figure 3.3a. Schlumberger medium-high mobility parameters.

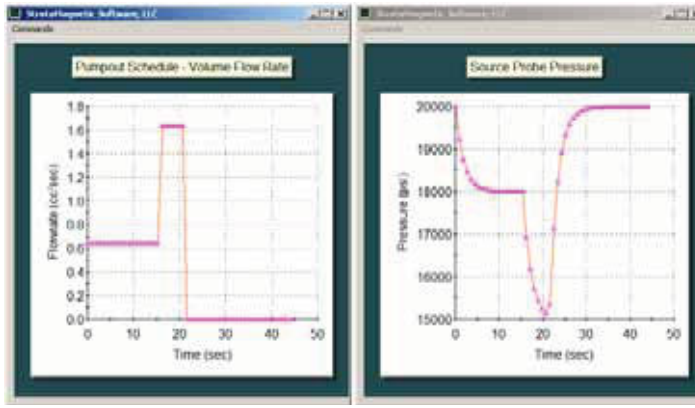

Figure 3.3b. Schlumberger medium-high mobility pressure response.

3.5 Mobility and Pore Pressure Using First Drawdown Data

We now reconsider the above example but increase the viscosity from 0.25 cp to 1 cp. For the parameters indicated, this increase is enough to eliminate the appearance of any steady-state pressure response, so that all drawdown pressures are highly transient. This low-mobility effect, together with any nonzero flowline volume, can be detrimental to formation permeability prediction. We will focus on the performance of the inverse method in as flowline volume increases from "acceptable" to large values for our 1 cp fluid.

3.5.1 Run No. 1, Flowline volume 200 cc

(Software reference, pta-dd-3-run-with-rft-numbers.exe)

In this example, we consider a flowline volume of 200 cc. This and the calculated pressure response are shown in Figure 3.4a. It is clear that no steady state exists, so that Equations 3.26b and 3.26c are inapplicable.

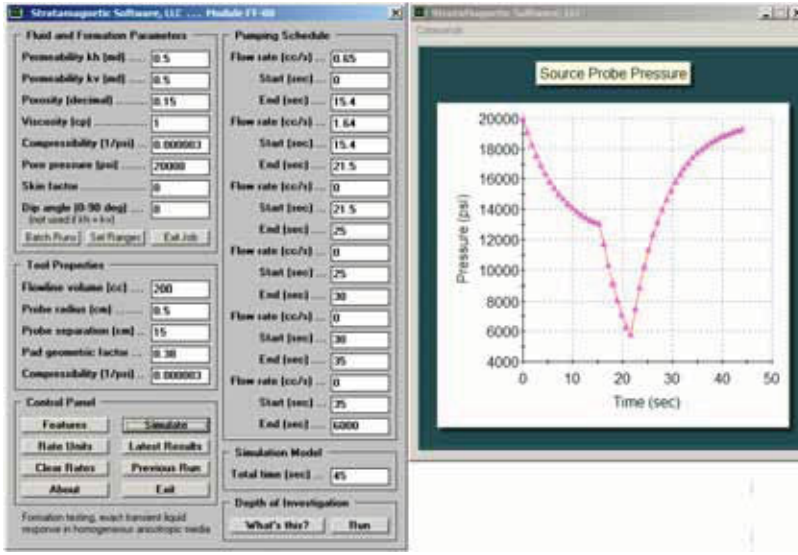

Figure 3.4a. Flowline volume, 200 cc.

Clicking on "Simulate" produces the exact transient source probe pressure response shown below (again, at 15.4 sec, the initial drawdown ceases and is replaced by a stronger one). We will use pressure results from 3.6, 9.9 and 14.4 sec (highlighted in **red** font) as inputs to our inverse model. This model will attempt to recover the mobility of 0.5 md/cp and the pore pressure of 20,000 psi assumed in the menu of Figure 3.4a. In Runs No. 1-4, we will use drawdown data from the very left of our pressure response curves.

EXACT FT-00 FORWARD ANALYSIS RESULTS

Time (s)	Rate (cc/s)	Ps* (psi)
0.000E+00	0.65000E+00	0.20000E+05
0.900E+00	0.65000E+00	0.19084E+05
0.180E+01	0.65000E+00	0.18275E+05
0.270E+01	0.65000E+00	0.17559E+05
0.360E+01	**0.65000E+00**	**0.16926E+05**
0.450E+01	0.65000E+00	0.16366E+05
0.540E+01	0.65000E+00	0.15871E+05
0.630E+01	0.65000E+00	0.15433E+05
0.720E+01	0.65000E+00	0.15045E+05
0.810E+01	0.65000E+00	0.14702E+05
0.900E+01	0.65000E+00	0.14398E+05
0.990E+01	**0.65000E+00**	**0.14129E+05**
0.108E+02	0.65000E+00	0.13891E+05
0.117E+02	0.65000E+00	0.13680E+05
0.126E+02	0.65000E+00	0.13493E+05
0.135E+02	0.65000E+00	0.13328E+05
0.144E+02	**0.65000E+00**	**0.13181E+05**
0.153E+02	0.65000E+00	0.13052E+05
0.162E+02	0.16400E+01	0.11688E+05
0.171E+02	0.16400E+01	0.10337E+05
0.180E+02	0.16400E+01	0.91422E+04
0.189E+02	0.16400E+01	0.80852E+04
0.198E+02	0.16400E+01	0.71500E+04

A superposition program was written to implement our inverse ideas. Screen outputs with iteration history are shown below. Convergence to 0.515 md/cp and 19,981 psi (shown in **red**) was achieved and agrees well with input values of 0.5 and 20,000. It is worth noting that none of the input pressures used are close to 20,000 psi. In general, pressure data near t = 0 should not be used. Computation time was approximately one second.

```
Volume flow rate (cc/s):       0.650
Pump probe, radius (cm):       0.500
Probe, geometric factor:       0.380
1st Point Time T1 (sec):       3.600
      Pressure P1 (psi):   16926.000
2nd Point Time T2 (sec):       9.900
      Pressure P2 (psi):   14129.000
1st Point Time T3 (sec):      14.400
      Pressure P3 (psi):   13181.000

    Run     Error  P0(psi)  Md/Cp
      1.  52.3 %    18532   0.009
      2.  52.0 %    18540   0.018
      3.  51.8 %    18548   0.027
      4.  51.5 %    18556   0.036
      5.  51.2 %    18564   0.044
      6.  51.0 %    18572   0.053
      7.  50.7 %    18580   0.061
      8.  50.5 %    18588   0.070
      9.  50.2 %    18596   0.078
     10.  49.9 %    18605   0.086
        .
        .
    130.   2.9 %    19911   0.511
    131.   2.4 %    19925   0.512
    132.   1.9 %    19939   0.513
    133.   1.3 %    19953   0.513
    134.   0.7 %    19967   0.514
    135.   0.2 %    19981   0.515

Stop - Program terminated.
```

3.5.2 Run No. 2, Flowline volume 500 cc

Here we increase the flowline volume to 500 cc with all other parameters unchanged. The source probe pressure response does not show any steady behavior at all.

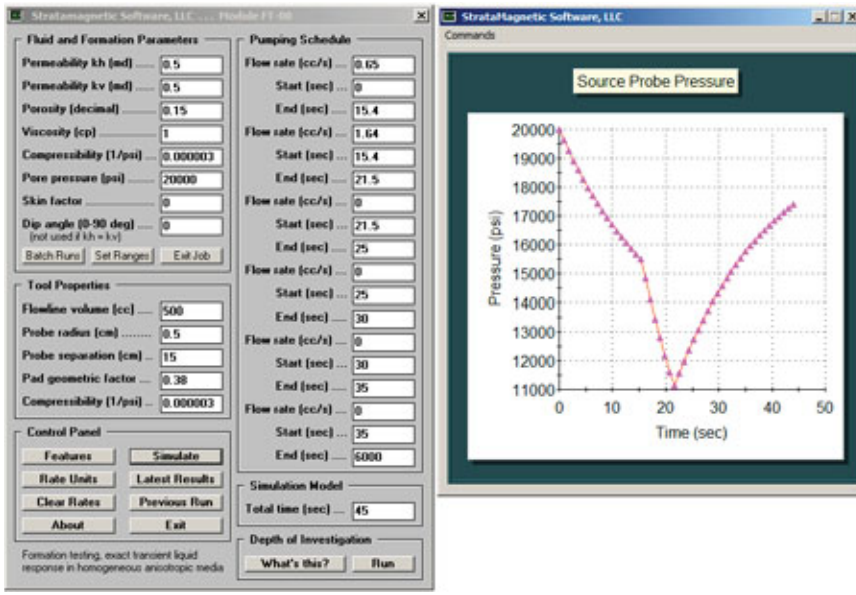

Figure 3.4b. Flowline volume, 500 cc.

```
EXACT FT-00 FORWARD ANALYSIS RESULTS
  Time (s)  Rate (cc/s)   Ps* (psi)
 0.000E+00  0.65000E+00  0.20000E+05
 0.900E+00  0.65000E+00  0.19620E+05
 0.180E+01  0.65000E+00  0.19258E+05
 0.270E+01  0.65000E+00  0.18913E+05
 0.360E+01  0.65000E+00  0.18585E+05
 0.450E+01  0.65000E+00  0.18273E+05
 0.540E+01  0.65000E+00  0.17976E+05
 0.630E+01  0.65000E+00  0.17693E+05
 0.720E+01  0.65000E+00  0.17423E+05
 0.810E+01  0.65000E+00  0.17167E+05
 0.900E+01  0.65000E+00  0.16922E+05
 0.990E+01  0.65000E+00  0.16690E+05
 0.108E+02  0.65000E+00  0.16468E+05
 0.117E+02  0.65000E+00  0.16257E+05
 0.126E+02  0.65000E+00  0.16056E+05
 0.135E+02  0.65000E+00  0.15865E+05
 0.144E+02  0.65000E+00  0.15683E+05
 0.153E+02  0.65000E+00  0.15509E+05
 0.162E+02  0.16400E+01  0.14828E+05
 0.171E+02  0.16400E+01  0.14116E+05
 0.180E+02  0.16400E+01  0.13439E+05
 0.189E+02  0.16400E+01  0.12794E+05
 0.198E+02  0.16400E+01  0.12180E+05
```

We again run our inverse program, as shown below. As expected, the pressure inputs taken at the same times as before are substantially changed. Here, we predict 0.512 md/cp and 19,995 psi – again close to the assumed values of 0.5 md/cp and 20,000 psi.

```
Volume flow rate (cc/s):       0.650
Pump probe, radius (cm):       0.500
Probe, geometric factor:       0.380
1st Point Time T1 (sec):       3.600
      Pressure P1 (psi):   18585.000
2nd Point Time T2 (sec):       9.900
      Pressure P2 (psi):   16690.000
1st Point Time T3 (sec):      14.400
      Pressure P3 (psi):   15683.000

    Run     Error  P0(psi)   Md/Cp
      1.  25.2 %    19673    0.013
      2.  24.8 %    19678    0.027
      3.  24.4 %    19684    0.040
      4.  24.0 %    19689    0.053
      5.  23.6 %    19694    0.066
      6.  23.2 %    19700    0.078
      7.  22.7 %    19705    0.091
      8.  22.3 %    19711    0.103
      9.  21.9 %    19717    0.115
     10.  21.5 %    19722    0.127
        .
        .
     50.   2.3 %    19968    0.486
     51.   1.8 %    19974    0.493
     52.   1.3 %    19981    0.499
     53.   0.7 %    19988    0.506
     54.   0.2 %    19995    0.512
Stop - Program terminated.
```

3.5.3 Run No. 3, Flowline volume 1,000 cc

Here we repeat the above calculation, except that flowline volume in increased to 1,000 cc. Calculations again demonstrate accurate predictions using early-time transient data. The mobility is 0.510 md/cp as opposed to 0.5 md/cp, and the pore pressure is almost identical to the 20,000 psi assumed in the FT-00 data generation.

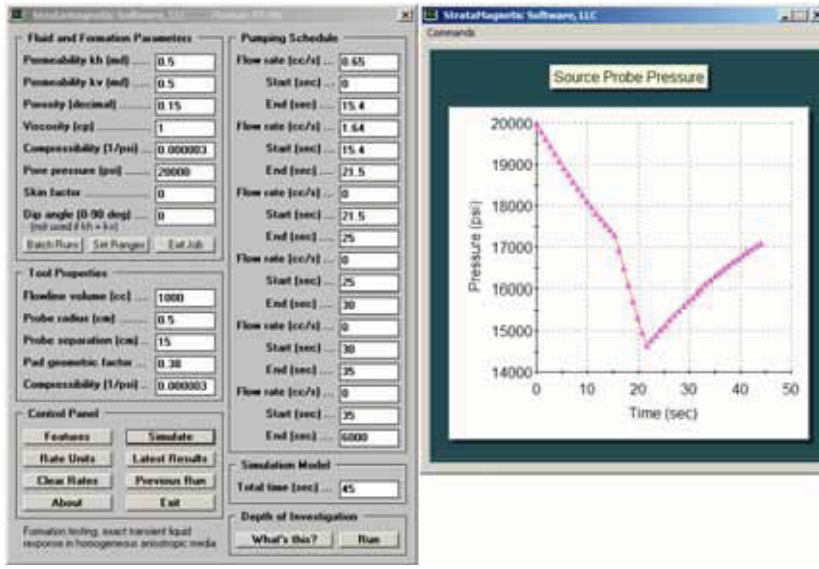

Figure 3.4c. Flowline volume, 1,000 cc.

```
EXACT FT-00 FORWARD ANALYSIS RESULTS
  Time (s)   Rate (cc/s)    Ps* (psi)
 0.000E+00  0.65000E+00  0.20000E+05
 0.900E+00  0.65000E+00  0.19807E+05
 0.180E+01  0.65000E+00  0.19620E+05
 0.270E+01  0.65000E+00  0.19436E+05
 0.360E+01  0.65000E+00  0.19258E+05
 0.450E+01  0.65000E+00  0.19083E+05
 0.540E+01  0.65000E+00  0.18913E+05
 0.630E+01  0.65000E+00  0.18747E+05
 0.720E+01  0.65000E+00  0.18585E+05
 0.810E+01  0.65000E+00  0.18426E+05
 0.900E+01  0.65000E+00  0.18272E+05
 0.990E+01  0.65000E+00  0.18122E+05
 0.108E+02  0.65000E+00  0.17975E+05
 0.117E+02  0.65000E+00  0.17831E+05
 0.126E+02  0.65000E+00  0.17691E+05
 0.135E+02  0.65000E+00  0.17555E+05
 0.144E+02  0.65000E+00  0.17422E+05
 0.153E+02  0.65000E+00  0.17292E+05
 0.162E+02  0.16400E+01  0.16904E+05
 0.171E+02  0.16400E+01  0.16493E+05
 0.180E+02  0.16400E+01  0.16092E+05
 0.189E+02  0.16400E+01  0.15701E+05
 0.198E+02  0.16400E+01  0.15320E+05
```

```
Volume flow rate (cc/s):       0.650
Pump probe, radius (cm):       0.500
Probe, geometric factor:       0.380
1st Point Time T1 (sec):       3.600
      Pressure P1 (psi):   19258.000
2nd Point Time T2 (sec):       9.900
      Pressure P2 (psi):   18122.000
1st Point Time T3 (sec):      14.400
      Pressure P3 (psi):   17422.000

    Run    Error  P0(psi)  Md/Cp
      1.  13.3 %   19910   0.022
      2.  12.8 %   19913   0.045
      3.  12.3 %   19916   0.067
      4.  11.8 %   19920   0.088
      5.  11.4 %   19923   0.110
      6.  10.9 %   19926   0.131
      7.  10.4 %   19929   0.151
      8.   9.9 %   19933   0.172
      9.   9.4 %   19936   0.192
     10.   8.9 %   19940   0.212
        .
        .
     20.   3.9 %   19974   0.396
     21.   3.3 %   19977   0.413
     22.   2.8 %   19981   0.430
     23.   2.3 %   19984   0.446
     24.   1.7 %   19988   0.463
     25.   1.2 %   19992   0.479
     26.   0.7 %   19995   0.495
     27.   0.1 %   19999   0.510

Stop - Program terminated.
```

3.5.4 Run No. 4, Flowline volume 2,000 cc

Finally in Run No. 4, the flowline volume is increased to a large 2,000 cc. Pore pressure prediction is again excellent at 19,999 psi, but mobility is still accurate and acceptable at 0.492 md/cp, as opposed to 0.5.

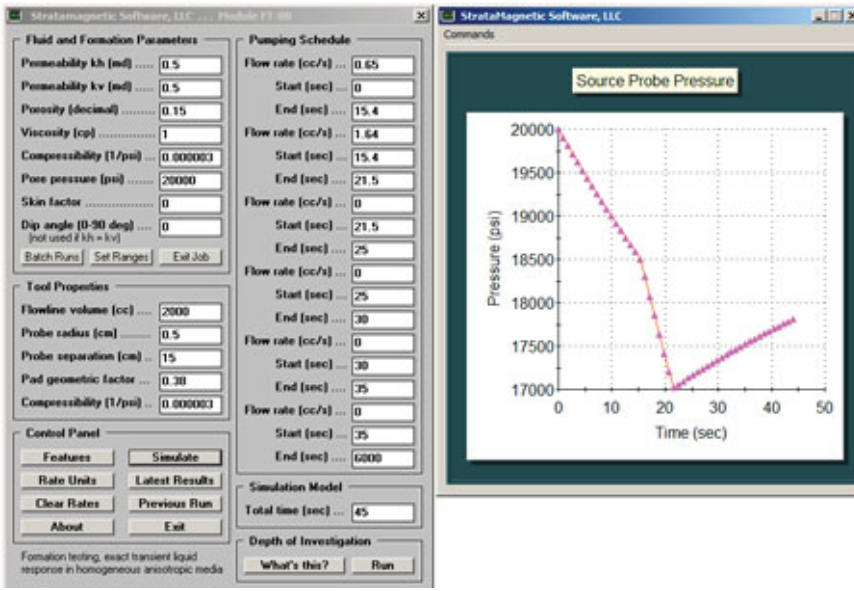

Figure 3.4d. Flowline volume, 2,000 cc.

```
EXACT FT-00 FORWARD ANALYSIS RESULTS
  Time (s)  Rate (cc/s)   Ps* (psi)
 0.000E+00  0.65000E+00  0.20000E+05
 0.900E+00  0.65000E+00  0.19903E+05
 0.180E+01  0.65000E+00  0.19807E+05
 0.270E+01  0.65000E+00  0.19713E+05
 0.360E+01  0.65000E+00  0.19620E+05
 0.450E+01  0.65000E+00  0.19527E+05
 0.540E+01  0.65000E+00  0.19436E+05
 0.630E+01  0.65000E+00  0.19346E+05
 0.720E+01  0.65000E+00  0.19257E+05
 0.810E+01  0.65000E+00  0.19170E+05
 0.900E+01  0.65000E+00  0.19083E+05
 0.990E+01  0.65000E+00  0.18997E+05
 0.108E+02  0.65000E+00  0.18913E+05
 0.117E+02  0.65000E+00  0.18829E+05
 0.126E+02  0.65000E+00  0.18746E+05
 0.135E+02  0.65000E+00  0.18665E+05
 0.144E+02  0.65000E+00  0.18584E+05
 0.153E+02  0.65000E+00  0.18505E+05
 0.162E+02  0.16400E+01  0.18295E+05
 0.171E+02  0.16400E+01  0.18071E+05
 0.180E+02  0.16400E+01  0.17850E+05
 0.189E+02  0.16400E+01  0.17632E+05
 0.198E+02  0.16400E+01  0.17416E+05
```

```
Volume flow rate (cc/s):       0.650
Pump probe, radius (cm):       0.500
Probe, geometric factor:       0.380
1st Point Time T1 (sec):       3.600
      Pressure P1 (psi):   19620.000
2nd Point Time T2 (sec):       9.900
      Pressure P2 (psi):   18997.000
1st Point Time T3 (sec):      14.400
      Pressure P3 (psi):   18584.000

    Run    Error  P0(psi)  Md/Cp
      1.   6.7 %   19977   0.041
      2.   6.2 %   19979   0.082
      3.   5.7 %   19981   0.121
      4.   5.2 %   19983   0.161
      5.   4.6 %   19984   0.200
      6.   4.1 %   19986   0.238
      7.   3.6 %   19988   0.276
      8.   3.1 %   19990   0.313
      9.   2.6 %   19992   0.350
     10.   2.0 %   19994   0.386
     11.   1.5 %   19995   0.422
     12.   1.0 %   19997   0.457
     13.   0.4 %   19999   0.492
Stop - Program terminated.
```

3.6 Mobility and Pore Pressure from Last Buildup Data

In Runs No. 5-8, we use the far-right buildup portion of the pressure curve to predict mobility and pore pressure, e.g., see Figure 3.4a. We emphasize that our "late time" portion of the response is significantly earlier than typical times used in Horner plots. The model now includes four linear superpositions, but the iterative process is identical to that for early drawdowns and only slightly slower, typically one second per inversion on Intel i5 machines. In the examples below, we randomly select time points for inverse model input.

3.6.1 Run No. 5, Flowline volume 200 cc

(Software reference, pta-two-dd-2.exe)

We again assume a modest 200 cc flowline volume. Exact pressure data computed from FT-00 are displayed corresponding to inputs in Figure 3.4a. Results highlighted in **red** are used in our inverse model – they are taken from the "zero flow rate" buildup portion of the table. The inverse program now includes two additional input parameters relative to the "early drawdown" model, namely, the drawdown ending times for the two pumping cycles. The predicted values of pore pressure and mobility, namely, 19,974 psi and 0.516 md/cp, are excellent when compared to the exact values 20,000 psi and 0.5 md/cp.

```
 Time (s)  Rate (cc/s)   Ps* (psi)
0.000E+00   0.65000E+00   0.20000E+05
0.900E+00   0.65000E+00   0.19084E+05
.
.
```

[Buildup begins at 21.5 seconds.]

```
 .
 0.189E+02  0.16400E+01  0.80852E+04
 0.198E+02  0.16400E+01  0.71500E+04
 0.207E+02  0.16400E+01  0.63226E+04
 0.216E+02  0.00000E+00  0.58616E+04
 0.225E+02  0.00000E+00  0.74926E+04
 0.234E+02  0.00000E+00  0.89330E+04
 0.243E+02  0.00000E+00  0.10206E+05
 0.252E+02  0.00000E+00  0.11332E+05
 0.261E+02  0.00000E+00  0.12327E+05
 0.270E+02  0.00000E+00  0.13208E+05
 0.279E+02  0.00000E+00  0.13986E+05
 0.288E+02  0.00000E+00  0.14676E+05
 0.297E+02  0.00000E+00  0.15285E+05
 0.306E+02  0.00000E+00  0.15825E+05
 0.315E+02  0.00000E+00  0.16302E+05
 0.324E+02  0.00000E+00  0.16725E+05
 0.333E+02  0.00000E+00  0.17099E+05
 0.342E+02  0.00000E+00  0.17430E+05
 0.351E+02  0.00000E+00  0.17723E+05
 0.360E+02  0.00000E+00  0.17982E+05
 0.369E+02  0.00000E+00  0.18212E+05
 0.378E+02  0.00000E+00  0.18415E+05
 0.387E+02  0.00000E+00  0.18595E+05
 0.396E+02  0.00000E+00  0.18754E+05
 0.405E+02  0.00000E+00  0.18896E+05
 0.414E+02  0.00000E+00  0.19021E+05
 0.423E+02  0.00000E+00  0.19131E+05
 0.432E+02  0.00000E+00  0.19229E+05
 0.441E+02  0.00000E+00  0.19316E+05

Vol flow rate Q1 (cc/s):       0.650
Vol flow rate Q2 (cc/s):       1.640
Pump probe, radius (cm):       0.500
Probe, geometric factor:       0.380
1st drawdown ends (sec):      15.400
2nd drawdown ends (sec):      21.500
1st Point Time T1 (sec):      22.500
      Pressure P1 (psi):    7492.600
2nd Point Time T2 (sec):      27.900
      Pressure P2 (psi):   13986.000
1st Point Time T3 (sec):      33.300
      Pressure P3 (psi):   17099.000

    Run    Error  P0(psi)  Md/Cp
      1.  51.8 % 1213219   0.000
      2.  51.5 %  611986   0.000
      3.  51.3 %  411575   0.001
      4.  51.0 %  311371   0.002
      .
      .
    100.  17.7 %   23054   0.375
    110.  13.2 %   21990   0.417
    120.   8.4 %   21108   0.456
    130.   3.3 %   20365   0.494
    131.   2.7 %   20298   0.498
    132.   2.2 %   20231   0.501
    133.   1.7 %   20165   0.505
    134.   1.2 %   20101   0.508
    135.   0.6 %   20037   0.512
    136.   0.1 %   19974   0.516

Stop - Program terminated.
```

3.6.2 Run No. 6, Flowline volume 500 cc

Here, the flowline volume is increased to 500 cc and Figure 3.4b applies. Exact FT-00 source probe pressures are given below and **red** values are taken as inputs to the inverse program. Calculated results give a pore pressure of 20,046 psi and a mobility of 0.509 md/cp, which compare favorably with known values.

Time (s)	Rate (cc/s)	Ps* (psi)
0.000E+00	0.65000E+00	0.20000E+05
0.900E+00	0.65000E+00	0.19620E+05
0.180E+01	0.65000E+00	0.19258E+05
.		
.		
0.189E+02	0.16400E+01	0.12794E+05
0.198E+02	0.16400E+01	0.12180E+05
0.207E+02	0.16400E+01	0.11595E+05
0.216E+02	0.00000E+00	0.11147E+05
0.225E+02	0.00000E+00	0.11572E+05
0.234E+02	**0.00000E+00**	**0.11975E+05**
0.243E+02	0.00000E+00	0.12359E+05
0.252E+02	0.00000E+00	0.12724E+05
0.261E+02	0.00000E+00	0.13072E+05
0.270E+02	0.00000E+00	0.13403E+05
0.279E+02	0.00000E+00	0.13718E+05
0.288E+02	0.00000E+00	0.14018E+05
0.297E+02	0.00000E+00	0.14303E+05
0.306E+02	**0.00000E+00**	**0.14575E+05**
0.315E+02	0.00000E+00	0.14834E+05
0.324E+02	0.00000E+00	0.15081E+05
0.333E+02	0.00000E+00	0.15315E+05
0.342E+02	0.00000E+00	0.15539E+05
0.351E+02	0.00000E+00	0.15751E+05
0.360E+02	0.00000E+00	0.15954E+05
0.369E+02	0.00000E+00	0.16147E+05
0.378E+02	0.00000E+00	0.16330E+05
0.387E+02	0.00000E+00	0.16505E+05
0.396E+02	0.00000E+00	0.16671E+05
0.405E+02	**0.00000E+00**	**0.16830E+05**
0.414E+02	0.00000E+00	0.16981E+05
0.423E+02	0.00000E+00	0.17125E+05
0.432E+02	0.00000E+00	0.17261E+05
0.441E+02	0.00000E+00	0.17392E+05

```
Vol flow rate Q1 (cc/s):        0.650
Vol flow rate Q2 (cc/s):        1.640
Pump probe, radius (cm):        0.500
Probe, geometric factor:        0.380
1st drawdown ends (sec):       15.400
2nd drawdown ends (sec):       21.500
1st Point Time T1 (sec):       23.400
      Pressure P1 (psi):    11975.000
2nd Point Time T2 (sec):       30.600
      Pressure P2 (psi):    14575.000
1st Point Time T3 (sec):       40.500
      Pressure P3 (psi):    16830.000
```

Run	Error	P0(psi)	Md/Cp
1.	36.4 %	374386	0.000
10.	31.3 %	49401	0.030
20.	25.2 %	31361	0.106
30.	18.6 %	25358	0.210
40.	11.5 %	22365	0.330
50.	3.7 %	20575	0.457
51.	2.9 %	20434	0.470
52.	2.1 %	20300	0.483
53.	1.3 %	20170	0.496
54.	**0.5 %**	**20046**	**0.509**

3.6.3 Run No. 7, Flowline volume 1,000 cc

Here the flowline volume is increased to 1,000 cc and Figure 3.4c applies. The predicted values of 20,043 psi and 0.506 md/cp are again very accurate.

```
  Time (s)  Rate (cc/s)   Ps* (psi)
 0.000E+00  0.65000E+00  0.20000E+05
 0.900E+00  0.65000E+00  0.19807E+05
 0.180E+01  0.65000E+00  0.19620E+05
  .
  .
 0.189E+02  0.16400E+01  0.15701E+05
 0.198E+02  0.16400E+01  0.15320E+05
 0.207E+02  0.16400E+01  0.14948E+05
 0.216E+02  0.00000E+00  0.14639E+05
 0.225E+02  0.00000E+00  0.14769E+05
 0.234E+02  0.00000E+00  0.14896E+05
 0.243E+02  0.00000E+00  0.15020E+05
 0.252E+02  0.00000E+00  0.15140E+05
 0.261E+02  0.00000E+00  0.15258E+05
 0.270E+02  0.00000E+00  0.15373E+05
 0.279E+02  0.00000E+00  0.15485E+05
 0.288E+02  0.00000E+00  0.15594E+05
 0.297E+02  0.00000E+00  0.15701E+05
 0.306E+02  0.00000E+00  0.15805E+05
 0.315E+02  0.00000E+00  0.15906E+05
 0.324E+02  0.00000E+00  0.16005E+05
 0.333E+02  0.00000E+00  0.16102E+05
 0.342E+02  0.00000E+00  0.16196E+05
 0.351E+02  0.00000E+00  0.16288E+05
 0.360E+02  0.00000E+00  0.16378E+05
 0.369E+02  0.00000E+00  0.16465E+05
 0.378E+02  0.00000E+00  0.16550E+05
 0.387E+02  0.00000E+00  0.16634E+05
 0.396E+02  0.00000E+00  0.16715E+05
 0.405E+02  0.00000E+00  0.16795E+05
 0.414E+02  0.00000E+00  0.16872E+05
 0.423E+02  0.00000E+00  0.16948E+05
 0.432E+02  0.00000E+00  0.17021E+05
 0.441E+02  0.00000E+00  0.17093E+05


Vol flow rate Q1 (cc/s):       0.650
Vol flow rate Q2 (cc/s):       1.640
Pump probe, radius (cm):       0.500
Probe, geometric factor:       0.380
1st drawdown ends (sec):      15.400
2nd drawdown ends (sec):      21.500
1st Point Time T1 (sec):      22.500
      Pressure P1 (psi):   14769.000
2nd Point Time T2 (sec):      28.800
      Pressure P2 (psi):   15594.000
1st Point Time T3 (sec):      35.100
      Pressure P3 (psi):   16288.000

    Run     Error  P0(psi)  Md/Cp
      1.  15.3 %  146133   0.001
      5.  13.2 %   41374   0.023
     10.  10.4 %   28281   0.085
     15.   7.5 %   23918   0.180
     20.   4.6 %   21737   0.301
     25.   1.5 %   20430   0.444
     26.   0.9 %   20229   0.475
     27.   0.3 %   20043   0.506

Stop - Program terminated.
```

3.6.4 Run No. 8, Flowline volume 2,000 cc

Here, the flowline volume is increased to a large 2,000 cc and Figure 3.4d applies. Nonetheless, the predicted 20,129 psi and 0.472 md/cp are in reasonable agreement with the known values of 20,000 psi and 0.5 md/cp.

Time (s)	Rate (cc/s)	Ps* (psi)
0.000E+00	0.65000E+00	0.20000E+05
0.900E+00	0.65000E+00	0.19903E+05
0.180E+01	0.65000E+00	0.19807E+05
.		
0.198E+02	0.16400E+01	0.17416E+05
0.207E+02	0.16400E+01	0.17204E+05
0.216E+02	0.00000E+00	0.17021E+05
0.225E+02	0.00000E+00	0.17057E+05
0.234E+02	0.00000E+00	0.17093E+05
0.243E+02	**0.00000E+00**	**0.17128E+05**
0.252E+02	0.00000E+00	0.17163E+05
0.261E+02	0.00000E+00	0.17198E+05
0.270E+02	0.00000E+00	0.17232E+05
0.279E+02	0.00000E+00	0.17266E+05
0.288E+02	0.00000E+00	0.17299E+05
0.297E+02	0.00000E+00	0.17332E+05
0.306E+02	**0.00000E+00**	**0.17364E+05**
0.315E+02	0.00000E+00	0.17397E+05
0.324E+02	0.00000E+00	0.17428E+05
0.333E+02	0.00000E+00	0.17460E+05
0.342E+02	0.00000E+00	0.17490E+05
0.351E+02	0.00000E+00	0.17521E+05
0.360E+02	0.00000E+00	0.17551E+05
0.369E+02	0.00000E+00	0.17581E+05
0.378E+02	0.00000E+00	0.17610E+05
0.387E+02	0.00000E+00	0.17639E+05
0.396E+02	**0.00000E+00**	**0.17668E+05**
0.405E+02	0.00000E+00	0.17697E+05
0.414E+02	0.00000E+00	0.17725E+05
0.423E+02	0.00000E+00	0.17752E+05
0.432E+02	0.00000E+00	0.17780E+05
0.441E+02	0.00000E+00	0.17807E+05

Vol flow rate Q1 (cc/s):	0.650
Vol flow rate Q2 (cc/s):	1.640
Pump probe, radius (cm):	0.500
Probe, geometric factor:	0.380
1st drawdown ends (sec):	15.400
2nd drawdown ends (sec):	21.500
1st Point Time T1 (sec):	24.300
Pressure P1 (psi):	17128.000
2nd Point Time T2 (sec):	30.600
Pressure P2 (psi):	17364.000
1st Point Time T3 (sec):	39.600
Pressure P3 (psi):	17668.000

Run	Error	P0(psi)	Md/Cp
1.	9.1 %	54706	0.003
2.	8.4 %	35976	0.013
3.	7.7 %	29733	0.029
4.	7.0 %	26611	0.051
5.	6.3 %	24738	0.078
6.	5.6 %	23490	0.111
7.	4.9 %	22598	0.149
8.	4.2 %	21929	0.192
9.	3.4 %	21409	0.239
10.	2.7 %	20993	0.291
11.	1.9 %	20652	0.348
12.	1.2 %	20369	0.408
13.	**0.4 %**	**20129**	**0.472**

3.6.5 Run No. 9, Time-varying flowline volume

In this very challenging final test of the inverse drawdown method, we create forward simulation pressure transient data using FT-07, a numerical finite difference model for ellipsoidal sources in transversely isotropic media with time-varying flowline storage developed in Chapter 9. The physical assumptions used are shown in the menu of Figure 3.5a. The grid system was calibrated so that the transient solution for source probe pressure was nearly identical to that produced by exact simulator FT-00 when the flowline volume is 200 cc. As shown below, a time-dependent flowline volume was assumed with 200 cc for the first two seconds, increasing to 5,000 cc by five seconds, and holding at 5,000 cc thereafter. The source solution, together with assumptions, are plotted in Figure 3.5b.

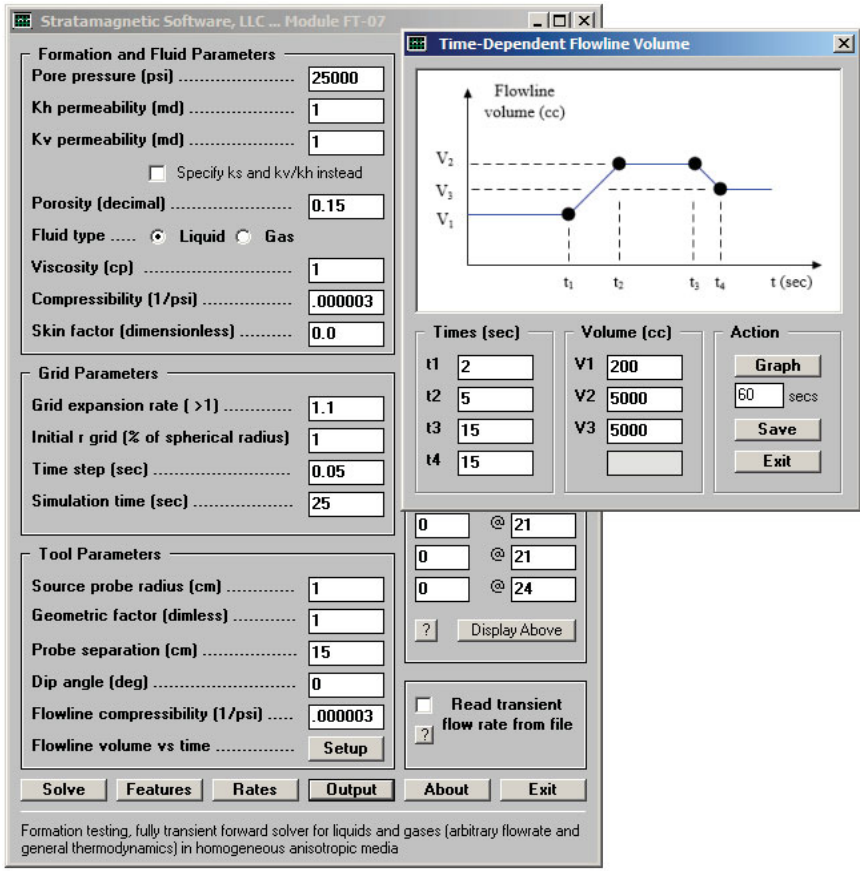

Figure 3.5a. Time-dependent flowline volume.

Figure 3.5b. Volume flow rate, flowline volume, source probe pressure.

We ran the inverse drawdown model using the transient drawdown data at 1, 2 and 4 seconds shown below. Additional computing time relative to previous examples was required, that is, about 1 sec total time.

```
C:\>pta-dd-3-run-with-rft-numbers-10000-iterations <Return>

Use decimals after all integers!

Volume flow rate (cc/s): 1.
Pump probe, radius (cm): 1.
Probe, geometric factor: 1.
1st Point Time T1 (sec): 1.
      Pressure P1 (psi): 24167.
2nd Point Time T2 (sec): 2.
      Pressure P2 (psi): 23949.
3rd Point Time T3 (sec): 4.
      Pressure P3 (psi): 23916.

    Run     Error   P0(psi)   Md/Cp

   1500.   44.5 %    25144    0.949
   1600.   37.6 %    25246    0.883
   1700.   29.9 %    25360    0.818
   1800.   21.4 %    25485    0.756
   1900.   12.0 %    25624    0.697
   2000.    1.5 %    25777    0.641
   2004.    1.0 %    25784    0.639
   2005.    0.9 %    25785    0.638
   2006.    0.8 %    25787    0.638
   2007.    0.7 %    25789    0.637
   2008.    0.6 %    25790    0.637
   2009.    0.5 %    25792    0.636
   2010.    0.4 %    25794    0.635
   2011.    0.3 %    25795    0.635
   2012.    0.1 %    25797    0.634
   2013.    0.0 %    25798    0.634
Stop - Program terminated.
```

The predicted pore pressure of 25,798 psi (vs 25,000) and mobility of 0.634 md/cp (vs 1.0) are reasonable, considering the fact that our inverse drawdown model was *never* intended to work with large, rapidly increasing flowline volumes.

3.7 Tool Calibration in Low Mobility Applications

In this section, we introduce the subject of tool calibration using our early-time, low-mobility models. The procedures are actually very straightforward and easily understood.

3.7.1 Steady flow model

We again revisit Figure 3.2a – also, we emphasize that the calibration constants in this section apply only to Schlumberger RFT tools, although surprisingly, the authors have found the equations below used indiscriminately for tools from different manufacturers.

If ΔP is the drawdown pressure, C is a flow shape factor, q is the volume flow rate, μ is the liquid viscosity, and r_p is an "effective probe radius," then the drawdown permeability can be calculated from the simple relation

$$k_d = Cq\mu/(2\pi r_p \Delta P) \tag{3.26b}$$

For convenience, the "$C/(2\pi r_p)$" is usually represented as a single number, say

$$k_d = 5{,}660\ q\mu/\Delta P \tag{3.26c}$$

Here k_d, q, μ and ΔP are expressed in md, cc/s, cp and psi. The constant 5,660 applies to the "standard" RFT probe. When the "large diameter" or the "fast-acting" probe is used, the constant should be 2,395; for the "large-area packer," the constant becomes 1,107 (see Log Interpretation Principles/Applications (1989) for details). These values are calibration constants accounting for non-spherical effects like borehole wall curvature and pad geometry.

There is nothing unique about "$k_d = Cq\mu/(2\pi r_p \Delta P)$," which we emphasize applies to medium-high permeabilities only. The aforementioned approach is a "recipe" and nothing more. What if we our logging applications focus more on low mobilities? The problems may be more subtle: for higher mobilities, flowline storage effects disappear quickly, but for lower mobilities, they are always present at the early times data are recorded. Thus, the "C" constants obtained in the above paragraph could not be expected to apply.

3.7.2 Example 1, Calibration using early-time buildup data
Software reference, FT-PTA-DDBU

In the next several sections, we will explain how to calibrate a single-probe formation tester tool using inverse program FT-PTA-DDBU for buildup and also "drawdown only" methods. We will describe them in a manner that follows field procedures closely. By "calibration," we mean that permeability/viscosity and pore pressure are known for a particular transient (or steady) pressure response.

We want to find the best "tool constants" to use with an inverse method so that, in field operations when future source probe responses are obtained, the correct mobility will be predicted (note, only is "mobility = permeability/viscosity" is important and not permability or viscosity individually). Let us assume that we *know* that the mobility for a formation is 1 md/cp (e.g., a 1 md permeability formation containing a 1 cp viscosity liquid) and the pore pressure is 25,000 psi. The volume flow rate and source response history are given in Figures 3.6a and 3.6b. What does FT-PTA-DDBU do? The software inputs are shown in Figure 3.6c.

The model is very powerful and requires minimal input data. It assumes that liquid is withdrawn at a constant volume flow rate until a time "TEND," at which point drawdown ends and buildup begins. The software uses buildup data. In particular, it requires (1) the time TEND at which pumping stops in seconds, (2) three pressure data points in time, i.e., (t_1, p_1), (t_2, p_2) and (t_3, p_3) in seconds and psi, (3) the volume flow rate in cc/sec during pumping, (4) the geometric radius (cm), and (5) the "geometric factor" which is an empirical tool constant associated with the tool pad and borehole curvature. The objective is to determine the geometric factor. Once we have this calibration constant, it "stays with the tool forever." Future predictions for mobility and pore pressure are based on this and it is essential to obtain this correctly.

Now refer to the top screen of Figure 3.6c. We enter TEND, the three pressure data points highlighted in red in Figure 1b, the volume flow rate, and a geometric radius of 1 cm. Note that for the geometric factor, we try "1" in the top screen. Clicking "Find" gives the mobility 1.64 md/cp. This is not bad, but it is not good compared to the known value of 1 md/cp. Thus, in the second screen, we try a geometric factor of 1.5. We find that the mobility now is 1.09 md/cp. This is much closer to the known 1 md/cp. In the bottom screen, we try 1.75. This gives a mobility of 0.94 md/cp. In the present example, all the pore pressures are identical, with the 24,980 psi close to the known 25,000 psi. It is clear that 1.5 (or maybe a bit more,)is best. Thus, we stop here and "keep 1.5 forever for this tool."

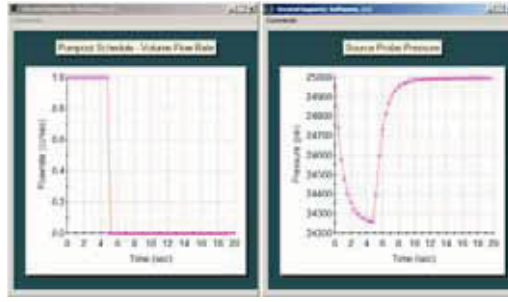

Figure 3.6a. Volume flow rate and source probe response history.

Time (s)	Rate (cc/s)	Ps* (psi)
0.000E+00	0.10000E+01	0.25000E+05
0.400E+00	0.10000E+01	0.24743E+05
0.800E+00	0.10000E+01	0.24581E+05
0.120E+01	0.10000E+01	0.24475E+05
0.160E+01	0.10000E+01	0.24405E+05
0.200E+01	0.10000E+01	0.24358E+05
0.240E+01	0.10000E+01	0.24326E+05
0.280E+01	0.10000E+01	0.24304E+05
0.320E+01	0.10000E+01	0.24288E+05
0.360E+01	0.10000E+01	0.24277E+05
0.400E+01	0.10000E+01	0.24269E+05
0.440E+01	0.10000E+01	0.24264E+05
0.480E+01	0.10000E+01	0.24259E+05

Pump stops, buildup begins . . .

0.520E+01	**0.00000E+00**	**0.24400E+05**
0.560E+01	0.00000E+00	0.24600E+05
0.600E+01	**0.00000E+00**	**0.24729E+05**
0.800E+01	**0.00000E+00**	**0.24949E+05**
0.100E+02	0.00000E+00	0.24984E+05
0.120E+02	0.00000E+00	0.24992E+05
0.140E+02	0.00000E+00	0.24995E+05
0.160E+02	0.00000E+00	0.24996E+05
0.180E+02	0.00000E+00	0.24997E+05

Figure 3.6b. Numerical values of source probe pressure versus time.

How do we know this is *really* the right answer? In Figure 3.6d, we show the assumptions used in FT-00, our exact forward simulator, used to create the pressure transient data (in an actual field example, the data would be created by Nature). Notice that we assumed a 1 md permeability and a 1 cp liquid viscosity, so that the mobility is 1 md/cp. Also, the pore pressure was 25,000 psi. For the present purposes, the probe radius was 1 cm and the pad geometric factor was "1.5," from the left middle menu, so that the "effective radius" is "1 cm × 1.5" or 1.5 cm. This 1.5 cm is exactly the value of effective radius used in the middle screen of Figure 3.6c (note that a geometric factor of 1.6 may have been a little better, but we will not try to make the match exact here). Note that the latest pressure point data taken is at 8 sec and the curve in Figure 3.6a has not reached steady-state yet.

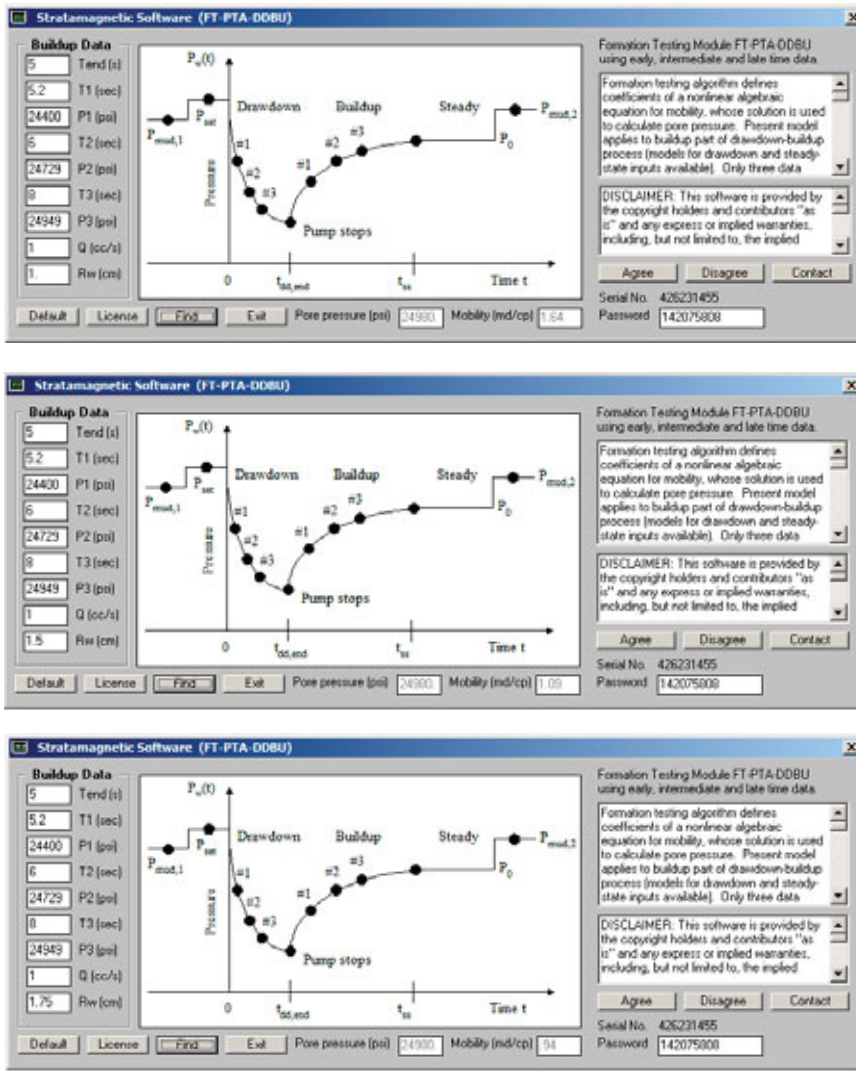

Figure 3.6c. FT-PTA-DDBU inverse method.

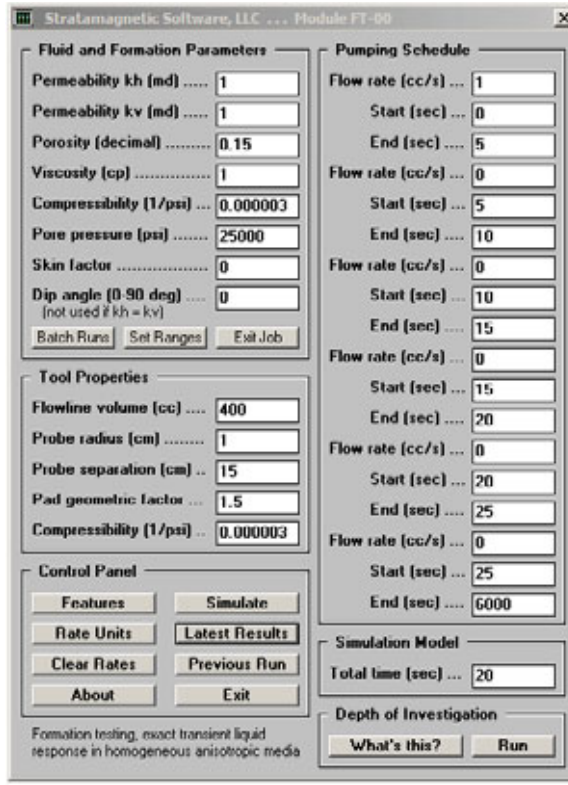

Figure 3.6d. FT-00 used to create pressure transient data, mobility of 1 md/cp.

3.7.3 Example 2, Calibration using early time-buildup data

Now let's try a more difficult example. As is obvious from Figure 3.7a, the mobility of the problem is smaller and flowline volume distortion is greater than in Example 1. Source probe pressure transient data is given in Figure 3.7b. Also, we *know* that the mobility os 0.5 md/cp and the pore pressure is 25,000 psi for our calibration. We will use data from 6, 8 and 12 sec – at 12 sec, note that steady-state has not yet been achieved. The screens in Figure 3.7c show predicted mobilities of 0.83, 0.56 and 0.48 md/cp, and all give pore pressures of 24,977 psi. The best geometric factors are in the range 1.5 – 1.6. Note from Figure 3.7d that an effective radius of 1.5 cm (corresponding to a geometric radius of 1 cm and a geometric factor of 1.5) was used to create the pressure transient data. Here, the pressure transient data was created by FT-00, but in the field, it would be created by Nature. It is important to emphasize that, from Figure 3.7d, the mobility assumed was very low, taking the value of 0.5 md/cp, and the flowline volume is very large at 600 cc.

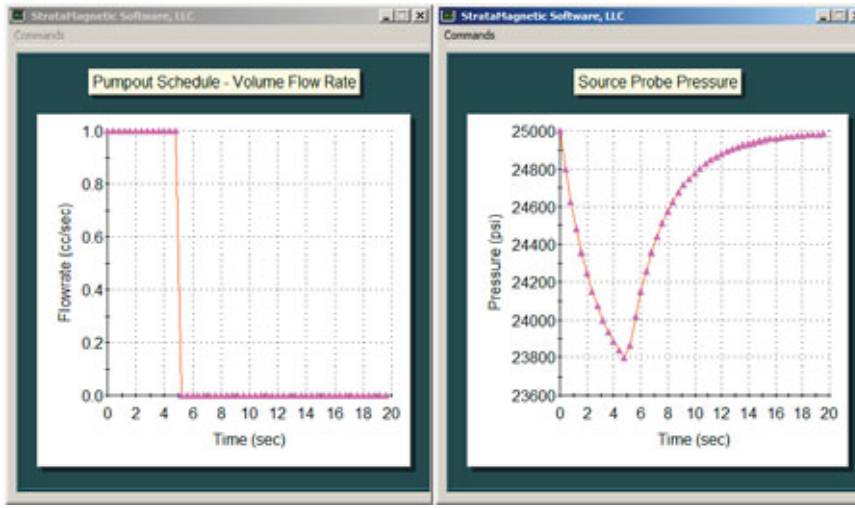

Figure 3.7a. Volume flow rate and source probe transient response.

Time (s)	Rate (cc/s)	Ps* (psi)
0.000E+00	0.10000E+01	0.25000E+05
0.400E+00	0.10000E+01	0.24799E+05
0.800E+00	0.10000E+01	0.24628E+05
0.120E+01	0.10000E+01	0.24481E+05
0.160E+01	0.10000E+01	0.24355E+05
0.200E+01	0.10000E+01	0.24246E+05
0.240E+01	0.10000E+01	0.24151E+05
0.280E+01	0.10000E+01	0.24070E+05
0.320E+01	0.10000E+01	0.23999E+05
0.360E+01	0.10000E+01	0.23937E+05
0.400E+01	0.10000E+01	0.23883E+05
0.440E+01	0.10000E+01	0.23836E+05
0.480E+01	0.10000E+01	0.23795E+05
Pumping stops, pressure buildup starts ...		
0.520E+01	0.00000E+00	0.23864E+05
0.560E+01	0.00000E+00	0.24018E+05
0.600E+01	**0.00000E+00**	**0.24149E+05**
0.640E+01	0.00000E+00	0.24261E+05
0.680E+01	0.00000E+00	0.24357E+05
0.720E+01	0.00000E+00	0.24440E+05
0.760E+01	0.00000E+00	0.24511E+05
0.800E+01	**0.00000E+00**	**0.24573E+05**
0.840E+01	0.00000E+00	0.24626E+05
0.880E+01	0.00000E+00	0.24673E+05
0.920E+01	0.00000E+00	0.24713E+05
0.960E+01	0.00000E+00	0.24748E+05
0.100E+02	0.00000E+00	0.24778E+05
0.104E+02	0.00000E+00	0.24805E+05
0.108E+02	0.00000E+00	0.24828E+05
0.112E+02	0.00000E+00	0.24848E+05
0.116E+02	0.00000E+00	0.24865E+05
0.120E+02	**0.00000E+00**	**0.24881E+05**
0.124E+02	0.00000E+00	0.24894E+05
0.128E+02	0.00000E+00	0.24906E+05
0.132E+02	0.00000E+00	0.24916E+05
0.136E+02	0.00000E+00	0.24925E+05
0.140E+02	0.00000E+00	0.24933E+05
0.144E+02	0.00000E+00	0.24940E+05
0.148E+02	0.00000E+00	0.24946E+05
0.152E+02	0.00000E+00	0.24952E+05
0.156E+02	0.00000E+00	0.24956E+05
0.160E+02	0.00000E+00	0.24961E+05
0.164E+02	0.00000E+00	0.24964E+05
0.168E+02	0.00000E+00	0.24968E+05
0.172E+02	0.00000E+00	0.24971E+05
0.176E+02	0.00000E+00	0.24973E+05
0.180E+02	0.00000E+00	0.24976E+05
0.184E+02	0.00000E+00	0.24978E+05
0.188E+02	0.00000E+00	0.24980E+05
0.192E+02	0.00000E+00	0.24981E+05
0.196E+02	0.00000E+00	0.24983E+05

Figure 3.7b. Numerical values of source probe pressure versus time.

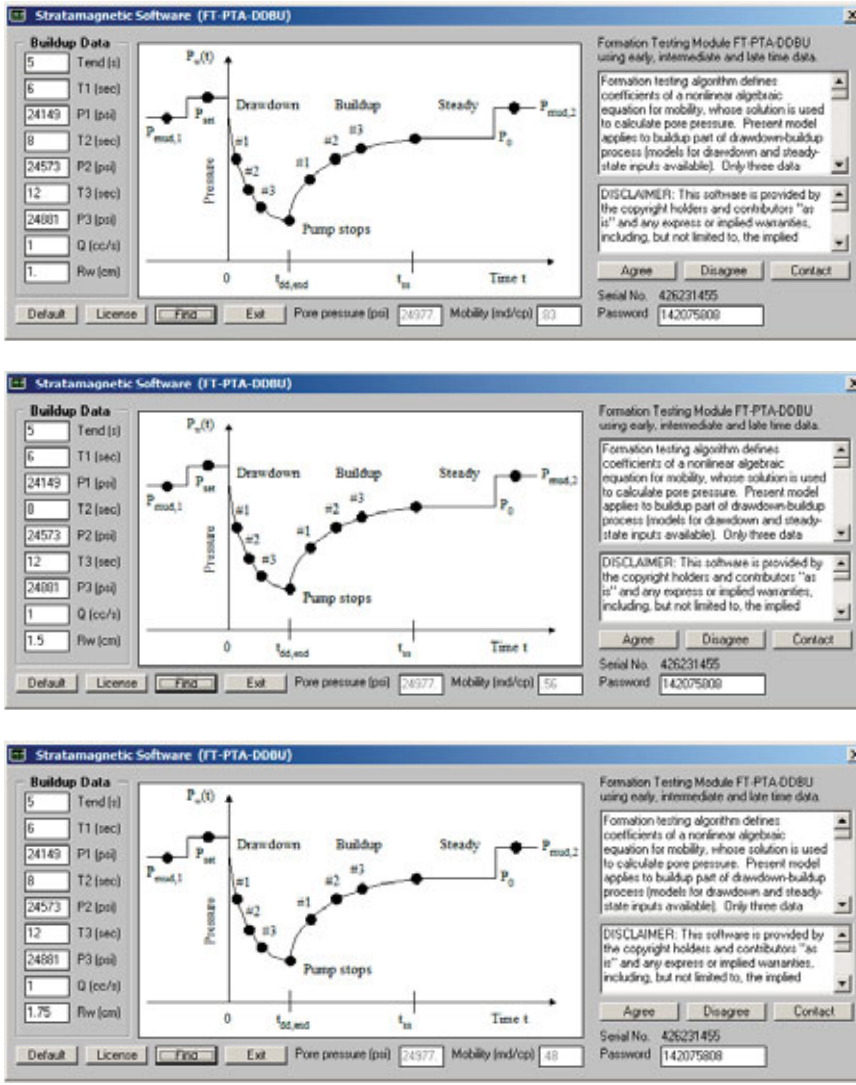

Figure 3.7c. FT-PTA-DDBU screens with different geometric factor guesses.

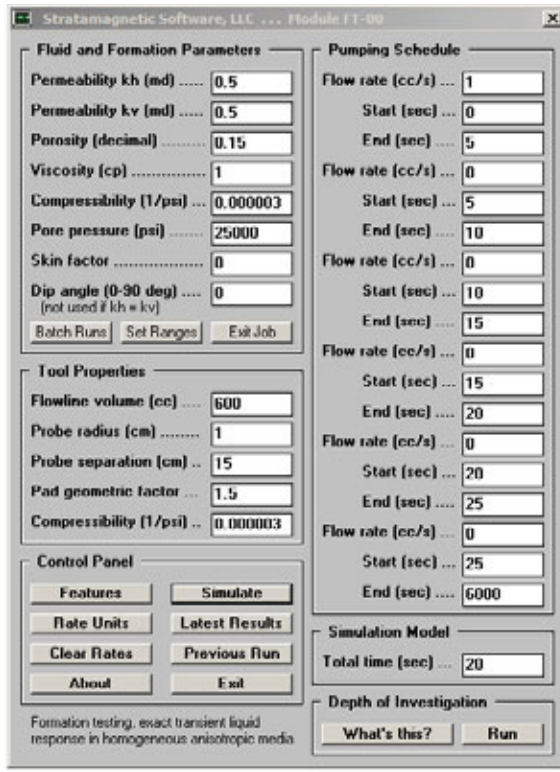

Figure 3.7d. FT-00 assumptions, showing effective radius of 1.5 cm, and a mobility of 0.5 md/cp.

3.7.4 Example 3, Example 1 using drawdown data

From Figure 3.6b, we have the drawdown data –

Time (s)	Rate (cc/s)	Ps* (psi)
0.000E+00	0.10000E+01	0.25000E+05
0.400E+00	0.10000E+01	0.24743E+05
0.800E+00	0.10000E+01	0.24581E+05
0.120E+01	0.10000E+01	0.24475E+05
0.160E+01	**0.10000E+01**	**0.24405E+05**
0.200E+01	0.10000E+01	0.24358E+05
0.240E+01	0.10000E+01	0.24326E+05
0.280E+01	**0.10000E+01**	**0.24304E+05**
0.320E+01	0.10000E+01	0.24288E+05
0.360E+01	0.10000E+01	0.24277E+05
0.400E+01	0.10000E+01	0.24269E+05
0.440E+01	0.10000E+01	0.24264E+05
0.480E+01	**0.10000E+01**	**0.24259E+05**

We use the blue data highlighted above, and use the software "pta-dd-3-run-with-rft-numbers-10000-iterations.exe" to find the results below (this software is identical to "pta-dd-3-run-rft-with-numbers" except that more iterations are performed and printed). Suppose, at first, we did not know the geometric factor, and took "1" as a guess. We would obtain the following screens.

```
C:\>pta-dd-3-run-with-rft-numbers-10000-iterations <Return>

Volume flow rate (cc/s): 1.
Pump probe, radius (cm): 1.
Probe, geometric factor: 1.
1st Point Time T1 (sec): 1.6
      Pressure P1 (psi): 24405.
2nd Point Time T2 (sec): 2.8
      Pressure P2 (psi): 24304.
3rd Point Time T3 (sec): 4.8
      Pressure P3 (psi): 24259.

    Run    Error  P0(psi)  Md/Cp
    801.   9.9 %   24830   2.005
    802.   9.8 %   24831   2.003
    803.   9.6 %   24831   2.002
    804.   9.5 %   24832   2.000
.
.
.
    870.   0.5 %   24876   1.884
    871.   0.4 %   24876   1.882
    872.   0.3 %   24877   1.880
    873.   0.1 %   24878   1.879
    874.   0.0 %   24878   1.877
Stop - Program terminated.
```

Notice that we could not get a good match to 25,000 psi and 1 md/cp which are given as original data. Therefore, we try a geometric factor of 1.5 next.

```
C:\>pta-dd-3-run-with-rft-numbers-10000-iteration <Return>

Volume flow rate (cc/s): 1.
Pump probe, radius (cm): 1.
Probe, geometric factor: 1.5
1st Point Time T1 (sec): 1.6
      Pressure P1 (psi): 24405.
2nd Point Time T2 (sec): 2.8
      Pressure P2 (psi): 24304.
3rd Point Time T3 (sec): 4.8
      Pressure P3 (psi): 24259.

    Run    Error  P0(psi)  Md/Cp
    801.   9.9 %   24830   1.337
    802.   9.8 %   24831   1.336
    803.   9.6 %   24831   1.334
    804.   9.5 %   24832   1.333
    805.   9.4 %   24833   1.332
    806.   9.2 %   24833   1.331
    807.   9.1 %   24834   1.330
    808.   9.0 %   24835   1.329
    809.   8.9 %   24835   1.328
    810.   8.7 %   24836   1.326
.
.
    871.   0.4 %   24876   1.255
    872.   0.3 %   24877   1.254
    873.   0.1 %   24878   1.252
    874.   0.0 %   24878   1.251
Stop - Program terminated.
```

The match to 1 md/cp is much better, so we attempt a geometric factor of 1.8 next.

```
C:\>pta-dd-3-run-with-rft-numbers-10000-iterations <Return>

Volume flow rate (cc/s): 1.
Pump probe, radius (cm): 1.
Probe, geometric factor: 1.8
1st Point Time T1 (sec): 1.6
      Pressure P1 (psi): 24405.
2nd Point Time T2 (sec): 2.8
      Pressure P2 (psi): 24304.
3rd Point Time T3 (sec): 4.8
      Pressure P3 (psi): 24259.

    Run    Error  P0(psi)  Md/Cp
    801.   9.9 %   24830   1.114
    802.   9.8 %   24831   1.113
    803.   9.6 %   24831   1.112
    804.   9.5 %   24832   1.111
    805.   9.4 %   24833   1.110
    806.   9.2 %   24833   1.109
.
.
    870.   0.5 %   24876   1.047
    871.   0.4 %   24876   1.046
    872.   0.3 %   24877   1.045
    873.   0.1 %   24878   1.044
    874.   0.0 %   24878   1.043
Stop - Program terminated.
```

Now, the 1.043 md/cp matches very well with the data of 1 md/cp, so we keep the geometric factor of 1.8. The assumed geometric factor of 1.8 does not agree with the 1.5 used in FT-00 because the drawdown inverse method is approximate while FT-00 is exact.

3.7.5 Example 4, Example 2 using drawdown data

Now, let us reconsider Example 2, but use the drawdown data obtained from Figure 3.7b –

Time (s)	Rate (cc/s)	Ps* (psi)
0.000E+00	0.10000E+01	0.25000E+05
0.400E+00	0.10000E+01	0.24799E+05
0.800E+00	**0.10000E+01**	**0.24628E+05**
0.120E+01	0.10000E+01	0.24481E+05
0.160E+01	0.10000E+01	0.24355E+05
0.200E+01	0.10000E+01	0.24246E+05
0.240E+01	0.10000E+01	0.24151E+05
0.280E+01	**0.10000E+01**	**0.24070E+05**
0.320E+01	0.10000E+01	0.23999E+05
0.360E+01	0.10000E+01	0.23937E+05
0.400E+01	0.10000E+01	0.23883E+05
0.440E+01	0.10000E+01	0.23836E+05
0.480E+01	0.10000E+01	0.23795E+05

This example is more difficult than Example 3 because the "known" mobility of 0.5 md/cp is smaller and the flowline volume is much larger at 600 cc. Again, suppose we selected the wrong geometric factor as "1." Then, we obtain –

```
C:\>pta-dd-3-run-with-rft-numbers-10000-iterations <Return>

Volume flow rate (cc/s): 1.
Pump probe, radius (cm): 1.
Probe, geometric factor: 1.
1st Point Time T1 (sec): 0.8
      Pressure P1 (psi): 24628.
2nd Point Time T2 (sec): 2.8
      Pressure P2 (psi): 24070.
3rd Point Time T3 (sec): 4.8
      Pressure P3 (psi): 23795.

    Run    Error  P0(psi)  Md/Cp
    302.   9.8 %   24964   0.754
    303.   9.7 %   24964   0.755
    304.   9.5 %   24965   0.756
    305.   9.3 %   24965   0.757
    306.   9.1 %   24966   0.759
.
    348.   1.2 %   24985   0.804
    349.   1.0 %   24985   0.805
    350.   0.8 %   24986   0.805
    351.   0.6 %   24986   0.806
    352.   0.4 %   24987   0.807
    353.   0.2 %   24987   0.808
    354.   0.0 %   24988   0.809
Stop - Program terminated.
```

The 0.809 md/cp is not good compared to the known 0.5 md/cp. Thus, let us try a geometric factor of 1.5.

```
C:\>pta-dd-3-run-with-rft-numbers-10000-iterations <Return>

Volume flow rate (cc/s): 1.
Pump probe, radius (cm): 1.
Probe, geometric factor: 1.5
1st Point Time T1 (sec): 0.8
      Pressure P1 (psi): 24628.
2nd Point Time T2 (sec): 2.8
      Pressure P2 (psi): 24070.
3rd Point Time T3 (sec): 4.8
      Pressure P3 (psi): 23795.

    Run    Error  P0(psi)  Md/Cp
    302.   9.8 %   24964   0.503
    303.   9.7 %   24964   0.503
    304.   9.5 %   24965   0.504
    305.   9.3 %   24965   0.505
    306.   9.1 %   24966   0.506
.
.
    350.   0.8 %   24986   0.537
    351.   0.6 %   24986   0.538
    352.   0.4 %   24987   0.538
    353.   0.2 %   24987   0.539
    354.   0.0 %   24988   0.539
Stop - Program terminated.
```

The geometric factor of 1.5, which agrees with the FT-00 assumption, gives a good match of 24,988 psi and 0.539 md/cp to the known 25,000 psi and 0.5 md/cp.

3.8 Closing Remarks

We first reviewed a well known RFT calculation method for drawdown permeability that used steady-state spherical flow formulas (with empirically corrected coefficients, e.g., "5,660," "2,395" and "1,107") together with equilibrated pressure data. Using this data, we calibrated our exact FT-00 model to produce the same steady drawdowns naturally, with ours additionally being able to create synthetic transient data useful for testing different classes of inverse models. Then, using a new procedure requiring only three time-pressure points (which may be unequally spaced), we showed how mobilities and pore pressures can be predicted accurately over a wide range of flowline volumes. The new method, based on our exact solution, permits use of early-time transient drawdown and buildup data in low mobility applications characterized by strong flowline effects, in contrast to conventional models which assume the exact opposite. The two methods presented extract fluid and formation parameters accurately and economically using unequilibrated pressures data. Thus, they support rapid and economical formation evaluation and, at the same time, significantly reduce the risk of stuck downhole tools. Moreover, because implementation requires just several lines of source code, the algorithm may be incorporated in downhole formation testing tools for real-time operation.

For medium-high mobility applications, the standard industry calibration methods used for RFT tools should be used – these are based on the steady-state formula connecting pressure drop to permeability or mobility. However, for lower mobility problems with significant flowline volumes, the present FT-PTA-DDBU and "drawdown only" methods are very powerful and should be used. They require minimum input information – they do not need flowline volume, formation porosity or fluid compressibility data as a Horner-type method would. As shown in examples, only three pressure data points are required along the buildup or the drawdown curve. They may be just seconds apart, may be arbitrarily spaced in time, and need not have reached steady-state. We have randomly selected the pressure data points. In field practice, there will be "scatter" among the data, and different groups of three points may be used to check on repeatability of the results.

In general, we use either method and vary the geometric factor to match known mobilities and pore pressures Once we obtain the geometric factor that provides the correct matching, the "geometric factor is kept forever" for that tool. This is a very simple procedure. Of course, the spherical or ellipsoidal flow models used to develop FT-00 and the drawdown-buildup methods are idealizations and not perfect. Thus, in the calibrating, it is best to use data obtained from similar circumstances. For example, if logging a six-inch well in Sand A, it is best to use data for a similar six-inch well in Sand A, if possible.

3.9 References

Bowles, D., "Bridging the Gap Between Wireline Formation, Drill Stem Testing," *Offshore Magazine*, June 1, 2004.

Chin, W.C., "FTWD-Processing-Algorithms-V56a," *Stratamagnetic Software Internal Report*, July 2012.

Chin, W.C., Zhou, Y., Feng, Y., Yu, Q. and Zhao, L., Formation Testing Pressure Transient and Contamination Analysis, John Wiley, New Jersey, 2014.

Dussan, E.B., Auzerais, F.M. and Kenyon, W.E., "Apparatus for Determining Horizontal and/or Vertical Permeability of an Earth Formation," United States Patent No. 5,279,153 awarded Jan. 18, 1994.

Proett, M.A. and Chin, W.C., "Multi-Probe Pressure Transient Analysis for Determination of Horizontal Permeability, Anisotropy and Skin in an Earth Formation," United States Patent 7,059,179 B2, awarded June 13, 2006.

Proett, M., Chin, W.C. and Chen, C.C., "Method of Formation Testing," United States Patent 5,703,286, awarded December 30, 1997.

Proett, M.A., Chin, W.C., and Mandal, B., "Advanced Permeability and Anisotropy Measurements While Testing and Sampling in Real-Time Using a Dual Probe Formation Tester," SPE Paper 64650, *Seventh International Oil & Gas Conference and Exhibition* in Beijing, China, November 2000.

Proett, M.A., Weintraub, P.N., Golla, C.A., and Simeonov, S.D., "Formation Testing While Drilling Data Compression," United States Patent 6,932,167 B2, awarded August 23, 2005.

Staff, Log Interpretation Principles/Applications, Schlumberger Wireline and Testing, Sugar Land, 1989.

4

Phase Delay and Amplitude Attenuation for Mobility Prediction in Anisotropic Media with Dip *

In electromagnetic logging, resistivity is determined by evaluating receiver amplitude attenuation or phase delay response of a sinusoidal transmitter signal using Maxwell's equations. As simple as this idea sounds, its first MWD/LWD implementation only appeared in the 1980's with NL Sperry Sun's introduction of its Electromagnetic Wave Resistivity™ (EWR) tool, building on advances in wireline induction logging. The formation tester can be analogously used to evaluate permeability. A periodic pressure signal created by the pump piston is measured at a second probe and rock properties can be deduced from waveform changes using Darcy's laws. And similar to resistivity methods employing multiple receiver coils, attenuations and delays between multiple observation probes can be used to determine permeability with analogous accuracy benefits.

In this chapter, methods for isotropic uniform media are motivated and developed and then extended to anisotropic homogeneous media for tools oriented at arbitrary dip angles. We will demonstrate how *both* k_h and k_v can be obtained using combined drawdown-buildup and phase delay methods; and, in the case when beds are thick, how two phase delay measurements taken at different dip angles (corresponding to different bit locations while the drillstring changes direction) likewise yield both permeabilities. These methods assume "one transmitter, one receiver" tools. Additionally, we show how "multiple receiver" (that is, multiple observation probe formation testers) can produce more accurate results using relative receiver (observation probe) measurements, as in electromagnetic logging. These results are entirely exact and analytical.

*Patent pending, multiple algorithms.

The mathematical formulation and numerical approach, together with three-dimensional extensions for layered media, are also presented. We note that the phase delay approach first appeared in "Formation Evaluation Using Phase Shift Periodic Pressure Pulse Testing," U.S. Patent No. 5,672,819 awarded to Chin and Proett and issued Sept. 30, 1997. This invention focused on isotropic media only and was never implemented operationally because two probes, one source and the second observation, were required; for the single spherical permeability characterizing such reservoirs, it was much more convenient using single source probe drawdown-buildup methods, such as those discussed in the previous chapter. In this chapter, we resurrect phase delay methods because, it turns out, it is possible to obtain *both* k_h and k_v in anisotropic applications. Moreover, *this can be achieved in low mobility formations using very early time data* The method discussed here is "patent pending" and open to licensing opportunities.

4.1 Basic Mathematical Results

In this section, we derive basic mathematical results which support the physical ideas introduced in this chapter. The assumptions used and required algebraic steps taken are clearly identified so that the conditions under which our interpretation models apply are unambiguous. Parallels between formation testing and electromagnetic logging are explained and exploited throughout.

4.1.1 Isotropic model

For slightly compressible liquids in isotropic homogeneous media, the standard model

$$\partial^2 p/\partial r^2 + 2/r\ \partial p/\partial r = (\phi\mu c/k)\ \partial p/\partial t \tag{4.1}$$

applies where ϕ, μ, c and k are porosity, viscosity, compressibility and isotropic permeability. We seek separable solutions in the form

$$p(r,t) = P(r)\ \exp(i\omega t) \tag{4.2}$$

Thus, the above real partial differential equation reduces to the complex ordinary differential equation

$$d^2P/dr^2 + 2/r\ dP/dr - i\omega\phi\mu c/k\ P = 0 \tag{4.3}$$

for a complex P(r). To solve this, we assume solutions of the form

$$P \sim r^{-1}\ \exp(ar) \tag{4.4}$$

where "a" is a complex constant. Then, substitution in Equation 4.3 shows that $a^2 = i\omega\phi\mu c/k$ which leads to

$$a = \pm (1 + i) \sqrt{\{\phi\mu c\omega/(2k)\}} \tag{4.5}$$

Hence, our pressure solution is

$$\begin{aligned} p(r,t) &= P(r) \exp(i\omega t) \\ &= (B/r) \exp[r\sqrt{\{\phi\mu c\omega/(2k)\}}]\exp [i(\omega t + r\sqrt{\{\phi\mu c\omega/(2k)\}})] \\ &+ (C/r) \exp[-r\sqrt{\{\phi\mu c\omega/(2k)\}}]\exp [i(\omega t - r\sqrt{\{\phi\mu c\omega/(2k)\}})] \end{aligned} \tag{4.6}$$

where B and C are complex constants (it is the lumped quantity shown in blue that is important and not any parameter individually). The solution associated with the B solution increases in amplitude away from the source probe and is associated with inward propagating solutions. Thus, we discard it, leaving

$$p(r,t) = (C/r) \exp[-r\sqrt{\{\phi\mu c\omega/(2k)\}}]\exp [i(\omega t - r\sqrt{\{\phi\mu c\omega/(2k)\}})] \tag{4.7}$$

This correctly decays for large r values away from the tool and enables outward propagating solutions. In fact, if we now choose the value

$$C = P_0 r_w \exp(+r_w\sqrt{\{\phi\mu c\omega/(2k)\}})\exp(ir_w\sqrt{\{\phi\mu c\omega/(2k)\}}) \tag{4.8}$$

where r_w is the "well radius" of the spherical source or pumping probe, the mathematical pressure solution becomes (4.9)

$$p(r,t) = P_0 (r_w/r) \exp[-(r-r_w) \sqrt{\{\phi\mu c\omega/(2k)\}}] \exp [i(\omega t-(r-r_w)\sqrt{\{\phi\mu c\omega/(2k)\}})]$$

Taking the real part gives the physical solution as (4.10)

$$p(r,t) = P_0 (r_w/r) \exp[-(r-r_w) \sqrt{\{\phi\mu c\omega/(2k)\}}] \cos [\omega t-(r-r_w)\sqrt{\{\phi\mu c\omega/(2k)\}}]$$

In summary, we state the result in simplified terms. A solution to Equation 4.1 takes the form

$$p(r,t) = A \cos (\omega t - \theta) \tag{4.11}$$

where the *real* quantities A and θ satisfy

$$A = P_0 (r_w/r) \exp[-(r-r_w) \sqrt{\{\phi\mu c\omega/(2k)\}}] \tag{4.12}$$

$$\theta = (r-r_w)\sqrt{\{\phi\mu c\omega/(2k)\}} \tag{4.13}$$

This solution describes the pressure field p(r,t) for all r; when $r = r_w$, we have $A = P_0$ and $\theta = 0$ so that $p(r,t) = A \cos \omega t$ at the source or pumping probe. It is applicable to the so-called "spherical source" representation of the formation testing pad shown in Figure 4.1 (the "ellipsoidal source" applies to flows in transversely isotropic media, which will be considered next).

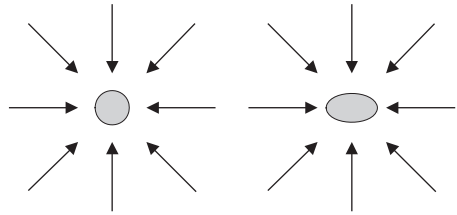

Spherical versus ellipsoidal source

Figure 4.1. Spherical source in isotropic media.

The above isotropic results are easily used to develop ideas in amplitude attenuation and phase delay interpretation in isotropic media. The basic approach is simple. Analogous to resistivity methods, we can use Equation 4.12 for amplitude analysis or Equation 4.13 for phase analysis. If, at the observation probe "p," where $r = r_p >> r_w$, the pressure amplitude A_p is measured, then $A_p = P_0 (r_w/r_p) \exp[-(r_p-r_w) \sqrt{\{\phi\mu c\omega/(2k)\}}]$ holds and the permeability k can be calculated from simple algebra. On the other hand, if the phase θ_p is measured, then we have $\theta_p = (r_p-r_w)\sqrt{\{\phi\mu c\omega/(2k)\}}$ and again k is available. As in resistivity or electromagnetic logging, larger frequencies give improved resolution with less depth of investigation; smaller frequencies provide less resolution but greater depth of investigation.

4.1.2 Anisotropic equations

We can extend the foregoing ideas to anisotropic media, and in particular, treat the important example of transversely isotropic media. For such problems, the effects of the dip angle δ are significant. In this case, the general Darcy partial differential equation for homogeneous media becomes

$$k_h (\partial^2 p/\partial x^2 + \partial^2 p/\partial y^2) + k_v \partial^2 p/\partial z^2 = \phi\mu c \, \partial p/\partial t \qquad (4.14)$$

Here k_h is the horizontal permeability in the x-y plane and k_v is the vertical permeability along the perpendicular z axis. It is desirable to solve this subject to boundary conditions on $x^2 + y^2 + z^2 = r_w^2$ since this is a spherical source surface with clear physical meaning. However, the solution is possible only numerically; note that computational solutions are not convenient for interpretation since tabulated values are cumbersome to use.

Fortunately, analytical closed-form solutions can be readily adapted for permeability interpretation following steps analogous to the isotropic derivation. As will be obvious, we should assume

$$p(x,y,z,t) = P(r^*,t) \qquad (4.15)$$

where

$$r^* = (x^2/k_h + y^2/k_h + z^2/k_v)^{1/2} \quad (4.16)$$

Straightforward manipulations lead to

$$\partial^2 P/\partial r^{*2} + 2/r^* \, \partial P/\partial r^* = \phi\mu c \, \partial P/\partial t \quad (4.17)$$

which takes on a near-isotropic form similar to Equation 4.1. An expected "k," not shown here, has been absorbed into the definition of r^*.

Also note that, because of the form of the independent variable assumed in Equation 4.16 (chosen to facilitate simple solutions), boundary conditions can only be applied along surfaces of constant r^* – that is, x, y and z values satisfying $r_w^* = (x^2/k_h + y^2/k_h + z^2/k_v)^{1/2}$ where "w" now refers to the ellipsoidal surface that has replaced our spherical well. The physical meaning of this ellipsoid is less clear, and unlike the sphere used in our isotropic analysis, now depends on horizontal and vertical permeability for general deviation angles. Thus, it is important that in the interpretation models we design, this confusion is understood and avoided.

Following steps identical to those taken for the isotropic flow derivation, we can write

$$P(r^*,t) = A \cos(\omega t - \theta) \quad (4.18)$$

$$A = P_0 (r_w^*/r^*) \exp[-(r^* - r_w^*) \sqrt{\{\phi\mu c\omega/(2)\}}] \quad (4.19)$$

$$\theta = (r^* - r_w^*)\sqrt{\{\phi\mu c\omega/(2)\}} \quad (4.20)$$

noting that

$$r_w^{*2} = x_w^2/k_h + y_w^2/k_h + z_w^2/k_v \quad (4.21)$$

$$r^{*2} = x^2/k_h + y^2/k_h + z^2/k_v \quad (4.22)$$

It is possible to reconsider our isotropic phase delay ideas in the context of the anisotropic model to vertical, horizontal and deviated wells using these results.

4.1.3 Vertical well solution

For vertical wells, x = y = 0 so that the tool axis coincides with the z axis. This leads to

$$P(r^*,t) = A \cos(\omega t - \theta) \quad (4.23)$$

$$A = P_0 (z_w/z) \exp[-(z - z_w) \sqrt{\{\phi\mu c\omega/(2k_v)\}}] \quad (4.24a)$$

$$\theta = (z - z_w)\sqrt{\{\phi\mu c\omega/(2k_v)\}} \quad (4.24b)$$

Here and henceforth, the subscript "w" denotes "well" or the surface of the spherical or ellipsoidal well that represents the source probe. It is also possible, although not necessary, to make the approximation $z >> z_w$, in which case we obtain the simplified results

$$A \approx P_0 (z_w/z) \exp[-z \sqrt{\{\phi\mu c\omega/(2k_v)\}}] \quad (4.25a)$$

$$\theta \approx z\sqrt{\{\phi\mu c\omega/(2k_v)\}} \quad (4.25b)$$

Thus, if A_z is known at the observation probe position z by measurement, then either Equation 4.24a or 4.25a can be used to derive the vertical permeability k_v. Similarly, if θ_z is known at z, then Equation 4.24b or 4.25b can be used to find k_v. Schematics for vertical, horizontal and general deviated wells are shown in Figure 4.2.

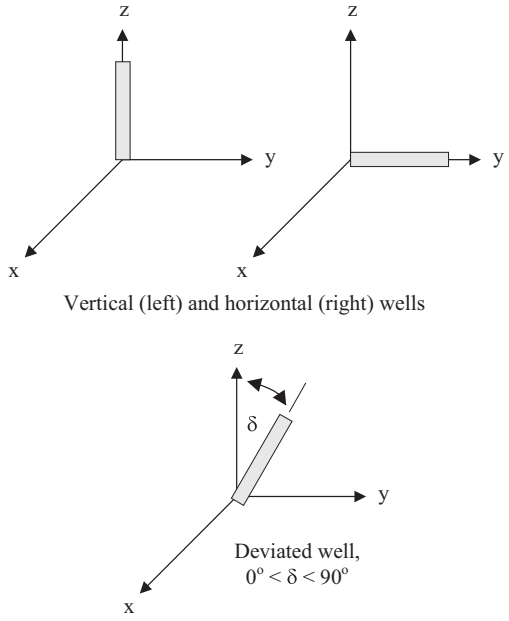

Figure 4.2. Vertical, horizontal and deviated wells.

4.1.4 Horizontal well solution

Here we assume that x = z = 0 so that the tool axis and the y axis are coincident. Then, Equations 4.18 – 4.20 can be simplified and results analogous to Equations 4.23 – 4.25 are

$$P(r^*,t) = A \cos(\omega t - \theta) \quad (4.26)$$

$$A = P_0 (y_w/y) \exp[-(y-y_w) \sqrt{\{\phi\mu c\omega/(2k_h)\}}] \quad (4.27a)$$

$$\theta = (y-y_w)\sqrt{\{\phi\mu c\omega/(2k_h)\}} \quad (4.27b)$$

and

$$A \approx P_0 \, (y_w/y) \exp[-y \sqrt{\{\phi\mu c\omega/(2k_h)\}}] \tag{4.28a}$$

$$\theta \approx y\sqrt{\{\phi\mu c\omega/(2k_h)\}} \tag{4.28b}$$

Thus, if A_y is known at the observation probe position y, then either Equation 4.27a or 4.28a can be used to derive the horizontal permeability k_h. Similarly, if θ_y is known at y, then Equation 4.27b or 4.28b can be used to find k_h. Equations 4.23 – 4.25 and Equations 4.26 – 4.28 are similar in structure to Equations 4.11 – 4.13 for isotropic applications, although they apply, respectively, to k_v and k_h determination.

4.1.5 Formulas for vertical and horizontal wells

For vertical and horizontal wells, simple formulas can be derived for permeability interpretation and tool microprocessor applications. Again, $P = A \cos(\omega t - \theta) = A \cos[\omega(t - \theta/\omega)]$, motivating us to write $P = A \cos \omega(t - \Delta t)$ where the time delay satisfies $\Delta t = \theta/\omega$. If we eliminate ω between this and $\theta \approx L\sqrt{\{\phi\mu c\omega/(2k)\}}$, where we have removed subscripts "h" and "v" for convenience, and also set $\omega = 2\pi f$ where f is the frequency in Hertz, we have the result

$$k = L^2\phi\mu c /[4\pi f(\Delta t)^2] \tag{4.29}$$

Note that the phase angle θ is large for small values of k; similarly, the time delay Δt is large for smaller k's. This means that phase delay methods are useful for interrogating low permeability (or more precisely, low mobility) formations since they are easily and quickly measured. We will offer numerical results later which illustrate the robust nature of phase delay predictions. Amplitude methods are less accurate. For instance, from Equation 4.28a, two factors contribute to amplitude reduction with distance, namely, an algebraic "geometric spreading" that is inversely proportion to distance, and an exponential effect related to formation effects. It is often difficult to separate the two effects from not-so-accurate field measurements. As we will later show, this problem is compounded by the fact that measurements at most employ two-to-three pumping cycles, hardly enough to fulfill the periodicity assumptions implicit in $P = A \cos(\omega t - \theta)$.

4.1.6 Deviated well equations

The above results for vertical and horizontal wells can be extended to general deviated wells with dip angle δ. The dip angle is 0^o for vertical wells and 90^o for horizontal wells. Note that Equation 4.29 *cannot* be used for general dip angles because it assumes "$\theta \approx L\sqrt{\{\phi\mu c\omega/(2k)\}}$" which applies only to vertical and horizontal wells. Deviated wells therefore require separate analysis. Again, let us recall that our anisotropic results are

$$P(r^*,t) = A \cos(\omega t - \theta) \tag{4.18}$$

$$A = P_0 (r_w^*/r^*) \exp[-(r^* - r_w^*) \sqrt{\{\phi\mu c\omega/(2)\}}] \tag{4.19}$$

$$\theta = (r^* - r_w^*)\sqrt{\{\phi\mu c\omega/(2)\}} \tag{4.20}$$

Without loss of generality, we assume that the tool is straight and located in the plane x = 0. If the observation probe is located a length L from the source probe, where the center of the ellipsoidal source is located at x = y = z = 0, we can write x = 0, y = L sin δ, and z = L cos δ where L is a reference length parallel to the tool axis. We seek specific results for amplitude and phase. The amplitude is governed by Equation 4.19, that is,

$$A = P_0 (r_w^*/r^*) \exp[-(r^* - r_w^*) \sqrt{\{\phi\mu c\omega/2\}}] \tag{4.30}$$

with the algebraic coefficient r_w^*/r^* derived from the square root of

$$r_w^{*2}/r^{*2} = (k_v x_w^2 + k_v y_w^2 + k_h z_w^2)/(k_v x^2 + k_v y^2 + k_h z^2) \tag{4.31}$$

having used Equations 4.21 and 4.22. This becomes z_w/z for vertical wells (when $x_w = y_w = 0$) and y_w/y for horizontal wells (when $x_w = z_w = 0$), both independent of permeability. For deviated angles between 0^o and 90^o, however, both vertical and horizontal permeabilities remain and the coefficient r_w^*/r^* remains complicated. Note that the approximation $r^* >> r_w^*$ will simplify the expression in the exponential of Equation 4.30, but r_w^*/r^* itself remains problematic, at least for now. We will deal with this later.

The phase function in Equation 4.20 is easier to work with. We can use the approximation $r^* >> r_w^*$ to obtain usable results, that is,

$$\theta = (r^* - r_w^*)\sqrt{\{\phi\mu c\omega/2\}} \tag{4.32}$$

$$\approx r^* \sqrt{\{\phi\mu c\omega/2\}} \tag{4.33}$$

$$\approx (0^2/k_h + L^2 \sin^2\delta/k_h + L^2 \cos^2\delta/k_v)^{1/2} \sqrt{\{\phi\mu c\omega/2\}} \tag{4.34}$$

Thus, we find that

$$\theta \approx L\sqrt{[\{\phi\mu c\omega/2\}\{\sin^2\delta/k_h + \cos^2\delta/k_v\}]} \tag{4.35}$$

which correctly reduces to $\theta \approx z\sqrt{\{\phi\mu c\omega/(2k_v)\}}$ when $\delta = 0^o$ (for vertical wells) and to $\theta \approx y\sqrt{\{\phi\mu c\omega/(2k_h)\}}$ when $\delta = 90^o$ (for horizontal wells). Again, we note that Equation 4.18 for the pressure response can be rewritten in the form $P(r^*,t) = A \cos(\omega t - \theta) = A \cos\omega(t - \Delta t)$ where the measured time delay is $\Delta t = \theta/\omega$. Thus, the phase delay in Equation 4.35 can be calculated from $\theta = \omega \Delta t = 2\pi f \Delta t$ where f is the frequency in Hertz.

4.1.7 Deviated well interpretation for both k_h and k_v

As noted, the expression for phase in deviated wells is considerably simpler than that for amplitude. In fact, if the phase θ_L at the observation probe distance L from the center of the source probe is known, then Equation 4.35 becomes

$$\theta_L \approx L\sqrt{[\{\phi\mu c\omega/2\}\ \{\sin^2\delta/k_h + \cos^2\delta/k_v\}]} \tag{4.36a}$$

thus providing, for the dip angle δ assumed, one equation of two needed to find both k_h and k_v. There are two approaches that can be taken, emphasizing that both apply to low mobility applications with data taken at early times.

In the first, suppose we have a thick uniform layer where the formation tester resides in a drillstring that is turning or changing direction. Then, Equation 4.36a can be evaluated at two different dip angles δ_a and δ_b so that we have two linearly independent equations

$$\theta_{L,a} \approx L\sqrt{[\{\phi\mu c\omega/2\}\ \{\sin^2\delta_a/k_h + \cos^2\delta_a/k_v\}]} \tag{4.36b}$$

$$\theta_{L,b} \approx L\sqrt{[\{\phi\mu c\omega/2\}\ \{\sin^2\delta_b/k_h + \cos^2\delta_b/k_v\}]} \tag{4.36c}$$

Then, Equations 4.36b and 4.36c provide two coupled equations in the two unknown permeabilities k_h and k_v which can be directly solved. The result, from simple algebra, is

$$k_h = (L^2\phi\mu c\omega/2)\,(\sin^2\delta_a\cos^2\delta_b - \sin^2\delta_b\cos^2\delta_a)\,/(\theta_a^2\cos^2\delta_b - \theta_b^2\cos^2\delta_a) \tag{4.36d}$$

$$k_v = (L^2\phi\mu c\omega/2)\,(\sin^2\delta_a\cos^2\delta_b - \sin^2\delta_b\cos^2\delta_a)\,/(\theta_b^2\sin^2\delta_a - \theta_a^2\sin^2\delta_b) \tag{4.36e}$$

We emphasize that Equations 4.36d and 4.36e represent two equations obtained at different dip angles and that the layer is assumed to be thick enough to allow measurements to be taken as the drillstring changes direction. As a check, setting $\delta_a = 0^o$ and $\delta_b = 90^o$, and conversely, lead to the simpler formulas derived earlier.

Of course, in thin geological layers, it is not physically possible from a drilling perspective to have a second equation at the same logging point as in Equations 4.36b and 4.36c for different dip angles – thus, having "two equations in two unknowns" as indicated above cannot be done. However, we can still obtain vertical and horizontal permeabilities as follows. Separately in this book, we developed a single-probe, drawdown-buildup method for low mobility applications which used early-time pressure transient data – we will refer to this as our "DDBU" method. We use this together with the phase delay approach.

In this second approach, we return to Equation 4.36a, which provides a relationship connecting k_h and k_v for measured values of the phase θ_L and dip angle δ. To determine horizontal and vertical permeabilities uniquely, a second constraint is needed. This is provided by DDBU models in which the spherical permeability k_s is predicted from early time pressure transient data, so that we know $k_s = k_h^{2/3} k_v^{1/3}$. Combining this with Equation 4.36a leads to relationships for the horizontal and vertical permeabilities k_h and k_v, namely,

$$\cos^2\delta\, k_h^3 - \{2\theta_L^2 k_s^3/(L^2\phi\mu c\omega)\}\, k_h + \sin^2\delta\, k_s^3 = 0 \tag{4.36f}$$

$$\tan^2\delta\, k_v^{3/2} - \{2\theta_L^2 k_s^{3/2}/(L^2\phi\mu c\omega\, \cos^2\delta)\}\, k_v + k_s^{3/2} = 0 \tag{4.36g}$$

$$\tan^2\delta\, \lambda - \{2\theta_L^2 k_s/(L^2\phi\mu c\omega\, \cos^2\delta)\}\, \lambda^{2/3} + 1 = 0 \tag{4.36h}$$

where

$$\lambda = k_v/k_h \tag{4.36i}$$

represents the so-called "anisotropy" or anisotropy ratio. The foregoing are cubic polynomial equations for k_h , $k_v^{1/2}$ and $\lambda^{1/3}$ which can be solved exactly from standard algebraic formulas. Different equations apply in different situations. In some situations, it may be preferable to work first with k_h if it is typically larger, as it would provide greater numerical accuracy. Once Equation 4.36f is solved, the vertical permeability can be obtained from $k_s = k_h^{2/3} k_v^{1/3}$ or Equation 4.36a. Similar comments apply to Equations 4.36 g and 4.36h. We importantly emphasize that in obtaining k_s using our drawdown-buildup methods, we also predict the pore pressure from early time data.

Also note that deviated well applications are associated with multiple permeability solutions for the same set of input parameters. Cubic equations provide two types of solutions, namely, (i) all real roots (some of which may be negative), and (ii) complex roots (with one real and one conjugate pair). Input data contaminated by noise, e.g., loose pads, sand in nozzle throats, bubbly solutions, and so on, may lead to false imaginary parts, and calculated solutions must be interpreted with care. We emphasize that this method requires a dual-probe tool because phase delay measurements are required.

In contrast to the dual-probe, steady-state pressure drop method described in Chapter 6 of the formation testing book of Chin *et al* (2014), which in practice requires higher mobilities, the present method is ideally suited to low mobilities (steady-states in low permeability formations may require hours of wait time for equilibration). DDBU was designed for low mobility applications. And in the present phase delay approach, the lower the permeability, the larger the time delay and easier the measurement is made. Thus, the lower the mobility, the better the signal-to-noise ratio, and the more accurate the predictions for both permeabilities.

Note that Equations 4.33 and 4.34 for amplitude, together with the DDBU model, can also be used to develop an analogous "two-equation, two unknown" system, however, this would be prone to inaccuracy since the values of x_w, y_w and z_w may be difficult to determine in practice.

4.1.8 Two-observation-probe models

In resistivity or electromagnetic logging, two methods are available for resistivity prediction. In the first, amplitude attenuation and phase delay are measured at a receiver displaced from a transmitter that broadcasts sinusoidal signals. The readings are interpreted using models developed from Maxwell's equations. In the second approach, two receivers are introduced; amplitude ratios and phase delays relative to the two receivers only are used for interpretation. This approach provides at least two benefits. Amplitude attenuation due to conductivity or formation effects, which when measured relative to the transmitter, which are typically "buried" in the rapidly decaying algebraic field associated with geometric spreading. This large source of error is eliminated by using two closer receivers. Also, the use of closely spaced receivers provides less sensitivity to larger scale heterogeneities in the borehole, and thus, allows for increased local accuracy.

We expect similar advantages in analogous "two-receiver" or "two observation probe" approaches for formation testing. Such a tool will have one source (pumping) probe and (at least) two passive observation probes. However, these do not require their own hydraulic pad thrusters, a requirement which would complicate mechanical design. The simple mechanical approach suggested in Figure 4.3 consists of an elongated pad driven by a single hydraulic thruster that presses the pad against the borehole wall. The pad, in turn, contains two ports which independently measure pressure by means of pressure transducers separated by several inches. Finally, for all of the methods discussed so far, the use constant frequency test frequencies is assumed. A simple question arises – in measuring time delay, how does the receiver "know" when a signal begins and ends? This is easily solved by transmitting a constant frequency signal and having its initial amplitude suddenly change to a different level. This creates a "marker" signaling when the test signal departs the transmitter. When the observation probe "sees" this marker, the elapsed time recorded would be the required time delay (that is, the "clock starts running" when the transmitter sends its first signals).

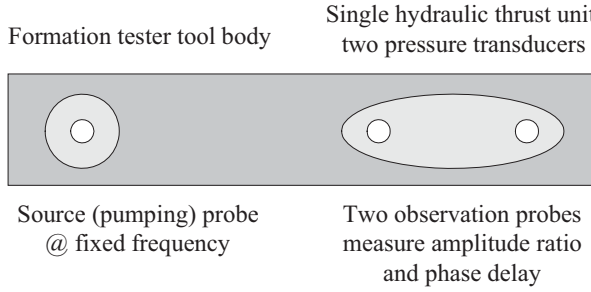

Figure 4.3. Simple "two-receiver" observation probe.

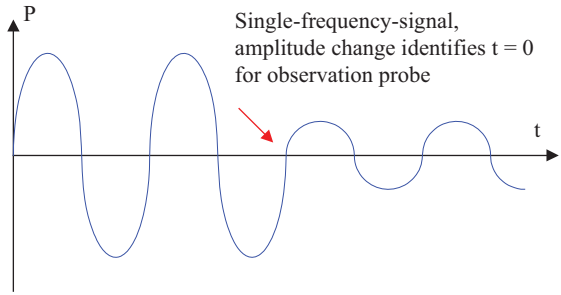

Figure 4.4. Transmitter "marker" signal defines instant of departure.

To obtain usable results for our "two observation probe" or "two receiver" approach, we can use the approximation $r^* >> r_w^*$ to simplify previously derived mathematical expressions; that is, both observation probes are assumed to be far from the source pumping probe. In this case, Equation 4.33 for amplitude becomes

$$A \approx P_0 \, (r_w^*/r^*) \exp[- r^* \sqrt{\{\phi\mu c\omega/2\}}] \tag{4.37}$$

Now suppose that two measurements, A_1 at r_1^* and A_2 at r_2^*, are available. Then we can write

$$A_1 \approx P_0 \, (r_w^*/r_1^*) \exp[- r_1^* \sqrt{\{\phi\mu c\omega/2\}}] \tag{4.38}$$

$$A_2 \approx P_0 \, (r_w^*/r_2^*) \exp[- r_2^* \sqrt{\{\phi\mu c\omega/2\}}] \tag{4.39}$$

Dividing Equation 4.38 by 4.39, we obtain

$$A_1/A_2 = r_2^*/r_1^* \exp [(r_2^* - r_1^*)\sqrt{\{\phi\mu c\omega/2\}}] \tag{4.40}$$

which is independent of P_0, and importantly, does not depend on the "ellipsoidal well radius" r_w whose physical meaning is not clear. Next we observe from Equation 4.22 that $r_2^* = L_2 \sqrt{(\sin^2\delta /k_h + \cos^2\delta /k_v)}$ and $r_1^* = L_1 \sqrt{(\sin^2\delta /k_h + \cos^2\delta /k_v)}$. It follows that

$$A_1/A_2 = (L_2/L_1)\exp\left[(L_2 - L_1)\sqrt{[\{\phi\mu c\omega/2\}\{\sin^2\delta/k_h + \cos^2\delta/k_v\}]}\right] \quad (4.41)$$

Equation 4.41 provides one of the equations needed in a "two equations, two unknowns" solution; the second is obtained from a DDBU test, in which the spherical permeability k_s is measured, thereby constraining $k_s = k_h^{2/3}k_v^{1/2}$.

To derive a complementary equation for phase, one might use Equation 4.20, again assuming that $r^* >> r_w^*$. This yields $\theta_1 = r_1^*\sqrt{[\{...\}}$ and $\theta_2 = r_2^*\sqrt{[\{...\}}$ which, on division, leads to $\theta_1/\theta_2 = L_1/L_2$ – this merely affirms that phase is linearly proportional to distance from the transmitter but otherwise no additional information is gained. The key lies in the calculation of phase differences between observation probes. This leads, using Equations 4.20 and 4.22 together with the definition of dip angle, to the simple relationship

$$\theta_2 - \theta_1 = (L_2 - L_1)\sqrt{[\{\phi\mu c\omega/2\}\{\sin^2\delta/k_h + \cos^2\delta/k_v\}]} \quad (4.42)$$

This provides one of the equations needed in a "two equations, two unknowns" solution; as before, the second is obtained from a DDBU test, in which the spherical permeability k_s is measured, thereby constraining $k_s = k_h^{2/3}k_v^{1/2}$. Finally, throughout our analysis, we have emphasized the differences between k_h and k_v – that is, the importance of anisotropy. Often, a second equation (say, using DDBU techniques) may not be available; in this case, one may replace both permeabilities by a single "k_{eff}," or "effective permeability" which provides order-of-magnitude estimates. However, we caution against this usage since horizontal and vertical permeability values may differ greatly.

4.2 Numerical Examples and Typical Results

So far, we have demonstrated how phase delay methods provide simple, fast and elegant alternatives to steady-state methods for permeability prediction in "low mobility" applications. However, we have not yet considered "how low is low" and also the pumping frequencies needed to excite the formation. Are these frequencies doable mechanically? Are they 10 Hz, 100 Hz . . . or perhaps 1,000 Hz? Also, the periodicity assumption behind "cos ωt" requires infinitely acting sinusoidal action – in practice, however, one can hope at best for two-to-three pump cycles which may not be perfect sinusoids. Numerical simulations have been defined to address these questions and representative results are described pointing to the practicality of the method. Both simple and more complicated examples are described that address these issues.

4.2.1 Example 1, Parameter estimates

The isotropic model in Equation 4.13 can be used to estimate the mechanical frequencies needed for low mobility applications. Again, because the governing equations are identical in form, this also applies to vertical and horizontal wells in transversely isotropic media. We have written two simple programs using our phase delay formula, namely, "phase-delay-estimates" and "phase-delay-permeability-calculation" to provide quick answers. These modules, based on a closed form solution, require no iteration, and results from typical simulations are shown in Figures 4.5a,b.

```
C:\phase-delay-estimates <Return>
Permeability ........... (md):  1.
Porosity .......... (decimal):  0.2
Viscosity .............. (cp):  1.
Compressibility ..... (1/psi):  0.000003
Probe separation ....... (cm):  15.
Frequency .............. (Hz):  0.5

Phase delay ............(deg):  0.1010E+03
Phase delay ........... (rad):  0.1763E+01
Time delay ............ (sec):  0.5611E+00
```

Figure 4.5a. Estimating time delays for given parameters.

```
C:\phase-delay-permeability-calculation <Return>
Probe separation ....... (cm):  15.
Porosity .......... (decimal):  0.2
Viscosity .............. (cp):  1.
Compressibility ..... (1/psi):  0.000003
Frequency .............. (Hz):  0.5
Time delay ............ (sec):  0.5611

Permeability ........... (md):  0.1000E+01
Phase delay  ........... (rad):  0.1763E+01
Phase delay ........... (deg):  0.1010E+03
```

Figure 4.5b. Predicting permeability from time delay.

The two programs provide consistent results. The numbers chosen for the calculations indicate that a mobility of 1 md/cp is adequately resolved by a pump piston frequency of 0.5 Hz, which is very doable in hardware. Moreover, the not-too-small time delay of 0.5611 sec between dual probes with typical fifteen cm separation should be obtainable accurately – in contrast to the extremely small delays found in resistivity logging. The method is also practical from a sampling perspective. In present formation testing tools, pressures are measured every 0.25 sec, too slow to characterize transients in high mobility formations. However, this rate is useful for time delay measurements since piston pump cycles occur over durations of approximately one second. These numbers provide "ballpark estimates" that also apply to anisotropic situations.

4.2.2 Example 2, Surface plots

Again, let us consider an isotropic uniform medium characterized by a permeability k and a porosity ϕ. The liquid viscosity and compressibility are μ and c. The action of the formation tester piston was modeled as a sinusoidally pulsating pressure source with strength P_o, radius r_w and frequency ω. Then, at any distant radial position $r > r_w$, the transient pressure response satisfies the exact solution $p(r,t) = A \cos(\omega t - \theta)$ where A and θ are the "amplitude" and "phase delay" functions at r given by $A = P_o (r_w/r) \exp[-(r - r_w)\sqrt{\{\phi\mu c\omega/(2k)\}}]$ and $\theta = (r - r_w)\sqrt{\{\phi\mu c\omega/(2k)\}}$. At the source position $r = r_w$, we note that $p(r_w,t) = P_o \cos(\omega t)$, the assumed form of the pressure excitation. But at $r > r_w$, a phase delay is found that is proportional to the product of probe separation and $\sqrt{\{\phi\mu c\omega/(2k)\}}$. For example, low permeabilities and high viscosities result in large phase shifts. As formation and fluid parameters are fixed, the excitation frequency ω can be used to control depth of investigation in a manner consistent with hardware sampling rates.

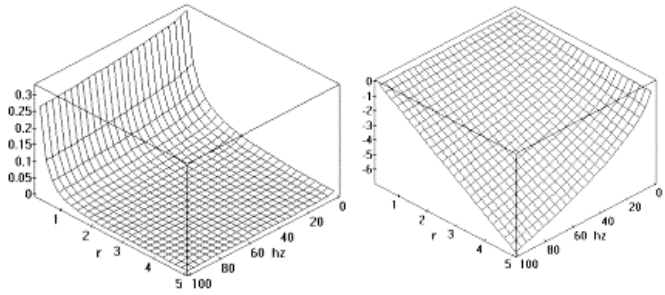

Figure 4.6. Amplitude (left) and phase delay (right) versus r and ω.

In Figure 4.6, typical amplitude and phase delay plots versus r and ω are shown. However, the analytical phase result can also be used to determine permeability when all other parameters are known – expressions for formation properties are easily derived, e.g., $\phi\mu c/k = (2/\omega)\{\theta/(r\text{-}r_w)\}^2$. Note that k can also be determined from amplitude measurements. However, these may be more prone to error than timing measurements since the attenuation field due to a weak exponential decay can be embedded in a more rapidly falling "1/r" associated with spherical geometric spreading. Amplitude measurements may also be undesirable for another reason. In practice, it is not possible to create a perfect sinusoid, and in fact, only two-to-three wave cycles would be taken (this is hardly periodic). The amplitudes for these cycles (created for a constant rate function) will vary significantly rendering amplitude data of little use. For this reason, phase-based permeability predictions may be more accurate and desirable. .

4.2.3 Example 3, Sinusoidal excitation

In this example, we follow the method of Figure 4.4 and define a constant frequency pump excitation with multiple amplitudes as shown at the bottom of Figure 4.7a. Strictly speaking, this is not a periodic signal, however, the intention is clear; the amplitude change is introduced only to provide a reference for measurement so that delays can be counted easily. The required pressure transient responses can be calculated from forward simulators FT-06 or FT-07. These are finite difference algorithms that allow numerical definition of volume flow rate versus time functions. The assumed parameters for the simulation are shown more clearly in Figure 4.7b. Importantly, note that the mobility is 1 md/1 cp or 1 md/cp.

To determine the time delay, we focus on the clearly discernible first group of small amplitude waves, and in particular, the center crest. The the circled values, we find that the time at the source probe is 3.8 sec while the time at the observation is 4.4 sec, yielding a time delay of 4.4 – 3.8 or 0.6 sec. Using one of the software programs discussed above, we find

```
C:\phase-delay-permeability-calculation <Return>

Probe separation ....... (cm):  15.
Porosity ......... (decimal):  0.2
Viscosity ............... (cp):  1.
Compressibility ..... (1/psi):  0.000003
Frequency ............... (Hz):  0.5
Time delay ............. (sec):  0.6

Permeability ........... (md):   0.8745E+00  (very close to 1 md)
Phase delay  ......... (rad):   0.1885E+01
Phase delay ........... (deg):   0.1080E+03
```

We find that the calculated 0.8745 md permeability is close to the known value of 1 md. Again, the pressure data was created from FT-06 (or equivalently FT-07) both of which are approximate numerical simulators. From Figure 4.7c, it is obvious that using amplitude-based methods is not desirable since these functions drift considerably. The flow rate in Figure 4.7a, defined by a single frequency, but with amplitude changes taken at distinct intervals (in fact, every three cycles), is important for another reason. At very low mobilities, phase delays with $\theta > 360^o$ may be large; using a single amplitude will not allow convenient phase delay measurement because it is difficult to distinguish one cycle from another. When amplitudes are "stepped" as shown, monitoring software used by the observation probe can count the number of 360^o transitions that have transpired, so that delays associated with this "phase wrapping" can be measured with minimal error. Of course, since θ is proportional to $\omega^{1/2}$, phase wrapping may be avoided by decreasing frequency; this allows, at the same time, increased depth of penetration of the pressure signal so that a greater portion of the formation is sampled.

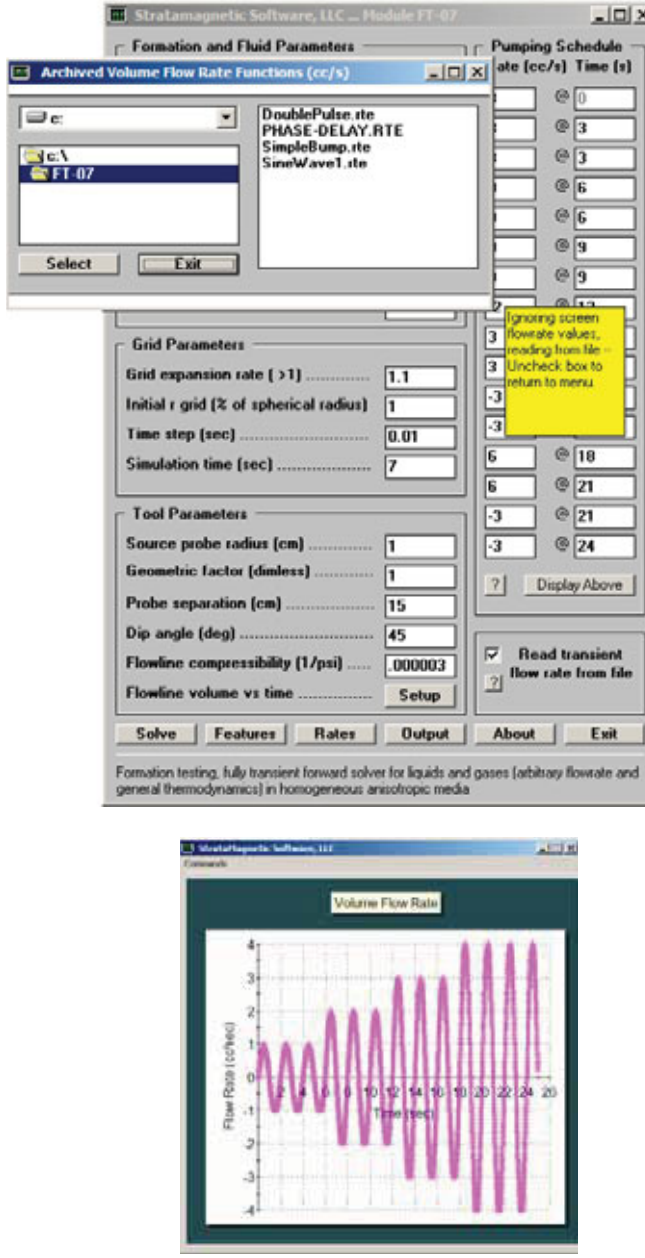

Figure 4.7a. Constant frequency pump excitation.

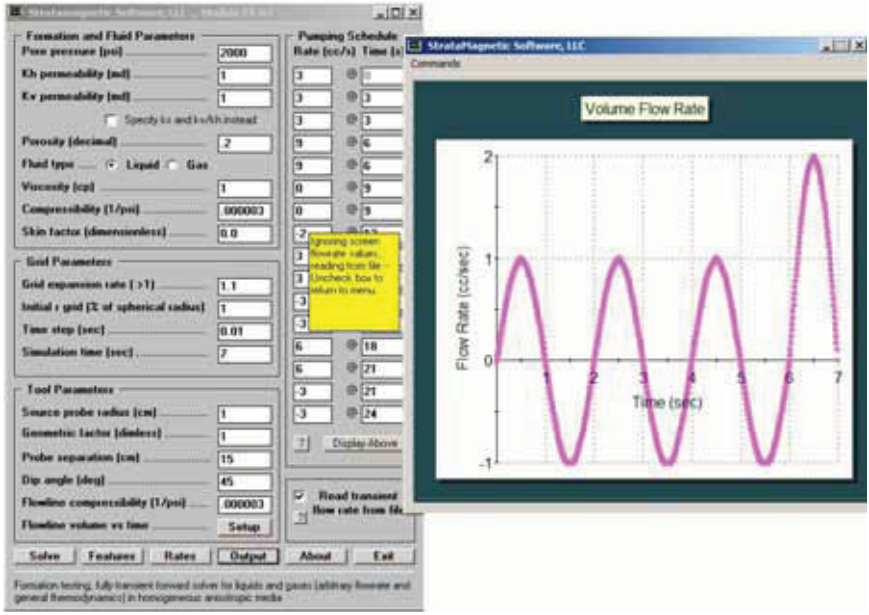

Figure 4.7b. Input data and exploded view.

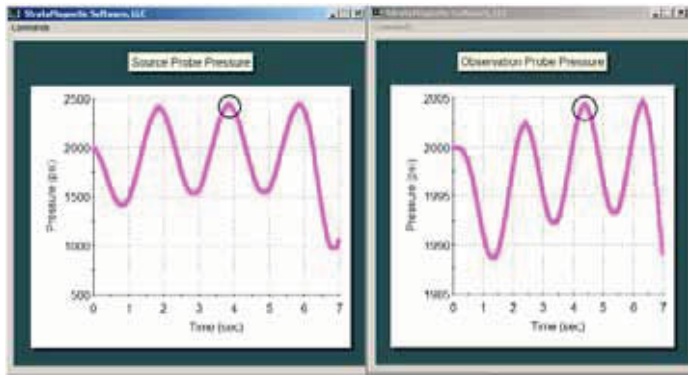

Figure 4.7c. Source and observation probe pressure.

4.2.4 Example 4, Rectangular wave excitation

In practical mechanical design, it is often not possible to pump exactly with sinusoidal precision. We consider an example showing phase delay results in one such instance. Recall that the underlying theory was derived assuming pressure disturbances which are proportional to exp (iωt), that is, that they are perfect sinusoids. In practice, one can hope for two-to-three wave cycles at best that may not be perfectly sinusoidal. In the input screen for exact forward simulator FT-00 in Figure 4.8a, a pump schedule having three wave cycles in six seconds, or a frequency of 0.5 Hz, was formed from sequences of rectangular functions. Such functions are hardly representative of theoretical Fourier components and it is instructive to understand the consequences. To ensure numerical accuracy, we used FT-00 because it provides an exact solution that is not compromised by sharp transitions in the flow rate functions. Also, note that the mobility is a low 0.1 md/1 cp or 0.1 md/cp. Calculated results in Figure 4.8b show that both amplitude functions at source and observation probes drift considerably and are not useful for computation. As in the foregoing example, we therefore turn to time delay measurements. Interestingly, examine the two circled points located at the midpoints of the pumping cycles. The time delay, obtained visually, is clearly "4-3" or 1 sec. What does this imply? We use a software program discussed previously, that is,

```
C:\phase-delay-permeability-calculation <Return>

Probe separation ....... (cm):  15.
Porosity .......... (decimal):  0.2
Viscosity ............... (cp):  1.
Compressibility ..... (1/psi):  0.000003
Frequency ............... (Hz):  0.5
Time delay ............. (sec):  1.

Permeability ........... (md):   0.3148E+00
Phase delay  ........... (rad):   0.3142E+01
Phase delay ............ (deg):   0.1800E+03
```

The calculated permeability of 0.3148 md, compared to the known input value of 0.1 md, is not bad, and acceptable when judged against present field logging standards. The discrepancy arises from two effects, namely, the length of the short duration test, and the use of rectangular as opposed to sinusoidal functions. These problems can be corrected by mechanical design.

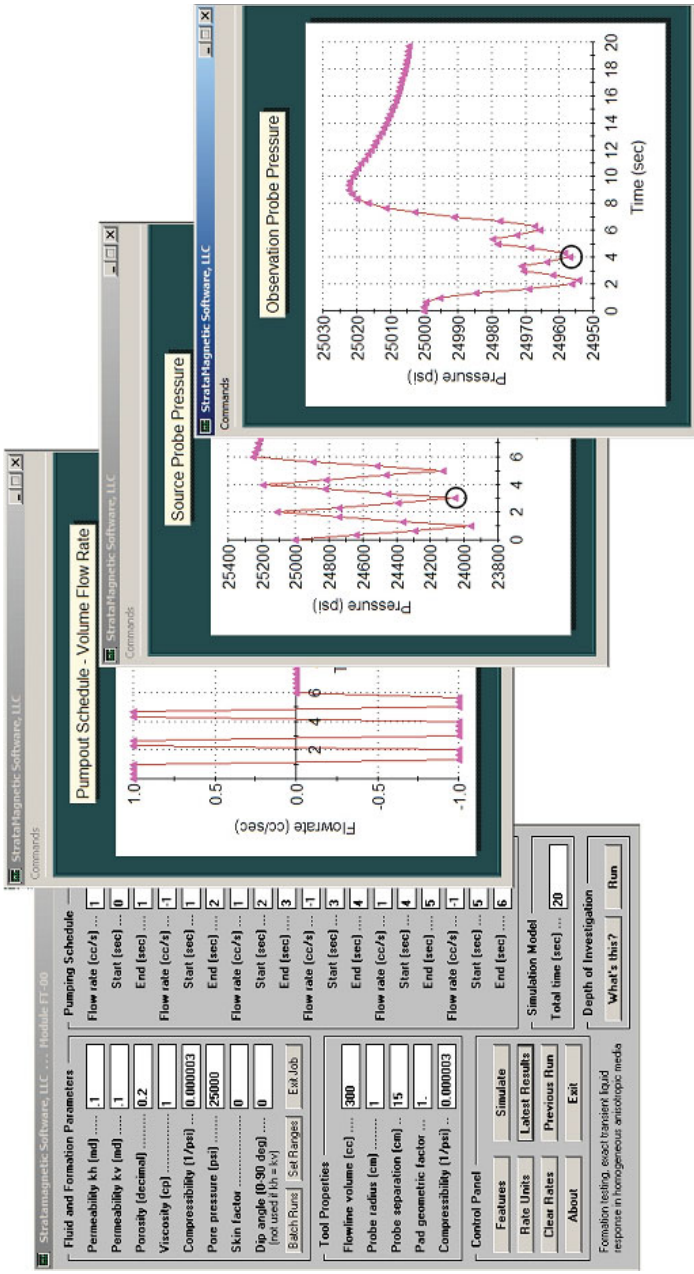

Figure 4.8a. Square wave assumptions and pressure responses.

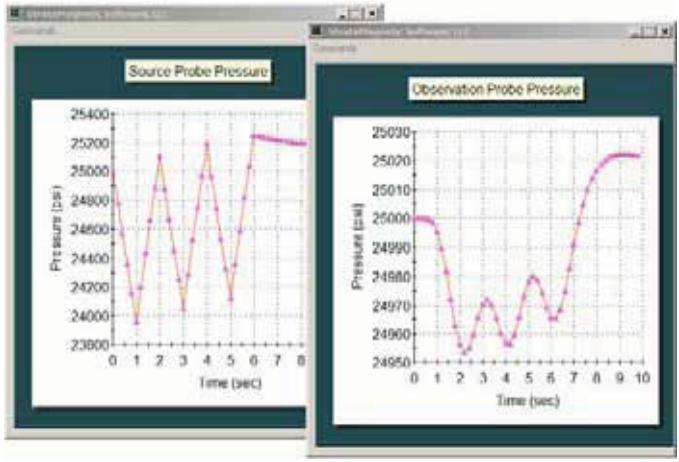

Figure 4.8b. Pressure responses, exploded view.

4.2.5 Example 5, Permeability prediction at general dip angles

In the calculations below, we demonstrate the numerical consistency of three software programs highlighted in red. The first two are isotropic models developed previously. We choose "random non-zero" numbers and make sure the two are consistent in everything, whether or not needed now, since internal quantities may be needed later. Perfect consistency is seen for the two isotropic codes.

```
C:\phase-delay-estimates <Return>

Permeability ........... (md):  1.234
Porosity .......... (decimal):  0.2
Viscosity .............. (cp):  1.1
Compressibility ..... (1/psi):  0.0000034
Probe separation ....... (cm):  15.
Frequency .............. (Hz):  1.2

Phase delay ............(deg):   0.1573E+03
Phase delay ........... (rad):   0.2745E+01
Time delay ............ (sec):   0.3640E+00

C:\phase-delay-permeability-calculation <Return>

Probe separation ....... (cm):  15.
Porosity .......... (decimal):  0.2
Viscosity .............. (cp):  1.1
Compressibility ..... (1/psi):  0.0000034
Frequency .............. (Hz):  1.2
Time delay ............ (sec):  0.3640

Permeability ........... (md):   0.1234E+01
Phase delay  .......... (rad):   0.2744E+01
Phase delay ........... (deg):   0.1572E+03
```

Next, we evaluate the cubic code "phase-delay-nonlinear.exe" for transversely isotropic media with *any nonzero dip angle* solving Equations 4.36f – 4.36i. We enter the above parameters as inputs, and in the first case, take a zero (that is, 0.01 deg) dip angle. Comparing outputs from all three programs shows everything is consistent. In particular, the second "2" root (highlighted in red) gives the isotropic permeability assumed in the two simpler programs.

```
C:\phase-delay-nonlinear (Return>

Probe separation ......... (cm):  15.
Porosity ............ (decimal):  0.2
Viscosity ................ (cp):  1.1
Compressibility ....... (1/psi):  0.0000034
Frequency ................ (Hz):  1.2
Time delay ............... (sec):  0.3640
Spherical permeability ... (md):  1.234
Dip angle ................ (deg):  0.01

Dip angle ................ (rad):  0.1745E-03
Phase delay .............. (rad):  0.2744E+01
Phase delay .............. (deg):  0.1572E+03

KH1 = -0.1234E+01 md, KV1 =  0.1234E+01 md
Caution:  KH permeability is negative

KH2 =  0.1234E+01 md, KV2 =  0.1234E+01 md

KH3 = -0.2429E-05 md, KV3 =  0.3186E+12 md
Caution:  KH permeability is negative
```

Again, it is important to have recovered the isotropic permeability of 1.234 md. Additionally, there are two (unrealistic) negative kh roots cited in the warning. In the next evaluation, we consider the horizontal well limit (with 89.8 deg) and we similarly recover the isotropic permeability as required (root "3"). However, we also obtain an additional anisotropic solution with high horizontal and very low vertical permeability.

```
C:\phase-delay-nonlinear (Return>

Probe separation ......... (cm):  15.
Porosity ............ (decimal):  0.2
Viscosity ................ (cp):  1.1
Compressibility ....... (1/psi):  0.0000034
Frequency ................ (Hz):  1.2
Time delay ............... (sec):  0.3640
Spherical permeability ... (md):  1.234
Dip angle ................ (deg):  89.8

Dip angle ................ (rad):   0.1567E+01
Phase delay .............. (rad):   0.2744E+01
Phase delay .............. (deg):   0.1572E+03

KH1 = -0.3541E+03 md, KV1 =  0.1499E-04 md
Caution:  KH permeability is negative
KH2 =  0.3529E+03 md, KV2 =  0.1509E-04 md  Additional solution.
KH3 =  0.1234E+01 md, KV3 =  0.1235E+01 md
```

Finally, we consider the same data but at 45 deg. We recover the isotropic solution in "root 2," but as before, obtain an additional anisotropic permeability set in "root 3" that satisfies the input data.

```
C:\phase-delay-nonlinear (Return>

Numbers must have decimals ...

Probe separation ......... (cm):  15.
Porosity ............ (decimal):  0.2
Viscosity ................ (cp):  1.1
Compressibility ....... (1/psi):  0.0000034
Frequency ................ (Hz):  1.2
Time delay ............... (sec):  0.3640
Spherical permeability ... (md):  1.234
Dip angle ................ (deg):  45.

Dip angle ................ (rad):   0.7854E+00 ok
Phase delay .............. (rad):   0.2744E+01
Phase delay .............. (deg):   0.1572E+03

KH1 = -0.1996E+01 md, KV1 =  0.4714E+00 md
Caution:  KH permeability is negative

KH2 =  0.1234E+01 md, KV2 =  0.1235E+01 md

KH3 =  0.7627E+00 md, KV3 =  0.3230E+01 md  Additional solution.
```

4.2.6 Example 6, Solution for a random input

In the three above examples using the "anisotropic, dip angle" algorithm, we recovered the isotropic permeability of "1.234 md" for dip angles 0^{o}+, 90^{o}- and 45^{o}, and in addition, found other roots for permeability. Our recovering isotropic permeabilities was expected, of course, because we used data created from the isotropic model; thus, the foregoing cases served as validations for the more complicated anisotropic model. Now, let us repeat the above example, but change *only* the input for measured time delay from 0.3640 sec to 0.5 sec. In this sense, we have a "random" data set for which there is no reason to suspect isotropic properties.

```
C:\phase-delay-nonlinear <Return>

Probe separation ......... (cm):  15.
Porosity ............ (decimal):  0.2
Viscosity ................ (cp):  1.1
Compressibility ....... (1/psi):  0.0000034
Frequency ................ (Hz):  1.2
Time delay ............... (sec):  0.5
Spherical permeability ... (md):  1.234
Dip angle ................ (deg):  45.

Dip angle ................ (rad):  0.7854E+00
Phase delay .............. (rad):  0.3770E+01
Phase delay .............. (deg):  0.2160E+03
```

```
KH1 = -0.2546E+01 md, KV1 =  0.2898E+00 md
Caution:  KH permeability is negative

KH2 =  0.2213E+01 md, KV2 =  0.3838E+00 md

KH3 =  0.3335E+00 md, KV3 =  0.1690E+02 md

Stop - Program terminated.
```

In fact, the above results give three real roots, one negative, one with $k_h > k_v > 0$ and the last with $0 < k_h < k_v$. The latter two represent anisotropic formations and both are possible permeability solutions that are consistent with the phase delay inputs. The correct choice, of course, requires additional logging data or other qualitative judgement.

4.3 Layered Model Formulation

In this investigation, the above capabilities are extended to transversely isotropic media with any number of layers and to tools with arbitrary dip angle and source-to-observation probe separation. These extensions require a three-dimensional numerical modeling and interpretation approach. In order to develop the mathematical formulation clearly, we will restrict the discussion to a single layer at first and then introduce the extensions needed to model multiple layers. Ultimately, the layered system represented by Figure 4.2 will be addressed, where "s" and "o" denote source and observation probes respectively.

4.3.1 Homogeneous medium, basic mathematical ideas

Let us consider a transversely isotropic formation with a horizontal permeability k_h in the x and y directions and a vertical permeability k_v in the z direction. Also, let ϕ be the porosity, μ be the viscosity of the assumed liquid and c be its compressibility. Then, the transient response in time satisfies

$$k_h (\partial^2 p/\partial x^2 + \partial^2 p/\partial y^2) + k_v \partial^2 p/\partial z^2 = \phi\mu c \, \partial p/\partial t \qquad (4.43)$$

When formation tester pistons pump fluids in general, drawdown and buildup transients are created – pressure responses not only depend on rock and fluid properties, but also on flowline storage parameters.

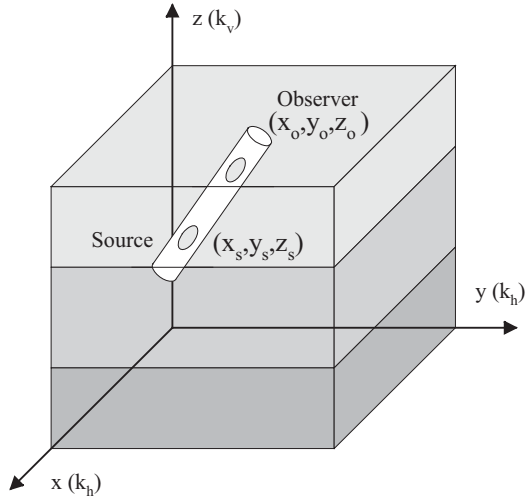

Figure 4.9. Layered anisotropic medium with dipping tool.

If, on the other hand, a sinusoidal pressure transient is assumed to exist at the source probe, e.g., an actual oscillatory disturbance or a harmonic component resolved from Fourier analysis, then flowline storage does not affect the propagation of this transient toward the observation probe – although it will affect the efficiency with which the signal is generated. With this view of the physics, the time response of the pressure signal at distant points is likewise sinusoidal, but with a time or phase delay that depends on formation properties and pumping frequency ω. This allows us to represent pressure as

$$p(x,y,z,t) = P(x,y,z)\, e^{i\omega t} \tag{4.44}$$

Here, p(x,y,z,t) and the steady P(x,y,z) may be complex, but real parts are taken as the relevant physical quantities. This analysis approach is common in harmonic analyses used in electrical engineering. For instance, the pressure at a source point "s" may be written in the form

$$p(x_s,y_s,z_s,t) = P(x_s,y_s,z_s)\, e^{i\omega t} = P_s\, e^{i\omega t} \tag{4.45}$$

where P_s is real, so that the assumed excitation is $P_s \cos \omega t$ and "i" is the imaginary number. The response at an observation point "o" is therefore the real part of

$$p(x_o,y_o,z_o,t) = P(x_o,y_o,z_o)\, e^{i\omega t} = P_o\, e^{i\omega t} = (P_o^{\,r} + i\, P_o^{\,i})\, e^{i\omega t} \tag{4.46}$$

or simply "$P_o^{\,r} \cos \omega t - P_o^{\,i} \sin \omega t$." In a highly permeable medium, the phase delay vanishes, that is, $P_o^{\,i} = 0$. However, the real amplitude $P_o^{\,r}$ does not reduce to P_s because "1/r" geometric spreading reduces the intensity of the signal.

4.3.2 Boundary value problem for complex pressure

Our objective is a robust, rapid and stable numerical solution for P(x,y,z) everywhere in the flow domain. When Equation 4.44 is substituted in Equation 4.43 and all $e^{i\omega t}$s cancel, we obtain the complex linear model

$$k_h(\partial^2 P/\partial x^2 + \partial^2 P/\partial y^2) + k_v\, \partial^2 P/\partial z^2 = i\phi\mu c\omega P \qquad (4.47)$$

representing two linearly coupled partial differential equations for P^r and P^i. The latter, associated with phase delay, vanishes for high permeabilities or low values of the product $\phi\mu c\omega$.

Note that, in obtaining Equation 4.47, all coefficients have been assumed as constant and not dependent on pressure so that the exponentials drop out – thus, the phase delay model presented in this chapter applies to liquids only. Nonlinear phase delays and amplitude attenuations for gases with varying compressibility are also possible, of course, but these must be modeled using transient numerical methods – the three-dimensional model in Chapter 7 and the two-dimensional numerical model of Chapter 8 can be used as applicable. Now, Equation 4.47 is solved subject to

$$P(x_s,y_s,z_s) = P_s \text{ (constant)} \qquad (4.48)$$

$$P \to 0 \text{ as } x^2 + y^2 + z^2 \to \infty \qquad (4.49)$$

where P is the dynamic pressure measured about steady-state conditions. The solutions to Equations 4.47 to 4.49 for homogeneous media lead to pure ellipsoidal flow, and in particular, to the analytical solutions given previously. In dealing with layered media, ellipsoidal flow cannot be assumed at the outset, and numerical techniques for homogeneous media that can be extended three-dimensionally to layered applications must be developed.

4.3.3 Iterative numerical solution to general formulation

The finite difference method will be used to solve Equation 4.47. We approximate the pressure at nodal intersections defined by the discretized grids $x_1, x_2, x_3, \ldots, x_{imax}$, $y_1, y_2, \ldots, y_{jmax}$ and $z_1, z_2, \ldots, z_{kmax}$ in Figure 4.10. For example, the partial derivative $\partial P/\partial x$ at (x_3, y_8, z_{15}) is simply given by the algebraic expression $\{P(x_4, y_8, z_{15}) - P(x_2, y_8, z_{15})\}/(x_4 - x_2)$ or $(P_{4,8,15} - P_{2,8,15})/(x_4 - x_2)$. If this procedure is carried out for Equation 4.47, the resulting difference formula can be rewritten as

$$[(z_{k+1} - z_{k-1})(z_k - z_{k-1})]^{-1} P_{i,j,k-1} \tag{4.50}$$

$$- [\{1/(z_{k+1} - z_k) + 1/(z_k - z_{k-1})\}/(z_{k+1} - z_{k-1})$$
$$+ (k_h/k_v) \{1/(x_{i+1} - x_i) + 1/(x_i - x_{i-1})\}/(x_{i+1} - x_{i-1})$$
$$+ (k_h/k_v) \{1/(y_{j+1} - y_j) + 1/(y_j - y_{j-1})\}/(y_{j+1} - y_{j-1})\} + i\,\phi\mu c\omega/(2k_v)] P_{i,j,k}$$

$$+ [(z_{k+1} - z_{k-1})(z_{k+1} - z_k)]^{-1} P_{i,j,k+1} =$$

$$- (k_h/k_v) \; [\{P_{i+1,j,k}/(x_{i+1} - x_i) + P_{i-1,j,k}/(x_i - x_{i-1})\}/(x_{i+1} - x_{i-1})$$
$$+ \{P_{i,j+1,k}/(y_{j+1} - yj) + P_{i,j-1,k}/(y_j - y_{j-1})\}/(y_{j+1} - y_{j-1})]$$

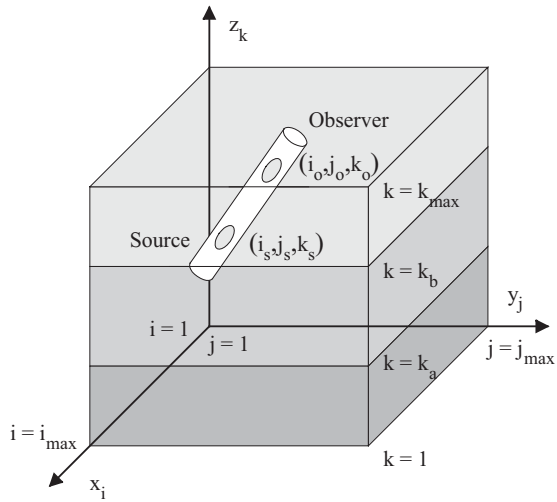

Figure 4.10. Discretized grid system.

4.3.4 Successive line over relaxation procedure

Before we explain why Equation 4.50 was constructed, we describe its use in obtaining solutions. To do so, we initialize P(x,y,z) to a first guess, which can be taken as zero (thus, satisfying farfield conditions). Now, focus our attention on any vertical line with frozen (i,j) values and write Equation 4.50 for k = 2, 3, . . . , k_{max}-1, thus yielding $k_{max} - 2$ equations for k_{max} variables. If $P_{i,j,1} = 0$ and $P_{i,j,kmax} = 0$ are invoked, a tridiagonal system of coupled algebraic equations of order k_{max} is obtained, requiring $O(3k_{max})$ operations to invert. This procedure is repeated for all (i,j) values, with latest values of $P_{i,j,k}$ always used to evaluate the right of Equation 4.50. Note that Equation 4.48 applies at the source point. When all (i,j) values are considered, one "sweep" of the three-dimensional flowfield is said to be completed. This sweeping is repeated until P(x,y,z) no

longer changes, at which time the solution converges. This "successive line over relaxation" (SLOR) process yields results that are consistent with the solutions of Proett, Chin and Mandal (2000) and the homogeneous anisotropic medium model in the previous section.

4.3.5 Advantages of the scheme

The finite difference model used for our SLOR model was taken in the form $A_k\ P_{i,j,k-1} + B_k\ P_{i,j,k} + C_k\ P_{i,j,k+1} = W_k$ which contains at most three unknowns per equation – such tridiagonal equations are efficiently inverted. Importantly, the absolute value of the middle diagonal exceeds the sum of those in its side-bands, and more particularly so, if $k_h >> k_v$. This diagonal dominance enhances the numerical stability and rapid convergence properties of the iterations. For this reason, the "$A_k\ P_{i,j,k-1} + B_k\ P_{i,j,k} + C_k\ P_{i,j,k+1} = W_k$" with varying "k" and not its complementary forms using i and j indexes was used.

Importantly, the iterative algorithm converges for any initial guess, even unrealistic ones, e.g., $P_{i,j,k} = i^2 + 5 + 21\ jk$ (Chin, 2002). However, a guess close to a solution will result in rapid convergence. Thus, the pressure solution for one set of formation properties can be saved to initialize other close solutions in order to minimize computation times – an important feature when numerous sequential simulations must be performed to support inverse applications.

4.3.6 Extensions to multiple layers

The above method applies to uniform media, however, it is clear that it also applies to different layers with different properties. Now, Equation 4.14 holds for field points but not at layer interfaces where rock properties change discontinuously. At interfaces, we instead invoke continuity of normal velocity and continuity of pressure. For example, let k^* be the index corresponding to a bed interface; then, as usual, $k^* + 1$ and $k^* - 1$ are indexes just above and below. However, we also need to introduce two other vertical locations, k^*_+ and k^*_- which are infinitesimally above and below k^*, as indicated in Figure 4.4.

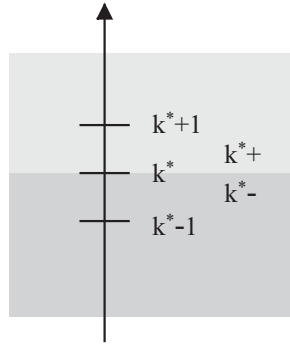

Figure 4.11. Layer interface details.

Continuity of normal velocity requires $(k_v\,\partial P/\partial z)\,|^{+} = (k_v\,\partial P/\partial z)|^{-}$ at $k = k^*$, or $k_v^{+}(P_{i,j,k^*+1} - P_{i,j,k^*+})/(z_{k^*+1} - z_{k^*}) = k_v^{-}(P_{i,j,k^*-} - P_{i,j,k^*-1})/(z_{k^*} - z_{k^*-1})$, where P_{i,j,k^*+} and P_{i,j,k^*-} denote pressures infinitesimally above and below k^*. These need not be equal if k^* supports pressure differences, e.g., as for shale streaks. When the interface consists of sand, the two are equal and we set $P_{i,j,k^*+} = P_{i,j,k^*-} = P_{i,j,k^*}$. In this limit, continuity of normal velocity and pressure imply that

$$\{k_v^{-}/(z_{k^*} - z_{k^*-1})\}\,P_{i,j,k^*-1} \qquad (4.15)$$

$$-\{k_v^{+}/(z_{k^*+1} - z_{k^*}) + k_v^{-}/(z_{k^*} - z_{k^*-1})\}\,P_{i,j,k^*} + \{k_v^{+}/(z_{k^*+1} - z_{k^*})\}\,P_{i,j,k^*+1} = 0$$

Like Equation 4.14, this differencing is tridiagonal and diagonally dominant. When all the field and interfacial points have been represented by equations, a large system of complex coupled unknowns is obtained and iteratively solved as outlined without direct recourse to lengthy Gaussian elimination. The method is rapidly convergent and numerically stable, e.g., a 25 × 25 × 25 system with over 30,000 complex unknowns converges in seconds on typical personal computers – thus, numerous forward calculations can be performed in support of inverse applications. Note that each field point represents a passive observation probe. The line joining it and the source point gives the probe separation while its inclination provides the dip angle.

4.3.7 Extensions to complete formation heterogeneity

For simplicity, we described our model assuming that formation properties are constant within layers. However, they often are variable with space – and certainly the case once a more complete understanding of the reservoir is available. When this is the case, terms containing products of spatial derivatives of permeability and first-order derivatives of pressure appear together with variable porosities. Obvious modifications to the governing equations can be derived and the more general model has been coded and successfully tested.

4.4 Phase Delay Software Interface

Our phase delay capabilities are hosted by the input screen in Figure 4.12, where white boxes are reserved for data entry. For brevity, only the interface for homogeneous media is discussed and examples are limited to such applications. The diagram reminds users of the coordinate conventions assumed. At the left, gridblock sizes and indexes are selected, as are source and observation probe properties. As these change, automatic calculated results for probe separation and dip angle appear in the opaque boxes. Overall dimensions shown in bold font in the diagram also change automatically as gridblock sizes and indexes change. Formation properties include layer permeabilities and porosities, bed interface indexes, viscosity and compressibility; excitation characteristics include source probe peak-to-peak pressure and frequency. The source code

implementing our pressure solution algorithm was written in Fortran. Its executable is called by a Windows-based front-end developed using Visual Basic which conveniently processes input data. Output color contour and line plots are developed in C-code, which is executed by both Fortran and Visual Basic programs.

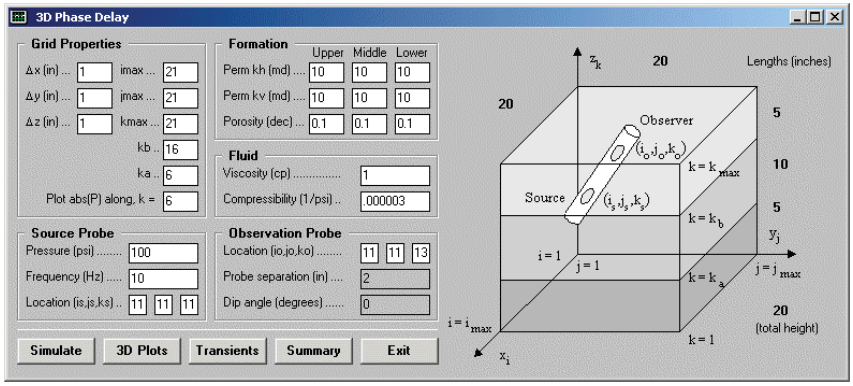

Figure 4.12. Windows-based program interface.

Once appropriate values are selected, the user – who does not require experience with programming or computational methods – clicks "Simulate" to automatically perform equation setup, matrix solution, all post-processing and output displays. For the parameters in Figure 4.12, the answer screens in Figures 4.13, 4.14 and 4.15 appear once a "Done simulating …" message box is acknowledged – typical simulations require just seconds on personal computers.

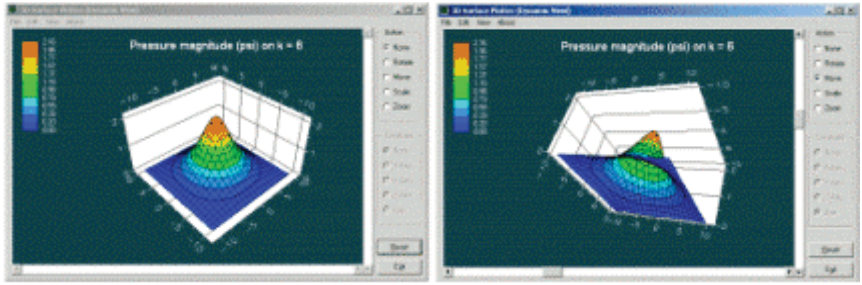

Figure 4.13. Rotatable plot of $\sqrt{(P^{r\,2} + P^{i\,2})}$ versus x and y for given layer.

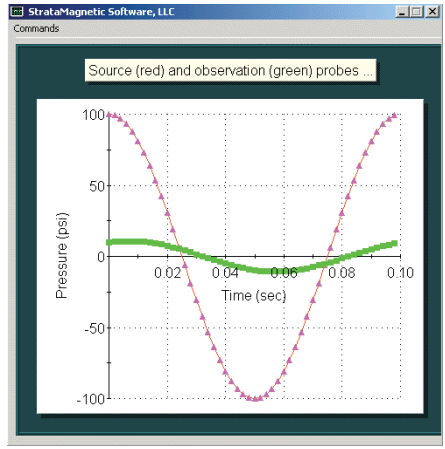

Figure 4.14. Phase delay plot (-100 to +100 psi for source pressure).

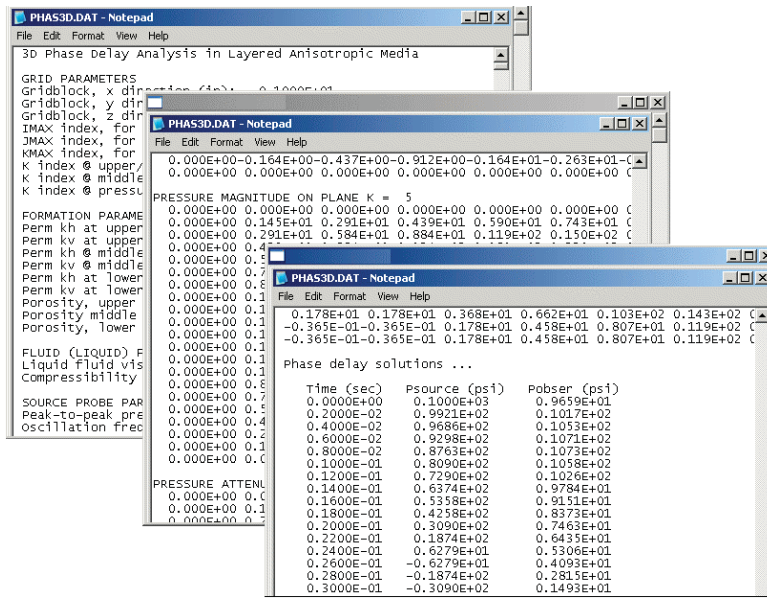

Figure 4.15. Output text summaries.

4.4.1 Output file notes

In this section, we briefly describe the screen shots visually captured above.

- Figure 4.13 plots $\sqrt{(P^{r\,2} + P^{i\,2})}$ versus x and y for the selected layer. It represents the absolute magnitude of pressure and measures amplitude changes due to geometric spreading and diffusion. The default view can be translated and rotated as desired. Plots for other quantities, e.g., the ratio P^i/P^r, the phase angle $\tan^{-1} P^i/P^r$ or the amplitude ratio between source and observation probes, are easily added by modifying source code logic.
- Figure 4.14 plots "pressure versus time" for source (red) and observation (green) probes. Note the much smaller magnitudes found for the observation probe. Time delays are read from intersections of these curves at the horizontal axes. For this run, the delays are small; nonetheless, amplitude changes are large, geometric divergence being the cause.
- Figure 4.15 displays input parameters, detailed ASCII file listings versus x and y for all z values, for real and imaginary pressures, absolute magnitude, amplitude attenuation and phase delay.

4.4.2 Special user features

Additional features are incorporated into the graphical interface and are briefly summarized.

- Figures 4.13, 4.14 and 4.15 can be individually recalled by clicking the "3D Plots," "Transients," and "Summary" buttons in Figure 4.12
- When source and observation probe locations change, or when grid sizes are altered, probe separations and dip angles are automatically calculated and displayed in the opaque boxes at the bottom left of Figure 4.12.
- When the observation probe falls outside the computational box, an error message appears and asks for revised data.

4.5 Detailed Phase Delay Results in Layered Anisotropic Media

Here, we perform representative calculations of engineering interest and elaborate on computed results, demonstrating important features of the model. We begin with the input of Figure 4.12, but modified so that all six permeabilities are a large 1,000 md. In this range, phase delays should be small and this is confirmed in Figure 4.16a (both curves intersect the time axis at the same locations, so that the phase delay is minimal).

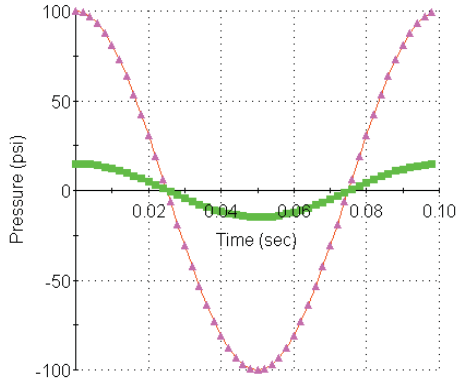

Figure 4.16a. Very high 1,000 md run.

Next, we reduce all six isotropic permeabilities to 100 md, 10 md and 1 md, with results shown in Figures 4.16b, 4.16c and 4.16d, respectively.

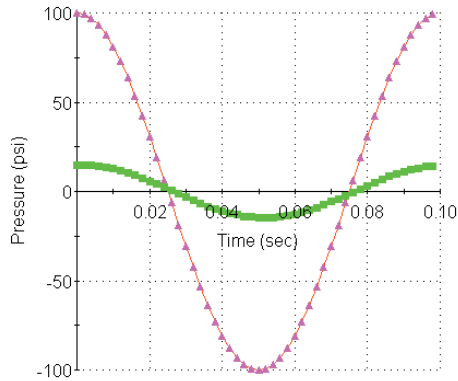

Figure 4.16b. High 100 md run.

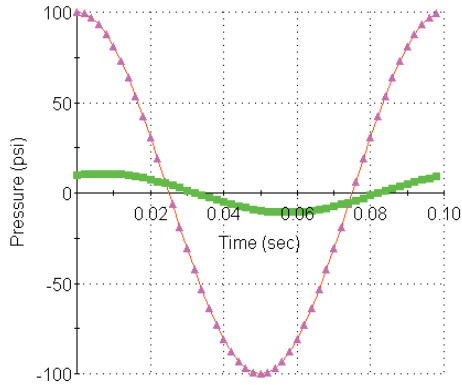

Figure 4.16c. Moderate 10 md run.

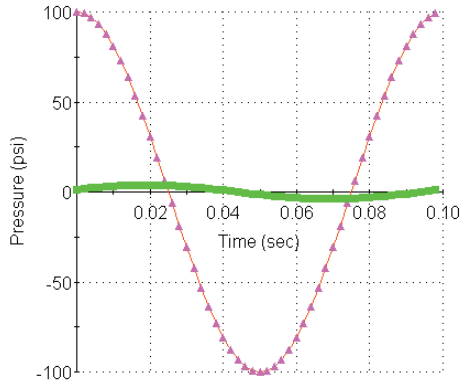

Figure 4.16d. Low 1 md run.

For the isotropic runs considered above, only the lumped parameter $\phi\mu c\omega/k$ enters, so that it is not necessary to repeat calculations with other variables changed. The results for 1,000 md and 100 md are almost identical – phase delays are minimal because there is little diffusion and the amplitude change from source to observation probe is entirely due to geometric spreading. The results for 10 md and 1 md show significant differences. Here, time shifts are clearly evident even visually. The additional amplitude decays arise from strong diffusion. If our source and observation probes are further displaced, distant amplitudes would be reduced and phase delays would increase.

We next provide results for more complicated layering schemes. In Figures 4.17a to 4.17d, assumed horizontal versus vertical permeability distributions are displayed along with computed time delays. For brevity, the remaining parameters are not changed, but we note that only the lumped parameters $\mu c\omega$ and "permeability/porosity" are important in the analysis.

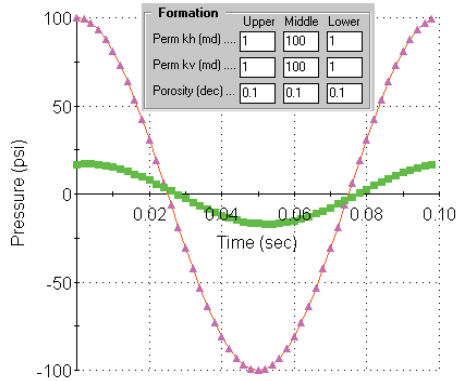

Figure 4.17a. Isotropic run, high permeability middle layer.

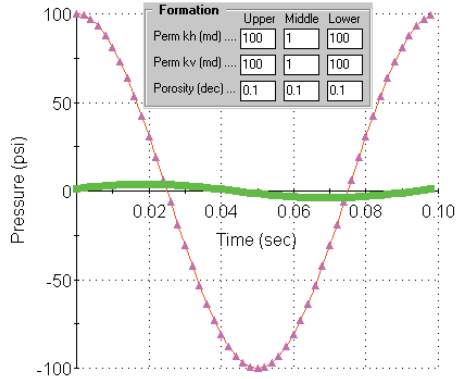

Figure 4.17b. Isotropic run, low permeability middle layer.

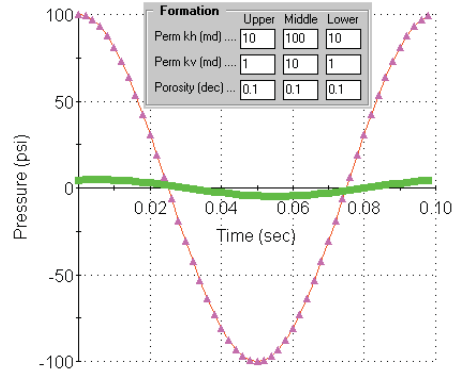

Figure 4.17c. Anisotropic run, high permeability middle layer.

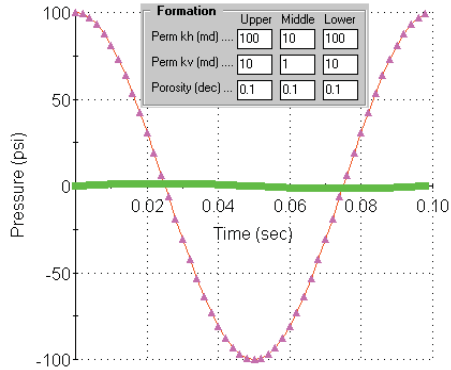

Figure 4.17d. Anisotropic run, low permeability middle layer.

In the next example, we fix all formation and fluid properties in the input screens of Figures 4.18a to 4.18c, noting that a layered anisotropic permeability distribution is assumed. As in the above examples, Figure 4.18a models a *vertical* tool with a source-to-observation probe separation of two inches. On the other hand, Figure 4.18b models the response of the same tool oriented horizontally – calculated amplitudes are larger although phase responses are similar (input dip angle is changed by editing the observation probe indexes).

Lastly, we determined the response at 45° dip by changing probe indexes and modifying gridblock sizes to maintain the desired two-inch probe separation. The amplitude response, shown in Figure 4.18c, falls between those of Figures 4.18a and 4.18b, as expected. Computation times for all simulations reported were less than five seconds.

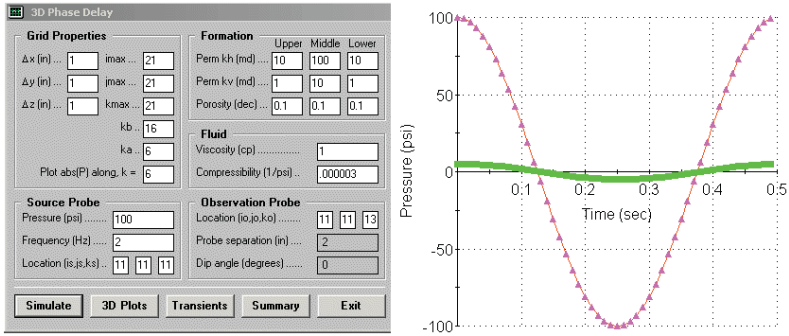

Figure 4.18a. Vertical tool (0° dip) in layered anisotropic medium.

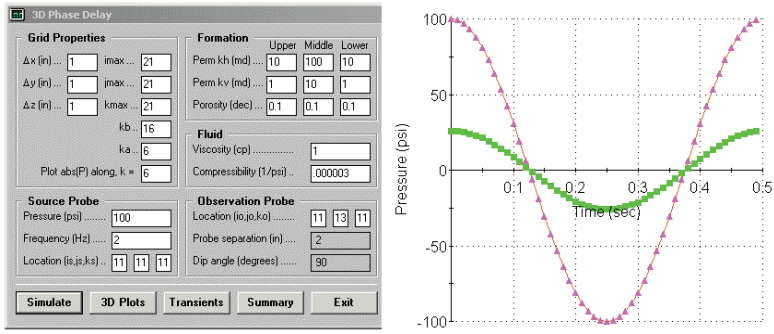

Figure 4.18b. Horizontal tool (90° dip) in layered anisotropic medium.

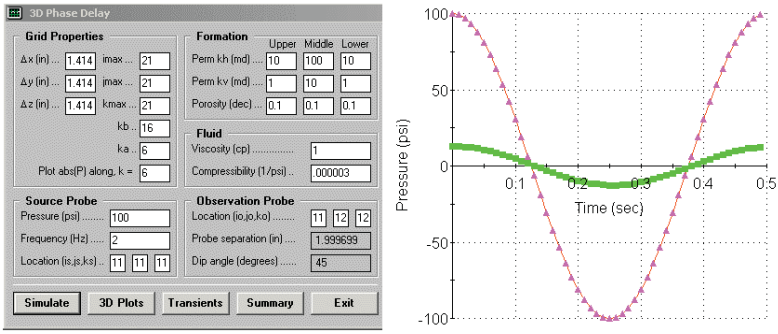

Figure 4.18c. Deviated tool (45° dip) in layered anisotropic medium.

In the next example, we move with the formation tester as it progresses vertically downward through a three-layer formation, taking a well logging perspective. We consider the isotropic layering in Figure 4.19a and a 1 Hz oscillation frequency. From Figure 4.19a, the upper interface index is kb = 16. From Figure 4.19b, the source probe is positioned at k = 17 while the observation probe is found at k = 19 – thus, the dual probe system lies entirely in the upper layer while the probe separation is 6 inches. The corresponding source and observation probe pressure traces are shown in Figure 4.19b. In Figure 4.19c, the source probe is found in the middle low permeability layer with k = 15 while the observation probe is positioned above the interface in the higher permeability layer at k = 17. The ten-fold reduction in permeability clearly decreases the amplitude response at the observation probe. In our Figure 4.19d, the formation tester is moved toward the center of the layer, so that the dual probe system is entirely within that layer. The larger time shift in our Figure 4.19d due to lower effective permeability relative to that in Figure 4.19b is clearly evident – pointing to the success of the method in resolving permeability contrasts between layers.

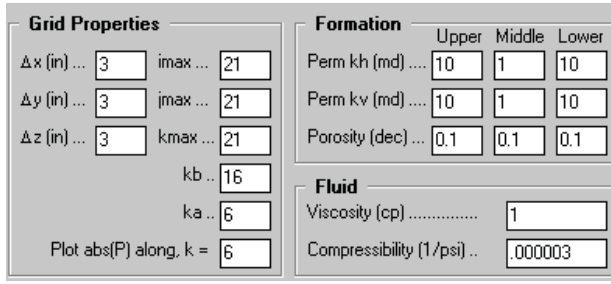

Figure 4.19a. Isotropic three-layer system.

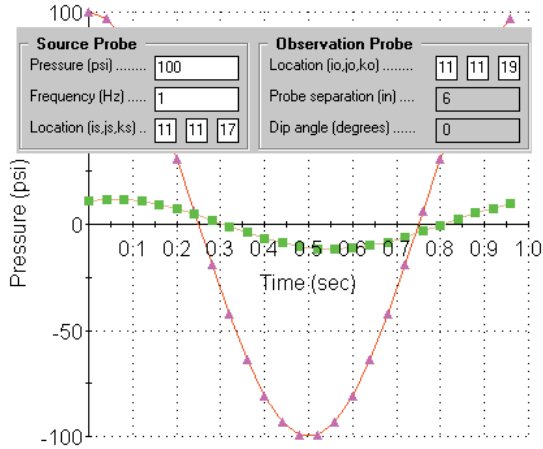

Figure 4.19b. Dual probe system entirely in top layer.

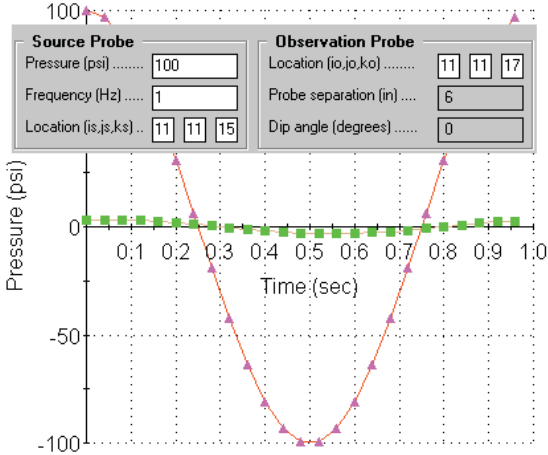

Figure 4.19c. Source in middle layer, observation probe outside.

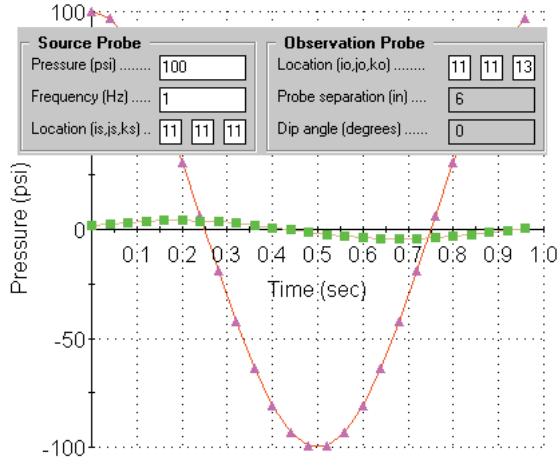

Figure 4.19d. Dual probe system entirely in middle layer.

In this final example, we consider the three-layer formation described in Figure 4.20a. Both source (ks = 9) and observation (ko = 15) probes are located within the middle layer (6 < k < 16). The green observation probe response for the assumed probe frequency of 10 Hz is shown at the left of Figure 4.20b. The response at the right assumes the same parameters, but the source frequency is decreased to 0.5 Hz. These two examples show that different responses are obtained. In practice, as the formation tester traverses past different layers, multiple frequencies can be used to probe the background geology. Rapid history matching, possible because the computational model is extremely fast, allows similarly rapid identification of layer properties.

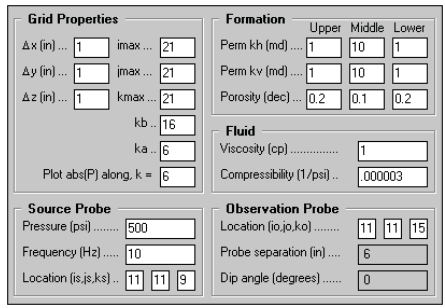

Figure 4.20a. Three layer example.

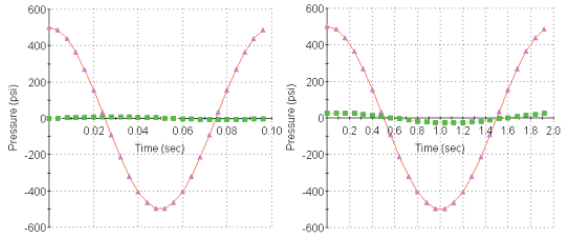

Figure 4.20b. Observation probe responses at 10 Hz (left) and 0.5 Hz (right).

4.6 Typical Experimental Results

Here we provide experimental results obtained with the linear core sample conceptually shown in Figure 4.21, instrumented with four pressure transducers separated by six inch distances. Pressure traces are shown at the right. The sudden change in pulsing amplitude is used to "mark" an initial time so that subsequent time delays can be measured. The initial questions raised when phase delay methods were first posed are several. "What frequencies can be used?" "Are the delays detectable and what level of electronic signal processing support is required?" "Is the method doable with existing formation testing pumps?" It turns out that frequencies in the range of 0.25 – 10 Hz lead to time delays that are visually detectable and can be easily implemented mechanically. Very rarely in engineering do all factors play so satisfactorily.

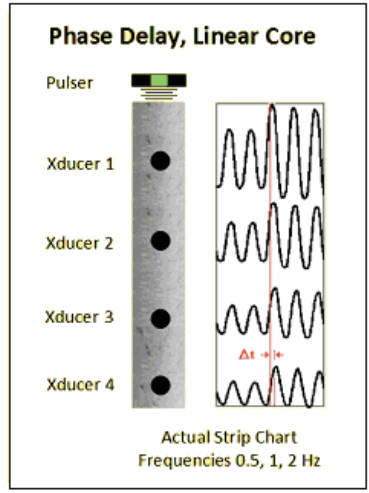

Figure 4.21. Actual strip chart, Δt delay visually seen.

Detailed strip chart results for 0.5, 1 and 2 Hz are given in Figures 4.22a, 4.22b and 4.22c below. Note how pressure amplitudes decrease going down the page, that is, as the pressure transducer distances increase from the piston pump. Time delays may be discerned which are in the one second range.

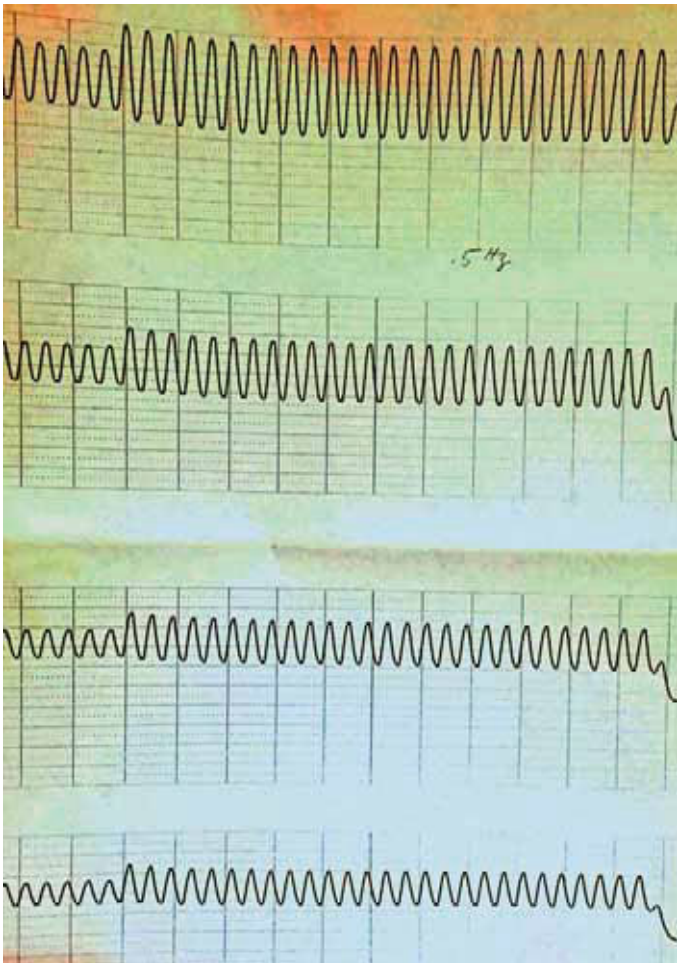

Figure 4.22a. Frequency 0.5 Hz, note amplitude attenuation with distance.

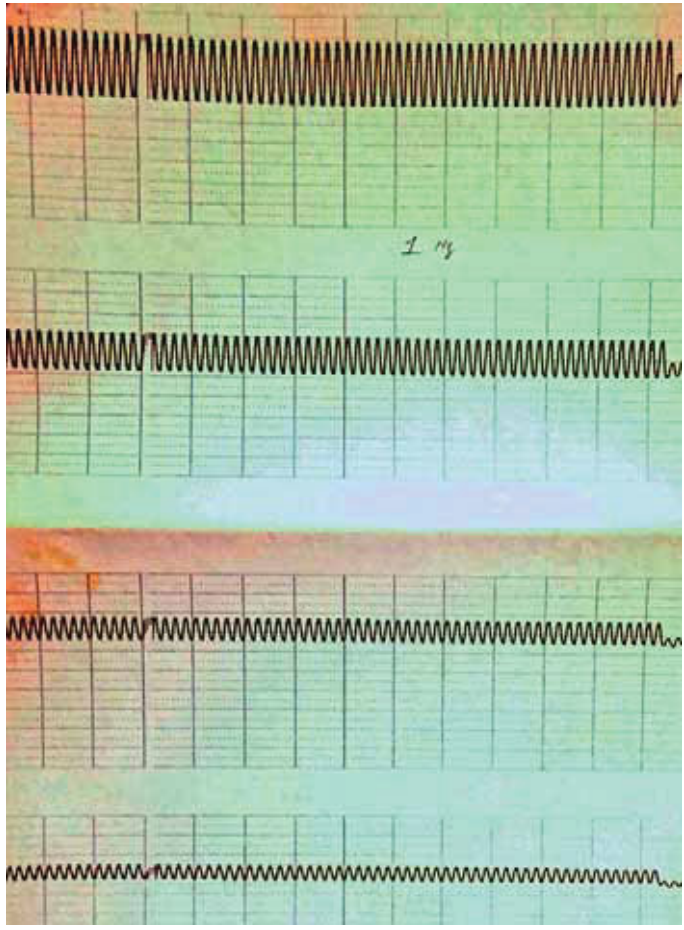

Figure 4.22b. Frequency 1 Hz, note amplitude attenuation with distance.

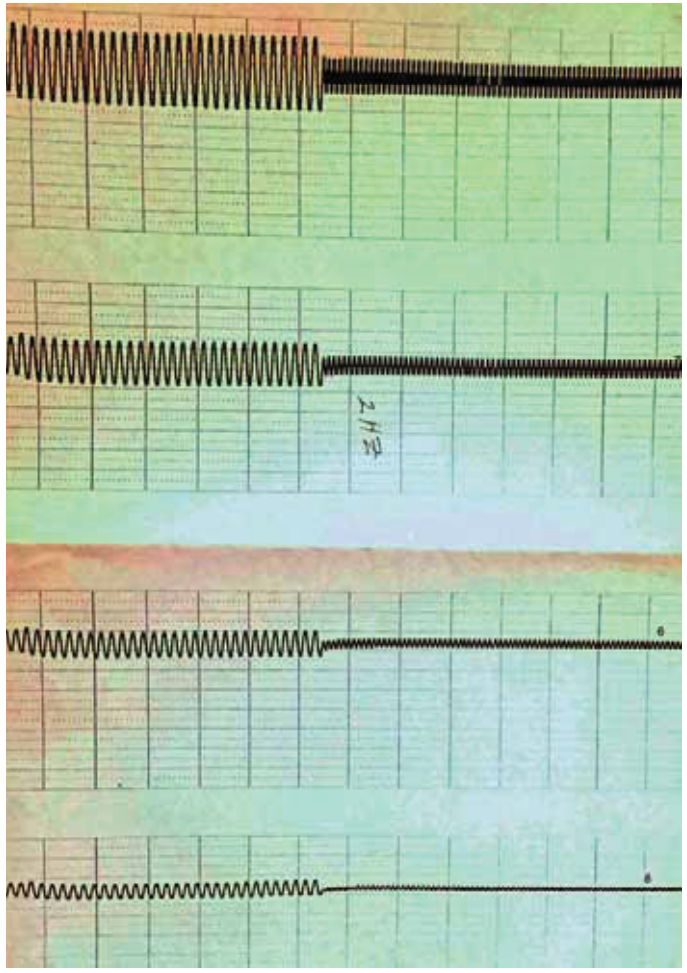

Figure 4.22c. Frequency 2 Hz, note amplitude attenuation with distance.

4.7 Closing Remarks – Extensions and Additional Applications

We have developed exact analytical results for phase delay interpretation in homogeneous anisotropic media at any dip angle and shown how it is possible to obtain both horizontal and vertical permeabilities for low mobility applications at early times. Also, a three-dimensional Darcy flow simulator capable of modeling compressible liquids in multilayer anisotropic formations is developed for more complicated interpretation questions. A formation tester creates sinusoidal pressure pulses at the source probe and changes to amplitude and phase are calculated at all other observation points – thus, solutions are provided for all probe separations and tool dip angles. The iterative algorithm, which is robust and stable, converges rapidly. Grid block systems ranging from $20 \times 20 \times 20$ to $30 \times 30 \times 30$ require at most five seconds on typical personal computers. The simulation engine can be used within nested do-loops to perform numerous forward runs in support of inverse applications.

Various improvements to the numerical model are possible. We note that our finite difference equations are developed for variable x_i, y_j and z_k grids. However, the Visual Basic interface for convenience assumed constant grids with different Δx, Δy and Δz values permitted. In general, this is not a requirement – the Fortran source code supports any variable grid system defined by the user although, of course, additional software must be developed to create and view these grids. And while the program is written for three layers, any number of layers may be added. Additional models can be created from our Fortran source code. For example, in the derivation leading to Equation 4.15, the difference model that invokes continuity of normal velocity and pressure across horizontal interfaces can be modified to handle other effects – shale streaks (which support pressure discontinuities) can be modeled by allowing $P_{i,j,k^{*}+} \neq P_{i,j,k^{*}-}$ at selected nodal locations. Chin (2002) explains how effects like fractures and shales can be included in matching conditions. Other model permutations include (i) changes to farfield boundary conditions, e.g., solid barriers, aquifer drives, (ii) extensions to heterogeneous media, and (iii) reformulation using cylindrical coordinates to account for borehole effects.

4.8 References

Chin, W.C., Quantitative Methods in Reservoir Engineering, Elsevier Science, Amsterdam, 2002.

Chin, W.C. and Proett, M.A., "Formation Evaluation Using Phase Shift Periodic Pressure Pulse Testing," U.S. Patent No. 5,672,819 issued Sept. 30, 1997.

Chin, W.C., Zhou, Y., Feng, Y., Yu, Q. and Zhao, L., Formation Testing: Pressure Transient and Contamination Analysis, John Wiley & Sons, New Jersey, 2014.

Proett, M.A., Chin, W.C. and Mandal, B., "Advanced Permeability and Anisotropy Measurements While Testing and Sampling in Real-Time Using a Dual Probe Formation Tester," SPE Paper 64650, *Seventh International Oil & Gas Conference and Exhibition*, Beijing, China, Nov. 2000.

5
Four Permeability Prediction Methods

Having discussed permeability prediction in all its mathematical detail in prior chapters, it is useful to "take a step back" to review some basic capabilities through examples. We start with two conventional models and discuss their assumptions. Previously we showed how the spherical source solution can be expanded in the form

$$P(R_w,t)_{\textit{late-time from exact}} = P_0 - Q_0\,\mu/(4\pi R_w k) + \{Q_0\,\mu/(4\pi k)\}\sqrt{\{\phi\mu c/(\pi k t)\}} \qquad (2.25)$$

This late time solution is independent of flowline storage, and depends not only on μ and k, but also the porosity ϕ and fluid compressibility c. Equation 2.25 also illustrate an algebraic "inverse-square-root" timewise decline in pressure. This large-time transient behavior forms the basis for Horner-type models which, while popular, require additional "ϕc" estimates which introduce the possibility of error. At very large times, a steady-state spherical response is found from

$$P(R_w,t)_{\textit{late-time from exact}} = P_0 - Q_0\,\mu/(4\pi R_w k) \qquad (2.26a)$$

which is essentially the well known "$k_s = CQ\mu/(2\pi r_p\,\Delta P)$" used conventionally but without the geometric correction. If the value of $P(R_w)$ is known from drawdown or buildup measurements, then this simple source-point formula can be used to estimate the value of the isotropic permeability k (our more general derivation of Chapter 2 shows that, in the no-skin limit, k can be replaced by $k_h^{2/3}k_v^{1/3}$ in transversely isotropic media).

The Horner type approach conventionally used also derives from the foregoing result. In Equation 2.25, a drawdown with a constant volume flow rate of Q_0 starts at t = 0. Now we wish to stop pumping at t = t*. To completely terminate the flow, the negative of the flow rate must be added. Thus, for t > t*, we have the superposition

$$P(R_w,t) = P_0 - Q_0\,\mu/(4\pi R_w k) + \{Q_0\,\mu/(4\pi k)\}\sqrt{\{\phi\mu c/(\pi k t)\}}$$
$$+ Q_0\,\mu/(4\pi R_w k) - \{Q_0\,\mu/(4\pi k)\}\sqrt{\{\phi\mu c/(\pi k(t-t^*))\}} \qquad (5.1)$$

or

$$P(R_w,t) = P_0 + \{Q_0\,\mu/(4\pi k)\}\ \sqrt{\{\phi\mu c/(\pi k)\}}\ \{1/\sqrt{t} - 1/\sqrt{(t-t^*)}\} \qquad (5.2)$$

If we view the last factor on the right of Equation 5.2 as a function of time, say $\tau = 1/\sqrt{t} - 1/\sqrt{(t-t^*)}$, then we can certainly write

$$P(R_w,\tau) = P_0 + \{Q_0\,\mu/(4\pi k)\}\ \sqrt{\{\phi\mu c/(\pi k)\}}\ \tau \qquad (5.3)$$

By plotting P versus τ, a straight-line is obtained and the permeability k or the mobility k/μ can be obtained from the slope. There are several drawbacks with this interpretation procedure. Note the porosity ϕ and the fluid compressibility c must be known, which necessarily invites uncertainty and error. Also, the fact that flowline storage does not appear in the equation used indicates that the method requires sufficiently large times.

These factors indicate that neither the "$k_s = CQ\mu/(2\pi r_p\,\Delta P)$" approach nor the Horner method are as robust as our low mobility, early-time drawdown and drawdown-buildup prediction methods which operate in the presence of high flowline volumes. We also add that these methods additionally provide pore pressure from highly transient unequilibrated data. The fast logging speeds enabled by these *single-probe* techniques imply reduced costs, higher resolution, plus the option to perform rapid and detailed pressure gradient plots for hydrocarbon and abnormal zone determination.

By contrast, the phase delay approach requires *dual-probes* as well as estimates for the product ϕc, and does *not* offer pore pressure. At first, these may appear as strong disadvantages – and they are is phase delays are used along. However, the important distinction is this. From Equation 4.35, the delay provides a direct measure of the quantity "$\sin^2\delta/k_h + \cos^2\delta/k_v$"

$$\theta \approx L\sqrt{[\{\phi\mu c\omega/2\}\{\sin^2\delta/k_h + \cos^2\delta/k_v\}]} \qquad (4.35)$$

while drawdown-only and drawdown-buildup methods procide measures of the spherical permeability $k_h^{2/3}k_v^{1/3}$. Thus, the two resulting equations for k_h and k_v provide predictions for *both* horizontal and vertical permeability. These are useful in hydraulic fracturing, production planning and rock stress analysis.

5.1 Steady-State Drawdown Example

In this exercise, we evaluate the steady-state drawdown permeability prediction approach using exact forward pressure data from our FT-00 simulator. The input assumptions are shown in Figure 5.1a and exact transient source probe results are displayed in Figures 5.1b and 5.1c.

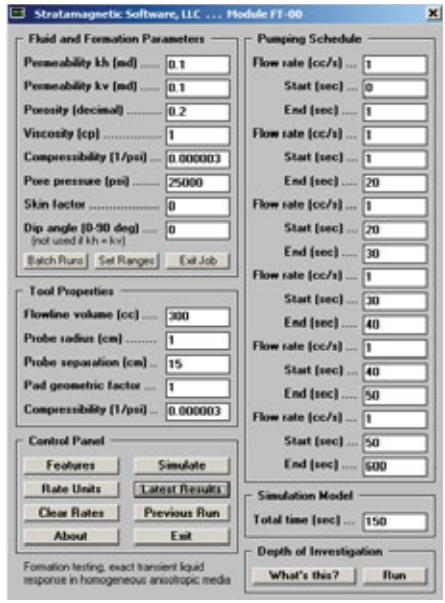

Figure 5.1a. FT-00 input assumptions.

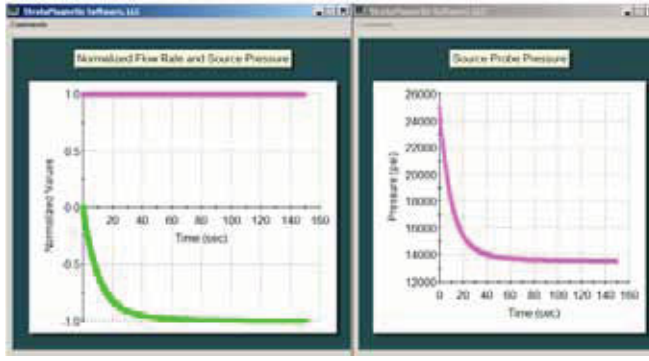

Figure 5.1b. Exact transient source probe results.

```
DEFINITIONS
Time ... Elapsed time (sec)
Rate ... Drawdown flow rate (cc/s)
Ps* .... Source pressure with hydrostatic (psi)
Pr* .... Observation pressure with hydrostatic (psi)
Ps** ... Source pressure, no hydrostatic (psi)
Pr** ... Observation pressure, no hydrostatic (psi)

          NOTE: Ps* or Pr* < 0 means volume flow
          rate cannot be achieved in practice
```

Time (s)	Rate (cc/s)	Ps* (psi)	Pr* (psi)	Ps**(psi)	Pr**(psi)	Pr**/Ps**
0.000E+00	0.10000E+01	0.25000E+05	0.25000E+05	0.00000E+00	0.00000E+00	----------
0.501E+01	0.10000E+01	0.20748E+05	0.24735E+05	-0.42520E+04	-0.26470E+03	0.62254E-01
0.100E+02	0.10000E+01	0.18167E+05	0.24527E+05	-0.68328E+04	-0.47276E+03	0.69191E-01
0.200E+02	0.10000E+01	0.15548E+05	0.24387E+05	-0.94516E+04	-0.61295E+03	0.64852E-01
0.301E+02	0.10000E+01	0.14481E+05	0.24352E+05	-0.10519E+05	-0.64829E+03	0.61629E-01
0.401E+02	0.10000E+01	0.14021E+05	0.24340E+05	-0.10979E+05	-0.65988E+03	0.60103E-01
0.501E+02	0.10000E+01	0.13809E+05	0.24334E+05	-0.11191E+05	-0.66582E+03	0.59495E-01
0.601E+02	0.10000E+01	0.13702E+05	0.24330E+05	-0.11298E+05	-0.67040E+03	0.59340E-01
0.702E+02	0.10000E+01	0.13643E+05	0.24325E+05	-0.11357E+05	-0.67459E+03	0.59400E-01
0.802E+02	0.10000E+01	0.13607E+05	0.24321E+05	-0.11393E+05	-0.67854E+03	0.59556E-01
0.902E+02	0.10000E+01	0.13582E+05	0.24318E+05	-0.11418E+05	-0.68223E+03	0.59749E-01
0.100E+03	0.10000E+01	0.13564E+05	0.24314E+05	-0.11436E+05	-0.68565E+03	0.59953E-01

Figure 5.1c. Numerical pressure responses.

A simple program was written for Equation 2.26a and is denoted by FT-13. What are the predicted permeabilities using this steady-state approach? The times in Figure 5.1c are listed in seconds. If one minute data is used, we find that ΔP = 25,000 – 13,600 = 11,400 psi, and a permeability of 0.102 md is obtained, comparing very favorably with the 0.1 md assumed in Figure 5.1a. On the other hand, if we use 30 sec data, we find that Δp = 25,000 – 14,481 = 10,519 psi and we obtain 0.111 md. Finally, if we use 10 sec data, then Δp = 25,000 – 18,167 = 6,833 psi and we find 0.171 md with a 71% error..

5.2 Early-Time, Low-Mobility Drawdown-Buildup

Here we evaluate the early-time, low-mobility drawdown-buildup approach. Figure 5.2a shows inputs assumed in our exact forward pressure simulator FT-00. Note that we have a very low 0.1 md/cp mobility and also an extremely short drawdown time of 1 sec. The calculated source probe response is shown in Figure 5.2b and tabulated results are given in Figure 5.2c.

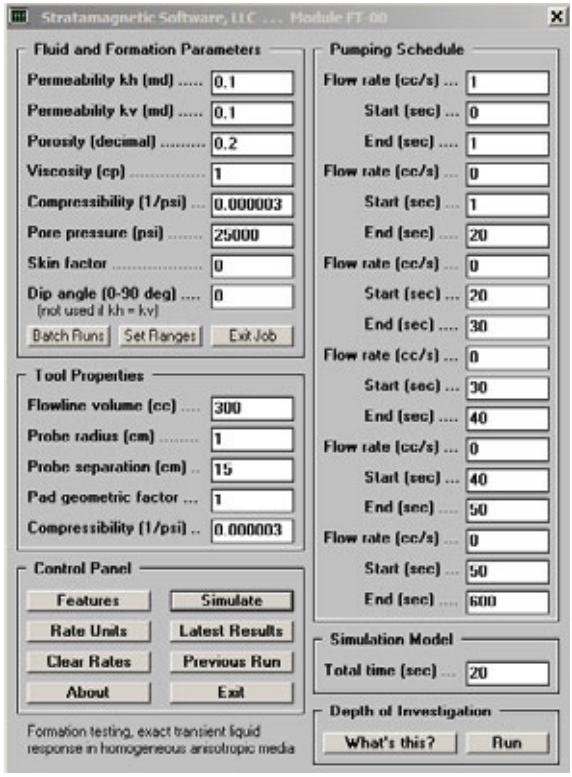

Figure 5.2a. FT-00 input parameters.

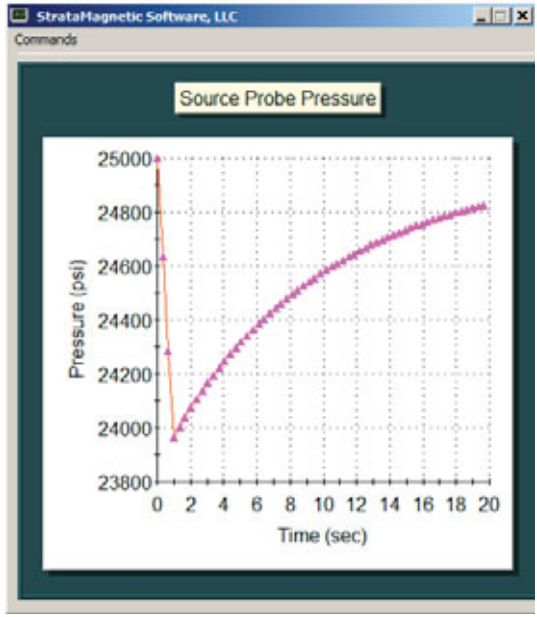

Figure 5.2b. Drawdown-buildup pressure response.

```
NOTE: Ps* or Pr* < 0 means volume flow
rate cannot be achieved in practice
```

Time (s)	Rate (cc/s)	Ps* (psi)	Pr* (psi)	Ps**(psi)	Pr**(psi)	Pr**/Ps**

Drawdown

0.000E+00	0.10000E+01	0.25000E+05	0.25000E+05	0.00000E+00	0.00000E+00	----------
0.339E+00	0.10000E+01	0.24634E+05	0.25000E+05	-0.36614E+03	-0.62553E-03	0.17085E-05
0.678E+00	0.10000E+01	0.24283E+05	0.25000E+05	-0.71715E+03	-0.49757E+00	0.69382E-03

Buildup

0.102E+01	0.00000E+00	0.23964E+05	0.24995E+05	-0.10361E+04	-0.49642E+01	0.47910E-02
0.136E+01	0.00000E+00	0.24004E+05	0.24984E+05	-0.99636E+03	-0.16208E+02	0.16267E-01
0.169E+01	0.00000E+00	0.24040E+05	0.24967E+05	-0.95993E+03	-0.32989E+02	0.34366E-01
0.203E+01	0.00000E+00	0.24074E+05	0.24950E+05	-0.92567E+03	-0.49814E+02	0.53814E-01
0.237E+01	0.00000E+00	0.24107E+05	0.24938E+05	-0.89318E+03	-0.62302E+02	0.69753E-01
0.271E+01	0.00000E+00	0.24138E+05	0.24930E+05	-0.86222E+03	-0.69932E+02	0.81107E-01
0.305E+01	0.00000E+00	0.24167E+05	0.24926E+05	-0.83263E+03	-0.73725E+02	0.88545E-01
0.339E+01	0.00000E+00	0.24196E+05	0.24925E+05	-0.80429E+03	-0.74841E+02	0.93053E-01
0.373E+01	0.00000E+00	0.24223E+05	0.24926E+05	-0.77711E+03	-0.74197E+02	0.95478E-01
0.407E+01	0.00000E+00	0.24249E+05	0.24928E+05	-0.75101E+03	-0.72439E+02	0.96455E-01
0.441E+01	0.00000E+00	0.24274E+05	0.24930E+05	-0.72592E+03	-0.70006E+02	0.96438E-01
0.475E+01	0.00000E+00	0.24298E+05	0.24933E+05	-0.70180E+03	-0.67191E+02	0.95742E-01
0.508E+01	0.00000E+00	0.24321E+05	0.24936E+05	-0.67858E+03	-0.64186E+02	0.94589E-01
0.542E+01	0.00000E+00	0.24344E+05	0.24939E+05	-0.65622E+03	-0.61117E+02	0.93134E-01
0.576E+01	0.00000E+00	0.24365E+05	0.24942E+05	-0.63469E+03	-0.58064E+02	0.91484E-01
0.610E+01	0.00000E+00	0.24386E+05	0.24945E+05	-0.61393E+03	-0.55080E+02	0.89716E-01
0.644E+01	0.00000E+00	0.24406E+05	0.24948E+05	-0.59393E+03	-0.52195E+02	0.87882E-01
0.678E+01	0.00000E+00	0.24425E+05	0.24951E+05	-0.57464E+03	-0.49430E+02	0.86019E-01
0.712E+01	0.00000E+00	0.24444E+05	0.24953E+05	-0.55603E+03	-0.46793E+02	0.84154E-01
0.746E+01	0.00000E+00	0.24462E+05	0.24956E+05	-0.53808E+03	-0.44287E+02	0.82306E-01

0.780E+01	0.00000E+00	0.24479E+05	0.24958E+05	-0.52076E+03	-0.41914E+02	0.80486E-01
0.814E+01	0.00000E+00	0.24496E+05	0.24960E+05	-0.50404E+03	-0.39669E+02	0.78703E-01
0.847E+01	0.00000E+00	0.24512E+05	0.24962E+05	-0.48790E+03	-0.37550E+02	0.76962E-01
0.881E+01	0.00000E+00	0.24528E+05	0.24964E+05	-0.47232E+03	-0.35550E+02	0.75267E-01
0.915E+01	0.00000E+00	0.24543E+05	0.24966E+05	-0.45727E+03	-0.33664E+02	0.73620E-01
0.949E+01	0.00000E+00	0.24557E+05	0.24968E+05	-0.44274E+03	-0.31886E+02	0.72021E-01
0.983E+01	0.00000E+00	0.24571E+05	0.24970E+05	-0.42870E+03	-0.30211E+02	0.70471E-01
0.102E+02	0.00000E+00	0.24585E+05	0.24971E+05	-0.41513E+03	-0.28631E+02	0.68968E-01
0.105E+02	0.00000E+00	0.24598E+05	0.24973E+05	-0.40203E+03	-0.27142E+02	0.67512E-01
0.108E+02	0.00000E+00	0.24611E+05	0.24974E+05	-0.38937E+03	-0.25738E+02	0.66102E-01
0.112E+02	0.00000E+00	0.24623E+05	0.24976E+05	-0.37713E+03	-0.24414E+02	0.64736E-01
0.115E+02	0.00000E+00	0.24635E+05	0.24977E+05	-0.36530E+03	-0.23165E+02	0.63413E-01
0.119E+02	0.00000E+00	0.24646E+05	0.24978E+05	-0.35387E+03	-0.21986E+02	0.62130E-01
0.122E+02	0.00000E+00	0.24657E+05	0.24979E+05	-0.34282E+03	-0.20873E+02	0.60888E-01
0.125E+02	0.00000E+00	0.24668E+05	0.24980E+05	-0.33213E+03	-0.19823E+02	0.59683E-01
0.129E+02	0.00000E+00	0.24678E+05	0.24981E+05	-0.32180E+03	-0.18830E+02	0.58515E-01
0.132E+02	0.00000E+00	0.24688E+05	0.24982E+05	-0.31181E+03	-0.17892E+02	0.57383E-01
0.136E+02	0.00000E+00	0.24698E+05	0.24983E+05	-0.30215E+03	-0.17006E+02	0.56284E-01
0.139E+02	0.00000E+00	0.24707E+05	0.24984E+05	-0.29280E+03	-0.16168E+02	0.55217E-01
0.142E+02	0.00000E+00	0.24716E+05	0.24985E+05	-0.28376E+03	-0.15375E+02	0.54181E-01
0.146E+02	0.00000E+00	0.24725E+05	0.24985E+05	-0.27502E+03	-0.14624E+02	0.53175E-01
0.149E+02	0.00000E+00	0.24733E+05	0.24986E+05	-0.26657E+03	-0.13914E+02	0.52198E-01
0.153E+02	0.00000E+00	0.24742E+05	0.24987E+05	-0.25839E+03	-0.13242E+02	0.51248E-01
0.156E+02	0.00000E+00	0.24750E+05	0.24987E+05	-0.25047E+03	-0.12605E+02	0.50325E-01
0.159E+02	0.00000E+00	0.24757E+05	0.24988E+05	-0.24281E+03	-0.12002E+02	0.49427E-01
0.163E+02	0.00000E+00	0.24765E+05	0.24989E+05	-0.23540E+03	-0.11430E+02	0.48554E-01
0.166E+02	0.00000E+00	0.24772E+05	0.24989E+05	-0.22823E+03	-0.10888E+02	0.47704E-01
0.169E+02	0.00000E+00	0.24779E+05	0.24990E+05	-0.22129E+03	-0.10374E+02	0.46877E-01
0.173E+02	0.00000E+00	0.24785E+05	0.24990E+05	-0.21458E+03	-0.98860E+01	0.46072E-01
0.176E+02	0.00000E+00	0.24792E+05	0.24991E+05	-0.20808E+03	-0.94235E+01	0.45288E-01
0.180E+02	0.00000E+00	0.24798E+05	0.24991E+05	-0.20179E+03	-0.89846E+01	0.44525E-01
0.183E+02	0.00000E+00	0.24804E+05	0.24991E+05	-0.19570E+03	-0.85680E+01	0.43782E-01
0.186E+02	0.00000E+00	0.24810E+05	0.24992E+05	-0.18980E+03	-0.81725E+01	0.43058E-01
0.190E+02	0.00000E+00	0.24816E+05	0.24992E+05	-0.18410E+03	-0.77970E+01	0.42352E-01
0.193E+02	0.00000E+00	0.24821E+05	0.24993E+05	-0.17857E+03	-0.74403E+01	0.41665E-01
0.197E+02	0.00000E+00	0.24827E+05	0.24993E+05	-0.17323E+03	-0.71014E+01	0.40995E-01

Figure 5.2c. Tabulated results.

In Figure 5.2d, the program FT-PTA-DDBU.EXE for early-time, low-mobility *buildup* data was used together with the red buildup data in Figure 5.2c. Very good predictions were obtained, namely, 24,947 psi versus 25,000 psi, and 0.12 md/cp versus 0.1 md/cp assumed.

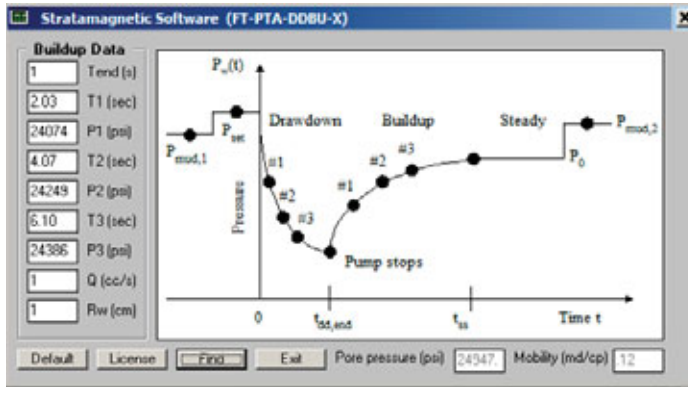

Figure 5.2d. Mobility prediction using *buildup* data.

5.3 Early-Time, Low-Mobility Drawdown Approach

In this exercise, we reconsider the example in the prior section and use *drawdown* data only. Recall that our drawdown time was deliberately chosen to be extremely short in order to test the robustness of the calculations. The software implementing the work of Chapter 2, "pta-dd-3-run-with-rft-numbers.exe," is used below.

```
C:\pta-dd-3-run-with-rft-numbers <Return>

Volume flow rate (cc/s): 1.
Pump probe, radius (cm): 1.
Probe, geometric factor: 1.
1st Point Time T1 (sec): 0.000
      Pressure P1 (psi): 25000.
2nd Point Time T2 (sec): 0.339
      Pressure P2 (psi): 24634.
3rd Point Time T3 (sec): 0.678
      Pressure P3 (psi): 24283.
```

The iteration history is selectively given below, with a total computing time of less than one second. Given the extremely short duration of the data interval, the predicted mobility of 0.133 md/cp is surprisingly good compared with the inputted value of 0.1 md/cp.

```
    Run     Error   P0(psi)   Md/Cp
      1.    4.1 %    25000    0.001
      2.    4.0 %    25000    0.002
.
.
     40.    2.8 %    25000    0.044
     50.    2.5 %    25000    0.055
     60.    2.1 %    25000    0.066
     70.    1.8 %    25000    0.077
     80.    1.5 %    25000    0.087
     90.    1.1 %    25000    0.098
    100.    0.8 %    25000    0.109
    110.    0.5 %    25000    0.119
    120.    0.1 %    25000    0.130
    121.    0.1 %    25000    0.131
    122.    0.0 %    25000    0.132
    123.    0.0 %    25000    0.133

Stop - Program terminated.
```

5.4 Phase Delay, Non-Ideal Rectangular Flow Excitation

In practical mechanical design, it is often not possible to pump exactly with sinusoidal precision. We consider an example showing phase delay results in one such instance. Recall that the underlying theory was derived assuming pressure disturbances which are proportional to exp (iωt), that is, that they are perfect sinusoids. Typically, one can hope for two-to-three wave cycles at best that may not be perfectly sinusoidal. In the input screen for exact forward simulator FT-00 in Figure 5.3a, a pump schedule having three wave cycles in six seconds, or a frequency of 0.5 Hz, was formed from sequences of *rectangular* flow rate functions. Such functions are hardly representative of theoretical Fourier components and it is instructive to understand the consequences. To ensure numerical accuracy, we used FT-00 because it provides exact solutions that are not compromised by sharp transitions in the flow rate functions. Also, note that the mobility is extremely low at 0.1 md/1 cp or 0.1 md/cp. Calculated results in Figure 5.3b show that both amplitude functions at source and observation probes drift considerably and are not useful for computation. As in the foregoing example, we therefore turn to time delay measurements. Interestingly, examine the two circled points located at the midpoints of the pumping cycles. The time delay, obtained visually, is clearly "4-3" or 1 sec. What does this imply? We use a software program discussed previously and obtain the results below.

```
C:\phase-delay-permeability-calculation <Return>

Probe separation ....... (cm):  15.
Porosity .......... (decimal):  0.2
Viscosity .............. (cp):  1.
Compressibility ..... (1/psi):  0.000003
Frequency .............. (Hz):  0.5
Time delay ............. (sec):  1.

Permeability ........... (md):   0.3148E+00
Phase delay  .......... (rad):   0.3142E+01
Phase delay ........... (deg):   0.1800E+03
```

The calculated permeability of 0.3148 md, compared to the known input value of 0.1 md, is not bad, and acceptable when judged against present field logging standards. The discrepancy arises from two effects, namely, the length of the short duration test, and the use of rectangular as opposed to sinusoidal functions. These problems can be corrected by mechanical design.

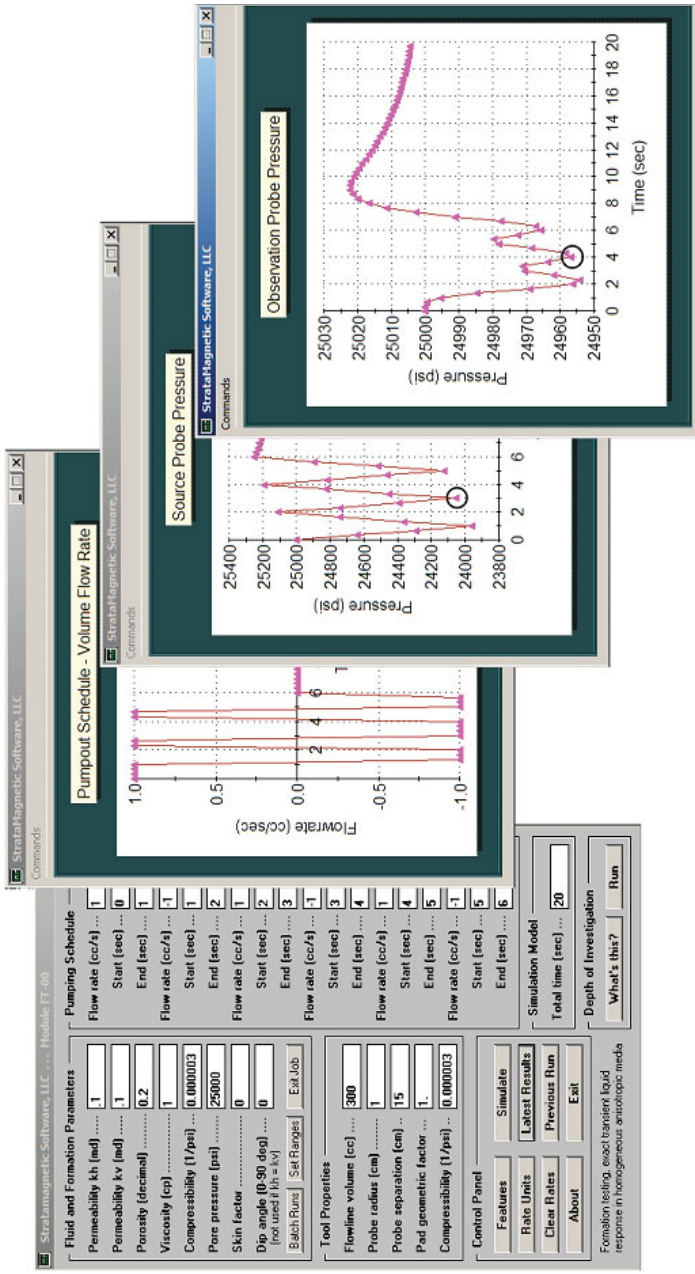

Figure 5.3a. Square wave assumptions and pressure responses.

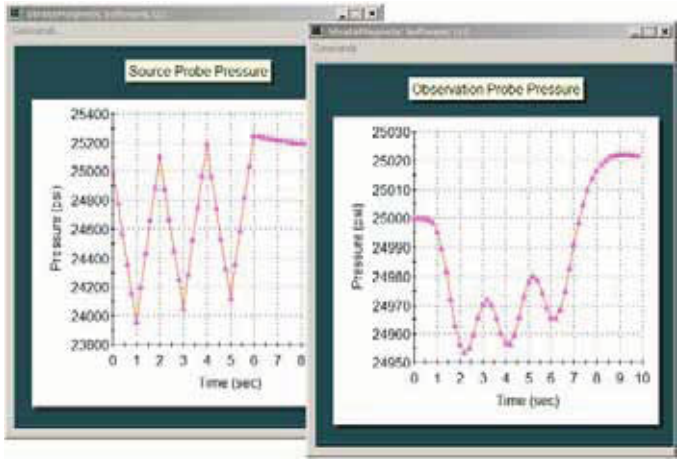

Figure 5.3b. Pressure responses, exploded view.

The foregoing examples demonstrate a degree of robustness in our drawdown-only, drawdown-buildup and phase delay approaches to permeability or mobility prediction that are lacking from classical steady-state and Horner type methods. Although much work remains in taking the methods to commercialization, the authors are confident that with improvements to mechanical design, e.g., more precise flow rate feedback and control, the ability to provide both k_h and k_v at early times in low mobility environments will be a reality. While theory and numerical computations suggest that the methods, based on spherical and ellipsoidal source models, are physically sound, non-ideal effects related to pad geometry and borehole curvature do need to be considered. Toward this end, a formation testing experimental fixture similar to the one discussed in Chapter 1 is under design and construction to evaluate the new methods and calibrate engineered tools.

6
Multiphase Flow with Inertial Effects

Water-based muds invade oil-bearing formations during drilling. This immiscible cylindrical invading flow depends on relative permeability and capillary pressure. Although the invasion can be described using basic reservoir engineering principles, unlike conventional reservoir flow models, a growing mudcake that is dynamically coupled to the flow within the reservoir controls this invasion. This coupling is especially significant when formation permeabilities are low. The formation tester withdraws fluid from the cylindrical invaded zone after supercharging invasion has begun. But now, the tester tool itself induces a local ellipsoidal (anisotropic) flow superposed on the cylindrical one. The resulting highly nonlinear combined flow is solved with special boundary conditions involving pump rate, skin effects, flow line storage and transient mudcake growth. When oil-based muds invade oil formations, similar physical mechanisms are at work. However, relative permeability and capillary pressure are no longer the controlling parameters. Instead, molecular diffusion becomes important. Nonetheless, immiscible and miscible flows share common features. In both cases, a governing transient partial differential equation for pressure must be solved; this is coupled to convective-diffusion equations for saturation (in the case of immiscible flow) and concentration (for miscible flow). When the first models for these phenomena appeared in the work of Chin and Proett (2005), conventional Darcy formulations assuming low-speed flow sufficed. In recent applications, pumping speeds have increased significantly that the prior models require changes to handle inertial effects. In this chapter, the earlier work is extended to include Forchheimer type flow extensions.

We first present a general immiscible formulation for vertical well flow in multi-layered anisotropic heterogeneous media. The time-dependent, coupled pressure-saturation field is solved by numerical "IMPES" (implicit pressure – explicit saturation) methods. The formulation does not assume constant density flow. Rather, the fluids are compressible and the model allows pressure transient interpretation. The simulator forms the basis for new interpretation methods in which heterogeneities and properties like relative permeability may be obtained from measurements.

Outputs are spatial "snapshots" of pressure and oil saturation fields as they vary in time. A "movie mode" software option replays changes in time. One useful line plot displays oil saturation at the probe versus time, giving the time needed to pump a good oil sample and the quality of that sample. Calculations show that wait times needed for clean samples with little filtrate are short for low permeability mudcakes – for more permeable cakes, invasion is strong and wait times are longer. A corresponding probe pressure versus time plot reveals a different time scale that depends on compressibility and phase redistribution. This is useful in pressure transient permeability prediction.

Modifications to the formulation are also given which allow miscible flow simulation involving various combinations of fluids, e.g., fresh water versus brine, and oil base mud invading formations containing oil. For instance, the level of contamination by oil base muds at the probe versus time can be computed once basic diffusion coefficients are estimated. All mathematical models, numerical formulations and solution methods, and computed outputs and practical applications, are described in detail for both immiscible and miscible job planning simulators in the vertical well context for single-probe, dual-probe and straddle packer nozzles. The models integrate pressure transient analysis and contamination prediction methodologies.

6.1 Physical Problem Description

Although both immiscible and miscible problems are considered, each satisfying a very unique and different partial differential equation (PDE) model, they share common physical flow characteristics that we discuss first. The latter descriptions are important to our development of boundary conditions.

6.1.1 The physical problem

We consider the axisymmetric problem in Figure 6.1 for a three-layer formation. Initially, high pressure mud from the newly drilled borehole invades the formation and forms a mudcake that grows with time. In a homogeneous medium, the flow would be cylindrical; however, when multiple layers are

present, significant vertical cross-flow can occur after pumping begins when permeability contrasts are moderate or high (this cross-flow is permitted in our general formulation). At some point in time, a single-probe formation tester begins to withdraw fluid from the formation and terminates after a given period while supercharging invasion continues at a slower rate. This withdrawal is associated with a pressure drawdown and buildup – importantly, the fluid initially withdrawn will be contaminated by mud filtrate while later time fluid is more representative of the formation fluid. The pressure measured by the probe is not the true formation pressure, but a combined pressure partly characteristic of the high pressure in the borehole. How the detected pressure is allocated between borehole and formation effects will affect pore pressure and permeability interpretation. For example, without understanding that invasion is continually present, an unrealistically high pore pressure may be predicted.

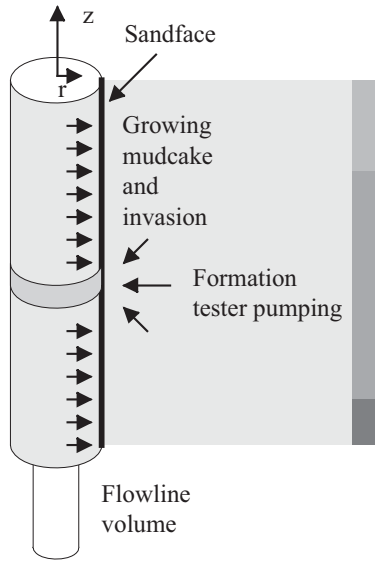

Figure 6.1. Single-probe supercharging and pumping model.

6.1.2 Job planning considerations

Two important operational questions arise. First, how long should the tool remain in place so that the recorded pressure transient curve can yield meaningful permeability and anisotropy information – without risking a stuck tool? And second, how long must pumping continue in order to obtain a clean sample, when various mud and formation properties can be estimated? These time scales are generally different. The answers to these basic questions are all but simple. In contamination applications, mixing time scales depend on whether the flow is immiscible or miscible. Different types of information are required. If the wellbore fluid is water and it invades an oil sand, fluid and formation properties like capillary pressure and relative permeability should be approximately known. Alternatively, if an oil-base mud invades an oil reservoir, an estimate of the anisotropic diffusion coefficients that control concentration changes of the fluids should be available. Thus, clear differences are associated with the immiscible or miscible nature of the flow. The role of a job planning simulator is crucial in permeability interpretation and fluid sampling.

In pressure interpretation, the pressure sensed by the tester probe represents formation effects only if the borehole wall is perfectly sealed by mudcake. However, this is never the case: the probe also senses the high pressure associated with the well. This supercharging of the formation may lead to erroneously high pore pressure predictions and incorrect permeabilities. The simulator is used to determine how much of the measured pressure is pertinent to actual formation evaluation and determines the true permeability associated with this pressure level.

In the fluid sampling application, the simulator is used to determine what percentage of the collected fluid represents uncontaminated fluid. Clearly, the longer the formation is pumped, the cleaner will be the fluid. However, it is also conceivable that an uncontaminated sample is never possible, e.g., if mudcake never builds to sufficient thickness or if it is not impermeable enough. For such problems, the role of the job planning simulator is invaluable. In both immiscible and immiscible problems, the dynamic coupling between growing mudcake and reservoir flow is important.

We emphasize the differences between the present work and the comprehensive model in Proett, Chin and Mandal (2000). That paper provided an exact, closed form, analytical solution to a formulation where the tester is modeled as non-zero radius source surface, that is, a spherical well in an isotropic formation and an ellipsoidal one in anisotropic media. Flowline storage, skin effects and general pumpout rates were permitted. However, a single phase fluid was assumed, so that contamination studies were not supported. Thus, while the results were “exact” in a mathematical sense, they are not completely descriptive of the actual downhole physics.

Furthermore, supercharging was not considered because a cylindrical borehole allowing invasion was not modeled. But the results are useful in pressure transient analyses and for providing permeability estimates. The earlier work, because it does not allow borehole invasion, is more applicable to wireline formation testing where the mudcake has sealed the sandface. The present model, because it permits borehole invasion, is applicable to both wireline and formation-testing-while-drilling (or, "FTWD") applications.

6.1.3 Modeling challenges

So far, we have spoken only qualitatively about overall fluid movement and mudcake growth. But, within the reservoir itself, predicting fluid species redistribution is complicated to the extent that different physical mechanisms are at work. In elementary single-phase flows, a single pressure differential equation applies – for example, the classical Laplace and heat equations apply in isotropic formations.

However, in immiscible flows, the pressure field associated with Darcy's law depends on relative permeabilities and capillary pressures which vary as local water saturation changes – pressure and saturation fields are governed by nonlinearly coupled PDEs. In miscible flows, relative concentrations vary with space and time and affect local fluid viscosity – the viscosity is controlled by a mixing law that depends on local concentrations. The governing pressure equation is dynamically coupled to an equation for concentration – one that is controlled by both by anisotropic diffusion and Darcy velocity convection.

Not only are the differential equations difficult to solve. The geometry of the flow domain affects the outcome of all job planning recommendations. We have assumed an axisymmetric flow – valid for vertical wells only – and noted the cylindrical nature of the problem. But this is only true initially. When the tester starts pumping, significant geometric changes are found locally at the probe – our model accounts for cylindrical flows with embedded ellipsoidal source zones. That is, the local probe flow is spherical or ellipsoidal accordingly as the problem is isotropic or anisotropic. In problems with borehole invasion, the tester's probe nozzle – modeled here as a ring source (as explained in Chapter 1) that admits flow from all directions – induces a complicated three-dimensional streamline pattern which is nonlinearly superposed over the supercharging cylindrical flow. As general as this may seem, the model in Figure 6.1 does not apply to deviated and horizontal wells, which introduce additional complications. For example, consider a formation with $k_h >> k_v$. In a vertical well, the tool would "see" a high k_h from all directions, so that the pressure drop for a prescribed pumping rate is low. In a horizontal well, for the same pumping rate, a tool situated far from any shales would see both k_h and the smaller k_v, and the resulting pressure drop is higher.

In a deviated well, of course, the pressure drop will fall somewhere between the vertical and horizontal well extremes. And when shale boundaries are close to the probe, sizable interference effects are anticipated. Precise geometric modeling of borehole, shale and nozzle boundary shapes is necessary – for such problems, even the simplest fluid flow models are 3D.

6.1.4 Simulation objectives

We return to the problem in Figure 6.1. Because the flow is axisymmetric, that is, two-dimensional – it can be described by radial and vertical coordinates r and z since azimuthal variations around the well do not exist. Then, whether the flow is immiscible or miscible, we focus on two output fields at any given instant in time – the pressure distribution in the r-z plane and its complementary contamination profile as in Figure 6.2.

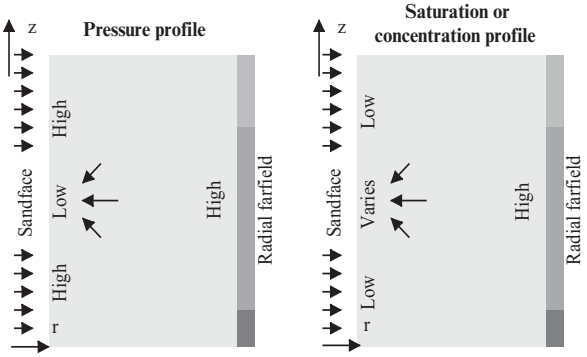

Figure 6.2. Pressure and contamination profiles in r-z plane.

Our simulations produce detailed color plots as suggested by Figure 6.2. The pressure diagram shows low pressure at the probe, assumed to be withdrawing formation fluid; at the same time, high supercharge pressure due to invading mud are found at either sides of the probe. Not shown are streamline reversals associated with the contaminant flow: fluid that invades the formation must turn and eventually enter the probe.

The contaminant diagram at the right of Figure 6.2 emphasizes, again for the three-layer formation assumed in our analysis, that high values of oil saturation are found in the radial farfield for immiscible flows – with high formation fluid concentrations in the case of miscible flows. At the sandface, low levels are identified with areas exposed to the mudcake. At the probe, saturations and concentrations are low initially and hopefully high eventually – however, there is no guarantee that uncontaminated samples are always or even sometimes possible. In the presence of substantial invasion, clean samples may be impossible to obtain regardless of pumping time.

Job planning simulators help to maximize sample quality by suggesting optimal mud parameters and pump rates and schedules. Thus, in addition to Figure 6.2, a line plot such as that suggested by Figure 6.3 is also important to job planning. By "sample quality," we mean oil saturation in the case of water-base muds invading oil formations, and formation fluid concentration when oil-base muds invade oil formations. The petrophysicist and drilling engineer both require the time t^* at which sample quality becomes acceptable, e.g., 90% to 95%, as suggested by the solid line. However, as noted, it is also possible that sample quality remains poor for a given set of mud, reservoir fluid, and formation and tool parameters – in this case, the job planning simulator might be used to identify positive changes that might be effected by using heavier mud and different pumping rates. Complementary to Figure 6.3 would be the pressure drawdown and buildup curve needed for permeability and anisotropy interpretation.

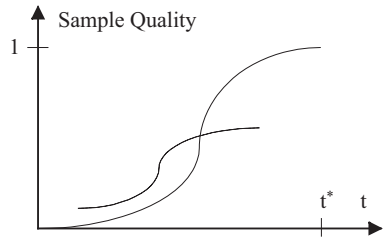

Figure 6.3. Sample quality versus time.

6.1.5 Modeling overview

With our physical explanations complete, we next summarize the mathematical and algorithmic formulations used in developing our immiscible and miscible flow simulators. Our exposition focuses on how different computational methodologies and physical models have been combined to provide unique capabilities important to formation testing job planning. The reservoir engineering fundamentals presented here, by necessity, are brief; however, for more detailed explanations, especially with regard to numerical modeling, the reader is referred to Peaceman (1977), Aziz and Settari (1979) and Chin (2002). The plan for this section is as follows – we begin with a summary of the mathematical formulation.

First, the partial differential equation (PDEs) for immiscible two-phase flow are derived, emphasizing in particular the compressibility of both fluid phases; the equations, therefore, allow us to study both mixing effects and pressure transient interpretation with a single self-consistent physical model. Second, finite difference modeling and advanced "alternating-direction-implicit" (ADI) methods are introduced, which allow rapid, robust and convenient simulation capabilities at rigsites and field offices using standard personal

computers. Third, boundary conditions describing (i) mudcake growth and dynamic coupling with the reservoir, (ii) pumpout modeling with flowline storage and skin damage, and (iii) dual probe and straddle packer source logic, are derived. This work is followed by extensions to miscible flow analysis, in which original viscosities no longer retain their identity: pressure and fluid concentration fields are coupled by a mixing law satisfied by the evolving viscosity distribution. Following our discussions on math and numerical formulation, we summarize software features deemed essential to successful use of the job planning simulator in field applications. Finally, representative calculations are presented that demonstrate operational usage of the software – these include a gamut of rigsite interpretation and job planning functions. The simulator developed here will be used to support a number of new formation evaluation endeavors, which will be introduced in our concluding remarks.

6.2 Immiscible Flow Formulation

In this section, a concise summary for partial differential equation development, boundary condition modeling and numerical solution methods is offered. Also offered are suggested references for readers interested in additional details. Let r and z denote the (horizontal) radial and vertical coordinates, and k_{rw}, k_{rn}, k_{zw} and k_{zn} represent r-wetting, r-nonwetting, z-wetting and z-nonwetting permeabilities, respectively. If $K_r(r,z)$ and $K_z(r,z)$ are absolute permeabilities in the r and z directions, and k_w and k_n are wetting and nonwetting relative permeabilities expressed as functions of the water saturation S_w, we can write $k_{rw} = K_r\, k_w(S_w)$, $k_{rn} = K_r\, k_n(S_w)$, $k_{zw} = K_z\, k_w(S_w)$ and $k_{zn} = K_z\, k_n(S_w)$.

The Darcy formulas for momentum conservation at low Reynolds numbers are $v_{zw} = -(k_{zw}/\mu_w)(\partial p_w/\partial z + \rho_w g)$, $v_{zn} = -(k_{zn}/\mu_n)(\partial p_n/\partial z + \rho_n g)$, $v_{rw} = -(k_{rw}/\mu_w)\,\partial p_w/\partial r$ and $v_{rn} = -(k_{rn}/\mu_n)\,\partial p_n/\partial r$. Here, p, ρ and μ represent pressure, density and viscosity, respectively, with g being the acceleration due to gravity. In reservoir flow, it is convenient to introduce the functions $f(S_w) = (k_w/\mu_w)/(k_w/\mu_w + k_n/\mu_n)$ and $h(S_w) = (k_w/\mu_w)(k_n/\mu_n)/(k_w/\mu_w + k_n/\mu_n)$. The pressures $p_w(r,z,t)$ and $p_n(r,z,t)$ of the wetting and non-wetting phases are often not directly used. They are replaced by an alternative pair, the capillary pressure $p_c = p_n - p_w$ and the average pressure $p_{avg} = \frac{1}{2}(p_n + p_w)$. Figure 6.4 gives typical immiscible flow properties, showing that $dp_c(S_w)/dS_w < 0$ and $df/dS_w > 0$. We further assume that $p_{avg} >> p_c$.

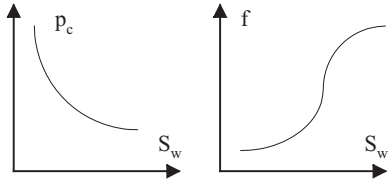

Figure 6.4. Typical immiscible flow functions.

In immiscible flow, two saturations exist, a water saturation $S_w(r,z,t)$ and an oil saturation $S_o(r,z,t)$, whose values are connected by $S_w + S_n = 1$. When volume changes are important, as in pressure transient analysis, fluid compressibilities c_w and c_n are required in addition to the properties previously introduced. Analysis of the governing equations shows that these act in concert through the "total compressibility" defined here by $c_t = \phi^{-1}\, d\phi/dp_{avg} + c_w S_w + c_n S_n$. This represents the expected saturation-weighted compressibility, corrected by a compaction term in which changes to the porosity ϕ with pressure are accounted for.

Pressure transients and saturation or concentration changes operate on different time scales, e.g., shapes of drawdown-buildup pressure curves depend mostly on compressibility, while times needed for uncontaminated samples depend mostly on relative permeabilities, capillary pressures and diffusion coefficients. Under the assumptions stated, the partial differential equations that follow from mass conservation for average pressure and water saturation are, namely,

$$\begin{aligned} &\partial[(k_{zn}/\mu_n + k_{zw}/\mu_w)\,\partial p_{avg}/\partial z]/\partial z \\ &+\partial[(k_{rn}/\mu_n + k_{rw}/\mu_w)\,\partial p_{avg}/\partial r]/\partial r \\ &+r^{-1}\,(k_{rn}/\mu_n + k_{rw}/\mu_w)\,\partial p_{avg}/\partial r = \\ &=\phi c_t\,\partial p_{avg}/\partial t - g\,\partial\{\rho_n k_{zn}/\mu_n + \rho_w k_{zw}/\mu_w\}/\partial z \end{aligned} \tag{6.1}$$

$$\begin{aligned} &\phi\,\partial S_w/\partial t + v_{zt} f'\partial S_w/\partial z + v_{rt} f'\partial S_w/\partial r = \\ &-K_z h P_c'\partial^2 S_w/\partial z^2 - K_r h P_c'\partial^2 S_w/\partial r^2 \\ &-\partial(K_z h P_c')/\partial z\,\partial S_w/\partial z - \partial(K_r h P_c')/\partial r\,\partial S_w/\partial r \\ &-r^{-1} K_r h P_c'\,\partial S_w/\partial r \\ &-\partial[g K_z h(\rho_n - \rho_w)]/\partial z + \phi c_t f\,\partial p_{avg}/\partial t \end{aligned} \tag{6.2}$$

where $v_{zt} = -(k_{zn}/\mu_n + k_{zw}/\mu_w)\,\partial p_{avg}/\partial z - (\rho_n k_{zn}/\mu_n + \rho_w k_{zw}/\mu_w)\,g$, $v_{rt} = -(k_{rn}/\mu_n + k_{rw}/\mu_w)\,\partial p_{avg}/\partial r$ and (') primes denote ordinary derivatives with respect to S_w.

6.2.1 Finite difference solution

Equations 6.1 and 6.2 are partial differential equations: they are coupled, multidimensional, nonlinear and time-dependent – and difficult to solve. Analytical methods are not applicable, and numerical methods, e.g., finite element, finite volume or finite difference, must be used. We focus, in this paper, on the latter methods. Finite difference methods are easily summarized. Consider the heat equation $v_t(x,t) = v_{xx} + v_{yy}$. It is convenient to introduce discretized spatial meshes, say "$x_1, x_2, x_3 \ldots x_{imax}$" representing x and "$y_1, y_2 \ldots y_{jmax}$" representing y, and correspondingly, "$t^1, t^2, t^3 \ldots t^{nmax}$" for time. The value of v for any $x = x_i$ and $y = y_j$ at time $t = t^n$ is denoted by $v^n_{i,j}$. If x, y and t discretizations are separated by constant values Δx, Δy and Δt, respectively, the value of, say, v_{xx} at (x_i,y_j,t^n), for instance, is given by the central difference operation $v_{xx}|^n_{i,j} = (v^n_{i-1,j} - 2v^n_{i,j} + v^n_{i+1,j})/\Delta x^2$.

Now, how might such discretizations be employed in solving the heat equation? At any (x_i,y_j,t^{n+1}), this partial differential equation might be approximated by $(v^{n+1}_{i,j} - v^n_{i,j})/\Delta t = (v^n_{i-1,j} - 2v^n_{i,j} + v^n_{i+1,j})/\Delta x^2 + (v^n_{i,j-1} - 2v^n_{i,j} + v^n_{i,j+1})/\Delta y^2$. This can be solved simply and explicitly as "$v^{n+1}_{i,j} = \ldots$" where all right-side terms are evaluated at the previous n^{th} time step. Starting with

suitable initial conditions, the overall solution can be advanced in time at each point in space without matrix solution. This "explicit" method, while conveniently programmed, is numerically unstable and not often used.

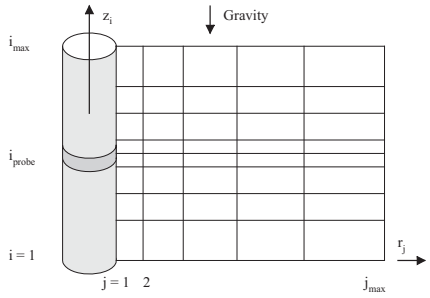

Figure 6.5. Variable finite difference grid.

On the other hand, if we assumed $(v^{n+1}_{i,j} - v^{n}_{i,j})/\Delta t = (v^{n+1}_{i-1,j} - 2v^{n+1}_{i,j} + v^{n+1}_{i+1,j})/\Delta x^2 + (v^{n+1}_{i,j-1} - 2v^{n+1}_{i,j} + v^{n+1}_{i,j+1})/\Delta y^2$ and evaluated this finite difference approximation at all points in the computational domain, it is clear that all the unknowns will be coupled by simultaneous equations. The resulting "implicit" method, because the coefficient matrix is not sparse, requires extensive computational resources for matrix inversion – especially since the inversion must be performed at each time step. However, the method is useful because it is stable: larger time steps can be used and these allow rapid practical solutions.

6.2.2 Formation tester application

The problem solving Equations 6.1 and 6.2 requires resources so significant that classical implicit methods are impractical. Thus, we turn to implicit methods known as "alternating-direction-implicit" schemes. While the previous scheme leads to dense matrixes, ADI methods make use of much simpler matrixes that can be quickly inverted. These are discussed in Peaceman and Rachford (1962) for rectangular flow domains – the model of Chow, Ho and Fong (1997) for axisymmetric problems is identical to that used here.

Consider Equation 6.1 in the form $\partial p/\partial t = \partial(\alpha\, \partial p/\partial z)/\partial z + \partial(\beta\, \partial p/\partial r)/\partial r + \beta/r\, \partial p/\partial r + G$. In addition to two time levels "n" and "n+1," an intermediate time level t^* halfway between t^n and t^{n+1} is introduced. Equation 6.3 advances "n" level values to "*," while Equation 6.4 advances "*" level values to "n+1."

$$(p^{*}_{i,j} - p^{n}_{i,j})/(\Delta t/2) = \partial(\alpha\, \partial p^{*}/\partial z)/\partial z + \partial(\beta\, \partial p^{n}/\partial r)/\partial r + \beta/r\, \partial p^{n}/\partial r + G^{n} \quad (6.3)$$

$$(p^{n+1}_{i,j} - p^{*}_{i,j})/(\Delta t/2) = \partial(\alpha\, \partial p^{*}/\partial z)/\partial z + \partial(\beta\, \partial p^{n+1}/\partial r)/\partial r + \beta/r\, \partial p^{n+1}/\partial r \quad (6.4)$$

To see that this sequence is self-consistent, simply add the two equations to obtain $(p^{n+1}_{i,j} - p^{n}_{i,j})/\Delta t = \partial(\alpha\, \partial p^{*}/\partial z)/\partial z + \partial(\beta\, \partial\, ½(p^{n} + p^{n+1})/\partial r)/\partial r + \beta/r\, \partial\, ½(p^{n} + p^{n+1})/\partial r + G^{n}$. Since $p^{*} = ½\,(p^{n} + p^{n+1})$, this is just the 2nd order accurate approximation to the partial differential equation.

Radial sweep

$$
\begin{aligned}
& [(\alpha_{i-1} + \alpha_i)/\{(z_i - z_{i-1})(z_{i+1} - z_{i-1})\}]\; p^{*}_{i-1,j} \\
- \; & [(\alpha_{i-1} + \alpha_i)/\{(z_i - z_{i-1})(z_{i+1} - z_{i-1})\} + (\alpha_i + \alpha_{i+1})/ \\
& \{(z_{i+1} - z_i)(z_{i+1} - z_{i-1})\} + 2/\Delta t]\; p^{*}_{i,j} \\
+ \; & [(\alpha_i + \alpha_{i+1})/\{(z_{i+1} - z_i)(z_{i+1} - z_{i-1})\}]\; p^{*}_{i+1,j} = \\
= & -2\, p^{n}_{i,j}/\Delta t - (\beta_j/r_j)\,(p^{n}_{i,j+1} - p^{n}_{i,j-1})/(r_{j+1} - r_{j-1}) + G^{n} \\
- \; & (\beta_j + \beta_{j+1})(p^{n}_{i,j+1} - p^{n}_{i,j})/\{(r_{j+1} - r_j)(r_{j+1} - r_{j-1})\} \\
+ \; & (\beta_{j-1} + \beta_j)(p^{n}_{i,j} - p^{n}_{i,j-1})/\{(r_j - r_{j-1})(r_{j+1} - r_{j-1})\}
\end{aligned}
\tag{6.5}
$$

Vertical sweep

$$
\begin{aligned}
& [(\beta_{j-1} + \beta_j)/\{(r_j - r_{j-1})(r_{j+1} - r_{j-1})\} \\
- \; & \beta_j/\{r_j(r_{j+1} - r_{j-1})\}\; p^{n+1}_{i,j-1} \\
- \; & [(\beta_{j-1} + \beta_j)/\{(r_j - r_{j-1})(r_{j+1} - r_{j-1})\} \\
+ \; & (\beta_j + \beta_{j+1})/\{(r_{j+1} - r_j)(r_{j+1} - r_{j-1})\} + 2/\Delta t\,]\; p^{n+1}_{i,j} \\
+ \; & [\,(\beta_j + \beta_{j+1})/\{(r_{j+1} - r_j)(r_{j+1} - r_{j-1})\} + \beta_j/\{r_j(r_{j+1} - r_{j-1})\}]\; p^{n+1}_{i,j+1} \\
= & -2\, p^{*}_{i,j}/\Delta t - (\alpha_i + \alpha_{i+1})(p^{*}_{i+1,j} - p^{*}_{i,j})/\{(z_{i+1} - z_i)(z_{i+1} - z_{i-1})\} \\
+ \; & (\alpha_{i-1} + \alpha_i)(p^{*}_{i,j} - p^{*}_{i-1,j})/\{(z_i - z_{i-1})(z_{i+1} - z_{i-1})\}
\end{aligned}
\tag{6.6}
$$

The advantages offered by Equations 6.3 and 6.4 are more clearly seen if we expand the right sides using the central difference operator used previously, leading to Equations 6.5 and 6.6. Let us suppose that starting initial conditions for p(r,z,0) are available. To advance the solution a single time step Δt, Equation 6.5 is "swept" once across the computational box in Figure 6.5.

Specifically, the far left value "j" is fixed and Equation 6.5 is written for all internal "i" nodal values. The resulting equations, supplemented by boundary conditions at the top and bottom, are solved. This procedure is repeated recursively for higher values of "j" to the right, until an entire "radial sweep" is completed. This is followed by a similar "vertical sweep" using Equation 6.6, supplemented by boundary conditions at the left and right. When both sweeps are completed, the spatial pressure solution has been incremented one step in time – numerous multiple steps, of course, are needed to simulate the pumping process and the diffusion of pressure signals from source to observation probes.

Careful examination of Equations 6.5 and 6.6 shows that the equations are "tridiagonal" in form, that is, the coefficient matrices contain but three diagonals, allowing rapid inversion. Moreover, the matrices are "diagonally dominant" – the higher magnitude of the center relative to the side terms along each row promotes numerical stability and leads to robust computations. In summary, ADI integrations are rapid, robust, easily programmed and maintained. Again, our problem is immiscible, involving coupled pressure and saturation fields. The coefficients of Equation 6.1 for $p_{avg}(r,z,t)$ are evaluated using latest available values of S_w and *implicit* ADI integrations are used to update average pressures everywhere. Once these are obtained, they are used to evaluate the coefficients of the saturation model in Equation 6.2.

The equation for S_w is solved using the *explicit* method described earlier (S_w is applied away from the probe, while $\partial S_w/\partial r = 0$ applies at the probe, at the sandface). For this reason, our approach is an "implicit pressure – explicit saturation" or "IMPES" method. This is used in many reservoir flow simulators and provides a cost-effective alternative to fully implicit methods. We have completed our discussion of PDEs and their solution methods. We now turn to the boundary conditions that constrain the problem. These are several in variety, namely, initial conditions (already described physically), farfield conditions (fixed pore pressure and specified fluid saturation or concentration), pressure and velocity continuity at layer interfaces – plus key models that we describe in greater detail next. These involve, specifically, (i) mudcake growth and dynamic coupling to tight formations, (ii) flowrate modeling including flowline storage and skin effects for single-probe tools, and (iii) subtleties related to dual probe and straddle packer modeling.

6.2.3 Mudcake growth and formation coupling at sandface

Proper modeling of mud invasion at the borehole wall is critical: its high pressures mask true formation pressure and also contaminate the fluid pumped by the tester probe. Accurate supercharge modeling and forward simulation is important to pore pressure and permeability prediction. Catscan experiments were reported in Chin *et al* (1986) in which quantitative measurements were made of mudcake thickness and invasion front displacement in linear and radial core samples. Typical results are shown in Figure 6.6. Consider, for example, the bottom right photo taken at large times relative to that at the top left. The fluid moves from left to right. It deposits a (black) mudcake at the surface of the linear core, positioned near the middle of the photograph. To the right of the mudcake, the light colored filtrate is seen to displace the darker fluid originally present in the sample.

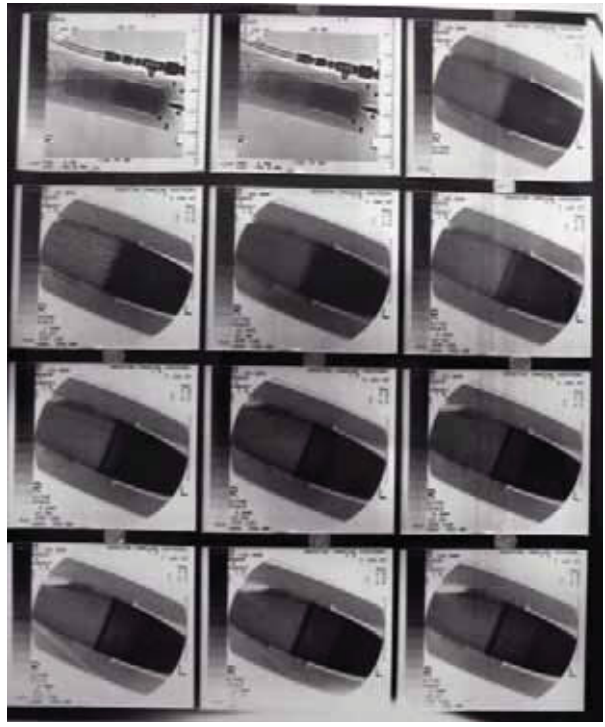

Figure 6.6. Catscans showing cake growth in time.

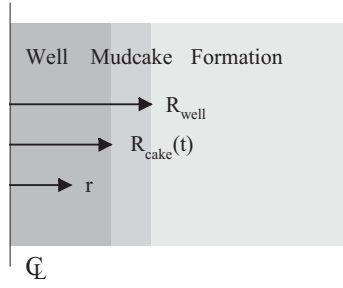

Figure 6.7. Cylindrical radial interfaces.

The results of detailed linear and radial flow experiments led to the mudcake model in Chin (1995, 2002) used here. In immiscible flow, radial velocity matching at the cake and formation interface is approximated by $(k_{cake}/\mu_{bh})\ \partial p/\partial r\ |_{cake} \approx \{k_{rw}(S_w)/\mu_w + k_{rn}(S_w)/\mu_n\}\ \partial p_{avg}/\partial r$ if capillary pressure is neglected – in miscible flows, the right curly { } bracket is replaced by the rock mobility at the sandface as viscosity is affected by concentration changes. This

boundary condition allows fluid responsible for solids deposition in the cake to invade and supercharge the formation. We assume that mudcake thickness is thin compared with the borehole radius so that a linear growth model applies. Thus, the radial pressure gradient satisfies $\partial p/\partial r\ |_{cake} \approx \{p_{mud} - p_{avg}(z,R_{well},t)\}/(R_{cake} - R_{well})$, where R_{cake} and R_{well} are radial values at the cake-mud interface and the sandface, with $R_{cake}(t)$ decreasing continually with time as the mudcake thickens.

The "$dx_c/dt = -\{f_s/[(1 - f_s)(1 - \phi_c)]\}\ |v_n|$" dynamic mudcake growth model in Chin (1995) relates the rate of thickness increase to the solid fraction f_s, the porosity ϕ_c and normal fluid velocity v_n. In radial single phase flow, this translates to $R_{well} - R_{cake} = \{f_s\ \Delta t/[(1 - f_s)(1 - \phi_c)]\}\ (k_{cake}/\mu_{bh})(p^n_{i,1} - p_{mud})/(R_{well} - R_{cake})$. A limiting value of "$R_{well} - R_{cake}$" is applied, i.e., an equilibrium thickness no larger than 0.2 inches, to model the erosive effects of dynamic filtration (see Figures 6.5 and 6.7 for nomenclature). This cake model is used to evaluate the radial velocity matching condition

$$\{(k_{cake}/\mu_{bh})(R_2 - R_{well})/[(k_{rw}(S_w)/\mu_w + k_{rn}(S_w)/\mu_n)_{j=1}(R_{well} - R_{cake})]\}\ (p_{i,1} - p_{mud}) = p_{i,2} - p_{i,1} \tag{6.7}$$

rewritten for two-phase flow. Two forms are required for ADI implementation since different matrix structures are obtained in radial versus vertical sweeps. In the first, we have $[1 + \{\}]\ p_{i,1} - p_{i,2} = \{\}\ p_{mud}$ – in the second, $p_{i,1} = [p_{i,2} + \{\}\ p_{mud}]/[1 + \{\}]$. These reduce to $p_{i,1} = p_{i,2}$ if $\{\} = 0$, applicable when $k_{cake} = 0$ for a perfectly sealed borehole. On the other hand, we obtain $p_{i,1} = p_{mud}$ if $\{\} \to \infty$. This limit applies to $k_{cake} >> k_n$ and k_w – that is, a mudcake does not exist, with the formation undergoing massive invasion.

6.2.4 Pumpout model for single-probe pad nozzles

In simple pumping without flowline storage and skin effects, we write $(Ak/\mu)\ \partial p/\partial r = Q$ where A is the cross-sectional probe area exposed to the flow, k is the permeability, μ is the viscosity and Q is the volume flow rate. Since $\partial p/\partial r = (p_2 - p_1)/(R_2 - R_1)$, the probe pressure update formula is $p_1 = p_2 - Q\mu(R_2 - R_1)/(Ak)$. The formula for ellipsoidal sources in infinite uniform media is given in Proett, Chin and Mandal (2000) and used to derive exact solutions for pressure transient analysis. As noted, the earlier work does not model cylindrical supercharging invasion. When simultaneous invasion at the borehole is important, cylindrical coordinates must be used. Detailed three-dimensional finite element analysis shows that a ring source model of the tester probe is appropriate, providing the required axisymmetry and allowing both vertical and radial fluid movement toward the probe (see Chapter 1).

The single phase extension to "$(Ak/\mu)\ \partial p/\partial r = Q$" is $(Ak/\mu)\ \partial p/\partial r - VC\ \partial p/\partial t + VCSR_{well}\ \partial^2 p/\partial r\partial t = Q(t)$. This can be discretized in the form

$$p^n_{iprobe,1} = \{1 + \mu VCSR_{well}/(Ak\Delta t)\}\ p^n_{iprobe,2}/ \qquad (6.8)$$
$$\{1 + \mu VC\Delta R/(Ak\Delta t) + \mu VCSR_{well}/(Ak\Delta t)\}$$
$$+\ \{-\mu Q_n \Delta R/(Ak) + \mu VC\Delta R p^{n-1}_{iprobe,1}/$$
$$(Ak\Delta t) - \mu VCSR_{well}(p^{n-1}_{iprobe,2} - p^{n-1}_{iprobe,1})\}$$
$$/\{1 + \mu VC\Delta R/(Ak\Delta t) + \mu VCSR_{well}/(Ak\Delta t)\}$$

where $\Delta R = R_2 - R_{well}$, $R_1 = R_{well}$, A is the source surface area, k is the radial permeability associated with the velocity entering the probe, S is the skin factor, V is flowline volume and C is flowline compressibility. In miscible flow, the viscosity is a time-dependent function of concentration. In immiscible flow, "k/μ" is replaced by "$\{k_{rw}(S_w)/\mu_w + k_{rn}(S_w)/\mu_n\}_{j=1}$." This boundary condition is applied at the single area element representing the nozzle. All of the above terms contain the flowline storage parameter "VC" with the exception of "$\mu Q_n \Delta R/(Ak)$." When this term is small, e.g., for large permeabilities or small volume flow rates, this pumpout boundary condition and computed results can be controlled by flowline storage noise.

6.2.5 Dual probe and packer surface logic

We have given pumpout boundary conditions for single-probe pad nozzles requiring only a single area element representation. For such probes, a simple balance between Darcy flow, flowline volume expansion, skin resistance and total flow rate suffices. But other nozzles are used in tester operations. For example, dual probes are used to increase pumping efficiency and reduce pumpout times, while straddle packer nozzles are used in unconsolidated and naturally fractured formations to enhance fluid withdrawal. Both are shown in Figure 6.8 acting in a multilayered formation.

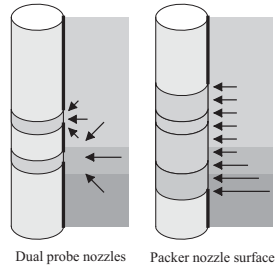

Figure 6.8. Dual probe and straddle packer models.

There are important physical differences between the single-probe pumpout model and the one required here. For dual probes and packers, multiple source (or sink) elements are open to the *same* pressure reservoir. Only the total volume flow rate can be controlled – thus, because each element may "see" different layer permeabilities, the velocity at each element is generally different. This is shown conceptually in Figure 8 where different size velocity vectors are used. In the context of packer modeling, the "uniform flux" model used by other investigators is incorrect. We have explained why this is so in layered media. However, it is wrong even in uniform media. Chin (1993, 2002) demonstrates analytically, using exact singular integral equation methods for steady flows, that velocities are in fact singular at the ends of line point source distributions with prescribed constant pressures – also, velocities along the source distribution are variable.

The correct boundary condition formulation is easily stated: total volume flow rate is specified subject to the condition that pressures are same among all surface elements – this pressure, itself an unknown, will vary with time in a manner consistent with flowline storage and skin effects. The arguments for this rule were given in Chin (1993, 2002) in the context of horizontal and multilateral well modeling and apply here. The left diagram of Figure 6.8 shows how different pump rates will be found at the dual probes of a formation tester residing across different layers. Measured differences in volume flow rate – interpreted using numerical fluid flow models – can be used to infer contrasts in interlayer permeability.

Now we formulate the boundary condition for the entire dual probe array and packer surface. For brevity, we give the skin-free derivation. Only the radial permeability (denoted "k^r") contributes to fluid influx. The volume flux is the product of the Darcy velocity $(k^r/\mu)_{source}\ \partial p/\partial r_{\ source}$ and the cylindrical area element A. Now, the first term on the left of $\Sigma\ A_i(k^r_{i,1}/\mu)(p^n_{i,2} - p^n_{i,1})/\Delta R - VC\ (p^n_{pk} - p^{n-1}_{pk})/\Delta t = Q(t_n) = Q_n$ represents the sum of all surface source point contributions where "i" is the vertical index. The "VC" term describes storage effects, Q is the total volume flow rate, while the "pk" subscript refers to packer and dual probe pressures. Note that $p^n_{i,1}$ is equal to p^n_{pk}, a (time-dependent) hydrostatic pressure which does not depend on position. Thus, we solve for p^n_{pk} explicitly to find

$$p^n_{pk} = \{- Q_n + VCp^{n-1}_{pk}/\Delta t \qquad (6.9)$$
$$+\ \ \Sigma(A_i k^r_{i,1} p^n_{i,2}/(\mu\Delta R)\}\ /\{VC/\Delta t + \Sigma A_i k^r_{i,1}/(\mu\Delta R)\}$$

where $\Delta R = r_2 - r_1$, which applies to a full time step $\Delta t = t_n - t_{n-1}$. In our ADI implementation, sweeps are taken from t^{n-1} to t^* and t^* to t^n – this boundary condition is rewritten for each sweep with Δt replaced by $\Delta t/2$. Equation 6.9 applies to single-phase flow. The required changes for immiscible and miscible flow noted for single-probe problems also apply here.

6.3 Miscible Flow Formulation

So far, we have discussed the pressure partial differential equation for immiscible flow and its coupled solution with water saturation. The boundary condition derivations given above also apply to miscible flows. We therefore complete our discussion by focusing on the governing equations for miscible flow. Let us introduce $\alpha = k_z /(\phi\mu c)$ and $\beta = k_r /(\phi\mu c)$, where $k_z(r,z)$ and $k_r(r,z)$ are absolute vertical and radial permeabilities, $\phi(r,z)$ is porosity, and $c(r,z,t)$ and μ are fluid compressibility and viscosity. The governing pressure equation for Darcy flow is $\partial p/\partial t = \partial(\alpha\, \partial p/\partial z)/\partial z + \partial(\beta\, \partial p/\partial r)/\partial r + \beta/r\, \partial p/\partial r$. This is identical in form to the equation for immiscible flow, so that the same ADI algorithm and software can be used. But there is one crucial difference. The viscosity $\mu(r,z,t)$ of the miscibly mixed fluid varies with space and time. It is here assumed to depend on the empirical Todd and Longstaff (1972) viscosity mixing model

$$\mu = \mu_{mud}\mu_{formation}/(C\mu_{mud}^{1/4} + (1 - C)\mu_{formation}^{1/4})^4 \qquad (6.10)$$

where $C(r,z,t)$ is formation fluid concentration in rock pore spaces. If mud never invades the reservoir, C remains at unity and $\mu = \mu_{formation}$ – but if mud completely displaces formation fluid, then $C = 0$ and $\mu = \mu_{mud}$. In our work, "1/4" and "4" are actually replaced with the more flexible "1/n" and "n."

Like Darcy pressure, concentration is also diffusive – but it satisfies a model more complicated than the heat equation. In sedimentary formations, anisotropic diffusion coefficients ε_z and ε_r in the vertical and radial directions apply, whose values depend on the pore structure of the rock formation. In addition to diffusion, fluid is convected by the local velocities $v_z = -(k_z /\mu)\, \partial p/\partial z$ and $v_r = -(k_r /\mu)\, \partial p/\partial r$. In cylindrical radial coordinates, concentration $C(r,z,t)$ varies like

$$\phi\, \partial C/\partial t + v_z\, \partial C/\partial z + v_r\, \partial C/\partial r \qquad (6.11)$$
$$= \varepsilon_z\, \partial^2 C/\partial z^2 + \varepsilon_r\, (\partial^2 C/\partial r^2 + r^{-1}\, \partial C/\partial r)$$

as shown in Chin (1995). Both pressure and concentration equations are coupled – they are solved subject to the supercharging invasion equations, the pad or packer pumping model, and the farfield and matching auxiliary conditions previously discussed. As with the pressure equation, an ADI procedure is used to solve for the concentration $C(r,z,t)$. In particular, corresponding to Equations 6.3 and 6.4, we now have Equations 6.12 and 6.13, which are differenced as shown in Equations 6.14 and 6.15. Equation 6.11 is solved with C applied away from the probe and $\partial C/\partial r = 0$ at the probe along the sandface. The sweeping processes described earlier apply here.

$$(C^{*}_{i,j} - C^{n}_{i,j})/(\Delta t/2) = (\varepsilon_z/\phi)\,\delta_z^2 C^{*}_{i,j} - (v_z/\phi)\delta_z C^{*}_{i,j} + (\varepsilon_r/\phi)\delta_r^2 C^{n}_{i,j} - (v_r/\phi - \varepsilon_r/(\phi r_j))\delta_r C^{n}_{i,j} \tag{6.12}$$

$$(C^{n+1}_{i,j} - C^{*}_{i,j})/(\Delta t/2) = (\varepsilon_z/\phi)\delta_z^2 C^{*}_{i,j} - (v_z/\phi)\delta_z C^{*}_{i,j} + (\varepsilon_r/\phi)\delta_r^2 C^{n+1}_{i,j} - (v_r/\phi - \varepsilon_r/(\phi r_j))\delta_r C^{n+1}_{i,j} \tag{6.13}$$

Radial sweep

$$\begin{aligned}
&[(2\varepsilon_z/\phi)/\{(z_i - z_{i-1})(z_{i+1} - z_{i-1})\} + (v_z/\phi)/(z_{i+1} - z_{i-1})]\, C^{*}_{i-1,j} \\
&[-(2\varepsilon_z/\phi)\,[1/\{(z_i - z_{i-1})(z_{i+1} - z_{i-1})\} \\
+\;& 1/\{(z_{i+1} - z_i)(z_{i+1} - z_{i-1})\}] - 2/\Delta t]\, C^{*}_{i,j} \\
+\;& [(2\varepsilon_z/\phi)/\{(z_{i+1} - z_i)(z_{i+1} - z_{i-1})\} - (v_z/\phi)/(z_{i+1} - z_{i-1})]\, C^{*}_{i+1,j} = \\
=\;& -2\, C^{n}_{i,j}/\Delta t + (v_r/\phi - \varepsilon_r/(\phi r_j))(C^{n}_{i,j+1} - C^{n}_{i,j-1})/(r_{j+1} - r_{j-1}) \\
-\;& (2\varepsilon_r/\phi)[C^{n}_{i,j-1}/\{(r_j - r_{j-1})(r_{j+1} - r_{j-1})\} + C^{n}_{i,j+1}/\{(r_{j+1} - r_j)(r_{j+1} - r_{j-1})\} \\
-\;& C^{n}_{i,j}\,\{1/\{(r_j - r_{j-1})(r_{j+1} - r_{j-1})\} + 1/\{(r_{j+1} - r_j)(r_{j+1} - r_{j-1})\}\}]
\end{aligned} \tag{6.14}$$

Vertical sweep

$$\begin{aligned}
&[(2\varepsilon_r/\phi)/\{(r_j - r_{j-1})(r_{j+1} - r_{j-1})\} + (v_r/\phi - \varepsilon_r/(\phi r_j))/(r_{j+1} - r_{j-1})]\, C^{n+1}_{i,j-1} \\
+\;& [-(2\varepsilon_r/\phi)[1/\{(r_j - r_{j-1})(r_{j+1} - r_{j-1})\} \\
+\;& 1/\{(r_{j+1} - r_j)(r_{j+1} - r_{j-1})\} - 2/\Delta t]\, C^{n+1}_{i,j} \\
+\;& [(2\varepsilon_r/\phi)/\{(r_{j+1} - r_j)(r_{j+1} - r_{j-1})\} - (v_r/\phi - \varepsilon_r/(\phi r_j))/(r_{j+1} - r_{j-1})]\, C^{n+1}_{i,j+1} = \\
=\;& -2\, C^{*}_{i,j}/\Delta t + (v_z/\phi)(C^{*}_{i+1,j} - C^{*}_{i-1,j})/(z_{i+1} - z_{i-1}) \\
-\;& (2\varepsilon_z/\phi)\,[C^{*}_{i-1,j}/\{(z_i - z_{i-1})(z_{i+1} - z_{i-1})\} + C^{*}_{i+1,j}/\{(z_{i+1} - z_i)(z_{i+1} - z_{i-1})\} \\
-\;& C^{*}_{i,j}\,\{1/\{(z_i - z_{i-1})(z_{i+1} - z_{i-1})\} + 1/\{(z_{i+1} - z_i)(z_{i+1} - z_{i-1})\}\}]
\end{aligned} \tag{6.15}$$

6.4 Inertial Effects with Forchheimer Corrections

The partial differential equations and their numerical implementation in Sections 6.1 – 6.3 are developed for conventional low-speed Darcy flows with small Reynolds numbers. With formation tester pumping speeds increasing in recent years, the effects of inertial must now be included. We now present the required modifications following Forchheimer (1901).

6.4.1 Governing differential equations

Let w, u and v represent velocities in the z, r and θ directions in a circular cylindrical coordinate system, and let t, ρ and ϕ denote time, mass density and porosity. Then, conservation of mass requires that

$$\partial(\rho\phi)/\partial t + \partial(\rho w)/\partial z + 1/r\,\partial(r\rho u)/\partial r + 1/r\,\partial(\rho v)/\partial\theta = 0 \qquad (6.16)$$

We wish to re-express this law for high-velocity, slightly compressible, liquid Darcy flows. For now, let us consider one-dimensional motion in the radial "r" (or horizontal) direction. If k_r, μ and p are horizontal permeability, viscosity and pressure, then the conventional Darcy equation "$-\partial p/\partial r = u\mu/k_r$" must be replaced by Forchheimer's law "$-\partial p/\partial r = u\mu/k_r + \beta u^n$," where β is a turbulence or inertial factor and the exponent n is generally taken as 2 (e.g., see Muskat (1937)). In other words,

$$-\partial p/\partial r = u\mu/k_r + \beta u^2 \qquad (6.17)$$

First, note that the radial term in Equation 6.16 can be expressed as

$$\begin{aligned} 1/r\,\partial(r\rho u)/\partial r &= \rho u/r + \rho\,\partial u/\partial r + u\,\partial\rho/\partial r \\ &= \rho u/r + \rho\,\partial u/\partial r + u\,\partial\rho/\partial p\;\partial p/\partial r \\ &= \rho u/r + \rho\,\partial(-k_r/\mu\;\partial p/\partial r - k_r/\mu\;\beta u^2)/\partial r - k_r/\mu\;(\partial p/\partial r + \beta u^2)\;\partial\rho/\partial p\;\partial p/\partial r \\ &= \rho u/r - \rho\,\partial(k_r/\mu\;\partial p/\partial r)/\partial r - (k_r/\mu)\,(\partial\rho/\partial p)\,(\partial p/\partial r)^2 \\ &\quad + \text{high-order-terms} \end{aligned}$$

where it is assumed that compressibility effects are more significant than inertial ones, that is, the derivative of the βu^2 term and the product $\beta\,\partial\rho/\partial p$ are small. In this limit,

$$\begin{aligned} 1/r\,\partial(r\rho u)/\partial r &\approx \rho u/r - \rho\,\partial(k_r/\mu\;\partial p/\partial r)/\partial r - (k_r/\mu)\,(\partial\rho/\partial p)\,(\partial p/\partial r)^2 \\ &\approx (\rho/r)\{-(k_r/\mu)\,\partial p/\partial r - (k_r/\mu)\,\beta u^2\} - \rho\,\partial(k_r/\mu\;\partial p/\partial r)/\partial r - (k_r/\mu)\,\rho\,(1/\rho)(\partial\rho/\partial p)\,(\partial p/\partial r)^2 \\ &\approx (\rho/r)\{-(k_r/\mu)\,\partial p/\partial r - (k_r/\mu)\,\beta u^2\} - \rho\,\partial(k_r/\mu\;\partial p/\partial r)/\partial r - (k_r/\mu)\,\rho c_f\,(\partial p/\partial r)^2 \end{aligned}$$

where we have introduced the fluid compressibility

$$c_f = (1/\rho)(\partial\rho/\partial p)_T \qquad (6.18)$$

with the subscript "T" denoting an isothermal process. In the small correction term "βu^2," we consistently approximate the radial velocity using $u = -(k_r/\mu)\,\partial p/\partial r$. When this is done,

$$1/r\,\partial(r\rho u)/\partial r \approx -\rho\,\partial(k_r/\mu\;\partial p/\partial r)/\partial r - \{\rho k_r/(\mu r)\}\,\partial p/\partial r - (\rho k_r/\mu)\,\{c_f + \beta k^2/(r\mu^2)\}\,(\partial p/\partial r)^2 \qquad (6.19)$$

Second, we observe that the transient term in Equation (1) can be re-written as

$$\begin{aligned}\partial(\rho\phi)/\partial t &= \phi\,\partial\rho/\partial t + \rho\,\partial\phi/\partial t \\ &= \phi\,\partial\rho/\partial p\,\partial p/\partial t + \rho\,\partial\phi/\partial p\,\partial p/\partial t \\ &= \phi\rho\,(1/\rho\,\partial\rho/\partial p)\,\partial p/\partial t + \rho\phi\,(1/\phi\,\partial\phi/\partial p)\,\partial p/\partial t \\ &= \phi\rho c_f\,\partial p/\partial t + \rho\phi c_r\,\partial p/\partial t \\ &= \phi\rho c\,\partial p/\partial t \end{aligned} \tag{6.20}$$

where we have introduced the rock and total compressibilities

$$c_r = (1/\phi)\,(\partial\phi/\partial p)_T \tag{6.21}$$

$$c = c_f + c_r \tag{6.22}$$

Third, we consider the remaining terms $\partial\,(\rho w)/\,\partial z$ and $1/r\,\partial\,(\rho v)/\,\partial\theta$ in Equation 6.16. In vertical-well formation testing applications, the borehole is represented by lines of constant "r," and liquid is pumped horizontally so that the radial velocity u satisfies $|u| >> |v|$ and $|u| >> |w|$. That is, near the nozzle, u is largest while v and w are vanishingly small as fluid turns into the nozzle, while u undergoes sudden starts and stops in the drawdown-buildup process. Thus, corrections analogous to those developed for $1/r\,\partial\,(r\rho u)/\partial r$ are not necessary and the usual Darcy representations suffice. Ignoring changes due to compressibility and inertia, we have

$$\partial\,(\rho w)/\,\partial z \approx -\rho\;\partial\,(k_z/\mu\,\partial p/\partial z)\,/\partial z \tag{6.23}$$

$$1/r\,\partial\,(\rho v)/\,\partial\theta \approx -\rho/r^2\,\partial\,(k_r/\mu\,\partial p/\partial\theta)\,/\partial\theta \tag{6.24}$$

where k_z is the vertical permeability. Substitution of Equations 6.19, 6.20, 6.23 and 6.24 in Equation 6.16 yields the required extended pressure partial differential equation for slightly compressible liquids in transversely isotropic media with weak inertial corrections, that is,

$$\begin{aligned}&\partial\,(k_z/\mu\,\partial p/\partial z)\,/\partial z + \partial\,(k_r/\mu\,\partial p/\partial r)/\partial r + \{k_r/(\mu r)\}\,\partial p/\partial r + (k_r/\mu)\,\{c_f + \\ &\beta k^2/(r\mu^2)\}\,(\partial p/\partial r)^2 + 1/r^2\,\partial\,(k_r/\mu\,\partial p/\partial\theta)\,/\partial\theta = \phi c\,\partial p/\partial t\end{aligned} \tag{6.25}$$

6.4.2 Pumpout boundary condition

Equation 6.25 is solved with boundary conditions relating the total volume flow rate Q(t) to the pressure gradient $\partial p/\partial r$. If A denotes the cross-sectional area of the source probe nozzle, the equation $Q = -Au = +Ak_r/\mu\,\partial p/\partial r$ is often used for simple pumpout modeling when flowline volume and compressibility effects are unimportant. However, this is rarely the case, especially in low mobility environments.

Chin and Proett (2005) or Chin (2014) instead show that $(Ak_r/\mu)\ \partial p/\partial r - VC\ \partial p/\partial t + VCSR_{well}\ \partial^2 p/\partial r\partial t = Q(t)$ where S is the skin factor, V is flowline volume and C represents fluid compressibility in the lines. To extend its validity to our classes of problems, we consider Equation 6.17 in the form $u = -(k_r/\mu)\ \partial p/\partial r - (k_r/\mu)\ \beta u^2 \approx -(k_r/\mu)\ \partial p/\partial r - (k_r/\mu)\beta\{(k_r/\mu)\ (\partial p/\partial r)\}^2$ so that $Au \approx -(Ak_r/\mu)\ \partial p/\partial r - A\beta(k_r/\mu)^3\ (\partial p/\partial r)^2$. Hence, we find that

$$(Ak_r/\mu)\ \partial p/\partial r + A\beta(k_r/\mu)^3\ (\partial p/\partial r)^2 - VC\ \partial p/\partial t + VCSR_{well}\ \partial^2 p/\partial r\partial t = Q(t) \tag{6.26}$$

Note that we have used the small β approximation

$$u = -(k_r/\mu)\ \partial p/\partial r - \beta\ (k_r/\mu)^3\ (\partial p/\partial r)^2 \tag{6.27}$$

At steady state, and additionally, when skin effects are ignored, the pumpout condition can be written in the form $Q = -uA = A(k_r/\mu)\ \partial p/\partial r + A\beta\ (k_r/\mu)^3\ (\partial p/\partial r)^2$. Inversion using the quadratic formula gives an explicit expression for $\partial p/\partial r$, namely,

$$\partial p/\partial r = -\{\mu Q/(k_r A)\}[1 + k_r\beta Q/(A\mu)] \tag{6.28}$$

This shows that the radial pressure gradient is changed by the amount "$k_r\beta Q/(A\mu)$" shown. Also, note that Equation 6.26 contains inertial corrections only, since properties related to compressibility (that is, derivatives with respect to pressure) do not appear in "$Q = -Au$."

6.4.3 Boundary value problem summary

In summary, we solve the transient diffusive partial differential equation in Equation 6.29a subject to the pumpout condition in Equation 6.29b derived above, namely,

$$\partial\ (k_z/\mu\ \partial p/\partial z)/\partial z + \partial\ (k_r/\mu\ \partial p/\partial r)/\partial r + \{k_r/(\mu r)\}\ \partial p/\partial r + (k_r/\mu)\ \{c_f + \beta k^2/(r\mu^2)\}\ (\partial p/\partial r)^2 + 1/r^2\ \partial\ (k_r/\mu\ \partial p/\partial\theta)/\partial\theta = \phi c\ \partial p/\partial t \tag{6.29a}$$

$$(Ak_r/\mu)\ \partial p/\partial r + A\beta(k_r/\mu)^3\ (\partial p/\partial r)^2 - VC\ \partial p/\partial t + VCSR_{well}\ \partial^2 p/\partial r\partial t = Q(t) \tag{6.29b}$$

The model of Chin and Proett (2005) or Chin (2014), which is linear in pressure, now contains the nonlinear corrections $(k_r/\mu)\ \{c_f + \beta k^2/(r\mu^2)\}\ (\partial p/\partial r)^2$ and $A\beta(k_r/\mu)^3\ (\partial p/\partial r)^2$ shown in blue. Thus, the "alternating-direction-implicit" (or, ADI) solution scheme based on tridiagonal linear inversion, originally developed in Chin (1993, 2002) must be replaced by a more complicated local linearization method. In addition to Equation 6.29b, dynamically coupled mudcake growth constraints on fluid invasion at the sandface, as derived in Chin (1995), are used, as are regularity conditions at infinity and quiescent flow conditions initially.

A word on numerical stability, which largely depends on the differential equation itself, is in order. The term "$\{k_r/(\mu r)\}\ \partial p/\partial r + (k_r/\mu)\ \{c_f + \beta k^2/(r\mu^2)\}\ (\partial p/\partial r)^2$" replaces the "$k_r/(\mu r)\ \partial p/\partial r$" in the conventional formulation. Absolutely convergent factorizations are available to solve baseline equations like $\partial^2 p/\partial z^2 + \partial^2 p/\partial r^2 = \alpha\ \partial p/\partial t$. The addition of an axisymmetric " $+ 1/r\ \partial p/\partial r$" term can be shown to stabilize numerical calculations while a negative sign would prove destabilizing. The multiplier to k_r/μ can be re-expressed as $[1/r + \{c_f + (\beta k^2)/(r\mu^2)\ \partial p/\partial r\}\ \partial p/\partial r$. In formation testing applications, liquids are typically withdrawn from the formation, so that $\partial p/\partial r > 0$. Thus, the modifier "$\{c_f + (\beta k^2)/(r\mu^2)\ \partial p/\partial r$," like " $+ 1/r$," is positive, and hence stabilizing. Calculated results are provided in Chapters 7 and 8 next.

6.5 References

Aziz, K. and Settari, A., Petroleum Reservoir Simulation, Applied Science Publishers, London, 1979.

Chin, W.C., Modern Reservoir Flow and Well Transient Analysis, Gulf Publishing, Houston, 1993.

Chin, W.C., Formation Invasion, with Applications to Measurement-While-Drilling, Time Lapse Analysis, and Formation Damage, Gulf Publishing, Houston, 1995.

Chin, W.C., Quantitative Methods in Reservoir Engineering, Elsevier Science, Amsterdam, 2002.

Chin, W.C. and Proett, M.A., "Formation Tester Immiscible and Miscible Flow Modeling for Job Planning Applications," *SPWLA 46th Annual Logging Symposium*, New Orleans, Louisiana, June 26-29, 2005.

Chin, W.C., Suresh, A., Holbrook, P., Affleck, L. and Robertson, H., "Formation Evaluation Using Repeated MWD Logging Measurements," *SPWLA 27th Annual Logging Symposium*, Houston, Texas, 1986.

Chin, W.C., Zhou, Y., Feng, Y., Yu, Q. and Zhao, L., Formation Testing: Pressure Transient and Contamination Analysis, John Wiley & Sons, New Jersey, 2014.

Chow, W.K., Ho, C.M., and Fong, N.K., "Evaluation of the Finite Control Volume Method in Simulating Thermal Fire Resistance of Building Elements," *Building Simulation, Fifth International IBPSA Conference*, Sept. 8-10, Prague, Czech Republic, Vol. 1, 1997, p. 273.

Forchheimer, P.,"Wasserbewegung durch Boden," *Zeitschrift des Vereines Deutscher Ingenieuer*, 45th Edition, 1901.

Muskat, M., The Flow of Homogeneous Fluids Through Porous Media, McGraw-Hill, New York, 1937.

Peaceman, D.W., Fundamentals of Numerical Reservoir Simulation, Elsevier Scientific Publishing, Amsterdam, 1977.

Peaceman, D.W. and Rachford, H.H., "Numerical Calculation of Multidimensional Miscible Displacement," *Society of Petroleum Engineers Journal*, Dec., 1962, pp. 327-339.

Proett, M.A., Chin, W.C. and Mandal, B., "Advanced Permeability and Anisotropy Measurements While Testing and Sampling in Real-Time Using a Dual Probe Formation Tester," *SPE Paper 64650, Seventh International Oil & Gas Conference and Exhibition*, Nov., Beijing, China, 2000.

Todd, M.R. and Longstaff, W.J., "The Development, Testing and Application of a Numerical Simulator for Predicting Miscible Flood Performance," *Journal of Petroleum Technology*, July 1972, pp. 874-882.

7
Multiphase Flow –
Miscible Mixing Clean-Up Examples

The discussions of Chapter 6 focused on mathematical modeling and numerical solution. The design of a job planning simulator that is useful in field and rigsite computations requires features that provide convenient input parameter definition and output display. These include (1) automatic variable time-stepping for increased computing speed, (2) multi-rate pumping schedule to model multiple pump rates and non-ideal pump effects, (3) color displays to report invasion, pressure and supercharging effects while simulating, (4) plots of pressure versus time and contamination versus time at all source and distant observation probes, (5) surface and contour plots of relevant flow properties, (6) user-friendly and intuitive Windows interfaces, and so on. We emphasize that the miscible flow simulators in Chin and Proett (2005) and Chin *et al* (2014) have been completely rewritten to incorporate nonlinear Forchheimer effects and new results are reported here. This work required changes to the equation solver to increase computing speed and numerical stability. A strong impetus for the new work was found in new tools like Schlumberger's Saturn^{TM} tester which operates at very high flow rates. This tool contains four "elongated pads" placed about the circumference and the flow is closely axisymmetric as assumed in our math model. New miscible results are reported here and a number of earlier examples have been re-run. However, the complementary immiscible model is still in development and progress will be reported at a later date.

7.1 Overview Capabilities

Because there are literally dozens of input parameters, and because the governing equations are extremely complicated, no general conclusions can be drawn from the limited number of simulations presented here. However, the results shown are representative of typical results that are physically expected. We will therefore dwell less on the particular input parameters and more on the way qualitative calculated results are consistent with expected downhole phenomena. We will focus on general capabilities and applications for which our job planning software was designed for.

7.1.1 Example 1, Single probe, infinite anisotropic media

For this first simulation, we describe our graphical output results in detail and explain their potential uses and implications. Once all input quantities are saved and the "Simulate" button in the user interface is clicked, interactive displays of pressure and oil saturation (or formation fluid concentration) field are displayed periodically in time. Consider Figure 7.1.1a, which contains two field plots, with pressure at the left and concentration at the right for a miscible run (for immiscible runs, concentration plots are replaced by oil saturations). For each of the diagrams in Figure 7.1.1a, the left vertical side corresponds to the sandface at the borehole wall – the right side corresponds to the radial farfield. The top and bottom horizontal lines coincide with the top and bottom of the reservoir. Therefore, these cross-sections display computed solutions in the r-z plane for the axisymmetric formulation considered in this paper.

The left pressure plot is uniform vertically, indicating identical pressure profiles at all z stations. The red at the left represents high mud pressure, relative to the lower blue formation pressure at the right. The right concentration plot again indicates a purely radial flow without z variations. Invading blue mud is displacing red formation fluid. The multicolored zones between blue and red in either case represent events in the diffusive mixing zone. Cylindrical radial invasion occurs while drilling. Sometimes the invasion time is short – at other times, it can exceed a day. For long invasion times, it is not necessary to simulate extraordinarily long – we equivalently model the invasion associated with a higher permeability mud for a shorter time. Equivalence formulas are given in Chin (1995, 2002). The relatively short times in Figures 7.1a and 7.1b mimic twenty-four hour invasion. Note how the effects of mud pressure and filtrate invasion are deeper at "1 min" than at "0.33 sec," as expected physically.

At some point in time designated by the user, the formation tester starts pumping – it can extract fluid from or inject fluid into the reservoir according to a multi-rate schedule. The left pressure plot in Figure 7.1.1c shows the effects of fluid withdrawal, that is, typical fluid sampling performed, in this case, by a single centered nozzle (in general, single, dual and straddle packer probes are permitted, which can be located arbitrarily along the sandface). The left side of the pressure plot in Figure 7.1.1c shows a blue-green area associated with the low pressure at the nozzle. Above and below this zone are red colored pressures which indicate higher pressures associated with supercharging – that is, as the nozzle withdraws fluid, high pressure mud invades the formation through the mudcake. Not shown in the pressure plot are reverse flow streamlines that would mark filtrate pumping by the formation tester nozzle.

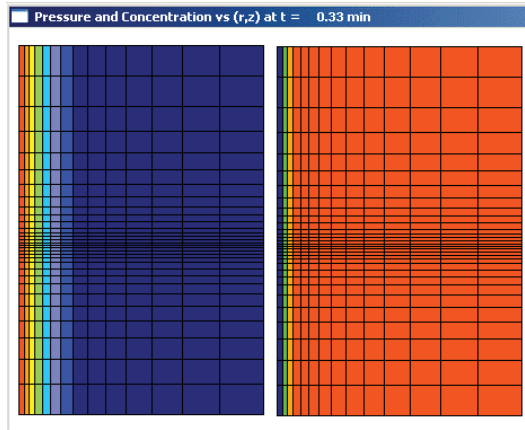

Figure 7.1.1a. Pressure-concentration profiles, 0.33 sec.

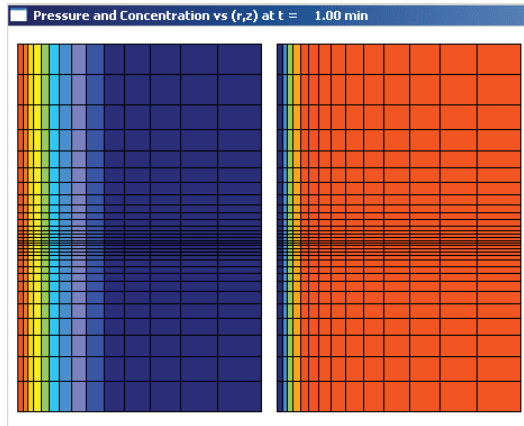

Figure 7.1.1b. Pressure-concentration profiles, 1.00 min.

The right plot in Figure 7.1.1c displays the corresponding concentration profile. The blue zone represents the mud filtrate that has penetrated the formation – it is now deeper than that shown in Figure 7.1.1b. Figures 7.1.1d and 7.1.1e illustrate similar phenomena at later times. Again, note the high supercharge pressures above and below the nozzle, indicating continuing filtrate invasion while the tester nozzle attempts to extract a clean sample. Whether or not this is possible for the input parameters assumed is one question the simulation addresses. There are several related objectives. Is a clean sample possible? If so, how long must the formation be pumped? If not, how might mud properties and weight to changed? The time scale for adequate clean-up is different from that for pressure transient interpretation. How long must be tool stay in place to ensure good pressure data for permeability and anisotropy

prediction – without risking a stuck tool? Good pressure data for permeability prediction, of course, can be obtained even when mud filtrate has not been flushed. Thus, for tools that do not collect samples (e.g., formation-testing-while-drilling tools), the job planning simulator can be used to study pressure transients – while, for wireline formation testers, the simulator serves dual clean-up and pressure transient objectives.

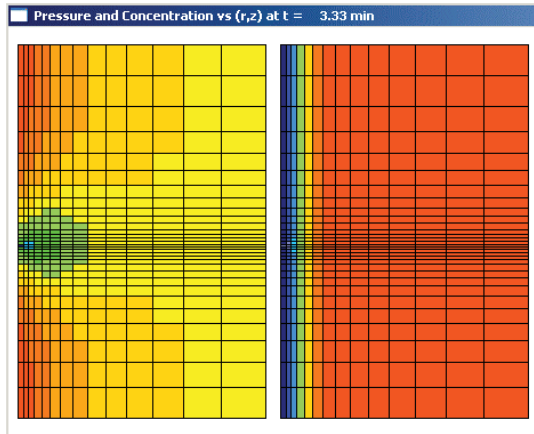

Figure 7.1.1c. Pressure-concentration profiles, 3.33 min.

The left plot of Figure 7.1.1c indicates probe presence because its low (blue-green) pressures contrast strongly with the high (red) ones due to supercharging. At the right, a small green zone associated with the probe is embedded in the blue filtrate – this small zone is not red because the fluid is still contaminated. The variable meshes used allow high resolution simulations near the probe.

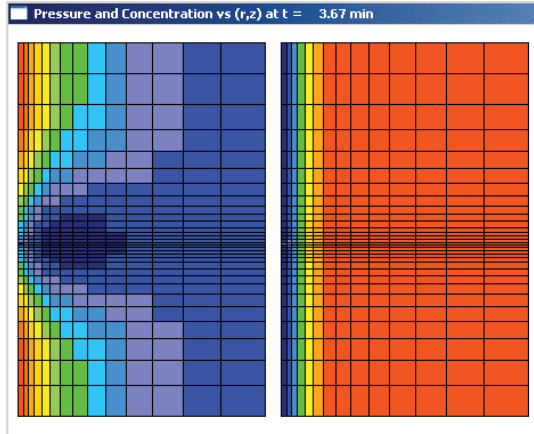

Figure 7.1.1d. Pressure-concentration profiles, 3.67 min.

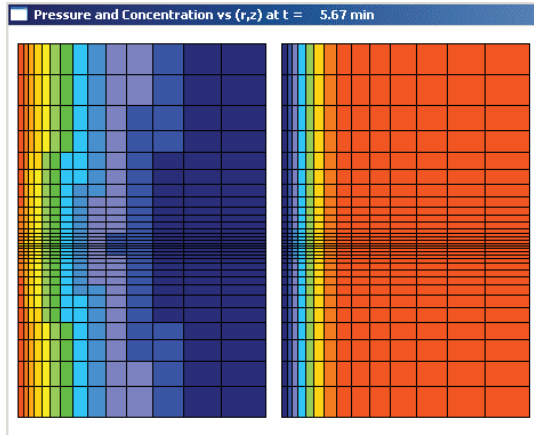

Figure 7.1.1e. Pressure-concentration profiles, 5.67 min.

At the end of the simulation – a point in time defined by the user, the pressure-concentration screens shown above may be played back in the software's "movie mode." This playback feature enhances the field engineer's physical intuition about the formation under consideration. In addition, three line graphs automatically appear that conveniently summarize computed results at source and observation probes. Figure 7.1.1f displays the concentration of formation fluid at the source probe. For the input parameters assumed in the present simulation, the results are not encouraging (we will show more optimistic results later). At first, the concentration is zero because the nozzle is not pumping. Once pumping commences, the formation fluid concentration increases to a maximum of 0.3 or 30% – not quite the 90-95% that is deemed adequate by petrophysicists.

There may be several reasons for low dilute levels. Figures 7.1.1a–7.1.1e show high levels of supercharge pressure while the nozzle is pumping – our nozzle may, in fact, be pumping filtrate just entering the formation. But even if not, it is possible that rapid diffusion between filtrate and formation fluid – encouraged by the particular pore structure in the rock – mixes the two quickly in a detrimental manner. One purpose of the job planning simulator is to identify the reasons for sample contamination and to recommend fixes.

Figure 7.1.1g displays the pressure drawdown and buildup calculated for the input parameters assumed. Pressure transient predictions are always checked against exact analytical results to ensure that spatial and time grid parameters yield accurate results. In our case, the complex complementary error function solution of Proett, Chin and Mandal (2000) was used. This solution assumes a pure spherical (ellipsoidal) source model, so that fluid invasion at the borehole wall is not modeled. Assumed meshes were therefore calibrated against exact results for a perfectly sealed borehole.

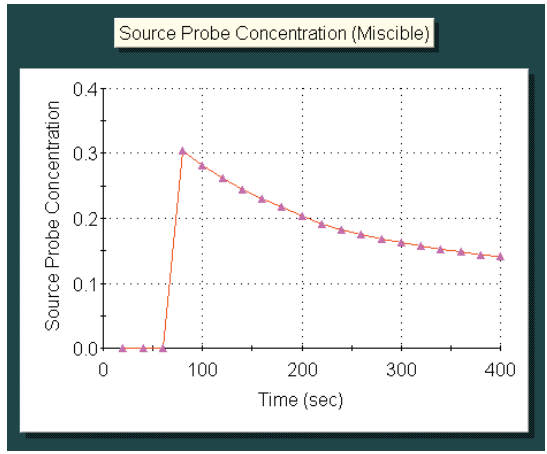

Figure 7.1.1f. Formation fluid concentration at source probe.

That our job planning simulator models both fluid mixing and pressure transient analysis (due to fluid compressibilities) is desirable because it is convenient – but more important, both objectives are accomplished using the same software, thus reducing the uncertainties associated with using multiple simulators. In addition, because the same equations as those in reservoir engineering are used here, the same software can be used for reservoir engineering production predictions by sealing the borehole, expanding the flow domain to field scale, and lowering the borehole pressure to those characteristic of production scenarios.

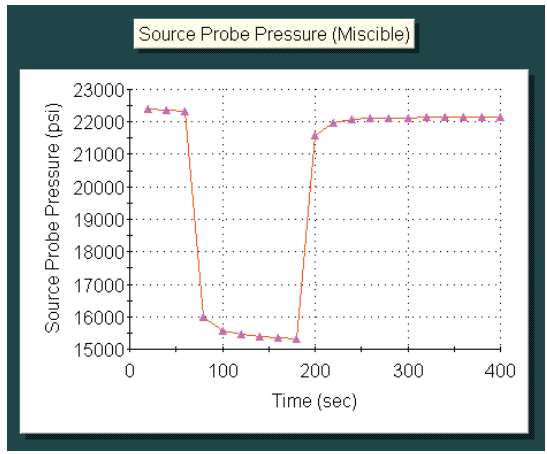

Figure 7.1.1g. Source probe pressure transient history.

Finally, as shown in Figure 7.1.1h, the software also produces pressure transient outputs at any observation probe location defined by the user. We emphasize that it is not necessary to have an observation probe in the tool to use the software model – that is, the software can be used with single-nozzle tool FTWD applications to ascertain depth of investigation or penetration. Of course, in dual probe applications, the use of pressure drops available at source and observation probes enables prediction of horizontal and vertical permeability. For the present simulation, it is of interest to note the high level of diffusion in Figure 7.1.1h relative to that in Figure 7.1.1g. Such indicators are useful in ascertaining the probability of success that might be achieved in so-called "mini-DST" applications. The observation probe can be chosen at any distance from the source probe, e.g., seven inches or ten feet.

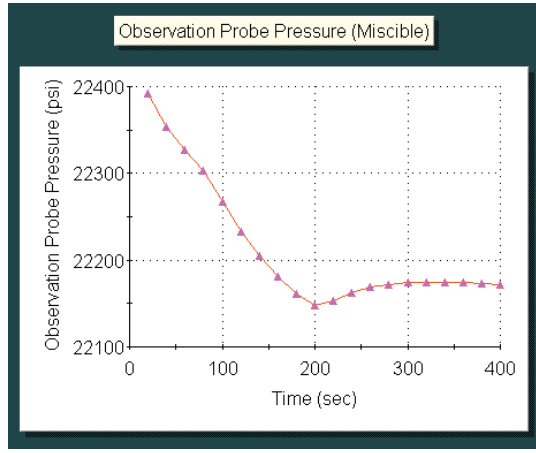

Figure 7.1.1h. Observation probe pressure transient history.

7.1.2 Example 2, Single probe, three layer medium

In this second simulation, we describe a situation without the upper-lower symmetries obtained earlier. Here the formation consists of three layers, with the lowest porosity layer at the top. Before pumping, there is strong cylindrical radial filtrate invasion into the formation, as is evident from the right-side plot of Figure 7.1.2a. The left-side pressure plot shows a small blue zone marking the lower pressures realized at the nozzle. That the entire plot is a single color indicates relatively little pressure variation otherwise, characteristic of the low permeabilities assumed.

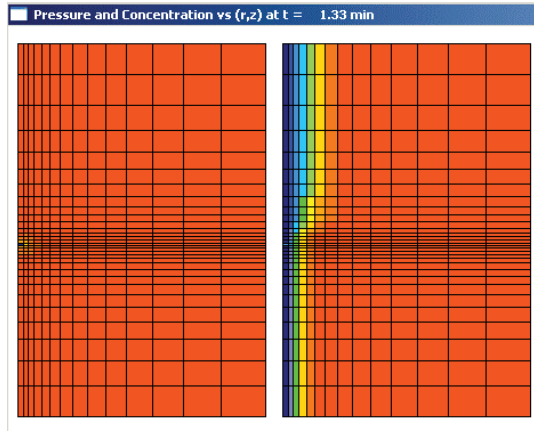

Figure 7.1.2a. Initial pumping, highly invaded upper zone.

Figure 7.1.2b gives pressure-concentration plots at a later point in time. The concentration plot shows continuing strong invasion in the low porosity layer. The pressure plot, with the high color contrast and the strong red zones above and below the probe along the sandface (left vertical boundary) indicates strong supercharging. The formation tester probe will measure high pressures, but the high values characterize more the high pressure in the mud than the pore pressure in the rock.

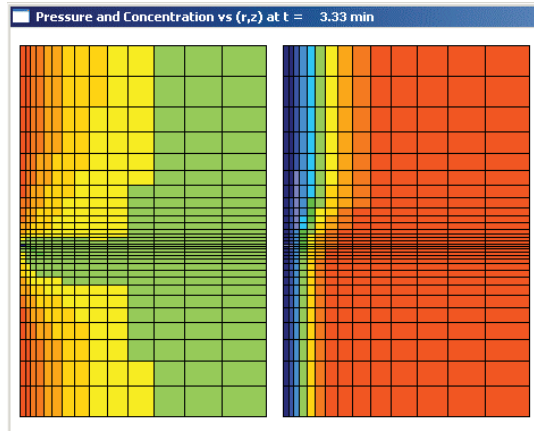

Figure 7.1.2b. Supercharging seen in left pressure plot.

The pressure-concentration behavior noted for Figure 7.1.2b continues with increased intensity in Figure 7.1.2c. In all the runs shown thus far, note our use of variable spatial grids in the radial and vertical directions. Internal software

logic also activates variable time gridding, enabling large time steps when flow gradients are small and smaller time steps when they are large. For example, smaller time steps are selected whenever a change in flow rate is imposed; higher grid densities are always selected near nozzles.

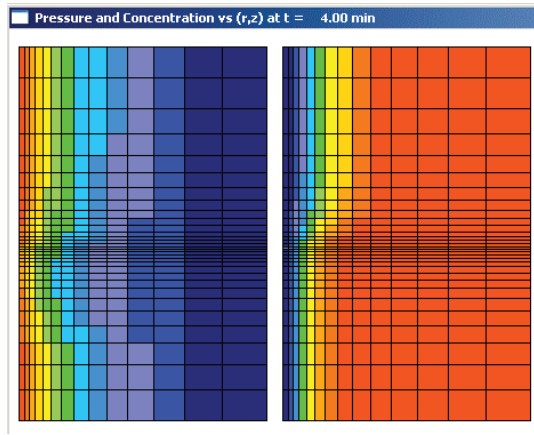

Figure 7.1.2c. Continued supercharging and invasion.

7.1.3 Example 3, Dual probe pumping, three layer medium

In this example, we consider a three layer medium again – the higher permeabilities here allow stronger pressure penetration as seen in the left pressure plot of Figure 7.1.3a.

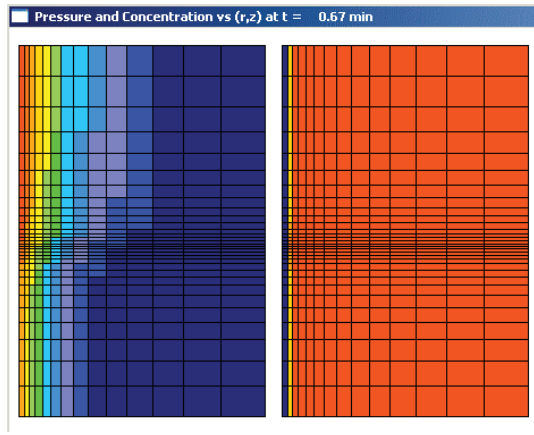

Figure 7.1.3a. Initial cylindrical invasion before pumping.

Pumping has initiated in Figure 7.1.3b. The two small blue areas in the left pressure plot mark the low pressure zones associated with two pumping nozzles. The two small red areas in the right concentration plot mark the high formation fluid concentrations associated with continued pumping. From Figure 7.1.3c, at large times pumping has ceased and supercharging at the sandface is evident from the left red pressure zones.

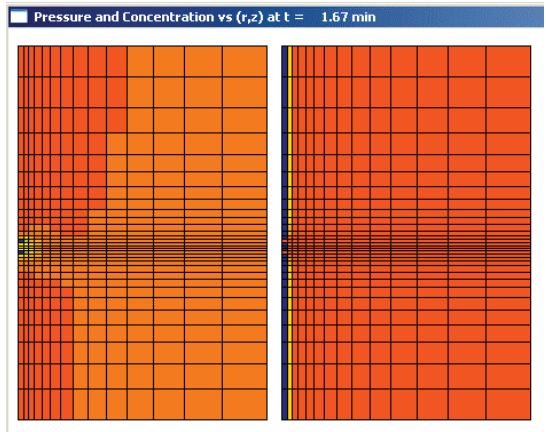

Figure 7.1.3b. Dual probe pumping initiated.

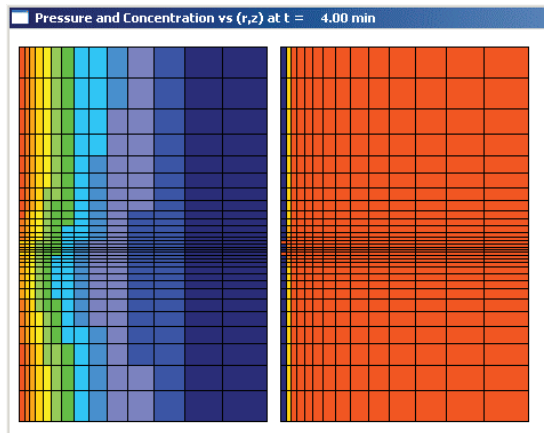

Figure 7.1.3c. Supercharging evident at large times.

7.1.4 Example 4, Straddle packer pumping

So far we have demonstrated how pumpouts using single probe and dual probe nozzles can be realistically simulated. In many field situations, particularly in unconsolidated sands and naturally fractured formations, pad nozzles may not be effective in reliably contacting producing zones. In such applications, straddle packer nozzles are employed. Whereas pad nozzles "see" a single point along the borehole wall, packer nozzles see axial extents that may be several feet in length and then pump from all azimuthal directions. Because they are associated with pump rates that may reach 1 gpm, they offer good depth of investigation and strong signal propagation – thus they are extremely useful in so-called "mini-DST" applications that seek to determine permeability over larger spatial scales than those normally possible with pad-type tools.

Again, we consider a layered region that is initially invaded by mud filtrate. The left pressure plot in Figure 7.1.4a shows an elongated low pressure zone associated with the length of the straddle packer. The nonuniform vertical pressure variations indicate that the radial flux into the tool is not uniform – computational evidence that "uniform flux" pumping models are not correct even the packer resides entirely within a uniform layer. The formation fluid concentration plot in Figure 7.1.4b highlights the continuing invasion of mud filtrate into the near-sandface rock.

The pressure plots in Figures 7.4c and 7.4d highlight the strong impact on local flow exerted by the straddle packer nozzle. Its long vertical extent allows it to withdraw large amounts of fluid into the tool. The low pressures at the bottom and bottom-right of the formation unfortunately encourage stronger invasion at the top, an effect clearly seen in the concentration plot of Figure 7.1.4d. Not shown are computed pressure plots along various tool stations. As noted earlier, while our algorithm allows nonuniform radial flux along the length of the tool, pressures along it do not vary although they do vary with time. Pressures fields away from the packer are deeper than they are for pad type nozzles because of the higher pump rates utilized.

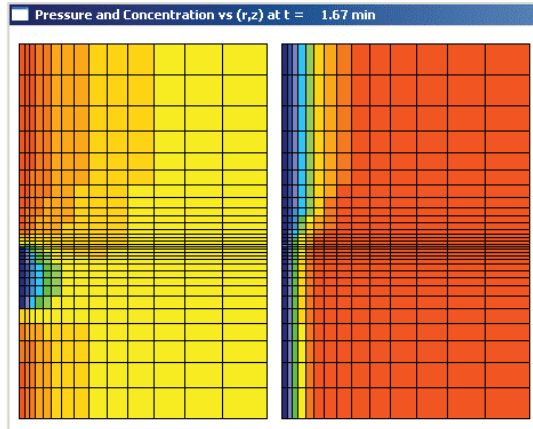

Figure 7.1.4a. Initial pumping of cylindrical invaded region.

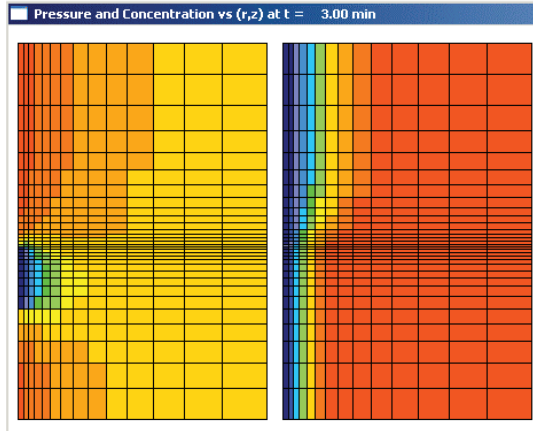

Figure 7.1.4b. Continued straddle packer pumping.

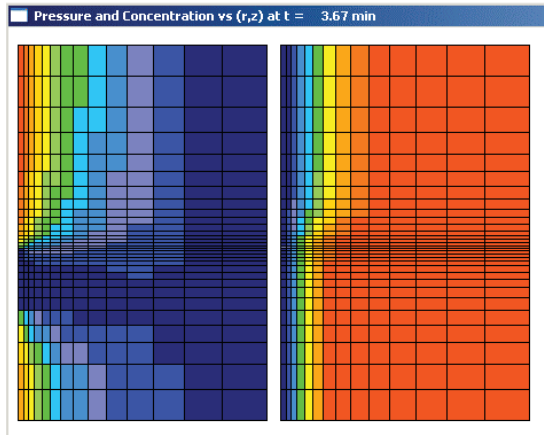

Figure 7.1.4c. Strong lateral pumping.

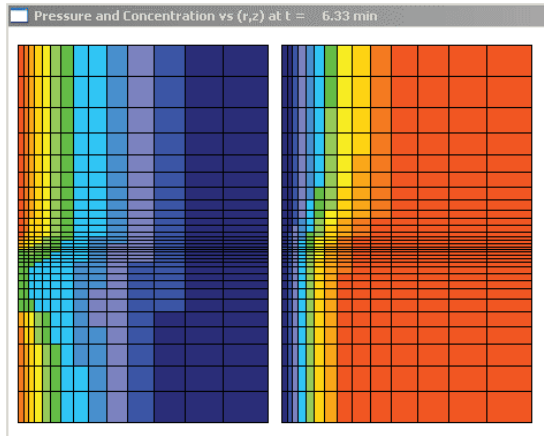

Figure 7.1.4d. Lower formation strongly affected.

7.1.5 Example 5, Formation fluid viscosity imaging

Our field examples apply to shallow wells drilled with an oil base mud. Inputs are representative of typical downhole conditions, but due to space limitations, only key parameters and qualitative results are summarized. We asked if differences in formation fluid viscosity are detectable through pressure responses. Mud viscosity is fixed at 1 cp, while formation fluid viscosity is taken as 1, 3 and 5 cp for top, middle and bottom calculations in Figure 7.1.5. As expected, pressure drops increase going downward for source and distant probes.

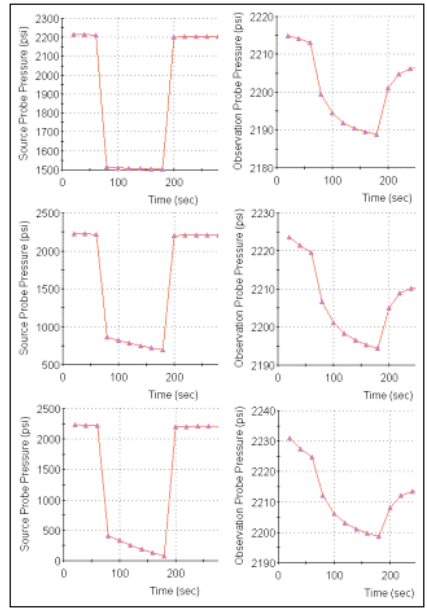

Figure 7.1.5. Source and observation probe pressures.

The source probe response is interesting. At the top left, the minimum pressure bottoms out as a flat line – both viscosities are 1 cp. In the middle and bottom left figures, where formation fluid viscosities exceed mud viscosity, minimum pressures decrease with time because flow resistance at the probe increases with time (average viscosity increases due to miscible mixing).

7.1.6 Example 6, Contamination modeling

"Formation fluid concentration (or saturation) vs time" plots at the source probe indicate changing contamination levels. In Figure 7.1.6, plots starting with the upper left and proceeding counterclockwise show typical concentrations increasing as fluid diffusion decreases – diffusion strongly affects sample quality.

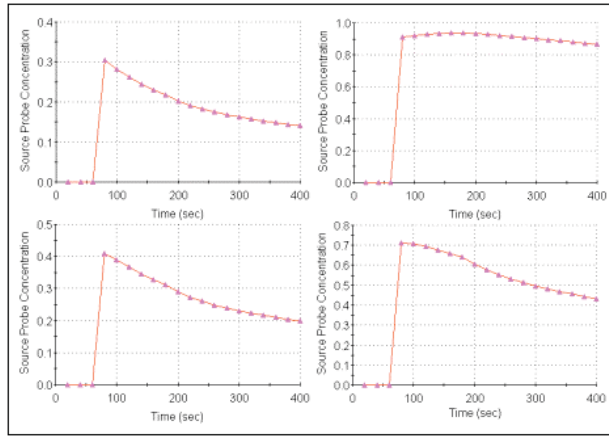

Figure 7.1.6. Source probe formation fluid concentration.

The upper left figure shows poor 30% sample quality obtained soon after pumping; when pumping stops, this decreases continuously as invasion continues. The upper right shows good 90% quality. Sample quality improves with decreasing mudcake permeability or well pressure. The simulator is used in job planning to test "what-if" scenarios controlled by numerous parameters.

7.1.7 Example 7, Multi-rate pumping simulation

Figure 7.1.7a shows three constant-rate pumping intervals separated by two quiescent periods over a thirty minute period. The red curve gives source probe pressure response and shows decreasing values with time (due to increasing viscosity at the probe as low mud and higher formation viscosity fluids mix).

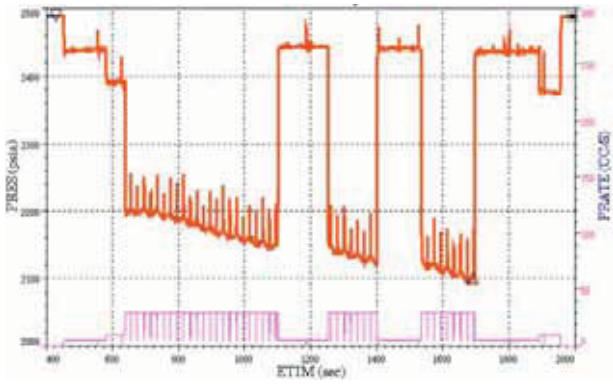

Figure 7.1.7a. Field log, multirate flow and pressure.

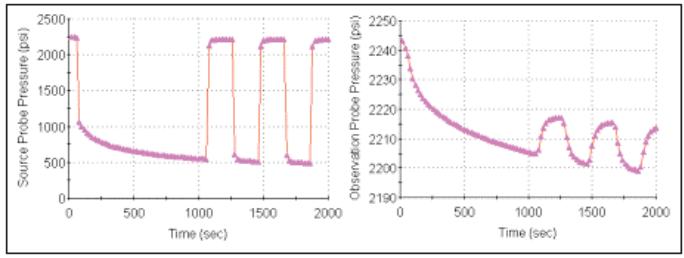

Figure 7.1.7b. Source and observation probe simulation.

The field source probe response of Figure 7.1.7a is successfully simulated at the left of Figure 7.1.7b, requiring about two minutes on typical personal computers. The observation probe response appears at the right. Both indicate that viscosity increases during transient mixing are detectable from time-varying pressure data.

We have provided an overview of validation and field examples illustrating our mathematical and numerical approach – and have shown that they predict events that are consistent with the physics. In particular, we have developed a reservoir engineering approach to model formation testing in borehole environments with dynamic mudcake growth and supercharging. The simulators, useful in permeability prediction from pressure transient analysis and contamination studies, are invaluable in inverse applications for horizontal and vertical permeabilities.

They are also important in job planning. For example, if formation properties are approximately known, what flow rates and sequences are needed for detectable signals at the observation probe? What mudcake properties are required for effective sealing to overcome supercharging problems? What is the depth of investigation and the vertical resolution associated with a particular flowrate? This work applies to vertical wells in layered media and is restricted to zero dip angle – it assumes that the permeability in a plane perpendicular to the well axis does not vary azimuthally. This does not mean that the model cannot be used for deviated and horizontal wells where both permeabilities change about the well. For example, one can always study worst case events by considering an isotropic uniform medium controlled by the lower of k_h and k_v.

7.2 Source Code and User Interface Improvements

The multiphase simulators of Chin and Proett (2005) have changed substantially and, for completeness, we describe key modifications. We address the user data input panel, key modifications to the source code engine, and typical color output plots.

7.2.1 User data input panel

Originally, all input boxes were placed on a single software screen, as shown in Figure 7.2.1. Users were required to enter vast amounts of data, comprising of physical properties, boundary conditions and grid generation variables. As one would expect, few combinations actually led to usable solutions, so that the simulation experience was less than ideal. Major rework has led to the modular menu system in Figures 7.2.2a and 7.2.2b.

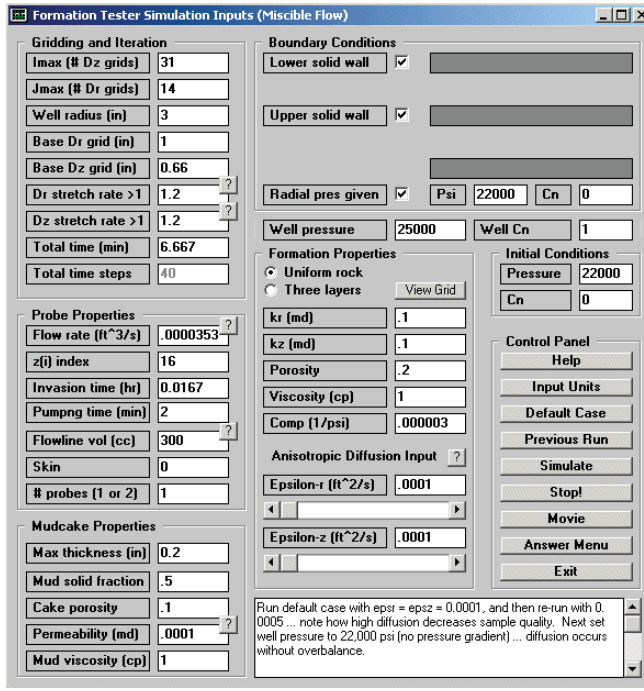

Figure 7.2.1. Original user interface.

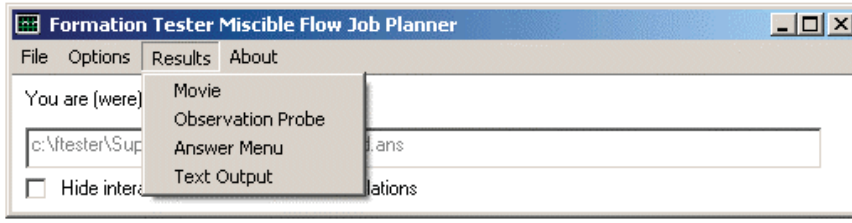

Figure 7.2.2a. New program structure (high level).

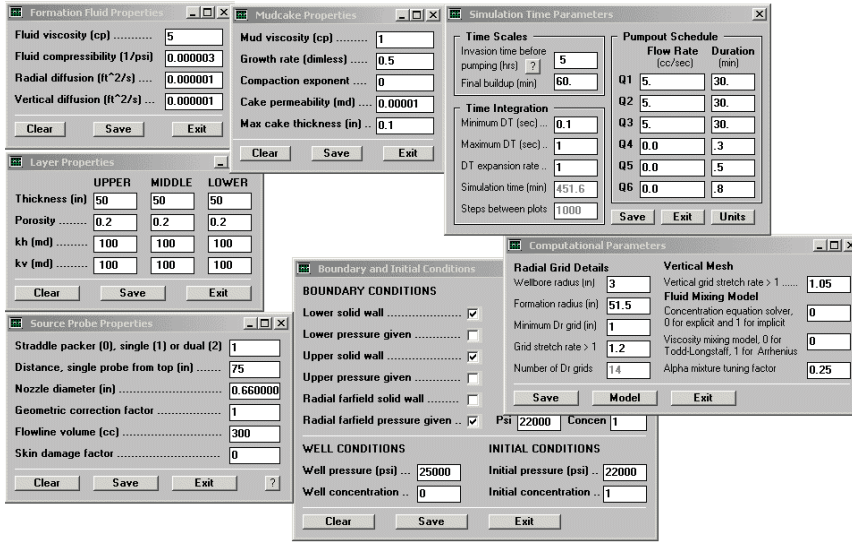

Figure 7.2.2b. Modularized submenus (low level).

In particular, the high-level control menu in Figure 7.2.2a opens any number of lower-level submenus, as shown in Figure 7.2.2b, each focusing on a particular function. Typical menus include "formation fluid properties," "layer properties," "mudcake parameters," "source probe type," "boundary conditions," "pumping schedules" and numerical gridding parameters. When a user has developed a meaningful simulation, he is provided the option to save that run and re-run the model at any time – or run changes to that simulation defined by editing one or more of the input screens in Figure 7.2.2b. This allows him to build a useful library of simulations for future use, accessible through database calls under "File Open." Compressed data files can now be shared by users working from different locations and color graphics plots and movies are always recreated "on the fly" to conserve disk storage space and to reduce file transmit times. These comments apply to miscible and immiscible simulators.

7.2.2 Source code engine changes

Key to the new work are inertial corrections of the Forchheimer type in order to account for rapid pumping speeds. The changes to the numerical formulation are nontrivial. As discussed in Chapter 6, the pressure equation is solved by an alternating-direction-implicit (ADI) approach, requiring sweeping in both radial and vertical directions, while the concentration or saturation equation is solved by an explicit method. The red logic is replaced by complicated blue terms involving the Forchheimer constant "FORCH" as noted. In addition, faster run times were achieved using the analytical invasion models developed in the formation invasion book of Chin (1995).

```
C     TRANSIENT CONCENTRATION **EXPLICIT** INTEGRATION
C
      DO 800  I=2,IMAXM1
      DO 800  J=2,JMAXM1
C     Concentration derivatives, Equation # 81
      CNIJ   =   CNOLD(I,J  )
      DCDR   =  (CNOLD(I,J+1) - CNOLD(I,J-1))/R3(J)
      D2CDR2 = ((CNOLD(I,J+1) - CNIJ         )/R4(J)
     1         - (CNIJ         - CNOLD(I,J-1))/R5(J))/R6(J)
      DCDZ   =  (CNOLD(I+1,J) - CNOLD(I-1,J))/Z3(I)
      D2CDZ2 = ((CNOLD(I+1,J) - CNIJ         )/Z4(I)
     1         - (CNIJ         - CNOLD(I-1,J))/Z5(I))/Z6(I)
C     Bracket terms other than POR dCN/dt in Equation # 81
C     Old logic ...
C     BRACKS = - VTZ(I,J)*DCDZ
C    1         - VTR(I,J)*DCDR
C    2         + EPSZ*D2CDZ2  + EPSR*(D2CDR2 + DCDR/R(J))
C
C     New extended multiphase logic ...
      IF(J.GT.1.AND.J.LT.JMAX) THEN
      DPDRTMP = (POLD(I,J+1)-POLD(I,J-1))/R3(J)
      VTR(I,J) = -MR(I,J)*DPDRTMP-FORCH*MR(I,J)**3*DPDRTMP**2
      ENDIF
      IF(J.EQ.1) THEN
      DPDRTMP = -MR(I,J)*(POLD(I,2)-POLD(I,1))/(R(2)-R(1))
      VTR(I,J) = -MR(I,J)*DPDRTMP-FORCH*MR(I,J)**3*DPDRTMP**2
      ENDIF
      IF(J.EQ.JMAX) THEN
      DPDRTMP = -MR(I,J)*(POLD(I,JMAX)-POLD(I,JMAXM1))/
     1           (R(JMAX)-R(JMAXM1))
      VTR(I,J) = -MR(I,J)*DPDRTMP-FORCH*MR(I,J)**3*DPDRTMP**2
      ENDIF
C
      BRACKS = - VTZ(I,J)*DCDZ
     1         - VTR(I,J)*DCDR
     2         + EPSZ*D2CDZ2  + EPSR*(D2CDR2 + DCDR/R(J))
C
      DTBPOR = DELTAT/PORMID
      IF(I.GE.IMIDT) DTBPOR = DELTAT/PORTOP
      IF(I.LE.IMIDB) DTBPOR = DELTAT/PORBOT
      CNNEW(I,J) = CNIJ + BRACKS*DTBPOR
 800  CONTINUE
C
```

Figure 7.2.3a. Forchheimer changes to explicit concentration solver.

```
C     IMPLICIT ADI PRESSURE SOLVER
C
C     SWEEP # 1 in radial direction (assumes first half of DELTAT)
      DO 760 J=2,JMAXM1
      DO 750 I=2,IMAXM1
      AA(I) =  (AL(I-1,J) + AL(I  ,J))/(Z5(I)*Z3(I))
      CC(I) =  (AL(I  ,J) + AL(I+1,J))/(Z4(I)*Z3(I))
      BB(I) =  -AA(I) -CC(I) -2./DELTAT
C
C     Old logic, commented out ...
C     WW(I) =  -2.*POLD(I,J)/DELTAT
C    1            -(BT(I,J)/R(J))*(POLD(I,J+1)-POLD(I,J-1))/R3(J)
C    2-(BT(I,J  ) + BT(I,J+1))*(POLD(I,J+1)-POLD(I,J  ))/(R4(J)*R3(J))
C    3+(BT(I,J-1) + BT(I,J  ))*(POLD(I,J  )-POLD(I,J-1))/(R5(J)*R3(J))
C
C     Extended multiphase logic, new ...
      PORCMP  = PORMID*COMP
      IF(I.GE.IMIDT) PORCMP  = PORTOP*COMP
      IF(I.LE.IMIDB) PORCMP  = PORBOT*COMP
      WW(I) =  -2.*POLD(I,J)/DELTAT
     1            -(BT(I,J)/R(J))*(POLD(I,J+1)-POLD(I,J-1))/R3(J)
     2            - BT(I,J)*((POLD(I,J+1)-POLD(I,J-1))/R3(J))**2
     3                     *(COMP + FORCH*PORCMP**2*BT(I,J)**2/R(J))
     4-(BT(I,J  ) + BT(I,J+1))*(POLD(I,J+1)-POLD(I,J  ))/(R4(J)*R3(J))
     5+(BT(I,J-1) + BT(I,J  ))*(POLD(I,J  )-POLD(I,J-1))/(R5(J)*R3(J))
 750  CONTINUE
.
.
.

C     SWEEP #2 in vertical direction
      DO 780 I=2,IMAXM1
      DO 770 J=2,JMAXM1
C     Old logic ...
C     AA(J) = (BT(I,J-1)+BT(I,J  ))/(R5(J)*R3(J)) - BT(I,J)/(R(J)*R3(J))
C     CC(J) = (BT(I,  J)+BT(I,J+1))/(R4(J)*R3(J)) + BT(I,J)/(R(J)*R3(J))
C     BB(J) = -AA(J) -CC(J) -2./DELTAT
C     WW(J) = -2.*PSTAR(I,J)/DELTAT
C    1-(AL(I  ,J) + AL(I+1,J))*(PSTAR(I+1,J)-PSTAR(I,J  ))/(Z4(I)*Z3(I))
C    2+(AL(I-1,J) + AL(I  ,J))*(PSTAR(I,J  )-PSTAR(I-1,J))/(Z5(I)*Z3(I))
C
C     New extended multiphase logic ...
C     Note, only single compressibility for two like miscible fluids used
      PORCMP  = PORMID*COMP
      IF(I.GE.IMIDT) PORCMP  = PORTOP*COMP
      IF(I.LE.IMIDB) PORCMP  = PORBOT*COMP
      PGRADOLD = (POLD(I,J+1)-POLD(I,J-1))/R3(J)
      AA(J)=(BT(I,J-1)+BT(I,J  ))/(R5(J)*R3(J)) - (BT(I,J)/(R(J)*R3(J)))
     1*(1.+R(J)*(COMP+FORCH*PORCMP**2*BT(I,J)**2/R(J))*PGRADOLD)
      CC(J)=(BT(I,  J)+BT(I,J+1))/(R4(J)*R3(J)) + (BT(I,J)/(R(J)*R3(J)))
     1*(1.+R(J)*(COMP+FORCH*PORCMP**2*BT(I,J)**2/R(J))*PGRADOLD)
      BB(J) = -AA(J) -CC(J) -2./DELTAT
      WW(J) = -2.*PSTAR(I,J)/DELTAT
     1-(AL(I  ,J) + AL(I+1,J))*(PSTAR(I+1,J)-PSTAR(I,J  ))/(Z4(I)*Z3(I))
     2+(AL(I-1,J) + AL(I  ,J))*(PSTAR(I,J  )-PSTAR(I-1,J))/(Z5(I)*Z3(I))
C
 770 CONTINUE
```

Figure 7.2.3b. Forchheimer modifications to implicit pressure solver.

7.2.3 Output color graphics

Color displays for time-varying pressure and concentration fields such as those in Section 7.1 were originally written in Fortran and did not offer flexible viewing options. However, because computing demands were low, the logic was reused to create movie playbacks which show how pressure and concentration fields evolve in time. This enhances an engineering understanding of flow interactions and aids in supercharge interpretation.

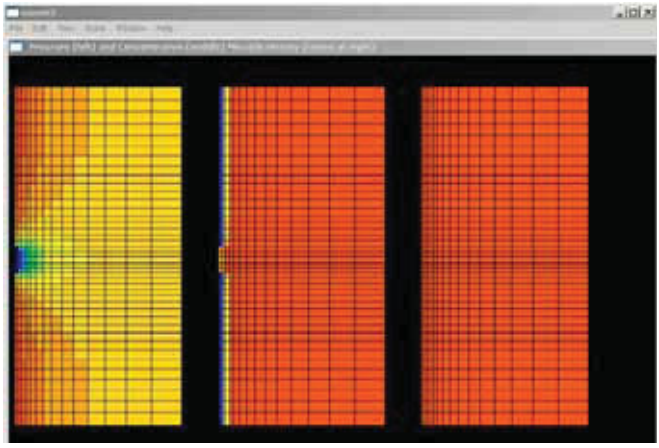

Figure 7.2.4. Movie display frame
(pressure left, concentration middle, lithology right).

Clicking "Observation Probe" in Figure 7.2.2a brings up the general observation probe post-processing menu shown in Figure 7.2.5a. This post-processor reads the entire array of results computed by the simulator. At the top of the menu is an information box that displays the vertical extent of the z grid and the location of the source. The user is allowed to enter any "observation value" z into the input box at the top right. The internal algorithm then internally interpolates values for pressure, concentration, pressure derivative and concentration derivative at the desired z location from computed values at nodes. The results are plotted against time, with three plotting options available. These are "pumping only," "invasion only," and "both." This observation probe post-processor can also be used with source points. This post-processing option is useful in planning mini-DST tests.

Clicking on "Answer Menu" brings up the menu shown in Figure 7.2.5b. The first five source probe items represent the line graphs available in various examples discussed in this chapter. Results for line plots are stored on the hard drive and can always be accessed from this menu. The "Observation and Source Probe" item invokes the menu shown in Figure 7.2.82. The present menu

importantly plots spatial field results, as noted on the bottom half of the calculator in Figure 7.2.5b. Movies and text output files can be accessed. However, it is also possible to plot P(r,z) and C(r,z) at the ending time in different types of color plots. Various plotting capabilities for pressure and concentration are illustrated without further comment in Figures 7.2.6a – 7.2.6h.

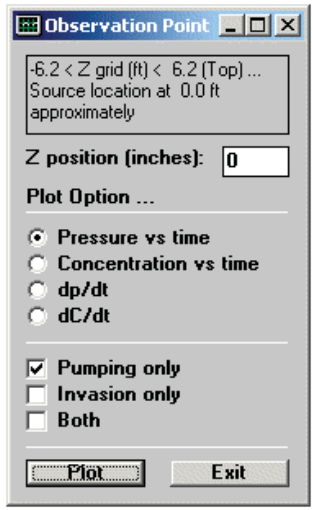

Figure 7.2.5a. Observation probe post-processing menu.

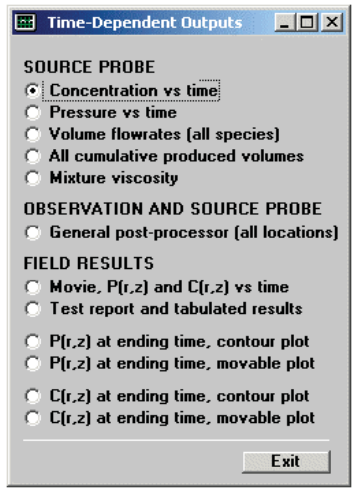

Figure 7.2.5b. Answer menu.

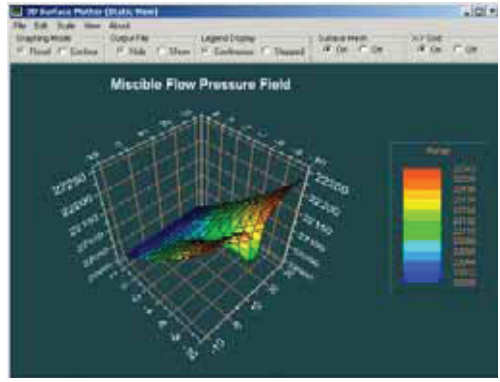

Figure 7.2.6a. Stationary pressure surface plot.

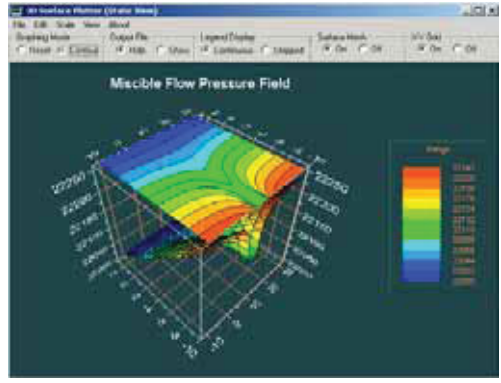

Figure 7.2.6b. Stationary pressure contour plot.

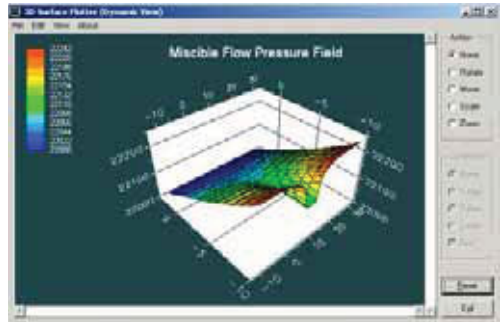

Figure 7.2.6c. Movable pressure plot, default view.

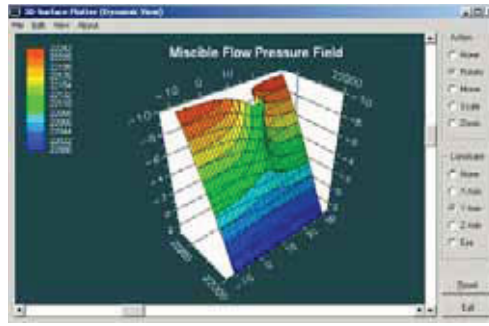

Figure 7.2.6d. Movable pressure plot, a different view (use mouse to rotate and translate figure).

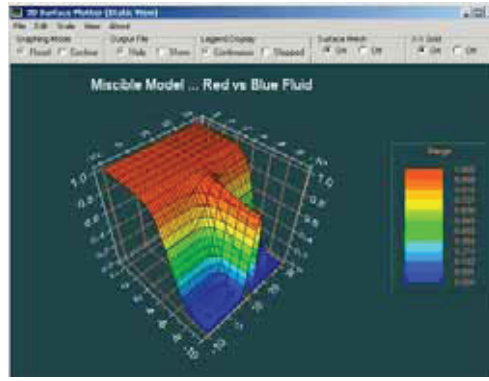

Figure 7.2.6e. Stationary concentration surface plot.

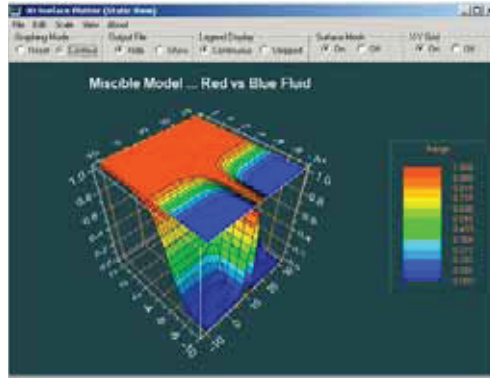

Figure 7.2.6f. Stationary concentration contour plot.

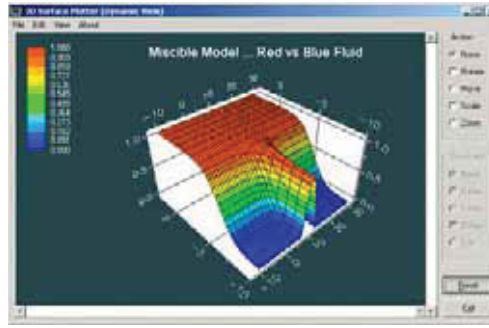

Figure 7.2.6g. Movable concentration plot, default view.

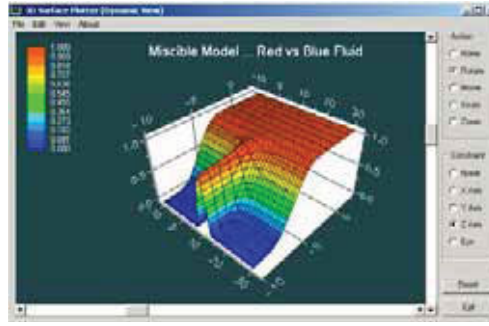

Figure 7.2.6h. Movable concentration plot, a different view (use mouse to rotate and translate figure).

7.3 Detailed Applications

In this section, we will illustrate different applications for our miscible multiphase job planning simulator. We will examine the effects of probe type, e.g., single, dual and packer nozzles, explore the consequences of diffusive mixing on clean-up, and provide examples for invasion versus pumping. Simulation runs are introduced in the order of increasing complexity in order to explain the physics clearly.

7.3.1. Run No. 1, Clean-up, single-probe, uniform medium

We consider formation clean-up about a single-probe tool in a uniform medium. The seven sub-menu inputs defining the run appear in Figure 7.3.1.

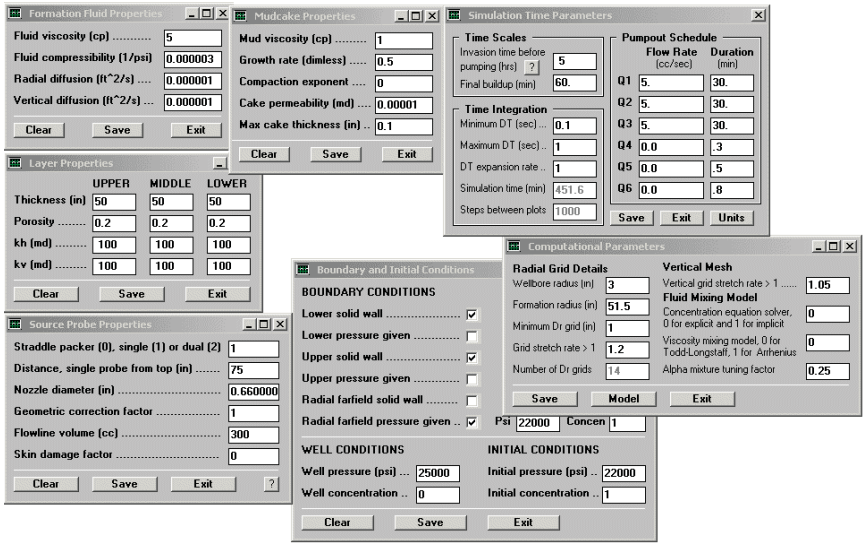

Figure 7.3.1. Seven submenus for input parameter definition.

We first summarize the physical assumptions behind the above simulation. The problem is shown schematically in Figure 7.3.2. At first, the borehole undergoes pure cylindrical radial invasion with dynamic mudcake buildup as indicated at the left – an actual wellbore with nonzero radius is assumed, and as will be demonstrated later, the (vertical) borehole can traverse up to three horizontal layers each having different thicknesses and formation properties. The color diagrams to the right of Figure 7.3.2 display complementary pressure P(r,z,t) and "contamination" or "concentration" C(r,z,t) profiles frozen at a time t, where r is the radial coordinate, z is the vertical coordinate.

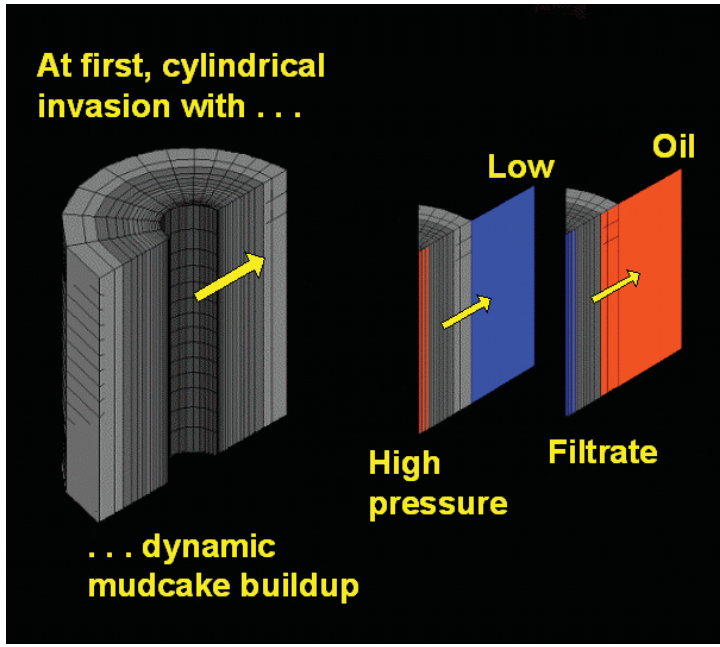

Figure 7.3.2. General problem definition – initial cylindrical invasion.

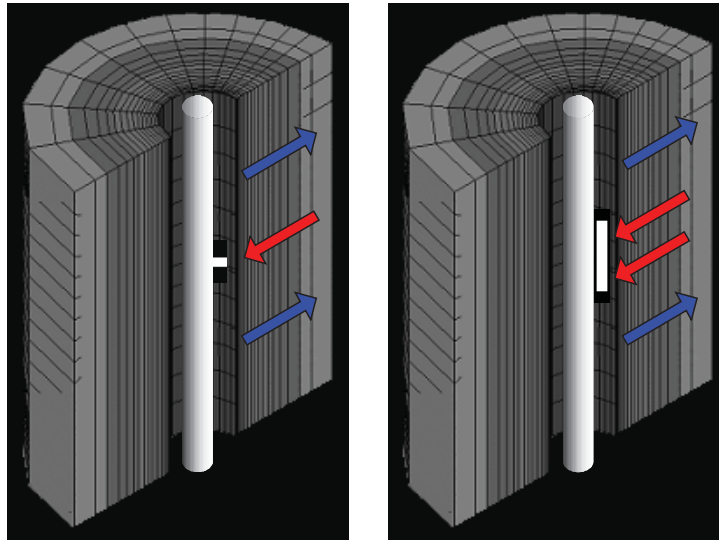

Figure 7.3.3. Pumping begins (single-probe, left, elongated pad, right).

The complete physical picture requires both P and C descriptors since these are coupled, and both are, in turn, dynamically coupled to mudcake growth. For pressure plots, red indicates high pressure while blue indicates low; for concentration plots, blue indicates "dirty" (filtrate) while red indicates "clean" (formation fluid). These twin pictures are displayed periodically during the simulations. Prior to pumping by the formation tester, of course, we expect purely cylindrical radial behavior.

At a time prescribed by the user, the formation tester will commence pumping. In Figure 7.3.3, a single-probe tool is shown at the left – the red arrows indicate fluid withdrawal by the tool while the blue arrows indicate continual invasion into the formation (an elongated probe is shown at the right for comparison, whose properties will be considered in later runs). The pressure-concentration profiles shown in Figure 7.3.2 will now change by virtue of this localized pumping. Low pressure will be evident at the pumping probes while high pressure will be evident along the borehole walls adjacent to the probes due to continuing invasion – this effect is known as "supercharging." The pressure calculated at the probes (and measured in reality by the tool) is a combination of wellbore mud pressure and formation pore pressure. One purpose of this present simulator is to explore the complicated relationship between measured probe pressure, borehole mud pressure and distant pore pressure. How much of the measured pressure is the pore pressure? Using incorrect pressure inputs in our inverse permeability methods will, of course, lead to errors in formation evaluation results.

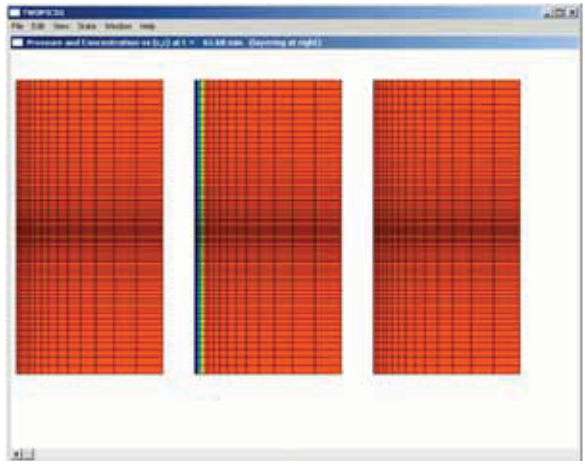

Figure 7.3.4a. Pressure-concentration-lithology display (61 min).

We now describe the sequence of events observed on screen. During simulations, a status screen appears that indicates that cylindrical invasion is proceeding – the physical time and the percentage of the simulation completed are displayed. A series of r-z color screen displays appears periodically at pre-set time intervals. Consider, for example, Figure 7.3.4a, which displays cross-sectional results at time t = 61.68 min. The left-most pressure plot is uniform in color indicating that the pressure is almost constant throughout since a very low permeability mudcake has been assumed – in later examples, greater color variations showing the effects of supercharging will be evident. The left side of each color diagram represents the borehole sandface while the right side represents farfield radial infinity as suggested in Figure 7.3.2. The top and bottom of each box correspond to the top and bottom of the reservoir. The center concentration plot indicates invasion, with blue filtrate at the left (borehole sidewall) and red reservoir fluid at the right. The right-most plot will, in simulations involving more than one layer, display lithology and layer thicknesses; for simulations in uniform media, it can be ignored.

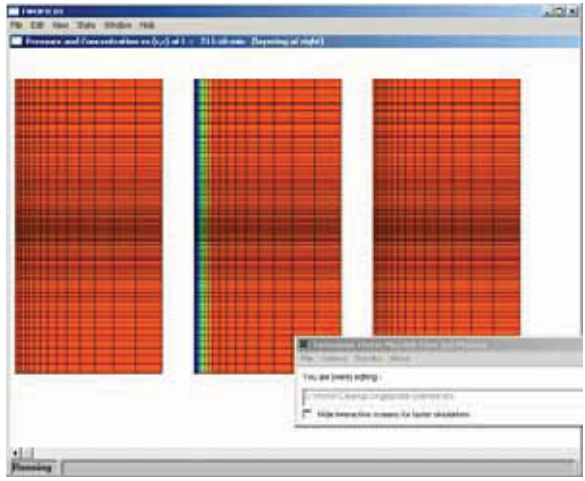

Figure 7.3.4b. Later time cylindrical radial invasion (211 min).

At 211 minutes, Figure 7.3.4b indicates that invasion has proceeded beyond that shown in Figure 7.3.4a, although from the history of color displays (not shown) the rate of radial invasion has slowed. This occurs because mudcake is dynamically building and slows the invasion rate – geometric spreading also contributes to the slower radial penetration. Once formation tester pumping starts, the computer status screen reflects that fact by indicating "pumping started," together with the elapsed physical time and percentage done.

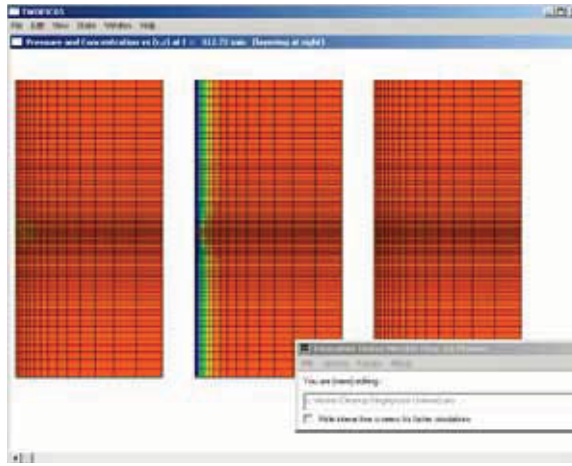

Figure 7.3.4c. Single-probe pumping (312 min).

Figure 7.3.4c shows the onset of pumping for the single-probe tool assumed. The left-most pressure plots shows a small blue low-pressure zone associated with the probe nozzle, while the center concentration plot shows an orange zone of contaminated fluid being withdrawn into the probe (this orange is a mixture of blue filtrate and red formation fluid). With time, the orange zone will – hopefully – turn into a completely red zone. There is, however, no guarantee that this will occur; for example, this is physically not possible if the mudcake is too permeable or if excessive diffusion is present in the formation fluid. Figures 7.3.4d and 7.3.4e display two additional screen dumps at later instants in time for comparison.

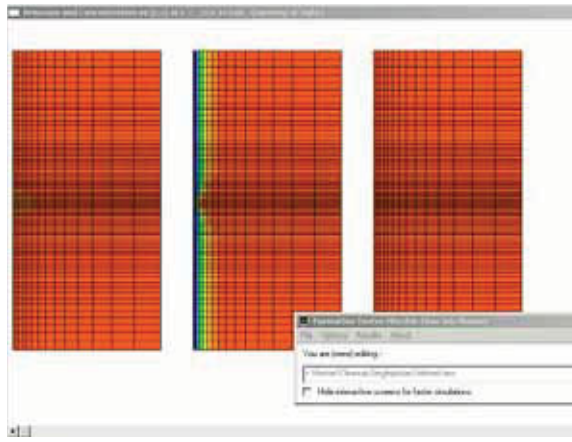

Figure 7.3.4d. Middle-time pumping result (324 min).

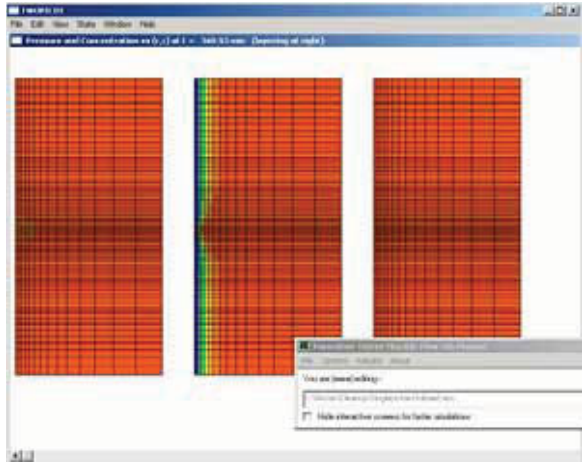

Figure 7.3.4e. Later time pumping result (340 min).

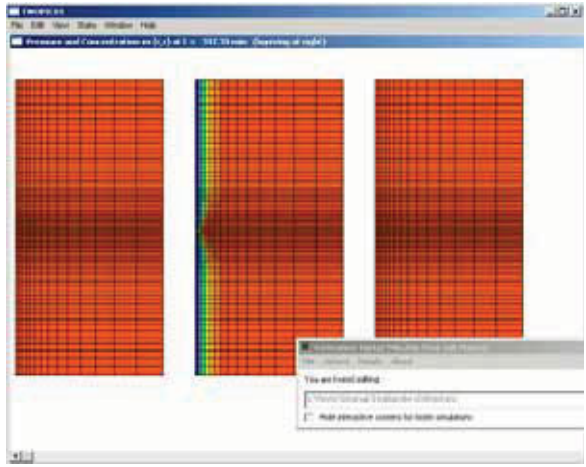

Figure 7.3.4f. Pumping ceases, but invasion continues (397 min).

In Figure 7.3.4f, the blue low-pressure zone at the nozzle has disappeared because the probe has stopped pumping (refer to the "Simulation Time Parameters" pump schedule in Figure 7.3.1). Again, the pressure plot is a single color because the reservoir pressure is almost uniform on account of low mudcake permeabilities – actually, a slight pressure variation exists but it cannot be resolved by the coarse color palette used to paint the screen – palette refinement is planned for software upgrades.

Although pumping has stopped, invasion continues through the mudcake – eventually, the "dent" seen in the central figure would equalize and tend toward a pure cylindrical radial pattern. When the simulation is completed and the last color screen has been displayed, five line plots of practical importance in pressure transient analysis (for permeability prediction) and contamination monitoring appear. Figure 7.3.4g shows the plot for pressure obtained at the source probe. Notice that, despite the high 100 md permeabilities assumed in the "Layer Properties" menu of Figure 7.3.1, the pressure trace has not yet "bottomed out" after almost 100 minutes as would be expected on the basis of single-phase flow. In fact, it appears that the source probe pressure is continuing its decline and that a steady response is nowhere in sight.

We remind the reader that the present simulator is designed to model two fluids with miscible mixing, although it will model single phase fluids if the two have equal initial viscosities. In the present example, the filtrate viscosity is 1 cp while the formation fluid viscosity is 5 cp. An initial five hour (300 minute) invasion has allowed low viscosity fluid to invade into the near-wellbore rock. Once formation tester pumping starts, we expect the usual pressure decline behavior – in this case, pressure decreases while the initially pumped filtrate is replaced by much more viscous formation oil. This presence of more and more viscous oil accounts for the continually decreasing pressure – the downward slope of this curve is an indicator that cleaning of the formation is ongoing. We emphasize, that while cleaning is in progress, the fluid is multiphase in nature so that the pressure transient curves cannot be interpreted for permeability using ideal single phase flow models. The present simulator must be used in pressure history matching whenever two-phase miscible mixing is involved. By "source probe pressure," we refer to the actual pressure at the source probe. This term also refers to the pressures at dual probe tools, which are identical since they are open to the same hydraulic reservoir; it additionally refers to the pressure along the axial extent of a dual packer, which must be constant.

The cleaning nature of the flow is directly apparent from Figure 7.3.4h, which gives the complementary coupled solution for concentration or contamination. When the well is first drilled, the concentration is 1.0 indicating pure formation fluid at the sandface. After five hours (refer to the pumping schedule in Figure 7.3.1) or 300 minutes, invasion has degraded the local fluid quality to such an extent that concentration is a low 0.24. Once pumping starts, the filtrate is removed and gradually replaced by formation oil. Figure 7.3.4h shows that, in about ninety minutes, the concentration at the source probe has increased to about 95%, which can also be interpreted as 5% contamination. Once pumping stops, the concentration at the probe location falls because continuing invasion from areas adjacent to it contaminates the local fluid.

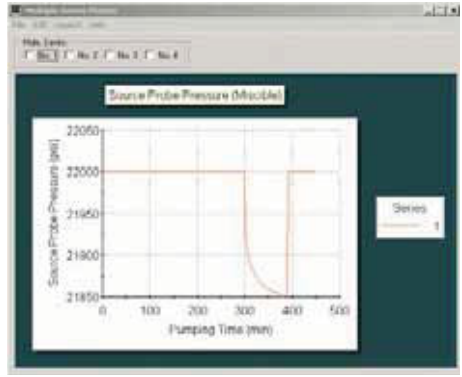

Figure 7.3.4g. Single-probe tool source pressure.

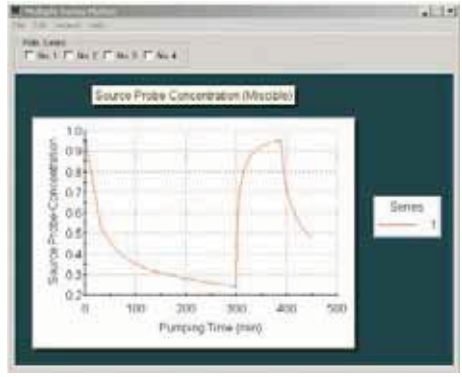

Figure 7.3.4h. Single-probe tool source concentration.

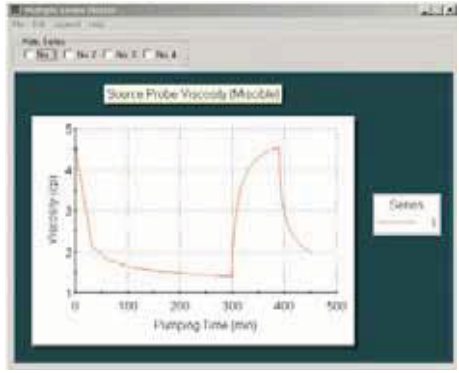

Figure 7.3.4i. Single-probe tool source viscosity.

Figure 7.3.4i displays the mixture viscosity obtained at the source probe. Initially, from the ”Mudcake Properties” and “Formation Fluid Properties” menus in Figure 7.3.1, we had assumed 5 cp for the formation fluid viscosity and 1 cp for the mud filtrate viscosity. The 5 cp adjacent to the well decreases rapidly to about 1.4 cp after five hours. Once pumping starts, the viscosity at the probe recovers to 4.5 cp before falling due to pumping stoppage. It is possible that additional pumping may improve the viscosity recovery. However, in any physical application, there is no guarantee that continual pumping implies continual cleaning. For example, when the diffusion level in the formation is high or when the mudcake is relatively permeable, the formation may be irreversibly contaminated and no amount of pumping can produce clean fluid. This simulator was designed to model such events and plan against their occurrence in the field.

From the “Pumpout Schedule” in the “Simulation Time Parameters” menu in Figure 7.3.1, we had chosen, for simplicity, a volume flow rate of 5 cc/s over ninety minutes. The volume flow rate specified in the menu is the total rate for the combined clean and dirty fluid: we cannot control the relative portions of dirty versus clean fluid ultimately pumped – the percentages are obtained from the simulation and cannot be prescribed a priori. In Figure 7.3.4j, the red total volume flow rate versus time plotted is back-calculated from the Darcy pressure field and not just the inputted number – that the red lines shows “5” exactly indicates that the second-order accurate numerical method is accurate indeed. The green line shows the volume flow rate associated with the dirty filtrate – at first, the amount of contaminated fluid pumped is great, but this is ultimately replaced by clean formation fluid. The gray line displays the volume flow rate associated with the formation fluid. At any instant in time, the sum of the green and gray flow rates equals that shown by the red.

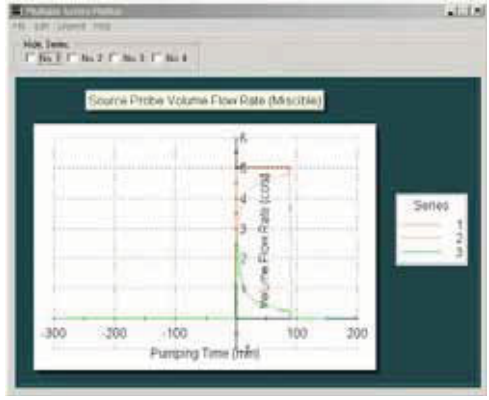

Figure 7.3.4j. Single-probe source volume flow rate.

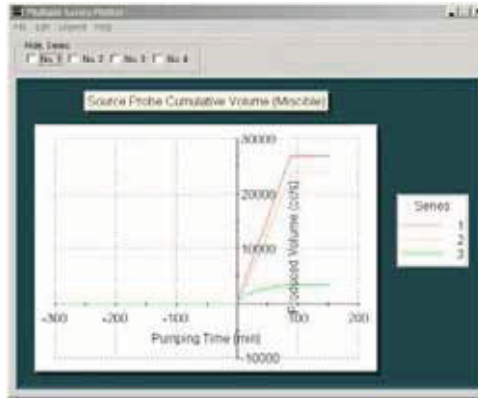

Figure 7.3.4k. Single-probe source cumulative volume.

Figure 7.3.4k displays the time integrals of the corresponding rate curves in Figure 7.3.4j. Consider, for example, the red line for the cumulative pumped volume for the combined dirty and clean fluids. The "5 cc/s" assumed over ninety minutes yields a total of "5 cc/s × 90 × 60 sec" or 27,000 cc as shown at the end of the pumping cycle. The gray line identifies the portion associated with formation fluids while the green line represents dirty mud filtrate. It is important to notice that, in general, the green line in the cumulative volume plot is not linear – its curvature is dictated by combined diffusion and borehole curvature (or geometric spreading) effects. The color "pressure versus concentration" plots, the five line plots and the DOS status screens appear automatically and do not require any special setup procedures or user commands. By "concentration" and "viscosity," we mean the average values for dual probe tools and center values for dual packer tools.

7.3.2. Run No. 2, Clean-up, dual-probe, uniform medium

Now, we consider clean-up for a dual-probe tool in uniform media, for which our sub-menu inputs appear in Figure 7.3.5a, which should be compared with Figure 7.3.1 – only the inputs in the "Source Probe Properties" menu at the bottom left have changed. For now, we wish to point out the qualitative differences between single and dual probe tools. For brevity, only several run-time screens are shown. A typical color "pressure-concentration" plot while pumping is shown in Figure 7.3.5b. The two blue zones in the left-most pressure plot above correspond to the two source probes, while the two mixed color regions in the middle concentration plot indicate that mixed fluid (that is, partly between blue and red) is to be found near both probes.

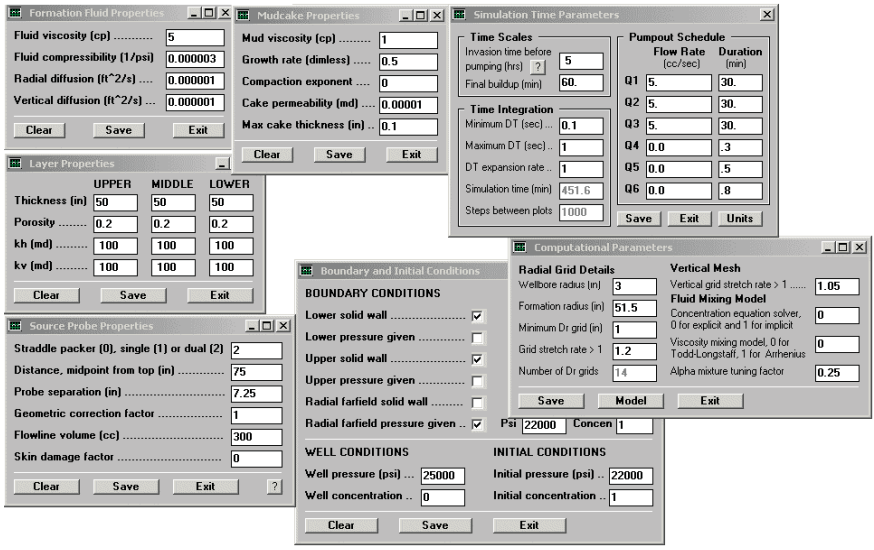

Figure 7.3.5a. Dual probe assumptions.

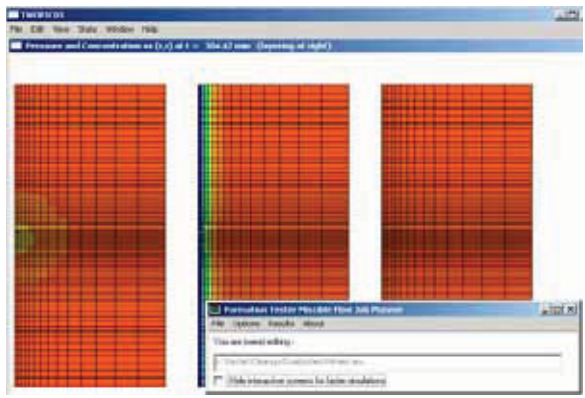

Figure 7.3.5b. Dual probe pressure-concentration fields (304 min).

The pressure probe line plot in Figure 7.3.5c is very informative. Recall that, for the single-probe run, the minimum pressure achieved was 21,850 psi. In the present simulation, which assumes an identical volume flow rate schedule, the minimum pressure is about 21,925 psi, which is greater than that obtained for the single-probe run. This is correct and expected physically because the same flow rate is now pumped through two nozzles having greater total area, resulting in less pressure drawdown. The reader is cautioned,

however, from placing too much emphasis on the exact pressure difference of 75 psi, since the two runs were performed on slightly different grids. Figures 7.3.5d,e,f,g display the corresponding contamination, viscosity, flow rate and cumulative volume results. For dual-probe runs, contamination and viscosity are average values obtained for the two probes. Rates and cumulative volumes refer to combined production from both probes.

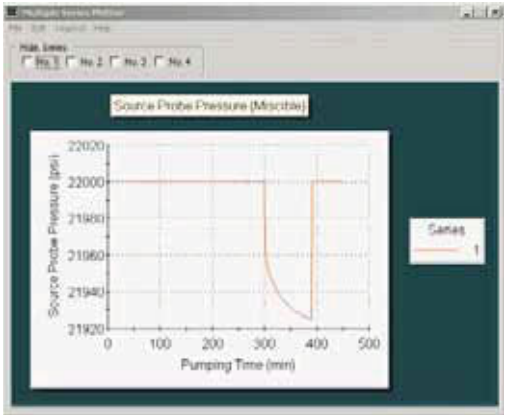

Figure 7.3.5c. Dual-probe source pressure.

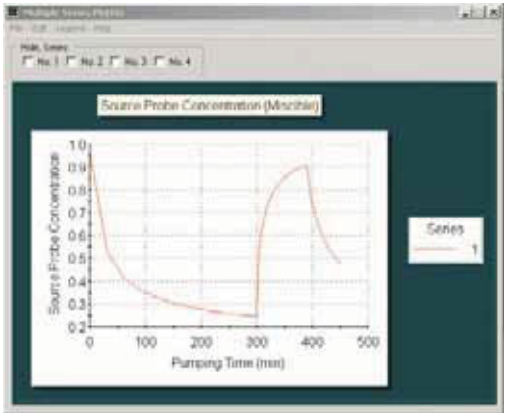

Figure 7.3.5d. Dual-probe average concentration.

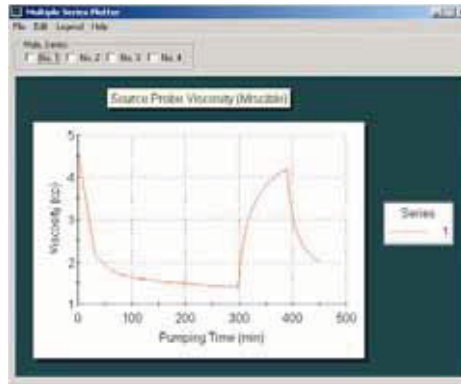

Figure 7.3.5e. Dual-probe average viscosity.

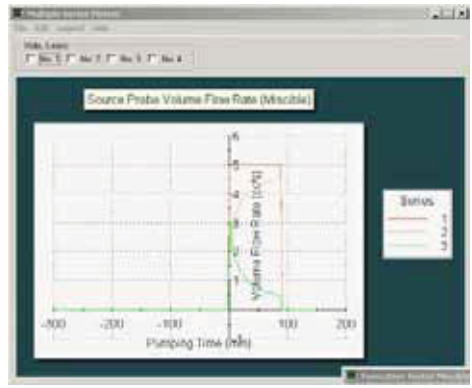

Figure 7.3.5f. Dual-probe combined volume flow rate.

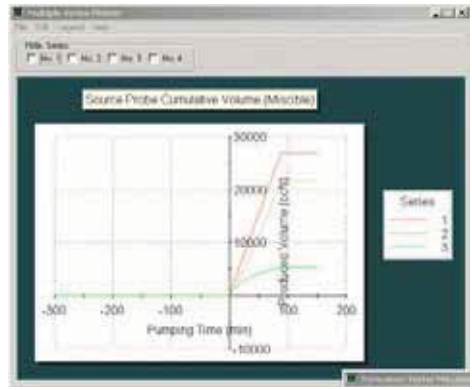

Figure 7.3.5g. Dual-probe cumulative volume production.

7.3.3. Run No. 3, Clean-up, elongated pad, uniform medium

Finally, to complete this first suite of three clean-up examples, we run an "elongated pad" clean-up simulation ("elongated pad," "oval pad" and "straddle packer" are used synonymously in this book since all are long in the axial direction). If the previous "ANS" file already exists, we can click on it and "recall old input menus for editing" as explained earlier. Once the required data is loaded, we can "Open All Menus" if desired, or we can open the only menu that has changed, in this case via the menu item in Figure 7.3.6a, leading to the input screen in Figure 7.3.6b.

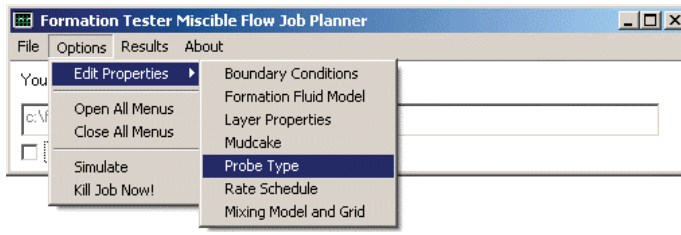

Figure 7.3.6a. Opening the source probe menu.

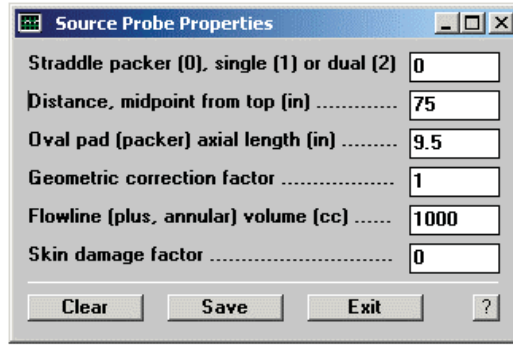

Figure 7.3.6b. Source probe menu.

The above menu shows that we have selected the "Straddle packer" probe option, which also models "oval pad" and "elongated sources." The packer axial length to 9.5 inches. If we now select "Options > Simulate," the following example "pressure-concentration" color screens for the reservoir cross-section are obtained. Figures 7.3.6c,d,e clearly show the increased domain of influence and depth of investigation exerted by the more elongated source. The front text box, again, indicates the filename of the ANS simulation under consideration. It is important to observe wider color contrasts than those obtained previously. This is consistent with rapid flow changes due to increased pumping rate.

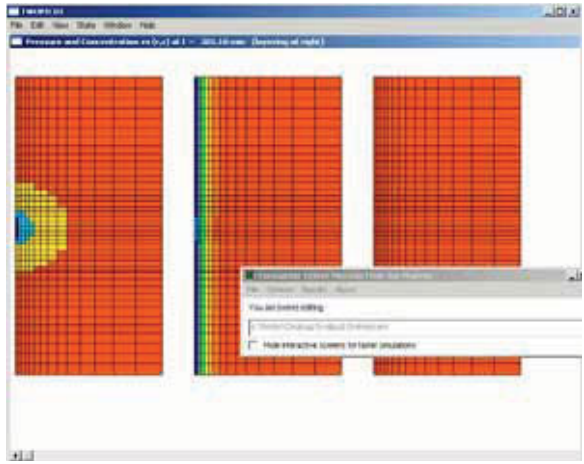

Figure 7.3.6c. Elongated pad pumping (301 min).

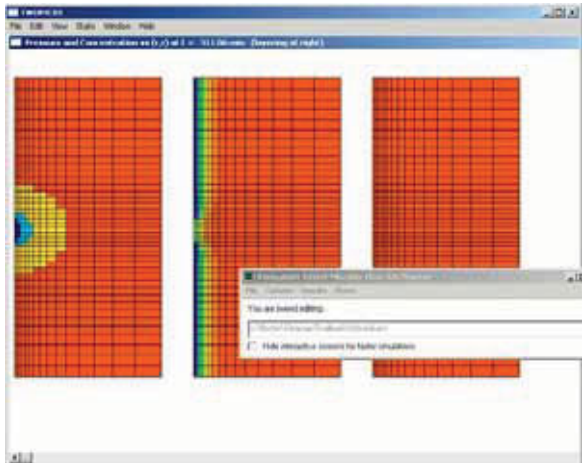

Figure 7.3.6d. Elongated pad pumping (311 min).

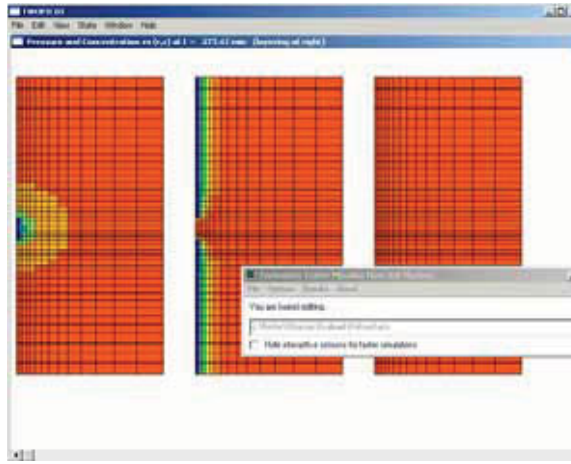

Figure 7.3.6e. Elongated pad pumping (377 min).

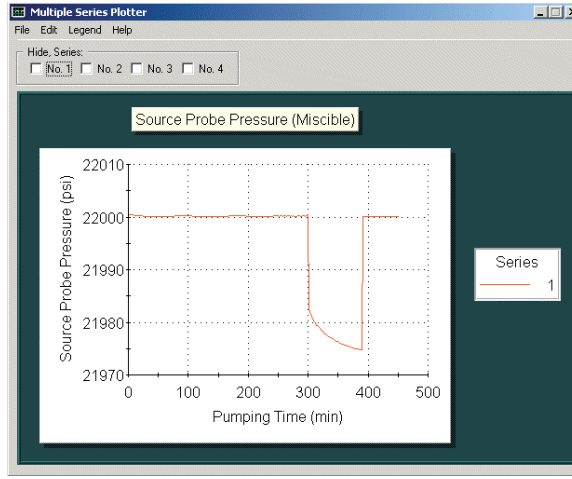

Figure 7.3.6f. Elongated pad source pressure.

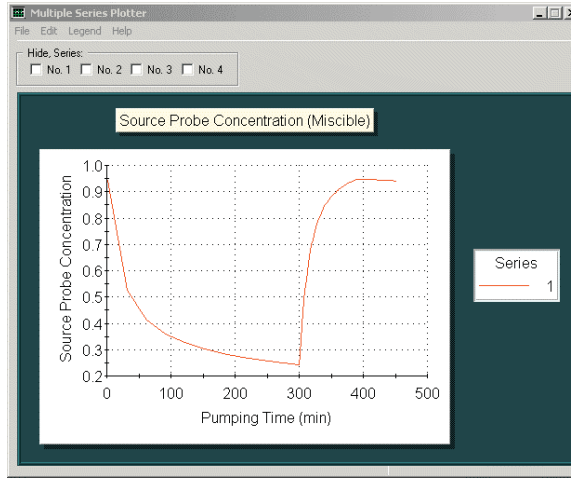

Figure 7.3.6g. Elongated pad concentration (center value).

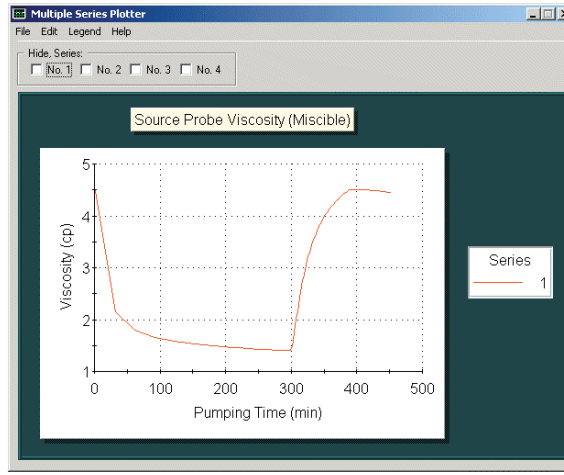

Figure 7.3.6h. Elongated pad viscosity (center value).

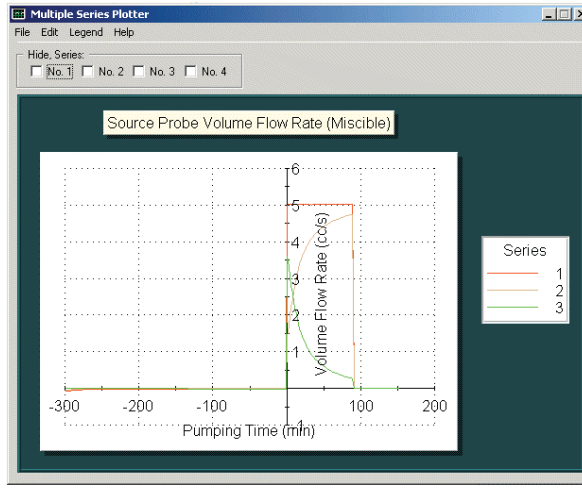

Figure 7.3.6i. Elongated pad volume flow rate.

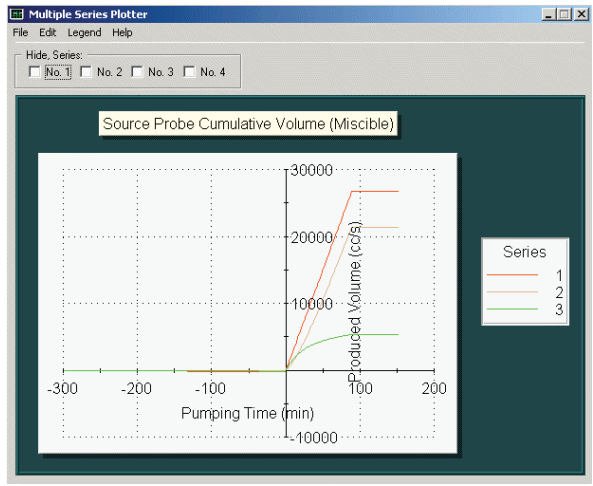

Figure 7.3.6j. Elongated pad cumulative volume.

Note that all three runs considered so far assume the same volume flow rate pumping schedule. This was done for illustrative purposes, in order to show that computed pressures are physically realistic when comparing different runs with different types of probes but identical flow rates. It is instructive to recall the minimum pressures obtained in our two previous runs. For the single probe tool, we had a minimum of 21,850 psi – this pressure is low because all of the

formation fluid is forced to travel through a single probe. When we replaced the single-probe tool with a dual probe tool, the increase in pumping area meant that an intense drawdown was not needed – in fact, a higher value of 21,925 psi sufficed. The use of an elongated pad, with a further significant increase in pumping area and its accompanying reduced resistance to flow allows a still higher source probe pressure, in this case 21,975 psi. We emphasize that slightly different grid systems are used for different probe types, so that the numbers should not be interpreted too literally; however, the order-of-magnitude pressure differences seen from run to run are qualitatively (and probably, to some degree, quantitatively) correct.

It is of interest to compare the concentration history of Figure 7.3.4h to that in Figure 7.3.6g above. In the former, source probe concentration decreases as filtrate invasion initially contaminates the formation; then, the concentration rebounds toward unity, and then rapidly falls when pumping stops and invasion continues. This late-time drop-off is less apparent for the oval pad run, as seen from Figure 7.3.6g – no rapid concentration drop-off is apparent at all. One would attribute this to the rapid cleaning allowed by oval pad pumping. More clean formation fluid replaces the dirty fluid removed by the pumping action, and the effect of continuing invasion through the relatively impermeable mudcake is less. Figures 7.3.6h,i,j provide the corresponding viscosity, flow rate and cumulative volume curves.

7.3.4. Run No. 4, A minimal invasion example

We close our discussions with several derivative calculations based on the "elongated pad" menus that are already open (these menus are "opened" whether or not they are visible). These additional examples illustrate the power and versatility of the user interface developed for the simulator and also indicate the physical correctness of the simulations. To perform our first derivative calculation, we "Open All Menus" so that the submenus corresponding to the run just completed appear on screen. In the "Simulation Time Parameters" submenu, we reduce the "Invasion time before pumping (hrs)" from five hours to 0.25 hours or fifteen minutes. This choice might simulate a formation testing while drilling application, e.g., a field scenario with very rapid drilling rates of penetration. The complete menus are shown in Figure 7.3.7a.

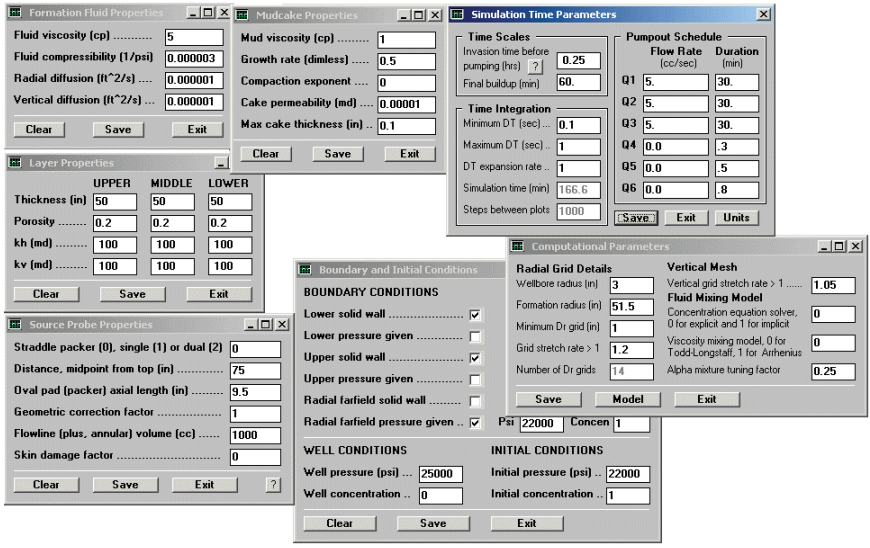

Figure 7.3.7a. A "formation testing while drilling" run with minimal invasion.

The computed results are very instructive. Figure 7.3.7b shows a typical "pressure-concentration" color screen obtained during the simulation. The pressure transient shown in Figure 7.3.7c, instead of continually decreasing as in the foregoing three runs, more or less equilibrates quickly and then actually increases. This occurs because, in this instance, the fluid in the overall neighborhood of the elongated pad – which is 9.5 inches in extent – is becoming less viscous due to invasion by lower viscosity filtrate. This will not be evident from Figure 7.3.7d, which gives viscosities at the center of the pad – viscosities near the ends of the pad are much lower due to less adequate cleaning. Figures 7.3.7d and 7.3.7e show that, in this example with minimal filtrate invasion due to the relatively impermeable mudcake, that the cleanup process is very efficient – the reservoir fluid (with a viscosity of 5 cp and a concentration of 1) is recovered quickly. Figures 7.3.7f and 7.3.7g indicate that the fluid pumped is largely reservoir fluid.

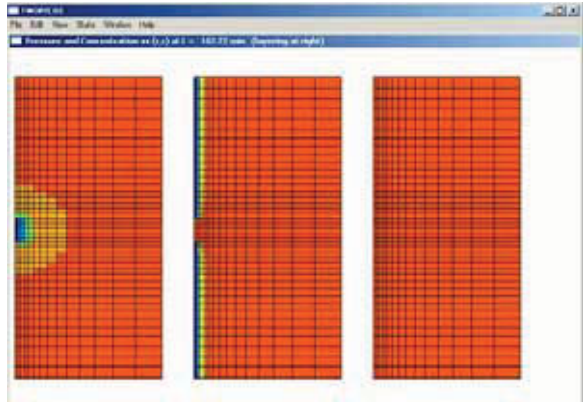

Figure 7.3.7b. A "formation testing while drilling" simulation (102 min).

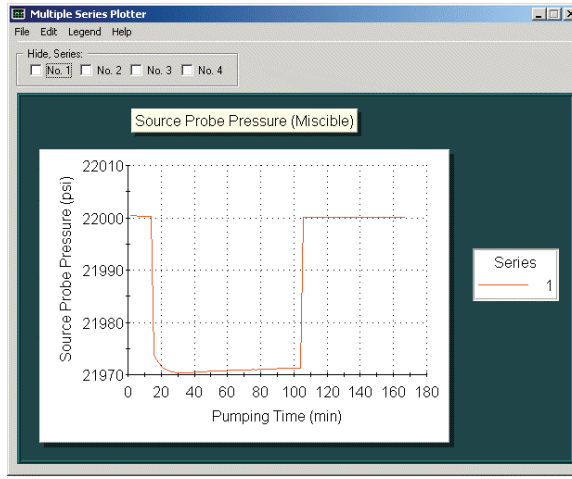

Figure 7.3.7c. A "formation testing while drilling" simulation.

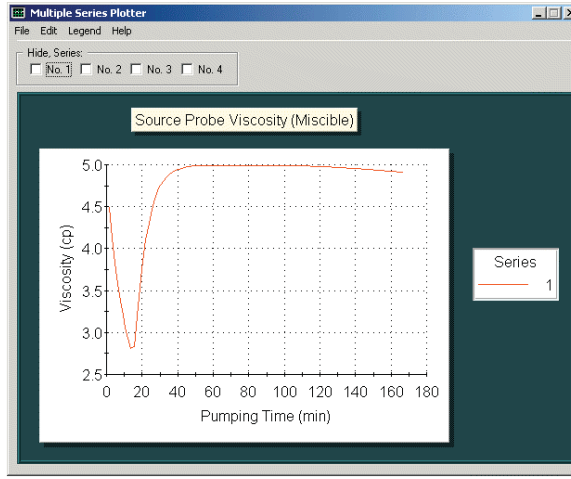

Figure 7.3.7d. A "formation testing while drilling" simulation.

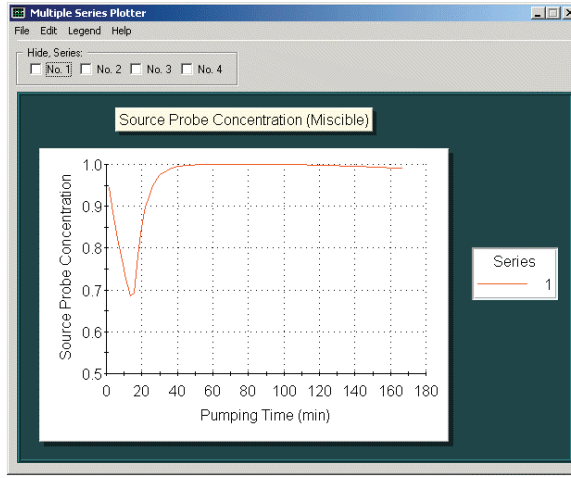

Figure 7.3.7e. A "formation testing while drilling" simulation.

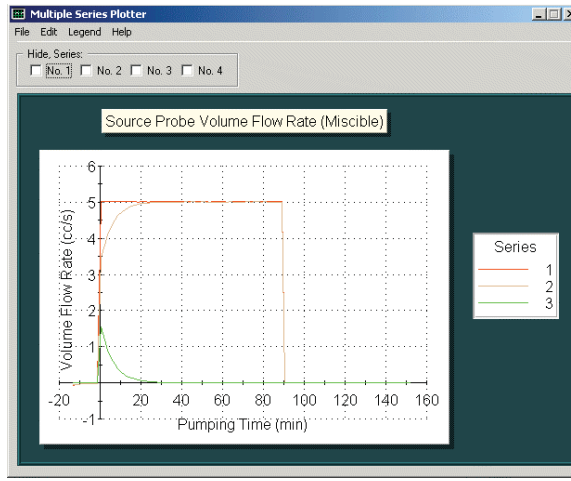

Figure 7.3.7f. A "formation testing while drilling" simulation.

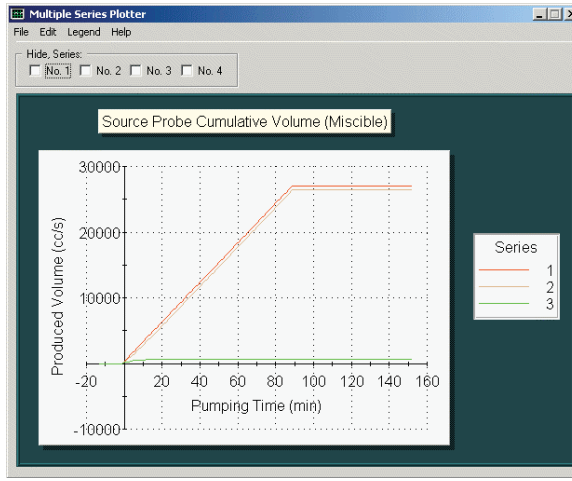

Figure 7.3.7g. A "formation testing while drilling" simulation.

7.3.5. Run No. 5, A single-phase fluid, constant viscosity example

In the present run, we make one change to the input assumptions of the previous simulation – the formation fluid viscosity is changed to 1 cp, so that it is identical to that of the mud filtrate. Thus, this run applies to a single-phase fluid. We caution that this simulator models the pumping in the presence of a borehole with nonzero radius – thus, the model is inherently different from idealized analytical models that assume purely spherical isotropic (or ellipsoidal, in the case of transversely isotropic media) flow and hence no borehole.

Both models are only consistent in the limit of extremely large borehole radii. This run was designed to verify the statement made in the previous run, explaining why the pressure curve turned upward slightly with time – again, we argued that the increase in pressure was due to decreased viscosity arising from filtrate invasion at the ends of the elongated pad. In this run, we emphasize that we have the same elongated pad source and that all other parameters remain unchanged, as indicated in Figure 7.3.8a. The pressure trace obtained at the end of the simulation is shown in Figure 7.3.8b. The bottom-out pressure of 21,993.5 psi is higher than the 21,970 psi obtained in Figure 7.3.7c because the constant viscosity of 1 cp here is much less than the average mixture viscosity of the previous run. The trace, aside from some minor numerical oscillation, is horizontal with time, as it should be in a high 100 md permeability formation.

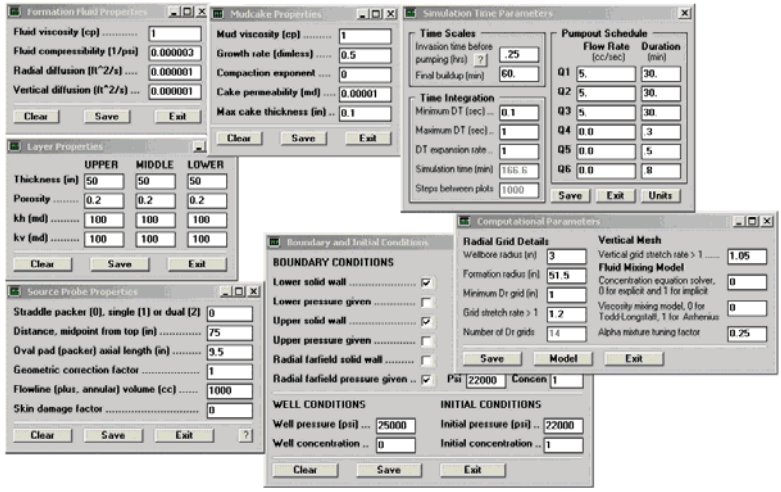

Figure 7.3.8a. A constant viscosity run.

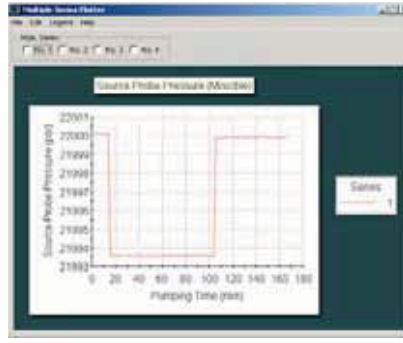

Figure 7.3.8b. A constant viscosity run.

7.3.6. Run No. 6, A low-permeability "supercharging" example

We now modify the above example by decreasing all formation permeability values from 100 md to 1 md. Also, we increase the mudcake permeability from 0.00001 md to 0.001 md. This example demonstrates the effects of invasion in low permeability reservoirs – in other words, we wish to observe "supercharging" as it evolves dynamically. The assumed menus are shown in Figure 7.3.9a.

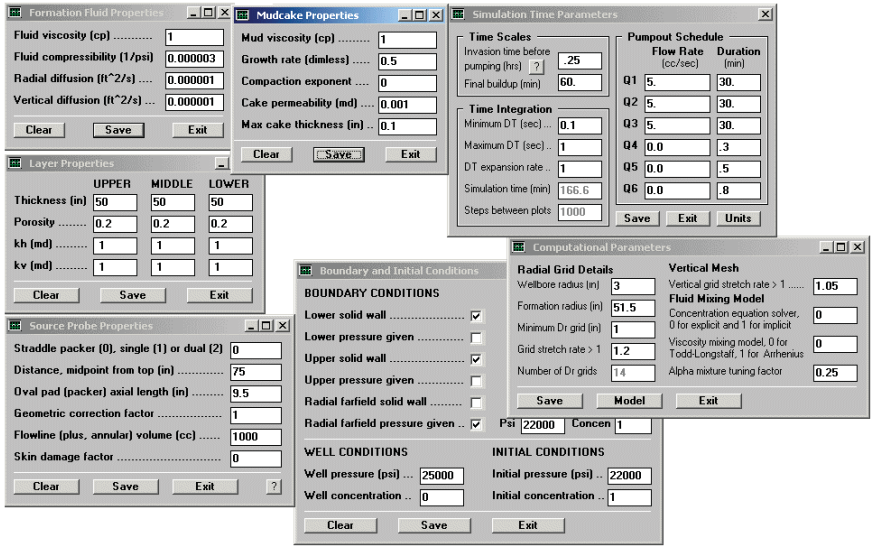

Figure 7.3.9a. A low permeability "supercharging" example.

This is a rather interesting run. Unlike the previous simulations in which our color pressure plots possessed more or less uniform red pressures, with only a small blue zone near the source probe, the pressure plots obtained here are much more colorful. Figure 7.3.9b displays the initial pressure and concentration fields associated with purely cylindrical radial invasion before pumping commences. Figures 7.3.9c and 7.3.9d display solutions obtained at two later instants in time.

The pressure plots are especially significant. While the probe is naturally associated with a low-pressure blue zone, it is of interest to observe the higher red pressures obtained adjacent to the probe along the sidewall of the well. This high pressure is indicative of "supercharging," that is, the high pressure resident in the borehole mud. The pressure measured by the tool in practice, and that calculated by the present simulator, is a combination of the pressure based on the mud pressure and the formation pore pressure.

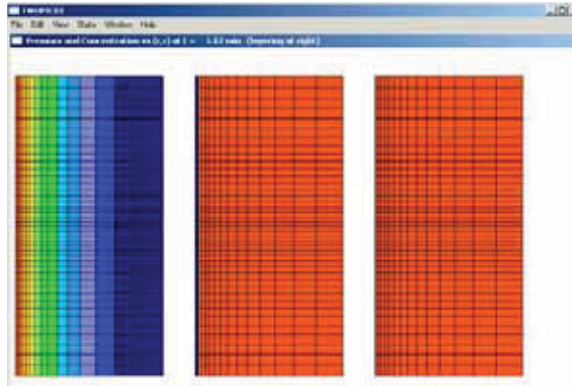

Figure 7.3.9b. A low permeability "supercharging" example (1.67 min).

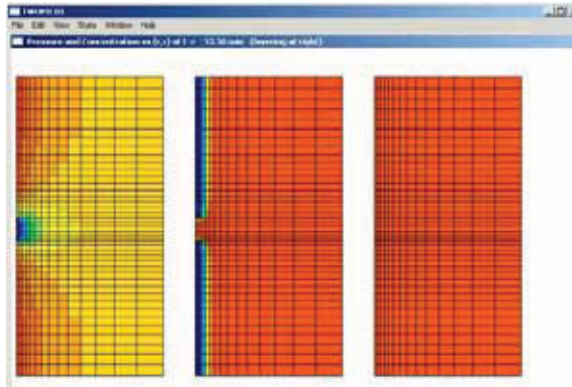

Figure 7.3.9c. A low permeability "supercharging" example (55 min).

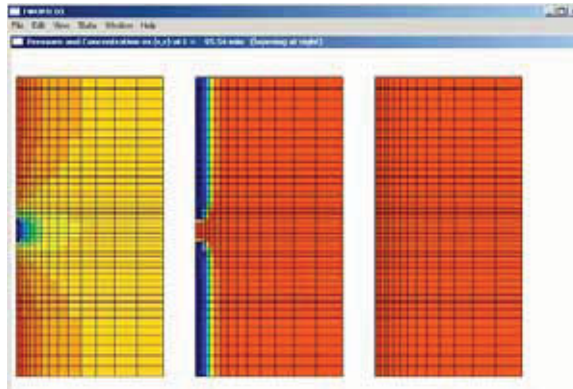

Figure 7.3.9d. A low permeability "supercharging" example (95 min).

The probe does *not* read formation pore pressure – the present simulator can be used to assist in proper extrapolation of pore pressure from measured readings. These figures also demonstrate that pressure variations and actual fluid invasion occur on different time scales. Pressure equilibrates much more rapidly while invasion is ongoing. In a way, this is expected for two reasons. First, the steady-state pressure distribution in an all-oil formation is identical to that in an all-water formation, and is independent of viscosity – and second, invasion will occur even in a "water-water" situation even without fluid changes. At the end of the simulation, the line plots discussed earlier appear automatically, but for brevity they are not reproduced here.

7.3.7. Run No., A three-layer simulation

We now reduce all formation permeabilities to 0.1 md; also, instead of the porosity taking the value of 0.2 in all three layers, we assume 0.1 in the middle layer. Our simulation assumptions are given in Figure 7.3.10a. Notice that we have changed our original permeabilities by several orders of magnitude. Also, the elongated pad is not centered in the grid. This decreased porosity implies more rapid invasion in the middle layer relative to the upper and lower layers. Together with the pumping that is occurring in this layer, a number of rapidly varying flow events are simultaneously evolving. Nonetheless, the simulator performs the required calculations with a high degree of numerical stability. This, together with the rapid middle layer invasion, is clearly seen in the time sequence of snapshots shown in Figures 7.3.10b,c,d,e. The diagrams at the far right of these figures indicate the relative heights associated with various layers. The present simulator, as is evident from the "Layer Properties" menu, permits arbitrary layer heights and formation properties. This concludes our discussion of diffusive miscible flow simulations.

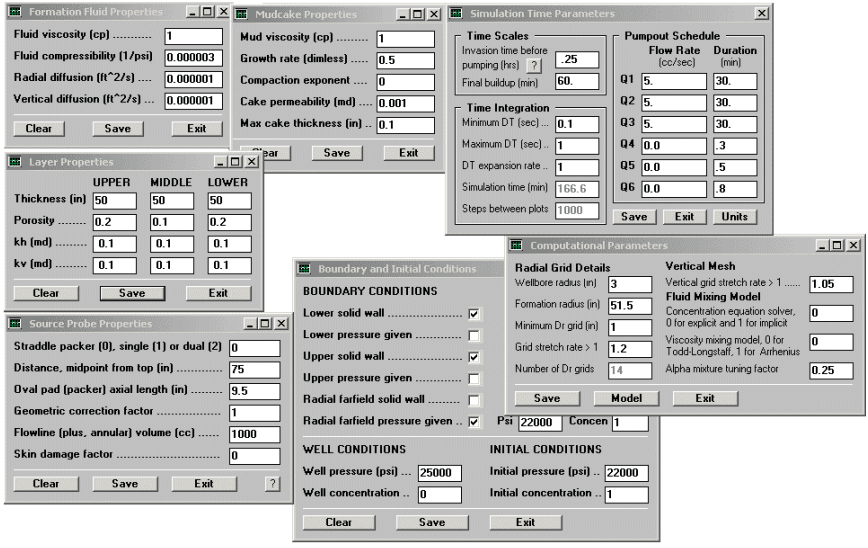

Figure 7.3.10a. Three layer run.

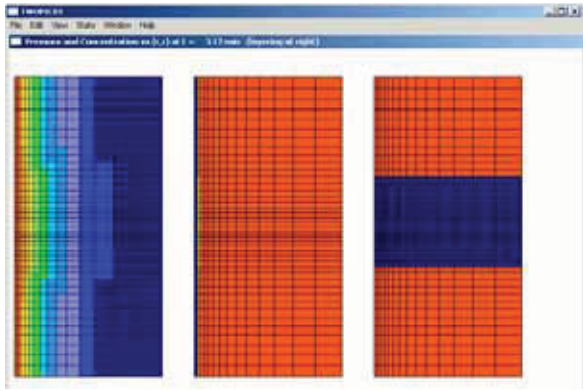

Figure 7.3.10b. Three layer cylindrical invasion before pumping (3 min).

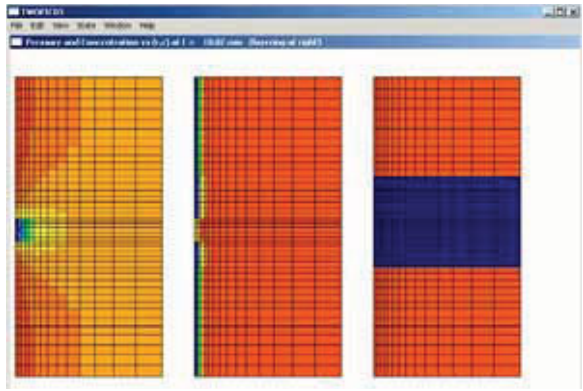

Figure 7.3.10c. Pumping in three-layer formation (18 min).

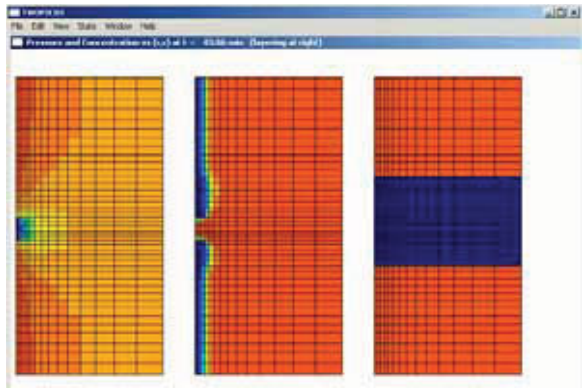

Figure 7.3.10d. Pumping in three-layer formation (83 min).

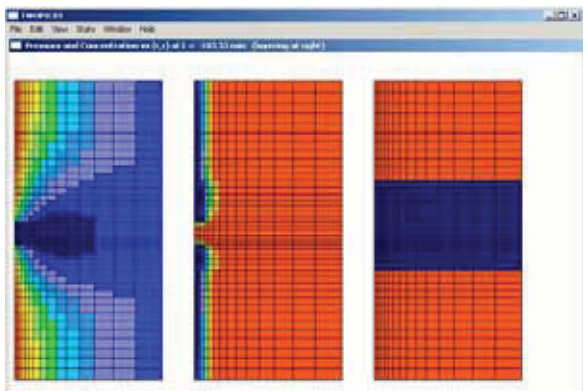

Figure 7.3.10e. Pumping in three-layer formation (105 min).

8
Time-Varying Flowline Volume

Large formation tester flowline volumes will distort pressure signals in low mobility environments, and transient Darcy pressures will be masked by mechanical compression and expansion effects that predicted permeabilities and pore pressures may not be accurate. Moreover, for inverse applications requiring observation probe data, predictive integrity may be compromised: signals can be simply bad or unmeasurable. Thus, we ask, "Is there a way to 'tune' the source probe pressure so that the overall prediction process is significantly improved?" The answer is, "Yes." Just as one tunes a radio or television to optimize reception, a formation tester can be tuned to optimize reception at one or more observation probes. A numerical simulator allowing for time-varying flowline volume is required, of course; it can be used to study how this reception can be improved and later incorporated in feedback and control electronics. In this chapter, the required algorithm is developed and different applications for flowline control are explored. Although this book emphasizes the key role of closed form analytical models whenever possible, the problem addressed in this chapter, because of its inherent difficulty, requires a computational approach. Why?

Simple analogy. Suppose one were to calculate the area of a circle, but did not have access to a calculator and the exact formula $A = \pi R^2$. An approximation might be the number of one-inch squares that fit within the perimeter; even better, half-inch or quarter inch squares might be used. Then again, why not rectangles or equilateral triangles? The particular choice and grid density define the "numerical algorithm," whose quality is determined by agreement with the exact solution. In our formation testing forward simulation work, the FT-00 algorithm provides one such exact "πR^2" solution. Although it is based on complicated "complex complementary error functions with complex arguments" which require numerical evaluation, the calculated solution is exact in an absolute sense.

Certain physical assumptions are taken, e.g., liquid, single-phase flow, constant flowline volume, ellipsoidal flow for transversely isotropic problems, and so on, but those of a numerical character are also used. In the case of our FT-00, we assume "piecewise constant" volume flow rates, that is, time intervals are characterized by flow rates that are constant, although that constant may vary from interval to interval. This assumption was made to enable exact, closed form, analytical solutions based on superposition methods that are useful for uncompromised results – results important to accurate forward modeling or in validating approximate inverse methods.

Algorithm FT-06, introduced in Chin *et al* (2014), on the other hand, is a numerical finite difference scheme that provides approximate solutions. However, it is highly flexible. For instance, (1) it can be used to model any type of time-dependent flow rate variation (pumping schedules may be triangular, trapezoidal, or even inputted as a numerical file, and (2) nonlinear gas transients are also permitted, since linear superposition methods are not used. In the same way that our use of rectangles or triangles in determining area must be "calibrated" by using an exact formula, FT-06 must be calibrated against FT-00 before first use in any application. Now, FT-06 was developed for constant flowline volumes that do not change in time. In this chapter, we envision time-varying flowline volumes, and on, our objective will be development of a numerically stable method to model such effects. The required calibration of FT-06 to FT-00 is discussed in the earlier book; here, algorithm FT-06 is extended to handle arbitrary changes that may be effected by mechanical volume controls.

8.1 Transient Anisotropic Formulation for Ellipsoidal Source

In this section, the equations governing transient linear liquid nonlinear gas flows are considered for formation tester applications. We will also solve the general problem using numerical finite difference integration schemes.

8.1.1 Formulation for liquids and gases

For slightly compressible, single-phase *liquids* in Darcy flow, the linear partial differential equation $k_v\ \partial^2P/\partial z^2 + k_h\ (\partial^2P/\partial x^2 + \partial^2P/\partial y^2\ ) = \phi\mu c\ \partial P/\partial t$ applies. When transient flows of gases are considered, this equation no longer holds. In the general case, Chin (2002) shows that

$$\partial\{k_x(x,y,z)/\mu\ \partial P^{m+1}/\partial x\}/\partial x + \partial\{k_y(x,y,z)/\mu\ \partial P^{m+1}/\partial y\}/\partial y + \partial\{k_z(x,y,z)/\mu\ \partial P^{m+1}/\partial z\}/\partial z = \phi c^*\ \partial P^{m+1}/\partial t \qquad (8.1)$$

where P(x,y,z,t) represents pressure with t denoting time and x, y and z the spatial coordinates. Here μ is the viscosity, ϕ is the porosity, and k_x, k_y and k_z

are permeabilities in the x, y and z directions. The dimensionless gas exponent "m" characterizes background thermodynamic conditions. It takes on the values

$$\begin{aligned} m &= 1, \text{ for isothermal expansion} \\ &= C_v/C_p, \text{ specific heat ratio for adiabatic expansion} \\ &= 0, \text{ for constant volume processes} \\ &= \infty, \text{ for constant pressure processes} \end{aligned} \tag{8.2}$$

The asterisked quantity

$$c^* = m/P(x,y,z,t) \tag{8.3}$$

plays the role of a compressibility and has dimensions of compressibility – in fact, we will show that it physically *is* the gas compressibility for an equivalent liquid to be defined later. However, its dependence on pressure renders Equation 8.1 nonlinear and therefore not amenable to analytical solution.

The above system must be solved together with additional constraints. The required initial and farfield auxiliary conditions are, respectively, $P(x,y,z,0) = P_0$ and $P(x,y,z,t) = P_0$ as $x^2 + y^2 + z^2 \to \infty$ with P_0 being the pore pressure. To complete the boundary value problem specification, pumpout conditions imposed at an effective ellipsoidal source surface Σ must be prescribed. We assume a transversely isotropic medium, with constant horizontal and vertical permeabilities $k_h = k_x = k_y$ and $k_v = k_z$. As in Chin (2014), we take Σ in the form

$$x^2/k_h + y^2/k_h + z^2/k_v = R_w^2 /(k_h^{2/3}k_v^{1/3}) \tag{8.4}$$

where R_W is a dimensional "effective ellipsoidal radius," which reduces to the spherical radius in "$x^2 + y^2 + z^2 = R_w^2$" for isotropic flows (where R_w would be a true radius). Its exact value is determined empirically using laboratory or field data, and will, of course, depend on pad geometry, borehole curvature and so on.

In general, the pumpout boundary condition applied on the surface Σ can be expressed in the form

$$-\int_\Sigma \mathbf{q} \cdot \mathbf{n}\, dS - VC\, \partial P/\partial t = Q(t) \tag{8.5}$$

where $\mathbf{q}$ is the Darcy velocity vector, dS is a differential surface area, $\mathbf{n}$ is the unit normal to dS, the area Σ represents the entire closed surface, and Q(t) is the prescribed total volume flow rate (the effects of skin damage at the nozzle, not modeled in the above relationship, will be discussed separately).

Equation 8.5 expresses volume conservation at the source. The $VC\, \partial P/\partial t$ term models the effects of flowline storage, i.e., the compression and expansion of fluid already within the formation tester hardware, where V is the flowline volume and C is the compressibility of the fluid within the lines, not necessarily equal to the formation fluid compressibility c. In practical applications, C may also be time-dependent – additionally, flowline composition may be affected by

condensation, fluid segregation, phase changes and other physical effects occurring within the flowline.

The closed surface integral at the left of Equation 8.5 represents the Darcy flow contribution to the total volume flowrate, e.g., $(k/\mu)\ \partial P/\partial r \times 4\pi R_w^2$ in a spherically symmetric isotropic flow. In this expression, $\partial P/\partial r$ would represent the pressure derivative with respect to the radial coordinate r and $4\pi R_w^2$ would represent the spherical surface area at the source radius R_w through which the velocity $(k/\mu)\ \partial P/\partial r$ flows. However, the integral takes a much more complicated structure in anisotropic media. In transversely isotropic media, the more general Darcy velocity takes the non-symmetric form

$$\mathbf{q} = -(k_h/\mu)\ \partial P/\partial x\ \mathbf{i} - (k_h/\mu)\ \partial P/\partial y\ \mathbf{j} - (k_v/\mu)\ \partial P/\partial z\ \mathbf{k} \tag{8.6}$$

where **i**, **j** and **k** are unit vectors in the x, y and z directions – to complicate matters, only the velocity flux normal to the ellipsoidal surface in Equation 8.4 contributes to Q(t) – making the integral in Equation 8.5 somewhat unwieldy.

8.1.2 Similarity transform

Although Equations 8.1 to 8.6 are correct, they are not immediately useful for analysis. To simplify the appearance of the general formulation, we introduce the dimensionless radial variable

$$r^* = \{x^2/k_h + y^2/k_h + z^2/k_v\}^{1/2} \tag{8.7}$$

Then, since $k_v\ \partial^2/\partial z^2 + k_h\ (\partial^2/\partial x^2 + \partial^2/\partial y^2) = \partial^2/\partial r^{*2} + 2/r^*\ \partial/\partial r^*$ holds, Equation 8.1 takes on a spherically symmetric form given by Equation 8.8, where we have additionally assumed that μ is constant (in field practice, slight variations of μ with P may be handled by using average values) in order to render mathematical simplifications.

Less obvious is the structure of the integral in Equation 8.5. However, the detailed analysis given in Chapter 5 of Chin (2014), which also applies to gas flows without change, leads to the complementary spherically symmetric boundary condition given by Equations 8.8 and 8.8. The complete boundary value problem can then be succinctly summarized, that is,

$$\partial^2 P^{m+1}/\partial r^{*2} + 2/r^*\ \partial P^{m+1}/\partial r^* = \phi\mu c^*\ \partial P^{m+1}/\partial t \tag{8.8}$$

$$(4\pi R_w^2\ k_v^{1/6}\ k_h^{1/3}/\mu)\ (\partial P/\partial r^*)_w - VC\ \partial P/\partial t = Q(t) \text{ along } \Sigma \tag{8.9}$$

$$P(x,y,z,0) = P_0 \tag{8.10}$$

$$P(x,y,z,t) = P_0 \text{ as } x^2 + y^2 + z^2 \to \infty \tag{8.11}$$

Note that the partial differential equation in Equation 8.8, so far containing both dimensional and nondimensional variables, is one for the function P^{m+1} – the coefficients shown arise from our use of Equation 8.7. Also note that the R_w in Equation 8.9 refers to the ellipsoidal surface in Equation 8.4. We further observe that Equation 8.9 does not include skin effects (the inclusion of skin

effects would introduce a term proportional to $\partial^2 P/\partial r \partial t$ on the left-hand-side). The above model assumes zero skin effects – skin is later considered numerically in Equation 8.19.

8.1.3 Transient flow numerical modeling

We wish to develop a method suitable for both liquids and gases. But for nonlinear gas flows, linear superposition methods applicable to liquids cannot be used. Some authors linearize pressure-dependent coefficients about "suitable" average values. Such practices introduce uncertainties that are difficult to quantify. In the final analysis, a direct numerical solution of the transient equations is required. There are many strategies to pursue, each offering unique advantages as well as disadvantages. In this section, we assume transversely isotropic formations that are infinite in extent – that is, we assume that time scales are short enough (or dissipation strong enough) that the effects of lateral boundaries associated with beds and bedding planes are negligibly small. This is a reasonable assumption for formation testers, since net volumes pumped are not large but relatively small.

When this is the case, the dimensionless radial variable introduced in Equation 8.7, namely, $r^* = \{x^2/k_h + y^2/k_h + z^2/k_v\}^{1/2}$, again provides the natural means to describe pressure phenomena, and again the boundary value problem described by Equations 8.8 to 8.11 applies. Of course, solutions must now be obtained numerically by direct time integration. Ideally, it is best to draw upon existing stable methods developed for transient liquid flows, e.g., as developed in Chin (2002) – and fortunately, this practical alternative is possible.

In order to pursue this strategy, we observe that the second derivative of the function f^{m+1} can be expanded in the form

$$d^2 f^{m+1}/dr^2 = (m+1)\,[f^m\, d^2 f/dr^2 + m f^{m-1}(df/dr)^2] \approx (m+1) f^m\, d^2 f/dr^2 \qquad (8.12)$$

where the small quadratic term is negligible compared to other O(1) terms (also note that $df^{m+1}/dr = (m+1) f^m\, df/dr$). This is the conventional assumption used in deriving Equations 8.1 and 8.8 for both spherical and cylindrical flows. Therefore, we can consistently apply Equation 8.12 and replace Equation 8.8 by

$$\partial^2 P/\partial r^{*2} + 2/r^*\, \partial P/\partial r^* = \phi \mu c^*\, \partial P/\partial t \qquad (8.13)$$

Equation 8.13 is interesting in its own right, taking the form of the differential equation for liquid Darcy flow without "m" appearing explicitly – except by way of the pressure-dependent $c^* = m/P$ in Equation 8.3. In other words, the flow of a gas behaves like the flow of a linear liquid but with a pressure-dependent compressibility to leading order. This "local linearization" – not a real linearization at all – arises in other areas of continuum mechanics, for example, high-speed aerodynamics, nonlinear elasticity, and so on.

When formation porosity and permeabilities are both fixed, the lumped parameter "μc^*" is the only one that distinguishes liquid from gas diffusion. On

this basis, we might ask, "How diffusive is a typical liquid relative to a typical gas?" For water, $\mu = 1$ cp and $c = 0.000003$ psi^{-1}, so that $\mu c = 0.000003$ cp/psi – but for an isothermal gas, one might have $m = 1$, $\mu = 0.01$ cp, $P = 5{,}000$ psi, leading to $\mu c^* = (0.01 \text{ cp})(1)/(5{,}000 \text{ psi})$ or 0.000002 cp/psi. Thus, the two flows are comparable – assuming, again, the same porosity and permeabilities. However, this is not to say that linear superposition methods are applicable to gas modeling – they are not.

8.1.4 Finite difference equation

Because Equation 8.13 is nonlinear, classical analysis methods employing Laplace transforms and superposition integrals cannot be used. In this section, an implicit finite difference integration algorithm is developed. Finite difference models replace the continuum space of r by the discretized space r_1, r_2, r_3 and so on, and similarly the time space of t by t^1, t^2, t^3 and so on. In general, P(r,t) is approximated by $P(r_i,t^n)$ or simply $P_{i,n}$.

Consider, for example, a continuous function f(r) with continuous first and second derivatives as shown in Figure 8.1. Now, from the definition of the derivative, it is clear that

$$df/dr|_i = (f_{i+1} - f_{i-1})/(r_{i+1} - r_{i-1}) \tag{8.14}$$

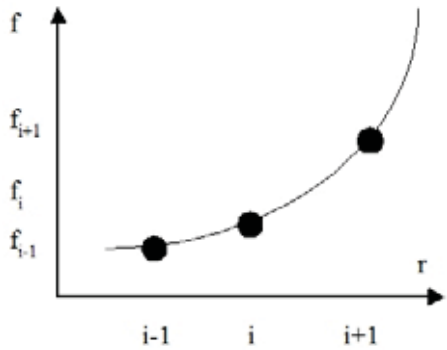

Figure 8.1. Finite difference discretization.

Then, twice application of Equation 8.14 leads to

$$d^2f/dr^2|_i = 2\,(f_{i+1} - f_i)\,/\{(r_{i+1} - r_i)\,(r_{i+1} - r_{i-1})\} - 2\,(f_i - f_{i-1})\,/\{(r_i - r_{i-1})\,(r_{i+1} - r_{i-1})\} \tag{8.15}$$

Equations 8.14 and 8.15 evaluate derivatives at "i" using function values to the left and right, and for this reason, represent "central difference" approximations. For the same mesh, such are more accurate than backward or forward difference schemes based on one-sided evaluations. Equation 8.13 contains both space and time derivatives. Consider the present time level t^n. If the spatial terms are

approximated at the (n-1)*th* time level and $\partial P/\partial t$ is represented by the backward difference $(P_{i,n} - P_{i,n-1})/\Delta t$, where the time step Δt may vary with time, an explicit formula for $P_{i,n}$ can be obtained in terms of quantities given earlier. This "explicit" method, yielding a formula amenable to simple pocket calculator analysis, is extremely unstable numerically and is almost never used in practice.

Instead, we approximate all spatial derivatives at the present n*th* time level. Then the use of Equations 8.14 and 8.15 in 8.13 leads to, upon some rearrangement, a finite difference representation of the form

$$\begin{aligned} &[1/(r^*_i - r^*_{i-1}) - 1/r^*_i]\, P_{i-1,n} \\ &-[1/(r^*_{i+1} - r^*_i) + 1/(r^*_i - r^*_{i-1}) + \phi\mu c^*(r^*_{i+1} - r^*_{i-1})/(2\Delta t)]\, P_{i,n} \\ &+[1/(r^*_{i+1} - r^*_i) + 1/r^*_i]\, P_{i+1,n} \\ &= -\phi\mu c^*(r^*_{i+1} - r^*_{i-1})P_{i,n-1}/(2\Delta t) \end{aligned} \tag{8.16}$$

8.1.5 Boundary conditions – flowline storage with and without skin effects

We now turn to the zero skin pumpout boundary condition $(4\pi R_w^2\, k_v^{1/6}\, k_h^{1/3}/\mu)\ (\partial P/\partial r^*)_w - VC\ \partial P/\partial t = Q(t)$ in Equation 8.9, which we emphasize is physically applied at the actual ellipsoidal surface

$$x^2/k_h + y^2/k_h + z^2/k_v = R_w^2/(k_v^{1/3}k_h^{2/3}) \tag{8.17}$$

and not at a virtual origin. In terms of the dimensionless radius r^* in our Equation 8.7, Equation 8.17 takes the form $x^2/k_h + y^2/k_h + z^2/k_v = r^{*2}_w$ where $r^*_w = R_w/(k_v^{1/6}k_h^{1/3})$.

How is this interpreted and used? For simplicity, first consider an isotropic flow with a permeability k – Equation 8.17 would describe the sphere $x^2 + y^2 + z^2 = R_w^2$ where R_w is an actual radius, while the dimensionless radius would take on the value $r^*_w = R_w/k^{1/2}$. In other words, the dimensionless domain is defined on $R_w/k^{1/2} \le r^* < \infty$ while the dimensional time domain would be defined on the range $0 \le t < \infty$.

For an anisotropic problem, the dimensional R_w would represent an effective radius determined empirically using laboratory or field data. The dimensionless radius $r^*_w = R_w/(k_v^{1/6}k_h^{1/3})$ is calculated from available permeabilities. Then the dimensionless domain $R_w/(k_v^{1/6}k_h^{1/3}) \le r^* < \infty$ is the one selected for finite difference computation. Once $P(r^*,t)$ is computationally available, source point values are obtained at $r^*_w = R_w/(k_v^{1/6}k_h^{1/3})$ while pressures at the observation probe are found at $r^* = L\ \{\sin^2\delta/k_h + \cos^2\delta\ /k_v\}^{1/2}$ where L is the probe separation and δ is the dip angle (this is derived later).

Now consider actual discretizations. If i = 1 denotes the surface of the ellipsoid in Equation 8.17, so that i = 2 is the node external to i = 1, our Equation 8.9 can be differenced as

$$- [( )/(r_2 - r_1) + VC/\Delta t] P_{1,n} + ( )/(r_2 - r_1) P_{2,n} = - VCP_{1,n-1}/\Delta t + Q_n \qquad (8.18a)$$

where ( ) denotes $(4\pi R_w^2 k_v^{1/6} k_h^{1/3}/\mu)$ and $Q_n = Q(t^n)$. The initial and farfield conditions in Equations 8.10 and 8.11 become, respectively,

$$P_{i,1} = P_0 \qquad (8.18b)$$

$$P_{imax,n} = P_0 \qquad (8.18c)$$

where $i = i_{max}$ is a sufficiently large index corresponding to farfield locations which – owing to Darcy diffusion – are unlikely to be affected by pump actions.

If skin effects are completely ignored, the boundary condition is given by Equation 8.9, that is, $(4\pi R_w^2 k_v^{1/6} k_h^{1/3}/\mu)\ \partial P/\partial r^* - VC\ \partial P/\partial t = Q(t)$, where P is the sandface pressure. When skin is to be accounted for, with S being the dimensionless skin factor, there exists an additional pressure drop through the surface resistance. If P again denotes sandface pressure, the source pressure boundary condition takes the form

$$(4\pi R_w^2 k_v^{1/6} k_h^{1/3}/\mu)\ \partial P/\partial r^* - VC\ \partial P/\partial t + \{R_w VCS/(k_v^{1/6} k_h^{1/3})\}\ \partial^2 P/\partial t \partial r^* = Q(t) \qquad (8.19)$$

with an additional second-order mixed derivative term. The pressure inside the tool, that is, the pressure within the source (external to the reservoir) is computed from

$$P_w = P - \{R_w S/(k_v^{1/6} k_h^{1/3})\}\ \partial P/\partial\partial r^* \qquad (8.20)$$

Equation 8.20 does not apply at the observation probe.

8.1.6 Detailed time integration scheme

The numerical integration of Equation 8.13 is straightforwardly performed. The state of the reservoir initially is described by Equation 8.18b for n = 1. Consider the next time step n = 2 and write Equation 8.16 for the internal nodes i = 2, 3, 4, . . . , i_{max}-1 to obtain i_{max}-2 equations in i_{max} unknowns. Two additional constraints are offered by Equations 8.18a and 8.18c. Each of the equations in the resulting coefficient matrix contains at most three unknowns. Such tridiagonal equations are very efficiently inverted. For example, a matrix with N unknowns requires O(3N) arithmetic operations for inversion versus, say, $O(N^3)$ for Gaussian elimination.

Once the inversion is accomplished, transient pressure solutions are available for n = 2, and the process is repeated for n = 3 and so on. Explicit schemes, as we have noted, are unstable and lead to unusable solutions. In contrast, the integration of Equation 8.16 is stable and allows larger time steps. This stability arises from the diagonal dominance of the scheme developed here

– that is, the absolute value of the middle diagonal exceeds the sum of the absolute values of the sidebands.

Equation 8.18a applies to skin-free problems. When the influence of skin cannot be ignored, stable numerical time integrations are achieved by computing the second-order mixed derivative in Equation 8.19 using the formula $\partial^2 P/\partial t \partial r^* = (P_{2,n} - P_{2,n-1} - P_{1,n} + P_{1,n-1})/\{(r^*_2 - r^*_1)\,\Delta t\}$ at the sandface i = 1 and time $t = t_n$.

8.1.7 Observation probe response

The pressure response at the source probe does not depend on dip angle – it is, of course, a function of all other fluid, formation and tool properties discussed so far. Observation probe response depends on probe separation L and dip angle δ, e.g., see Figure 8.2. In our finite difference calculations, the dimensional pressure $P(r^*,t)$ in Equation 8.13 is stored as an output array file. It can be interrogated for pressure values for all values of L and δ. The required r^* is found by setting $x^2 + y^2 = L^2 \sin^2\delta$ and $z = L \cos\delta$ in Equation 8.7 to produce $r^* = L\ \{\sin^2\delta/k_h + \cos^2\delta/k_v\}^{1/2}$. If this value does not coincide with a spatial node, its associated pressure can be obtained by linear interpolation of pressure values obtained at the observation point's left and right pressure values.

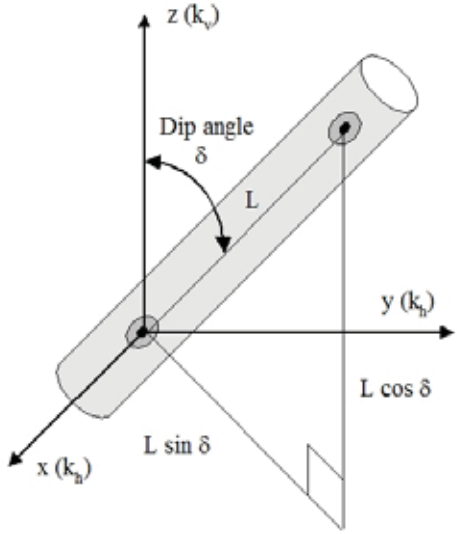

Figure 8.2. Dip angle δ in transversely isotropic media.

8.2 FT-06 Software Interface and Example Calculations

A powerful Windows-based graphical user interface has been designed to host several simulation models and analytical limits developed. The numerical transient gas *and liquid* solver screen menu system is displayed in Figure 8.3a, showing text boxes for fundamental input parameters. Again, FT-06 applies to constant flowline volumes which do not change in time – extensions to FT-07 for time-varying problems are discussed later. The volume flowrate schedule shown at the right, easily edited by the user, can be displayed on-screen by clicking "Display." Note that both continuous and discontinuous rates, which can be positive and negative, can be inputted in any order to model very general operating conditions.

Figure 8.3b emphasizes that both (nonlinear) gas and (linear) liquid transient responses are handled by two program codes incorporated within the simulator. The default selection chooses "liquid." If this is changed to "gas," a message screen appears that suggests typical values of the thermodynamic exponent needed to model variable compressibility appropriately. If the user returns to "liquid," a reminder appears which gives the constant compressibility assumed by water. Note how the label of the corresponding input boxes alternates between "Dimensionless exponent M" and "Compressibility (1/psi)."

Very often, it is inconvenient to construct rate schedules at the keyboard – very complicated transients, in fact, cannot be inputted. Previously stored schedules representing fully transient rates, e.g., created by other compiled programs, spreadsheet routines or actual tool production profiles, may be stored on the hard drive for use in subsequent applications. Entire ASCII file libraries of rate schedules can be created following simple rules and stored for future use. This option is activated by checking "Read transient flow rate from file" at the bottom right of the input screen, as shown in Figure 8.3c. Discontinuous piecewise constant rates are used in conventional tester applications to model step changes, while continuous rates, e.g., the triangular or trapezoidal functions, can be used to model gas pumping or non-ideal pump piston effects. Short or long periodic flowrates, for instance, can be used to facilitate "pulse interaction" inverse analysis, e.g., see Chin *et al* (2014) or "phase delay" permeability prediction (see Chapter 4 for details) in a completely nonlinear setting.

Checking this box overrides the displayed schedule, causing two messages to appear. The first reminds the user that the on-screen schedule will be ignored, while the second informs him that fine time increments of 0.01 sec between flow rate entries are (and must be) assumed for all stored rate files. Figure 8.3d displays the list box that appears once the "read file" option is selected. The desired rate is chosen by clicking on the appropriate "rte" file previously constructed and named by the user. This produces the flow rate display shown. Clicking on "Select" activates the selection for simulation purposes.

The double-pulse displayed, incidentally, is used in powerful source-to-observation-probe "phase delay" studies which assess permeability in tight formations. Additional simulation options are possible. These include, for example, time-dependent flowline compressibilities that model liquid-gas phase segregation within the tool, initial spatial grid selections adjacent to the spherical source, more complicated viscosity functions, and so on.

Again, all gas integrations involve a nonlinear partial differential equation with pressure-dependent compressibilities. Figure 8.3e illustrates one example of an extended user interface developed recently. Unlike the basic model shown in Figure 8.3a, the extension allows users to (1) specify the spherical permeability k_s and the anisotropy k_v/k_h instead of k_v and k_h – text labels, as shown, automatically change when different options are selected, (2) define the initial finite difference spatial grid as a percentage of the spherical (ellipsoidal) radius, and (3) prescribe a dimensionless geometric factor to model changes to source radius as they would depend on borehole size, pad dimensions and so on.

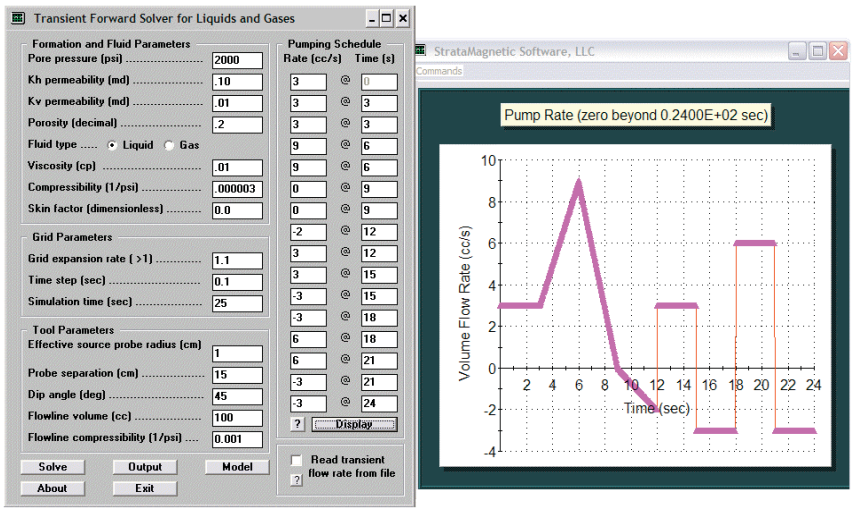

Figure 8.3a. User interface, transient gas and liquid solver.

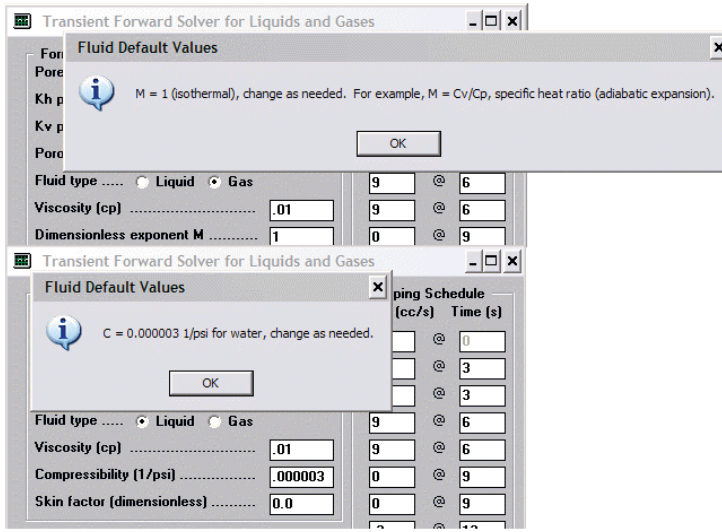

Figure 8.3b. Applicability to gas and liquid flows.

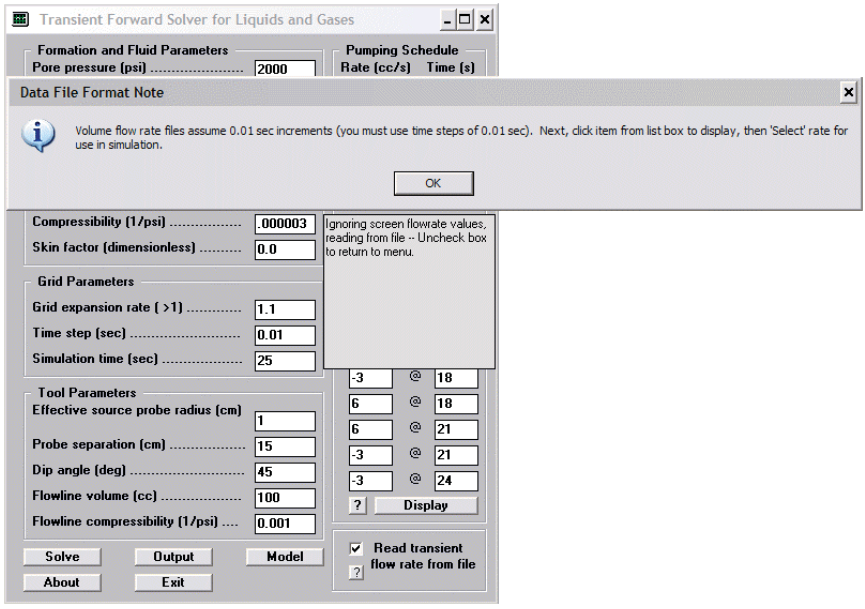

Figure 8.3c. Selecting "read flow rate from file."

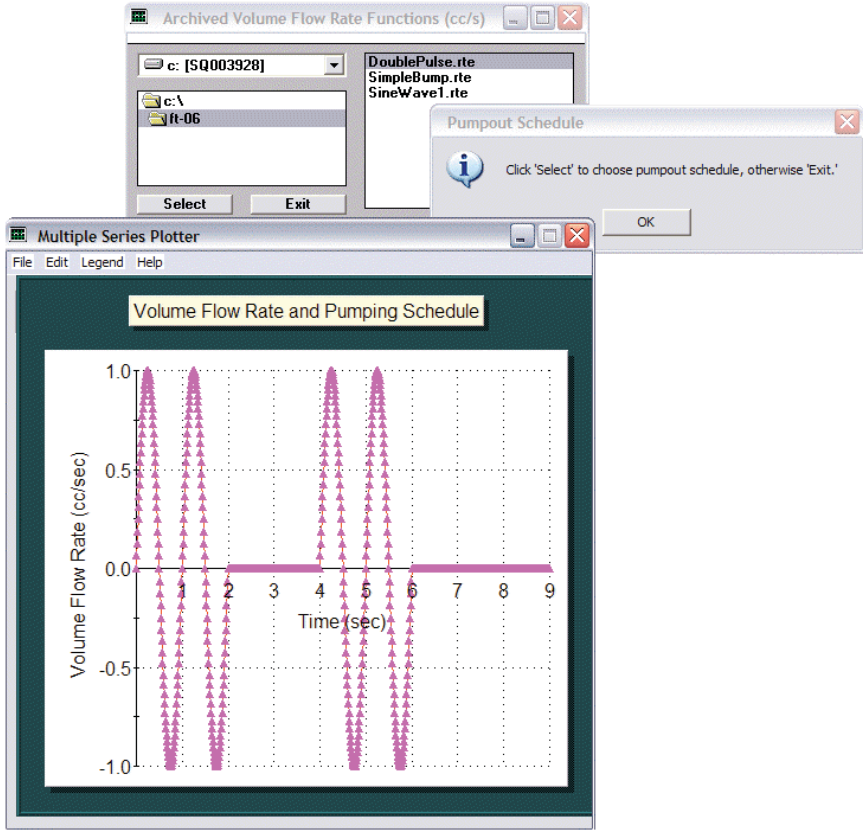

Figure 8.3d. Flowrate list box and example stored entry.

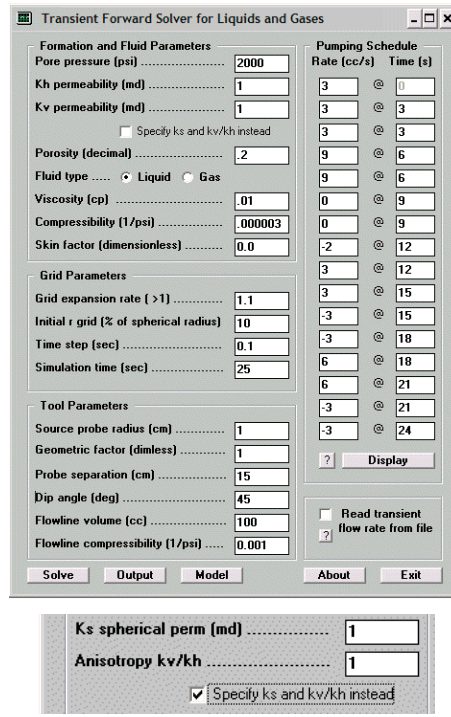

Figure 8.3e. Extended interface (below, alternate permeability option).

Figure 8.4a gives results for a simple constant rate drawdown-buildup test, a flowrate assumption suitable for liquid pumping. As noted earlier, gases do not displace immediately with piston motion, since they compress before the onset of motion. Thus, there is inherent delay – the rate assumption in our Figure 8.4b is more realistic and the corresponding pressure response is shown (a trapezoidal assumption is just as easily inputted). In Figure 8.4c, by contrast, gas is initially withdrawn and subsequently injected into the formation.

In each of these runs, time steps of 0.1 sec are assumed over a 100 sec simulation. All source probe response points are plotted, with the smoothness of the line plots highlighting the stability of the implicit scheme. Figure 8.5 shows interpolated pressure values at a distant observation probe, plotted for the entire time history of the simulation. All of the prior examples assume negligible skin effects. In Figure 8.6, transient source probe liquid pressure responses are given for three values of the dimensionless skin coefficient S, namely, S = 0, 1 and 10, for the flowrate schedule shown. The results provide an indication of the added pressure drop associated with pumping fluid through a skin resistance. Required integration times are about one second on typical personal computers for a one-hundred node variable spatial mesh system.

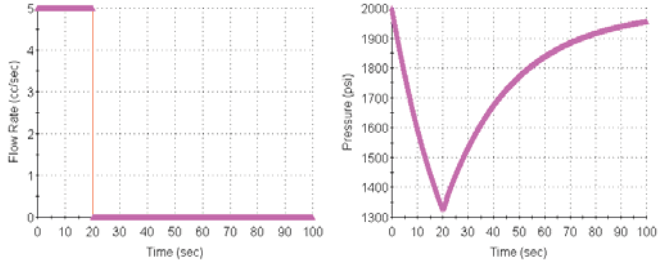

Figure 8.4a. Source probe response, simple drawdown and buildup.

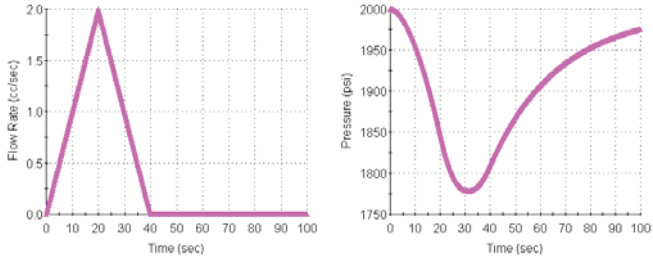

Figure 8.4b. Source probe response, triangular pump rate function.

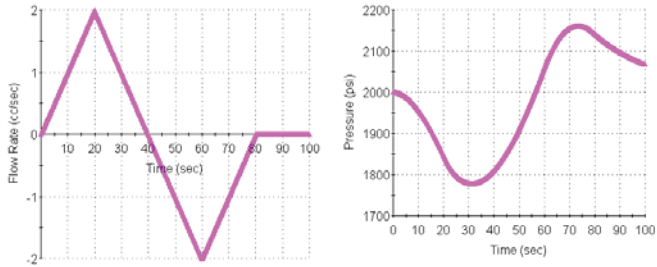

Figure 8.4c. Source probe, gas withdrawal followed by injection.

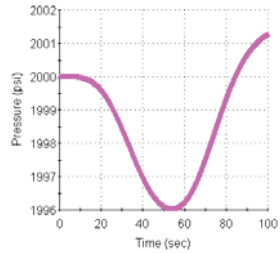

Figure 8.5. Observation probe at 10 cm, large pressure diffusion.

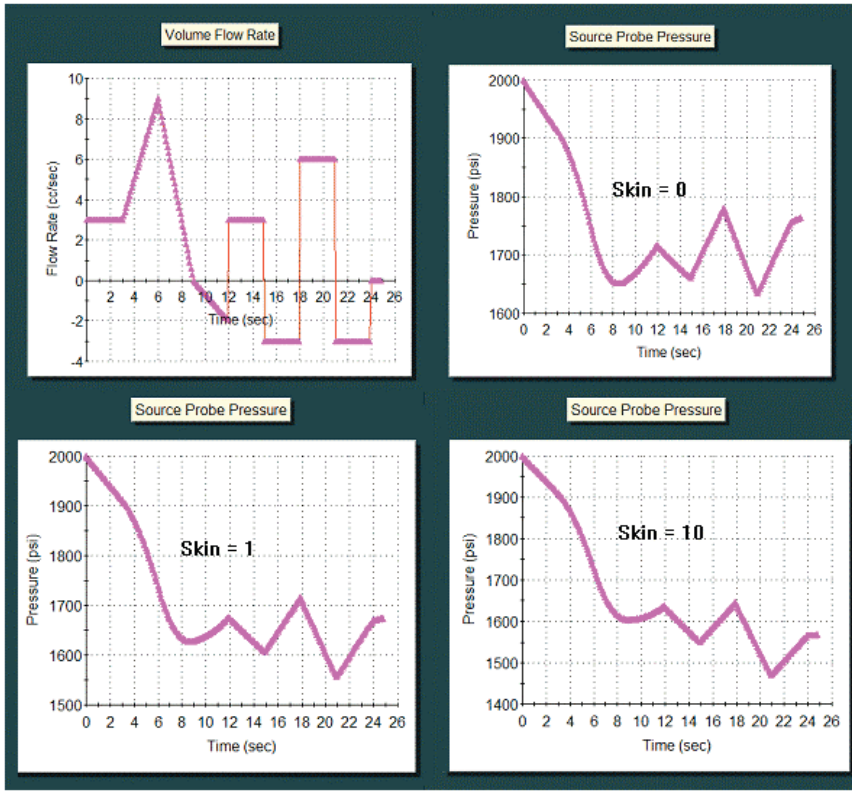

Figure 8.6. Effect of nonzero skin at the source probe.

8.3 Time-Varying Flowline Volume Model

In our model for time-varying flowline volume, the constant V is replaced by a user-specified function of time V(t). The modified finite difference algorithm must be designed so that the numerical integrations are stable despite rapid time variations. If the spatial terms are approximated at the (n-1)*th* time level and $\partial P/\partial t$ is represented by the backward difference $(P_{i,n} - P_{i,n-1})/\Delta t$, where the time step Δt may vary with time, an explicit formula for $P_{i,n}$ can be obtained in terms of quantities given earlier. This "explicit" method, yielding a formula amenable to simple pocket calculator analysis, is extremely unstable numerically and is almost never used in practice. Instead, we approximate all spatial derivatives at the present n*th* time level, thus yielding a set of "implicit" equations that must be inverted by tridiagonal matrix solvers. Similarly, we evaluate V(t) at $t = t_n$ using $V(t_n)$ or V_n. The diagonally dominant nature of the

three-band equation system provides sufficient numerical stability to render even rapid changes in V(t) stable, thus leading to useful computational results. This simulator supports hardware design applications and software interpretation development, e.g., use of variable flowline changes in time to shape pulses for easier detection in phase delay methods. We now compare FT-06 to FT-07.

8.3.1 Example 1, Software calibration

We again emphasize that FT-00 provides an exact analytical solution to the general formulation posed, whereas FT-06 and FT-07 solve the problem numerically and approximately but with fewer engineering restrictions. In order to establish confidence in any application, the exact and computational models must be "calibrated" at an agreed upon point. Figure 8.7a displays software input screens for FT-00 and FT-06 set up to solve identical physical problems.

In general, one cannot expect numerical solutions to agree with exact ones for any choice of grid. In Figure 8.7a, note the presence of a "Grid Parameters" menu with three adjustable inputs, that is, spatial grid expansion rate, initial spatial grid size, and time step. Typically, accuracy requires that all of these variables be small in some sense, in order to reduce numerical truncation errors. Following these guidelines, some trial-and-error allows us to match source probe pressure transient responses, say, and when this is achieved, changes in other FT-06 input parameters may be undertaken with confidence. Note that it is generally not possible to match everything. For instance, matching source response may lead to differences in observation probe behavior, and vice-versa. The objectives will depend on the application and are defined by the user. Figure 8.7a illustrates one example where FT-00 and FT-06 both produce nearly identical source probe responses, as shown in Figures 8.7b and 8.7c.

Still another modeling category arises when flowline volumes are not constant but variable. For example, sampling chambers may fill-up or empty liquids or gases, mechanical valves may open or shut in time, and so on. As a practical matter, we address the question, "What types of transient pressure responses are created which can be analyzed by inverse methods to provide useful predictions for mobility and pore pressure – and, in particular, using early-time data when mobilities are low and flowline volumes are large? For this purpose, a modified version of FT-06 was developed to handle flowline volumes that may change arbitrarily in time, which we label as FT-07. This required special numerical operators that acted stably when large changes in flowline volume are executed over short time intervals. The basic FT-07 menu is identical to that for FT-06, as shown in Figure 8.7d, except for one difference: at the bottom, a constant flowline volume input box is replaced by a "Setup" button. When this button is pressed, the graphical user menu shown appears and a fairly general flowline history can be defined.

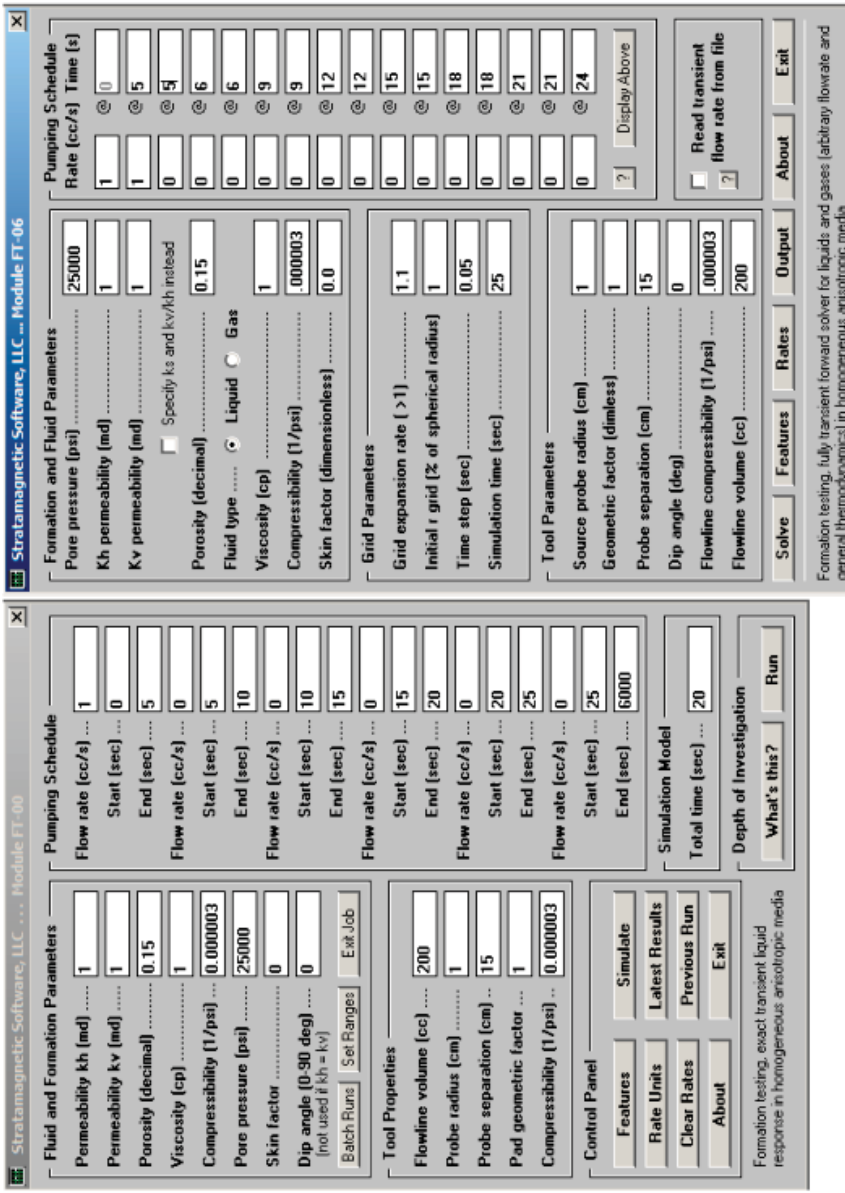

Figure 8.7a. FT-00 (lower) and FT-06 (upper) screens solving identical physical problem.

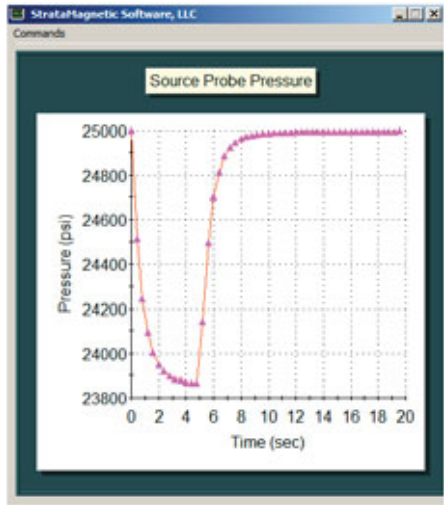

Figure 8.7b. FT-00 source probe pressure

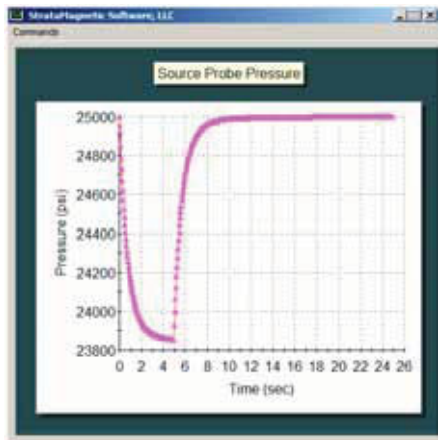

Figure 8.7c. FT-06 source probe pressure

Clicking "Solve," as before, automatically creates tabulated solutions and line plots for transient source and observation probe responses, assumed volume flow rate history, as well as time-dependent flowline volume. In Figure 8.7e, we simply re-ran the "200 cc" simulations already considered, simply to show that a solution identical to that for FT-06 is obtained. However, in Figures 8.7f and 8.7g we assume a drastically different flowline volume with substantial changes in time. The absence of "wiggles" demonstrates that we have computed the solutions stably.

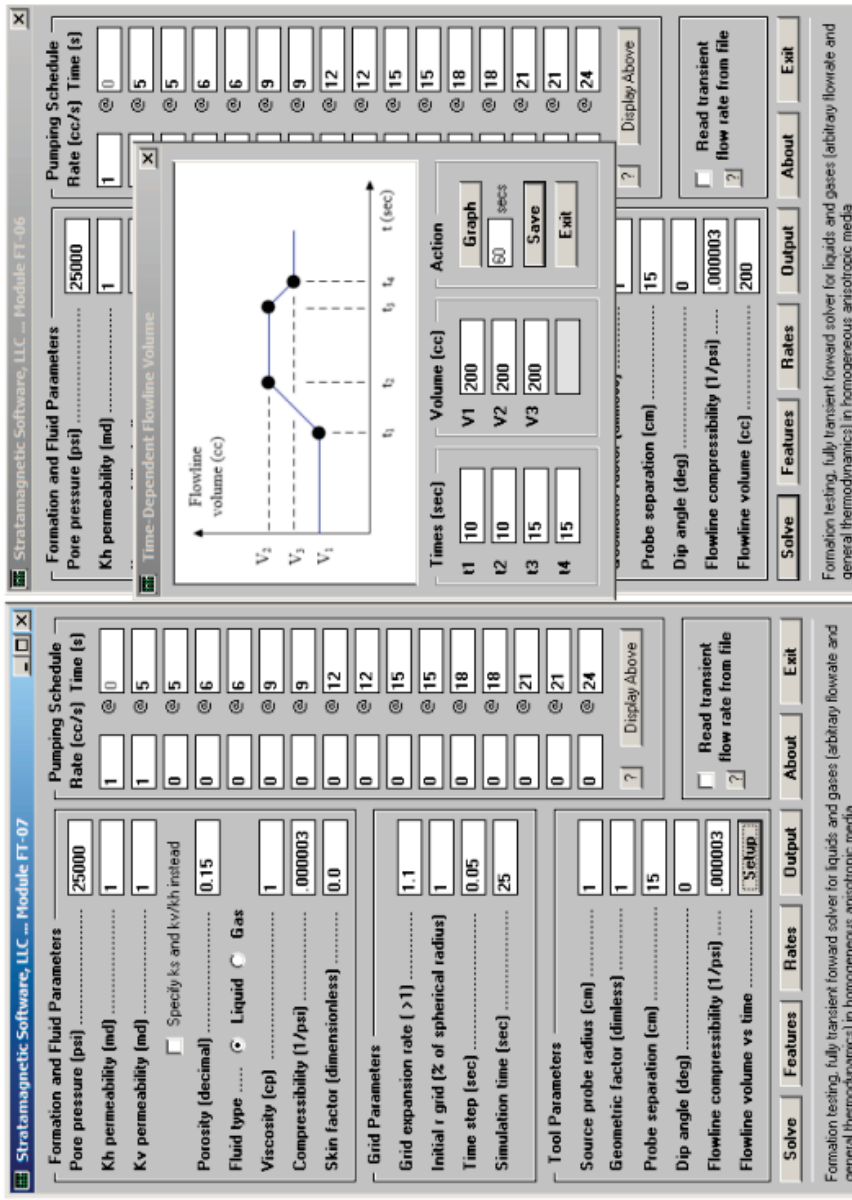

Figure 8.7d. FT-06 and FT-07 differences.

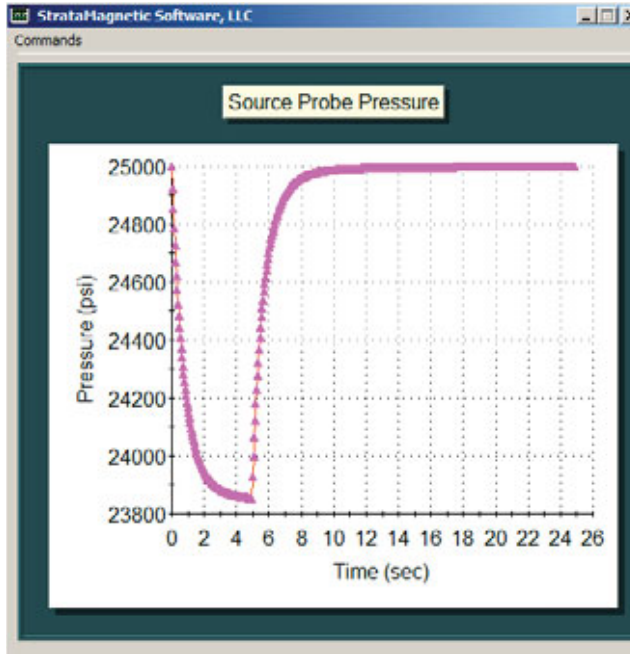

Figure 8.7e. FT-07 source probe pressure (200 cc flowline volume)

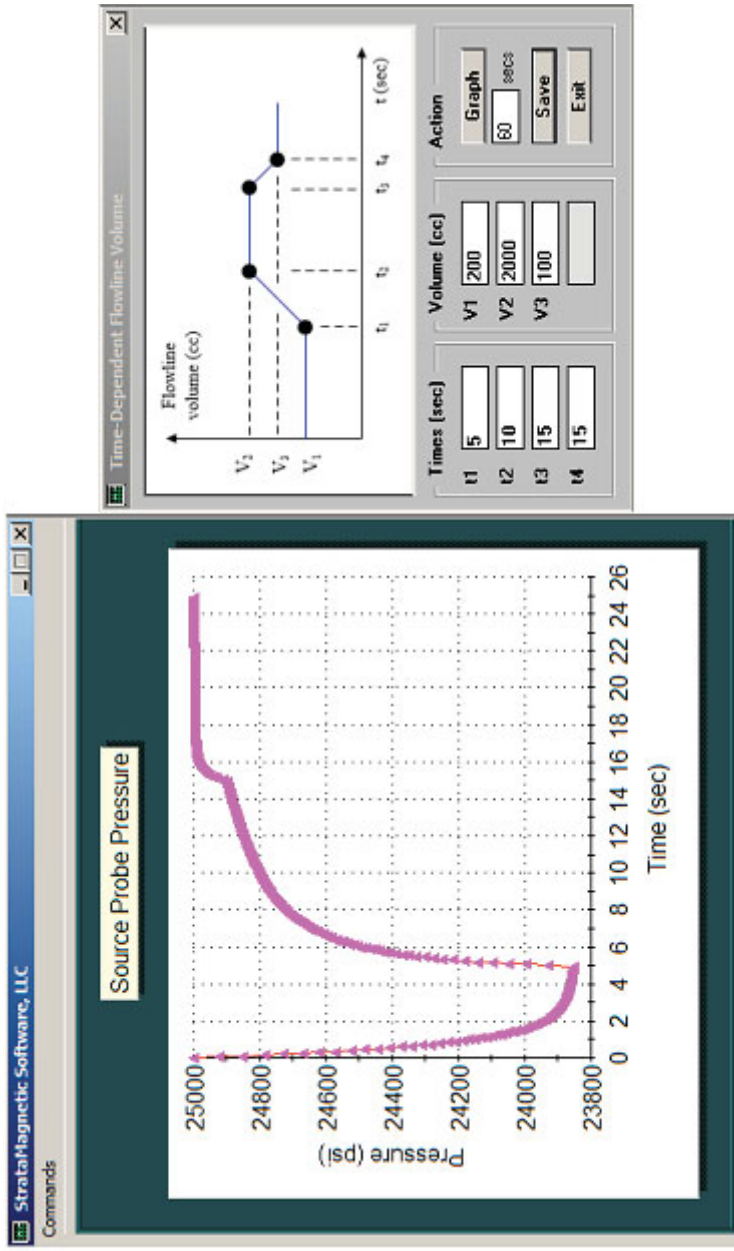

Figure 8.7f. FT-07 source probe pressure (highly variable flowline volume)

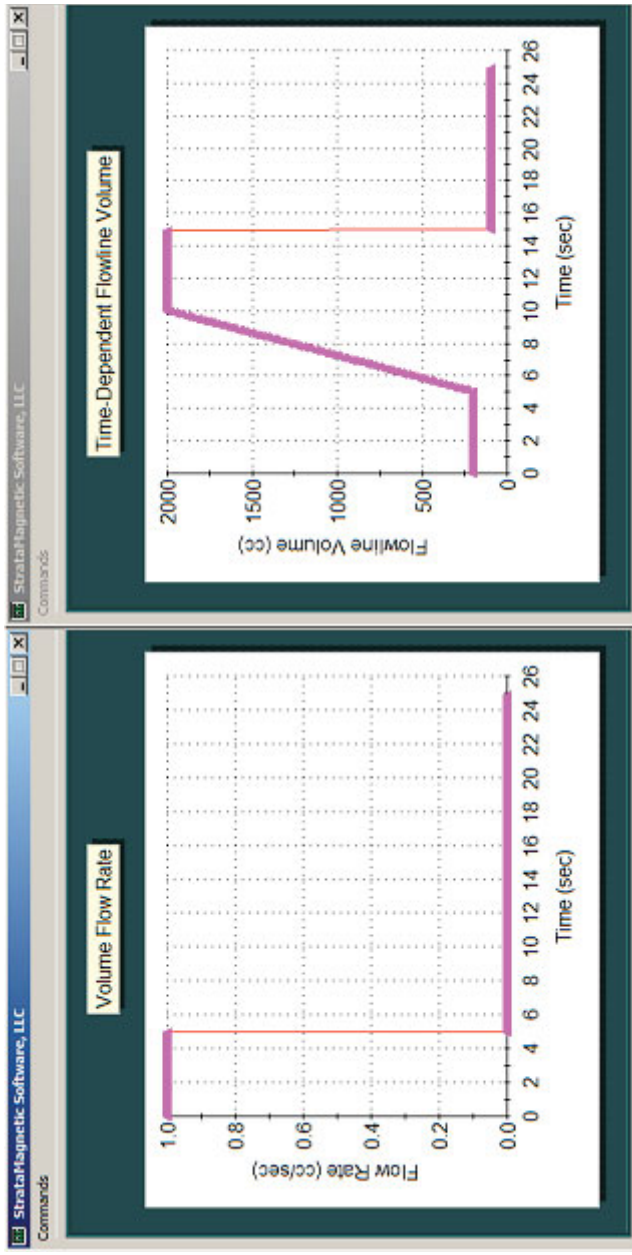

Figure 8.7g. FT-07 volume flow rate and flowline volume variations

8.3.2 Example 2, Simple interpretation using numerical pressure data

In this second example, we use numerical model FT-07 to create the source probe pressure transient response for a flowline volume of 1000 cc. We wish to determine if the information in the transient curve can be interrogated to predict mobility and pore pressure under the present low mobility, early-time, transient environment. We could have used the more exact FT-00 solver to address this question, however, we use FT-07 because ultimately we will ask the same question for time-dependent flowline volumes.

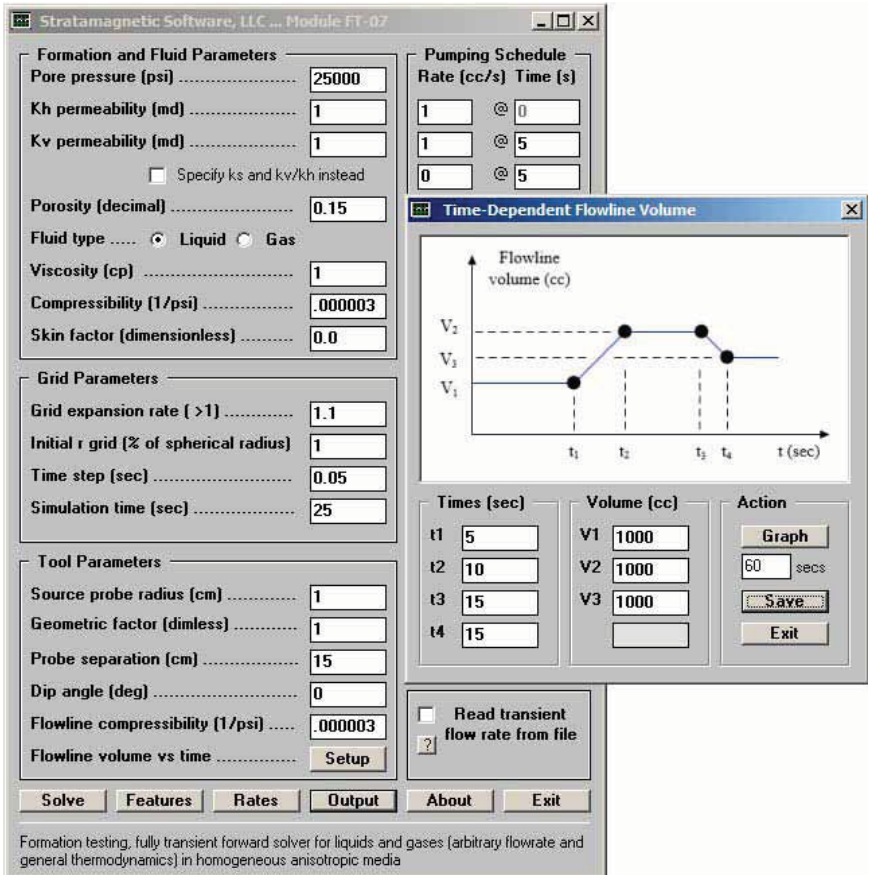

Figure 8.8a. Constant flowline volume of 1,000 cc.

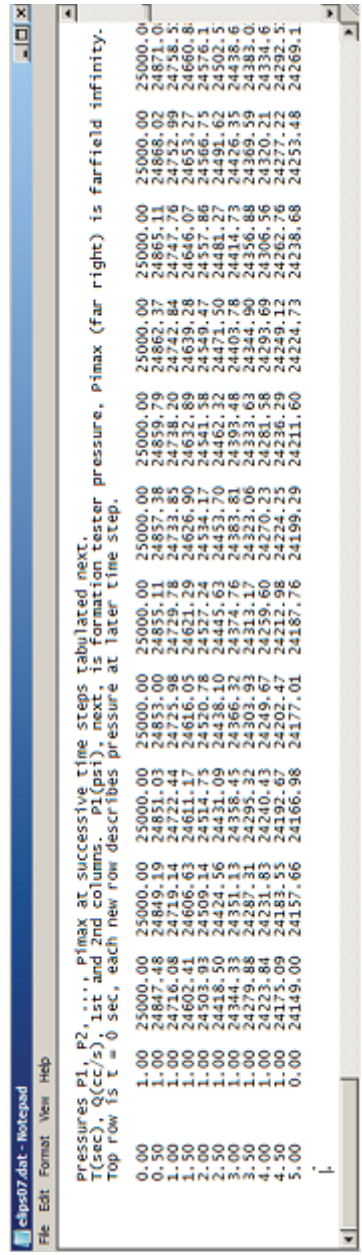

Figure 8.8b. Numerical solutions.

Both FT-06 and FT-07 solutions are tabulated and plotted as indicated earlier. Figure 8.8b shows the numerical solution obtained for the inputs in Figure 8.8a. The first column gives elapsed time in seconds, the second provides volume flow rate in cc/s, while the third lists the pressure obtained at the source probe. Now, we turn to a prior algorithm, namely "pta-dd-3-run-with-rft-numbers.exe" developed to predict mobility and pore pressure from the initial drawdown history for a low mobility application using only three-point {t,p(t)} data. The algorithm is discussed in Chapter 3, however, the screen dumps showing assumptions and history yield the following results using data from 1, 2 and 4 seconds –

```
C:\pta-dd-3-run-with-rft-numbers-500-iterations <Return>

Use decimals after all integers!

Volume flow rate (cc/s): 1.
Pump probe, radius (cm): 1.
Probe, geometric factor: 1.
1st Point Time T1 (sec): 1.
      Pressure P1 (psi): 24716.
2nd Point Time T2 (sec): 2.
      Pressure P2 (psi): 24503.
3rd Point Time T3 (sec): 4.
      Pressure P3 (psi): 24223.


    Run     Error   P0(psi)   Md/Cp
      1.   34.2 %    24929    0.006
     20.   32.3 %    24933    0.109
     30.   31.3 %    24935    0.161
     40.   30.2 %    24937    0.211
     50.   29.2 %    24939    0.260
     75.   26.5 %    24945    0.376
    100.   23.7 %    24951    0.483
    125.   20.9 %    24957    0.581
    150.   17.9 %    24963    0.672
    175.   14.9 %    24969    0.755
    200.   11.7 %    24976    0.832
    225.    8.5 %    24982    0.902
    250.    5.1 %    24989    0.966
    275.    1.6 %    24996    1.024
    280.    0.9 %    24997    1.035
    281.    0.8 %    24998    1.037
    282.    0.7 %    24998    1.039
    283.    0.5 %    24998    1.041
    284.    0.4 %    24998    1.043
    285.    0.2 %    24999    1.045
    286.    0.1 %    24999    1.047
Stop - Program terminated.
```

From Figure 8.8a, the assumed mobility is 1 md/1 cp or 1 md/cp while the pore pressure is 25,000 psi. At 286 iterations, requiring approximately 1 second of computation on Intel Core i5 machines, the converged values of 1.047 md/cp and 24,999 psi are extremely good. This shows that the numerically calculated pressures are reliable and represent physically viable solutions.

8.3.3 Example 3, Simple interpretation using numerical pressure data

Here we re-run above example with a flowline volume of 2000 cc, all parameters otherwise unchanged.

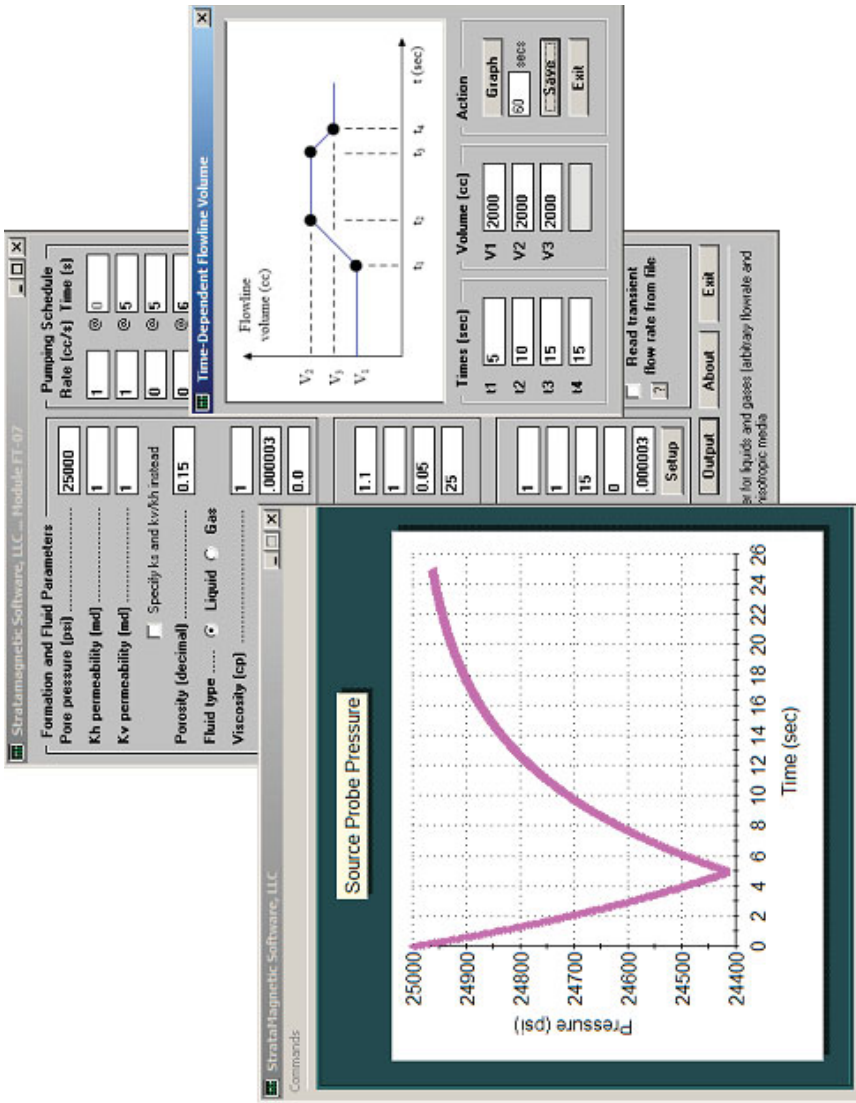

Figure 8.9a. Constant flowline volume of 2,000 cc.

Here we increase the flowline volume to 2,000 cc, again using FT-07 to create forward simulation solutions. The inverse solution history is shown below, together with time and pressure inputs obtained from the tabulated file.

```
C:\pta-dd-3-run-with-rft-numbers <Return>

Use decimals after all integers!

Volume flow rate (cc/s): 1.
Pump probe, radius (cm): 1.
Probe, geometric factor: 1.
1st Point Time T1 (sec): 1.
      Pressure P1 (psi): 24846.
2nd Point Time T2 (sec): 2.
      Pressure P2 (psi): 24713.
3rd Point Time T3 (sec): 4.
      Pressure P3 (psi): 24499.


    Run     Error   P0(psi)   Md/Cp
      1.   19.4 %    24979    0.009
     20.   17.1 %    24981    0.174
     40.   14.6 %    24984    0.338
     60.   12.0 %    24987    0.492
     80.    9.4 %    24990    0.637
    100.    6.6 %    24992    0.773
    120.    3.9 %    24995    0.900
    140.    1.0 %    24998    1.020
    141.    0.8 %    24999    1.025
    142.    0.7 %    24999    1.031
    143.    0.6 %    24999    1.037
    144.    0.4 %    24999    1.042
    145.    0.3 %    24999    1.048
    146.    0.1 %    24999    1.054
Stop - Program terminated.
```

Again, the predicted 1.054 md/cp and 24,999 psi agree extremely well with inputted FT-07 values. This shows that the numerically calculated pressures are reliable and represent physically viable solutions.

8.3.4 Example 4, Simple interpretation using low permeability data

Here we re-run the "2,000 cc" case in Example 3, but reduce permeability ten-fold. Now, the inputted mobility is 0.1 md/cp, while the prediction gives 0.128 md/cp – a very acceptable value.

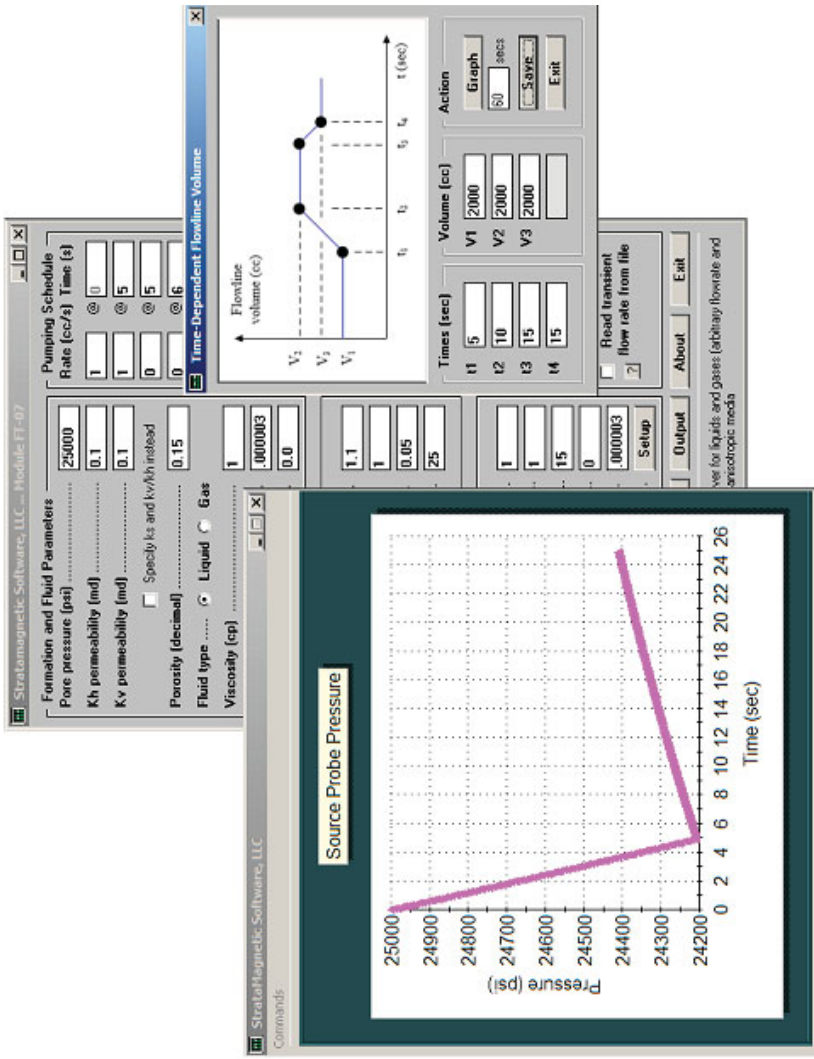

Figure 8.10a. Large constant flowline volume, extremely low mobility.

```
C:\pta-dd-3-run-with-rft-numbers <Return>

Use decimals after all integers!

Volume flow rate (cc/s): 1.
Pump probe, radius (cm): 1.
Probe, geometric factor: 1.
1st Point Time T1 (sec): 1.
      Pressure P1 (psi): 24835.
2nd Point Time T2 (sec): 2.
      Pressure P2 (psi): 24672.
3rd Point Time T3 (sec): 4.
      Pressure P3 (psi): 24355.


    Run     Error   P0(psi)   Md/Cp
      1.    2.6 %    24998    0.007
      5.    2.0 %    24998    0.036
     10.    1.3 %    24999    0.072
     15.    0.6 %    25000    0.107
     16.    0.4 %    25000    0.114
     17.    0.3 %    25000    0.121
     18.    0.1 %    25000    0.128 very good
Stop - Program terminated.
```

8.3.5 Example 5, Simple interpretation using numerical pressure data

We re-run the foregoing example which assumed an extremely low permeability, but now, assume a rapidly increasing flowline volume that quickly reaches 5,000 cc. Calculated results for this unusual flowline history are shown below. We were motivated by the following challenge: what does it take to deliberately "crash" our inverse method? In this extreme example, our pore pressure of 28,726 psi over-predicts the exact value by more than 3,000 psi, while the mobility of 0.172 md/cp is not too different from the assumed 0.1 md/cp value. More work is in progress to test the limits of our inverse method under highly transient conditions.

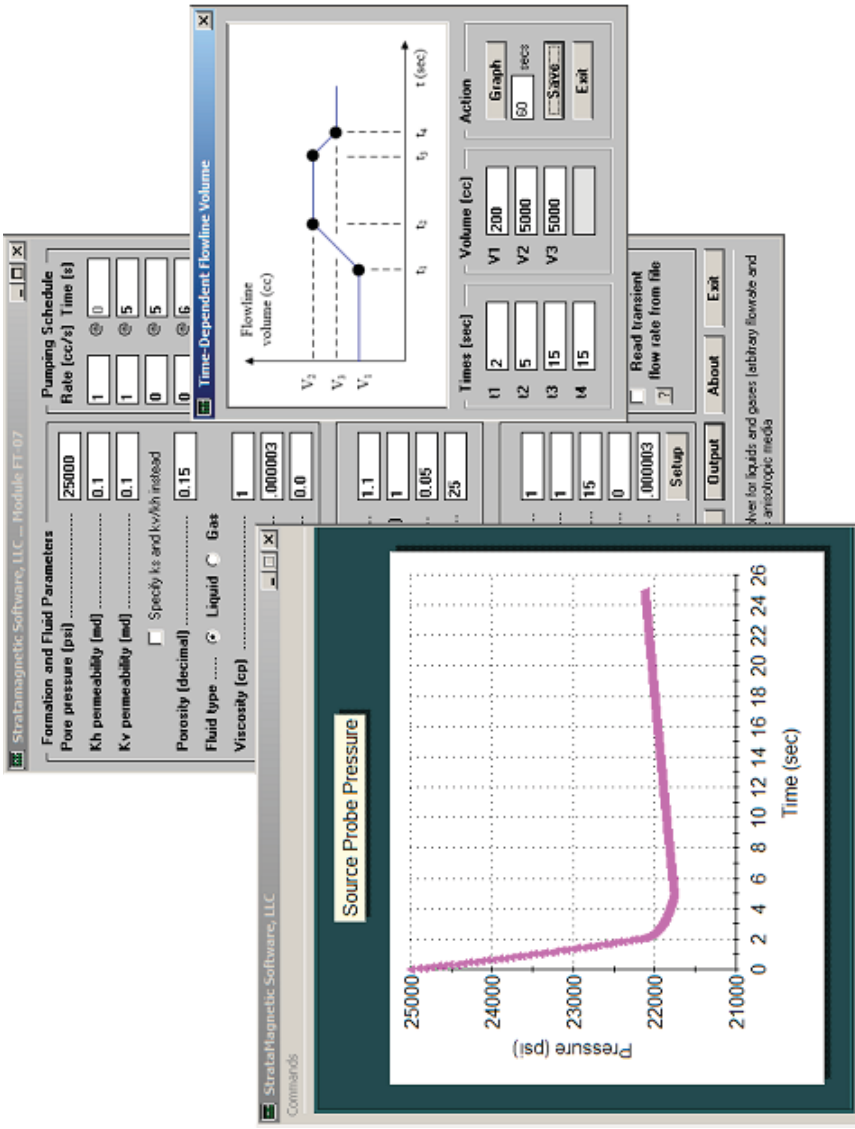

Figure 8.11a. Rapidly increasing flowline volume, very low permeability and source probe response.

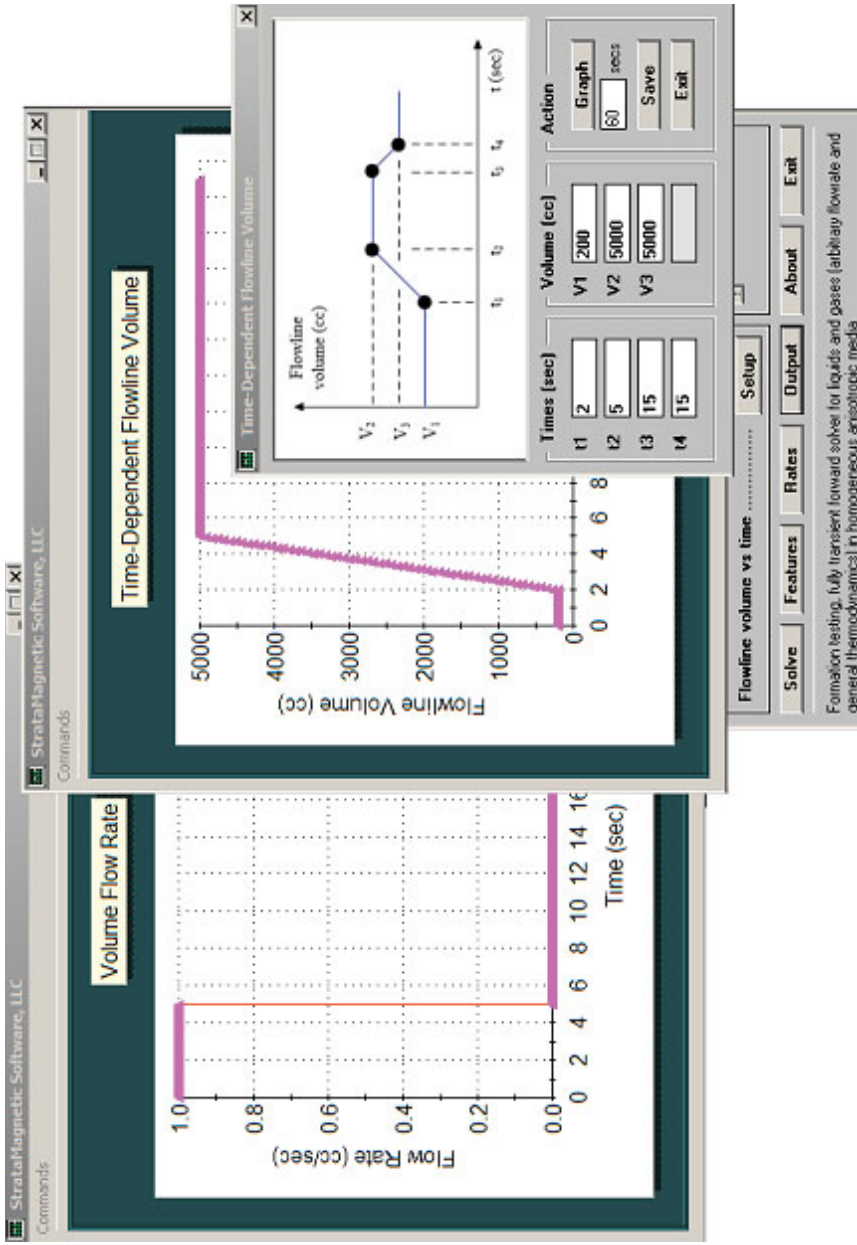

Figure 8.11b. Volume flow rate and flowline volume plots.

```
C:\pta-dd-3-run-with-rft-numbers-10000-iterations <Return>

Volume flow rate (cc/s): 1.
Pump probe, radius (cm): 1.
Probe, geometric factor: 1.
1st Point Time T1 (sec): 1.
      Pressure P1 (psi): 23491.
2nd Point Time T2 (sec): 2.
      Pressure P2 (psi): 22205.
3rd Point Time T3 (sec): 4.
      Pressure P3 (psi): 21812.


    Run     Error   P0(psi)   Md/Cp

    900.   46.6 %    26654    0.224
    950.   43.0 %    26816    0.220
    976.   41.1 %    26903    0.218
   1000.   39.3 %    26986    0.216
   1050.   35.3 %    27165    0.211
   1092.   31.8 %    27323    0.207
   1100.   31.1 %    27354    0.206
   1200.   22.0 %    27760    0.195
   1300.   11.9 %    28209    0.184
   1400.    0.6 %    28706    0.172
   1401.    0.5 %    28711    0.172
   1402.    0.3 %    28716    0.172
   1403.    0.2 %    28721    0.172
   1404.    0.1 %    28726    0.172
Stop - Program terminated.
```

8.3.6 Example 6, Simple interpretation using numerical pressure data

In Example 5, a mobility of 0.1 md/cp was selected for inverse evaluation; here, we increase it to 1 md/cp to observe anticipated improvements. Again, from Figure 8.12a, note that flowline volume is highly transient during the first five seconds. The prediction of 25,798 psi and a mobility of 0.634 md/cp is acceptable, close to the assumed 25,000 psi and 1 md/cp.

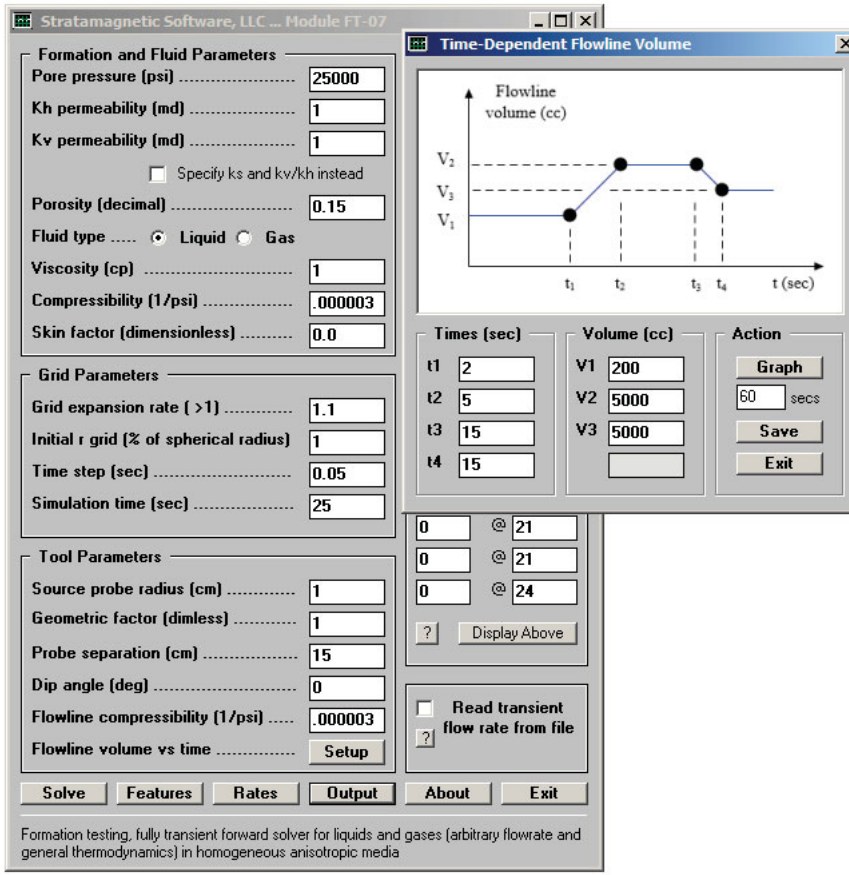

Figure 8.12a. Mobility, 1 md/cp evaluation.

Figure 8.12b. Volume flow rate, flowline volume, source probe pressure.

```
C:\pta-dd-3-run-with-rft-numbers-10000-iterations <Return>

Volume flow rate (cc/s): 1.
Pump probe, radius (cm): 1.
Probe, geometric factor: 1.
1st Point Time T1 (sec): 1.
      Pressure P1 (psi): 24167.
2nd Point Time T2 (sec): 2.
      Pressure P2 (psi): 23949.
3rd Point Time T3 (sec): 4.
      Pressure P3 (psi): 23916.

    Run     Error   P0(psi)   Md/Cp

   1500.   44.5 %    25144    0.949
   1600.   37.6 %    25246    0.883
   1700.   29.9 %    25360    0.818
   1800.   21.4 %    25485    0.756
   1900.   12.0 %    25624    0.697
   2000.    1.5 %    25777    0.641
   2004.    1.0 %    25784    0.639
   2005.    0.9 %    25785    0.638
   2006.    0.8 %    25787    0.638
   2007.    0.7 %    25789    0.637
   2008.    0.6 %    25790    0.637
   2009.    0.5 %    25792    0.636
   2010.    0.4 %    25794    0.635
   2011.    0.3 %    25795    0.635
   2012.    0.1 %    25797    0.634
   2013.    0.0 %    25798    0.634 (not bad, close to 25000 and 1 md/cp)
Stop - Program terminated.
```

8.3.6 Example 7, Enhancing phase delay detection in very low permeability environments

This example represents the most important application of the time-varying flowline algorithm and addresses phase delay detection in very low mobility environments. We will first give an example where a useful pressure signal cannot be found at all at the observation probe, that is, consider a mobility of 0.1 md/cp with a constant flowline volume of 1,000 cc. The relevant data are presented in Figures 8.13a and 8.13b. On the other hand, if the flowline volume were constant at 10 cc, Figures 8.13d and 8.13d indicate that a measurable phase is possible. Figure 8.13e shows a flowline volume that dynamically decreases from 1,000 cc to 10 cc in fifteen seconds. In Figure 8.13f, we find that the observation probe pressure reappears and provides time data for phase analysis.

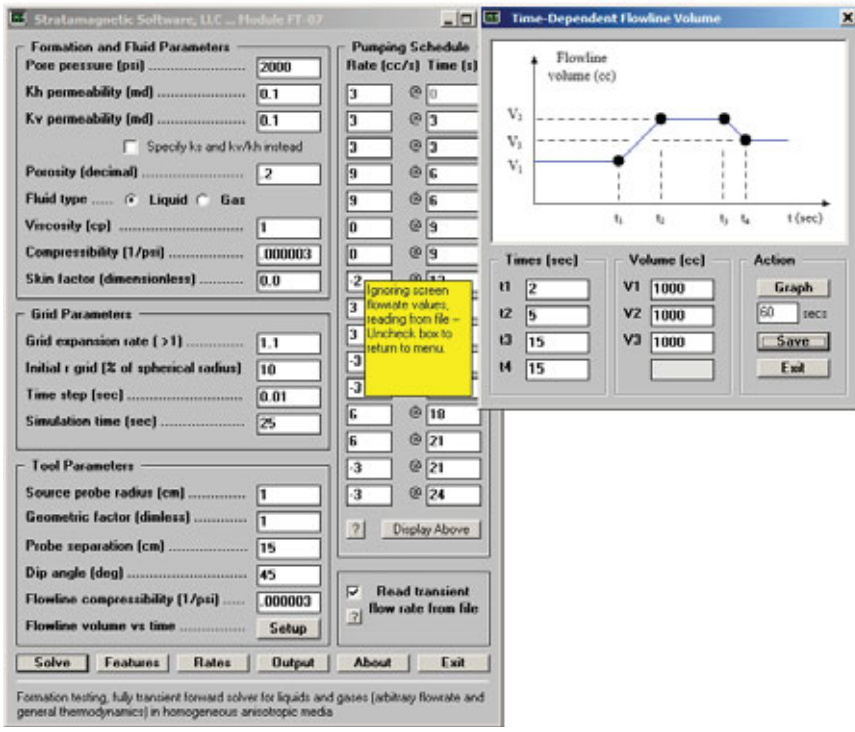

Figure 8.13a. Very large flowline volume of 1,000 cc.

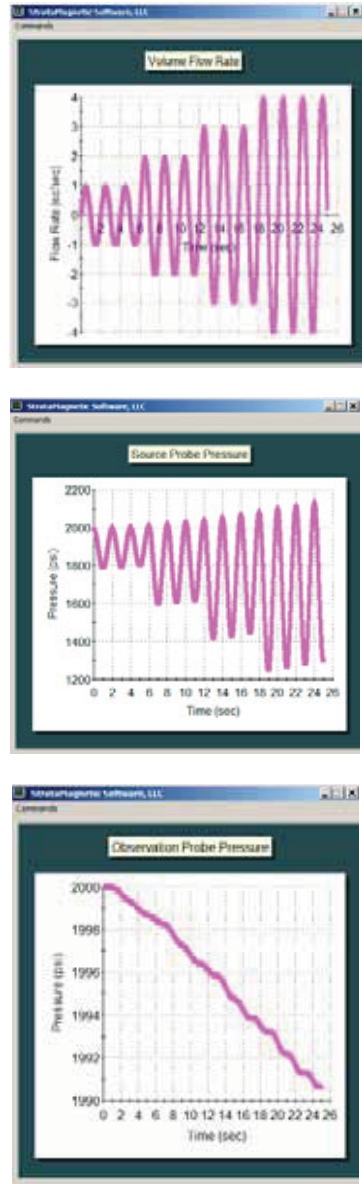

Figure 8.13b. No measurable pressure at observation probe (bottom).

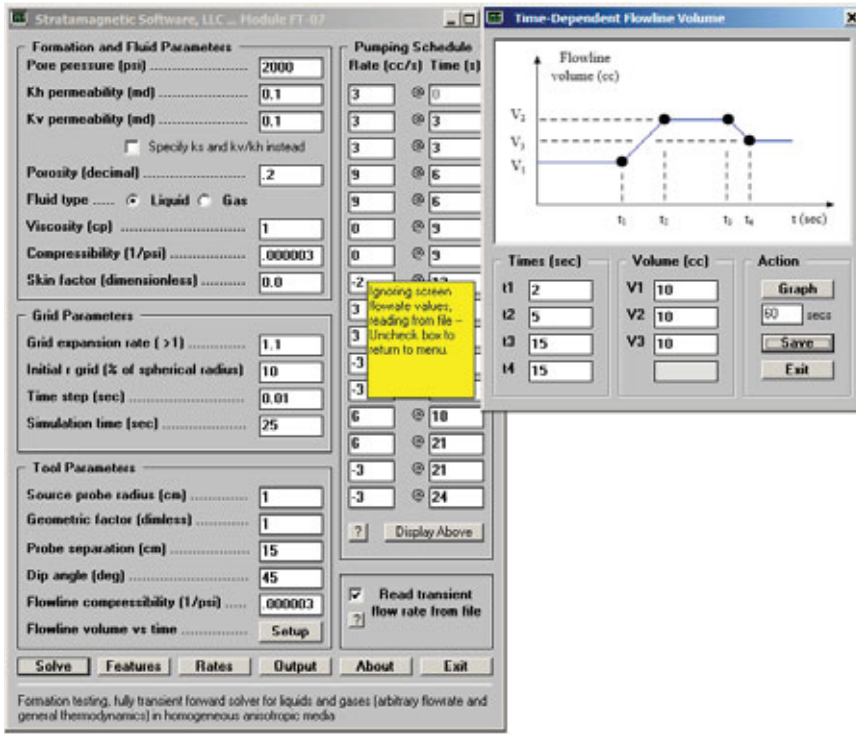

Figure 8.13c. Very small flowline volume of 10 cc.

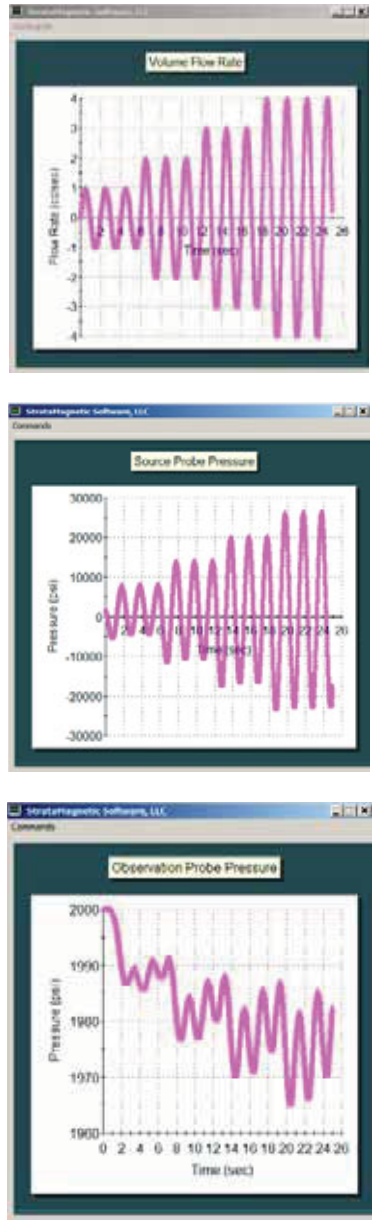

Figure 8.13d. Detectable phase signal at observation probe (bottom).

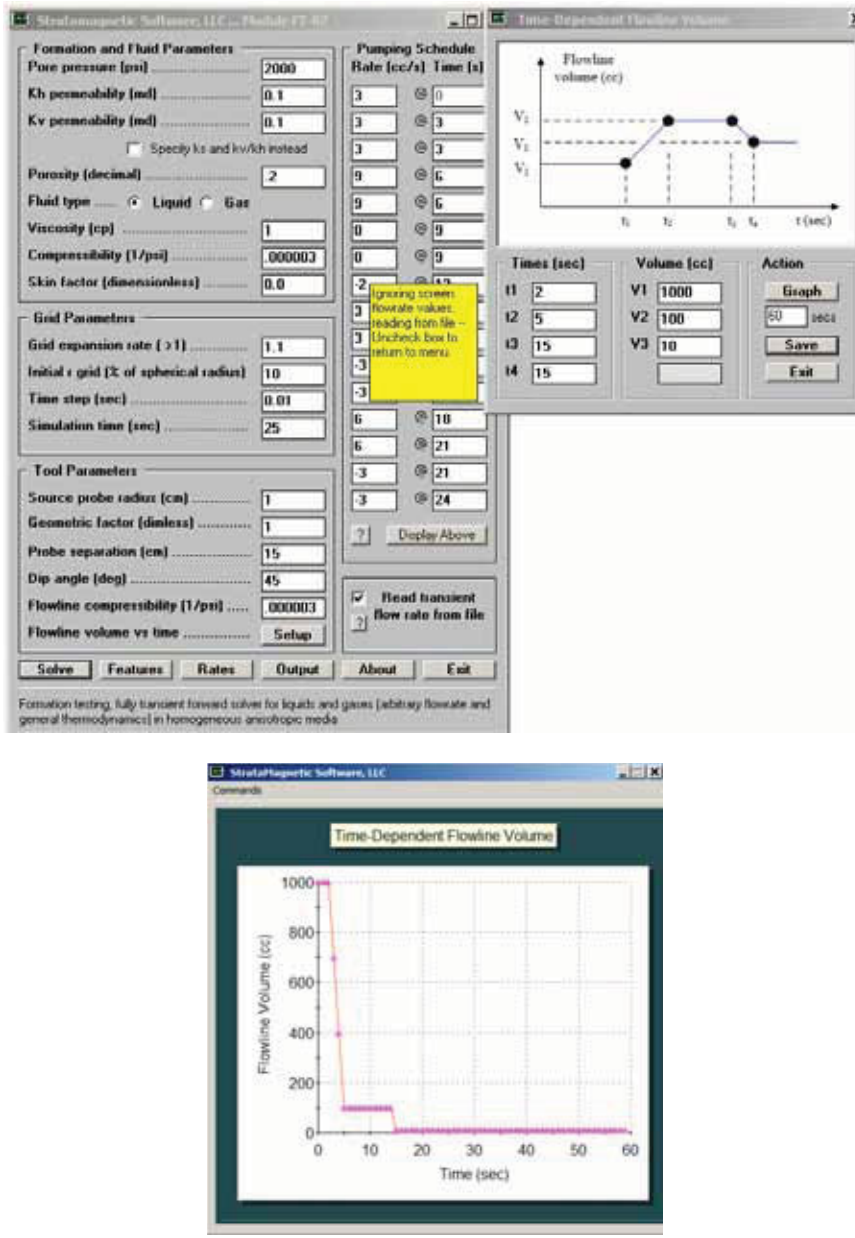

Figure 8.13e. Time-varying flowline volume.

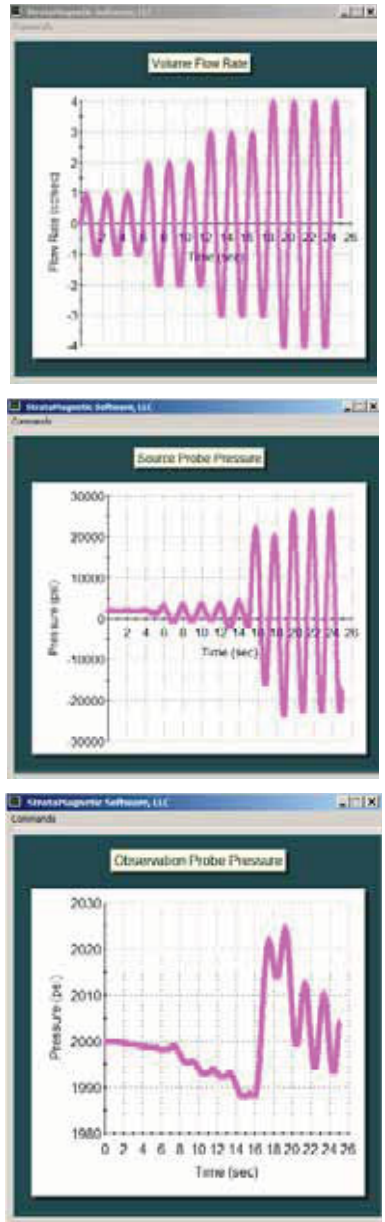

Figure 8.13f. Detectable phase at observation probe (bottom).

9
Closing Remarks

Our book Formation Testing: Pressure Transient and Contamination Analysis, published as recently as 2014, aside from exact forward models like FT-00 for pressure analysis and fully numerical multiphase approaches for clean-up investigations, focused on inverse models that predicted permeabilities when steady-state pressure drops at source and observation probes were available. In fact, we developed exact analytical models for both liquids and gases at general dip angles – and successfully showed how horizontal and vertical permeabilities could be predicted – that were consistent with the assumptions used to create the synthetic pressure data. That work, while very important, applied only to medium-high mobility applications where pressure equilibrates rapidly. We could have stopped with that research, but we didn't. One strong benefit in having good theoreticians interact with experienced hardware designers is the synergy that develops when both parties are attuned to the needs of the commercial marketplace.

And in our case, having celebrated a decade-long partnership, and getting to know and understand each other well, this led to the resolution of several longstanding questions that plagued modern low-mobility well logging. How can we *quickly* predict *spherical permeabilities* using drawdown data? Buildup pressures? Double-drawdown and buildup data? And even more perplexing, how can we *quickly* predict *both horizontal and vertical permeabilities* using standard dual-probe tools? By "quickly," we meant *really* quick: seconds instead of minutes, whereas the previous norm had been many minutes and even hours. And so, we invented advanced phase delay methods. When this suffered at extremely low mobilities, we developed time-varying flowline models that help us automatically "fine tune" our tools to produce sharper observable pulses. To handle high pumping speeds, we revisited earlier multiphase models and added inertial Forchheimer corrections. At this writing, experimental test fixtures that help us calibrate new tools to our software models are being designed and built. As always, CNOOC/COSL management has allowed us open access to its people and technology. In the following pages, we share some of our thoughts with our readers – showing that *people* develop technology. And they continue in these endeavors even with oil prices in free fall.

Figure 9.1. Dual-probe formation tester.

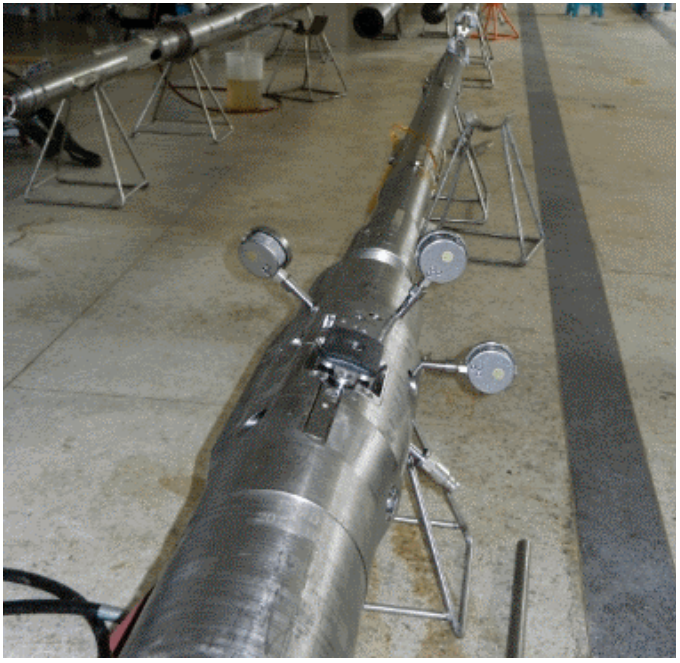

Figure 9.2. Single-probe tool, calibration.

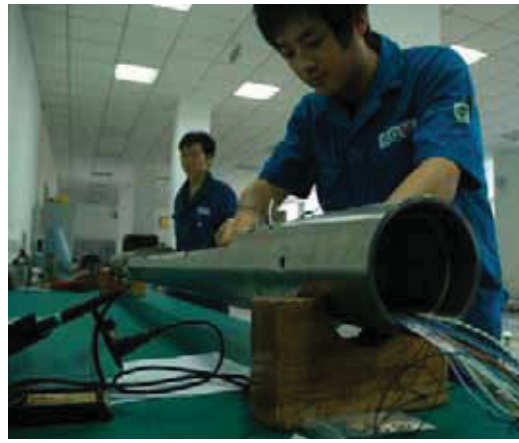

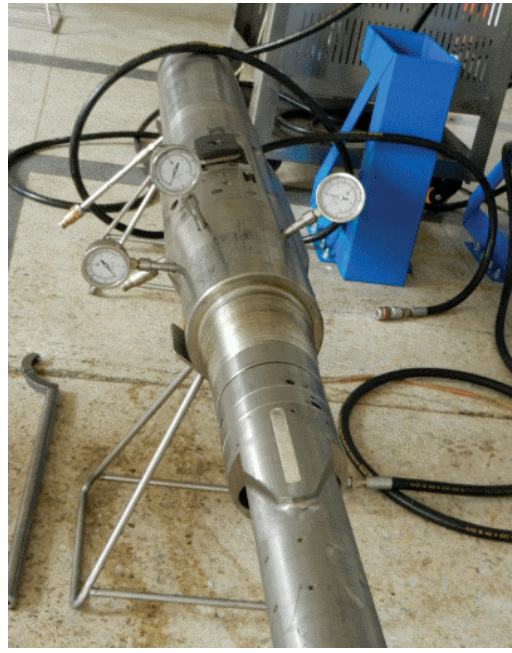

Figure 9.3. Tool assembly.

Figure 9.4. Tool assembly.

Figure 9.5. COSL test well in Beijing, formation tester being lowered.

Figure 9.6. Evaluating the dual-probe formation tester.

Figure 9.7. Chin, Zhuang, Feng and Zhou discussing phase delay.

Figure 9.8. Software performance on Microsoft Surface 3 tablet.

Figure 9.9. Formation tester with multiple observation probes (top), analogous to resistivity tool with multiple receiver coils.

Figure 9.10. Zhou rehearses talk for Middle East petroleum conference.

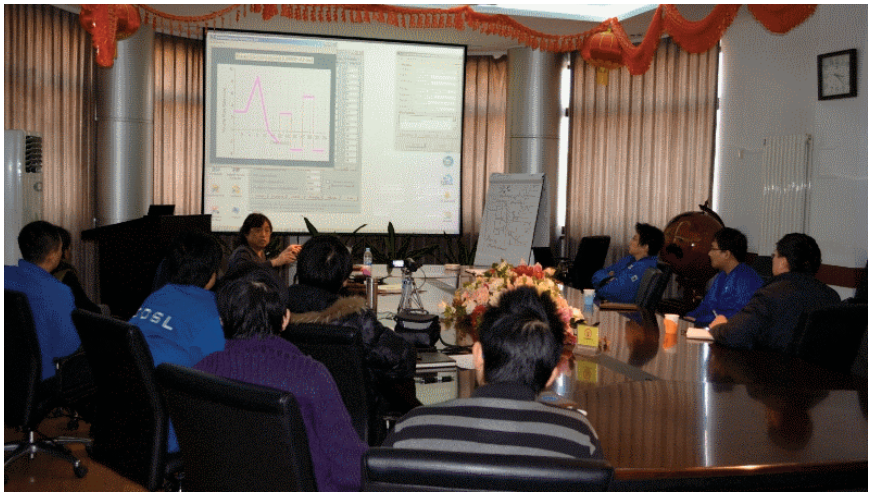

Figure 9.11. Chin explains how FT-06 and FT-07 model non-ideal pumping.

Figure 9.12. Chief Engineer Feng with CAD drawings and layout.

Figure 9.13. More discussions and presentations.

Figure 9.14. COSL seminar at Stratamagnetic Software's Houston offices (top) – Zhuang and Chin discuss progress at the day's end (bottom).

References

Abramowitz, M., and Stegun, I. A., *Handbook of Mathematical Functions*, Dover Publications, New York, 1970.

Adeyemi, O.S. and Edwards, M.D., "Matrix Selection for Conventional and Non-conventional Testing and Sampling in Gas Reservoirs," SPE Paper No. 96972, *2005 SPE Annual Technical Conference and Exhibition*, Dallas, Texas, Oct. 9-12, 2005.

Akkurt, R., Bowcock, M., Davies, J., Del Campo, C., Hill, B., Joshi, S., Kundu, D., Kumar, S., O'Keefe, M., Samir, M., Tarvin, J., Weinheber, P., Williams, S., Zeybek, M., "Focusing on Downhole Fluid Sampling and Analysis," *Oilfield Review*, Winter 2006/2007.

Al-Mohsin, A., Tariq, S. and Haq, S.A., "Application of Wireline Formation Tester (Openhole and Cased-Hole) Sampling Techniques for Estimation of Non-hydrocarbon Gas Content of Khuff Reservoir Fluids in the North Field, Qatar," IPTC Paper No. 10622, *International Petroleum Technology Conference*, Doha, Qatar, Nov. 21-23, 2005.

Andrews, R.J., Beck, G., Castelijns, K., Chen, A., Cribbs, M.E., Fadnes, F.H., Irvine-Fortescue, J., Williams, S., Hashem, M., Jamaluddin, A., Kurkjian, A., Sass, B., Mullins, O.C., Rylander, E., and van Dusen, A., "Quantifying Contamination Using Color of Crude and Condensate," *Oilfield Review*, Autumn 2001.

Angeles, R., Torres-Verdin, C., Lee, H.J., Alpak, F.O. and Sheng, J., "Estimation of Permeability and Permeability Anisotropy from Straddle Packer Formation Tester Measurements Based on the Physics of Two-Phase Immiscible Flow and Invasion," *SPE Journal*, Sept. 2007, pp. 339-354.

Ayan, C., Hafez, H., Hurst, S., Kuchuk, F., O'Callaghan, A., Peffer, J., Pop, J., and Zeybek, M., "Characterizing Permeability with Formation Testers," *Oilfield Review*, Autumn 2001.

Aziz, K. and Settari, A., *Petroleum Reservoir Simulation*, Applied Science Publishers, London, 1979.

Bassiouni, Z. and Yildiz, T., "Interpretation of Wireline Formation Tester (WFT) Data in Tight Gas Sands," *Journal of Canadian Petroleum Technology*, June 1999, Vol. 38, No. 6, pp. 29-36.

Bowles, D., "Bridging the Gap Between Wireline Formation, Drill Stem Testing," *Offshore Magazine*, June 1, 2004.

Brigham, W.E., Peden, J.M., Ng, K.F., and O'Neill, N., "The Analysis of Spherical Flow with Wellbore Storage," SPE Paper No. 9294, *55th Annual Fall Technical Conference and Exhibition of the Society of Petroleum Engineers of AIME*, Dallas, Texas, Sept. 21-24, 1980.

Carnahan, B., Luther, H.A., and Wilkes, J.O., *Applied Numerical Methods*, John Wiley, New York, 1969.

Carslaw, H.S., and Jaeger, J.C., *Conduction of Heat in Solids*, Oxford University Press, London, 1946.

Chin, W.C., *Modern Reservoir Flow and Well Transient Analysis*, Gulf Publishing, Houston, 1993.

Chin, W.C., *Formation Invasion, with Applications to Measurement-While-Drilling, Time Lapse Analysis, and Formation Damage*, Gulf Publishing, Houston, 1995.

Chin, W.C., *Computational Rheology for Pipeline and Annular Flow*, Butterworth-Heinemann, Reed Elsevier, Boston, 2001.

Chin, W.C., *Quantitative Methods in Reservoir Engineering*, Elsevier Science, Amsterdam, 2002.

Chin, W.C., "FTWD-Processing-Algorithms-V56a," *Stratamagnetic Software Internal Report*, July 2012.

Chin, W.C., "Formation Tester Flow Analysis in Anisotropic Media With Flowline Storage and Skin at Arbitrary Dip," *Well Logging Technology Journal*, Xi'an, China, Feb. 2013.

Chin, W.C. and Proett, M.A., "Formation Evaluation Using Phase Shift Periodic Pressure Pulse Testing," United States Patent No. 5,672,819 issued Sept. 30, 1997.

Chin, W.C. and Proett, M.A., "Formation Tester Immiscible and Miscible Flow Modeling for Job Planning Applications," *SPWLA 46th Annual Logging Symposium*, New Orleans, Louisiana, June 26-29, 2005.

Chin, W.C., Suresh, A., Holbrook, P., Affleck, L. and Robertson, H., "Formation Evaluation Using Repeated MWD Logging Measurements," *SPWLA 27th Annual Logging Symposium*, Houston, Texas, June 9-13, 1986.

Chin, W.C., Zhou, Y., Feng, Y., Yu, Q. and Zhao, L., *Formation Testing: Pressure Transient and Contamination Analysis*, John Wiley & Sons, Hoboken, New Jersey, 2014.

Chin, W.C. and Zhuang, X., "Formation Tester Inverse Permeability Interpretation for Liquids in Anisotropic Media with Flowline Storage and Skin at Arbitrary Dip," *SPWLA 48th Annual Logging Symposium*, Austin, Texas, June 3-6, 2007.

Chow, W.K., Ho, C.M., and Fong, N.K., "Evaluation of the Finite Control Volume Method in Simulating Thermal Fire Resistance of Building Elements," *Building Simulation, Fifth International IBPSA Conference*, Sept. 8-10, 1997, Prague, Czech Republic, Vol. 1, p. 273.

Cole, J.D., *Perturbation Methods in Applied Mathematics*, Blaisdell Publishing, Waltham, Massachusetts, 1968.

Crombie, A., Halford, F., Hashem, M., McNeil, R., Thomas, E.C., Melbourne, G. and Mullins, O.C., "Innovations in Wireline Fluid Sampling," *Oilfield Review*, Autumn 1998.

Doll, Henri-Georges, "Methods and Apparatus for Determining Hydraulic Characteristics of Formations Traversed by a Borehole," U. S. Patent No. 2,747,401, issued May 29, 1956.

Dussan, E.B., Auzerais, F.M. and Kenyon, W.E., "Apparatus for Determining Horizontal and/or Vertical Permeability of an Earth Formation," United States Patent No. 5,279,153 awarded Jan. 18, 1994.

Fan, L., Harris, B.W., Jamaluddin, A., Kamath, J., Mott, R., Pope, G.A., Shandrygin, A., Whitson, C.H., "Understanding Gas-Condensate Reservoirs," *Oilfield Review*, Winter 2005/2006.

Goode, P.A. and Thambynayagam, R.K.M., "Analytic Models for a Multiple Probe Formation Tester," SPE Paper No. 20737, *65th Annual Technical Conference and Exhibition of the Society of Petroleum Engineers*, New Orleans, Louisiana, Sept. 23-26, 1990.

Goode, P.A., and Thambynayagam, R.K.M., "Permeability Determination With a Multiprobe Formation Tester," *SPE Formation Evaluation Journal*, Dec. 1992, pp. 297-303.

IMSL Library Reference Manual, Vol. 3, Chapter M. IMSL Inc., June 1982.

Ireland, T., Joseph, J., Colley, N., Reignier, P., Richardson, S. and Zimmerman, T., "The MDT Tool: A Wireline Testing Breakthrough," *Oilfield Review*, April 1992.

Jones, C., Alta, W., Singh, J., Engelman, B., Proett, M. and Pedigo, B., "Collecting Single-Phase Retrograde Gas Samples at Near-Dewpoint Reservoir Pressure in Carbonates Using a Pump-Out Formation Tester with an Oval Pad," SPE Paper No. 110831, *2007 SPE Annual Technical Conference and Exhibition*, Anaheim, Ca., Nov. 11-14, 2007.

Joseph, J.A., and Koederitz, L.F., "Unsteady-State Spherical Flow with Storage and Skin," *Society of Petroleum Engineers Journal*, Dec. 1985, pp. 804-822.

Kasap, E., Huang, K., Shwe, T. and Georgi, D., "Formation-Rate-Analysis Technique: Combined Drawdown and Buildup Analysis for Wireline Formation Test Data," SPE Reservoir Evaluation and Engineering Journal, June 1999 (this is a revision of SPE Paper No. 36525, *Society of Petroleum Engineers Annual Technical Conference and Exhibition*, Denver, Colorado, Oct. 6-9, 1996).

Kool, H., Azari, M., Soliman, M.Y., Proett, M.A., Irani, C.A., Dybdahl, B., "Testing of Gas Condensate Reservoirs - Sampling, Test Design and Analysis," SPE Paper No. 68668, *SPE Asia Pacific Oil and Gas Conference and Exhibition*, Jakarta, Indonesia, April 17-19, 2001.

Liu, W, Hildebrand, M.A., Lee, J. and Sheng, J., "High-Resolution Near-Wellbore Modeling and Its Applications in Formation Testing," SPE Paper 90767, *SPE Annual Technical Conference and Exhibition*, Houston, Texas, Sept. 26-29, 2004.

Moran, J. H. and Finklea, E.E., "Theoretical Analysis of Pressure Phenomena Associated with the Wireline Formation Tester," *Journal of Petroleum Technology*, August 1962, pp. 899-908.

Peaceman, D.W., *Fundamentals of Numerical Reservoir Simulation*, Elsevier Scientific Publishing, Amsterdam, 1977.

Peaceman, D.W. and Rachford, H.H., "Numerical Calculation of Multidimensional Miscible Displacement," *Society of Petroleum Engineers Journal*, Dec., 1962, pp. 327-339.

Proett, M.A. and Chin, W.C., "Supercharge Pressure Compensation with New Wireline Formation Testing Method," *Annual Meeting of the Society of Professional Well Log Analysts*, New Orleans, Louisiana, June 1996.

Proett, M.A. and Chin, W.C., "Supercharge Pressure Compensation Using a New Wireline Testing Method and Newly Developed Early Time Spherical Flow Model," SPE Paper No. 36524, *Annual Technical Conference and Exhibition of the Society of Petroleum Engineers*, Denver, Colorado, Oct. 1996.

Proett, M.A. and Chin, W.C., "Multi-Probe Pressure Transient Analysis for Determination of Horizontal Permeability, Anisotropy and Skin in an Earth Formation," United States Patent No. 7,059,179 issued June 13, 2006.

Proett, M.A., Chin, W.C., Beique, J.M., Hardin, J.R., Fogal, J.M., Welshans, D., and Gray, G.C., "Methods for Measuring a Formation Supercharge Pressure," United States Patent No. 7,243,537, issued July 17, 2007.

Proett, M.A., Chin, W.C. and Mandal, B., "Advanced Permeability and Anisotropy Measurements While Testing and Sampling in Real-Time Using a Dual Probe Formation Tester," SPE Paper No. 64650, *Seventh International Oil & Gas Conference and Exhibition*, Beijing, China, Nov. 2000.

Proett, M.A., Chin, W.C., Manohar, M., Gilbert, G.N., and Monroe, M.L., "New Dual Probe Wireline Formation Testing and Sampling Tool Enables Real-Time Permeability and Anisotropy Measurements," SPE Paper No. 59701, *2000 SPE Permian Basin Oil and Gas Recovery Conference*, Midland, Texas, Mar. 21-23, 2000.

Proett, M.A., Seifert, D., Chin, W.C., Lysen, S., and Sands, P., "Formation Testing in the Dynamic Drilling Environment," *SPWLA 45th Annual Logging Symposium*, Noordwijk, The Netherlands, June 6–9, 2004.

Proett, M.A. and Waid, M.C., "Wireline Formation Testing for Low Permeability Formations Utilizing Pressure Transients," United States Patent No. 5,602,334, awarded February 11, 1997.

Proett, M.A., Weintraub, P.N., Golla, C.A., and Simeonov, S.D., "Formation Testing While Drilling Data Compression," United States Patent 6,932,167 B2, awarded August 23, 2005.

Raghavan, R., *Well Test Analysis*, Prentice Hall, Englewood Cliffs, New Jersey, 1993.

Schlumberger Staff, *Fundamentals of Formation Testing*, Schlumberger Marketing Communications, Sugar Land, Texas, 2006.

Sheng, J.J., Georgi, D.T. and Burge, J., "Concept of Geometric Factor and Its Practical Application to Estimate Horizontal and Vertical Permeabilities," SPE Reservoir Evaluation and Engineering Journal, December 2006, pp. 698-707.

SPWLA Staff, *SPWLA Wireline Formation Testing Technology Workshop*, 28th SPWLA Annual Symposium, Society of Professional Well Log Analysts, Houston, Texas, June 15-18, 1997.

SPWLA Staff, *SPWLA Formation Testing: Applications and Practices*, Spring Topical Conference, Society of Petrophysicists and Well Log Analysts, Taos, New Mexico, Mar. 28 – April 1, 2004.

Staff, *Log Interpretation Principles/Applications*, Schlumberger Wireline and Testing, Sugar Land, 1989.

Stehfest, H., "Numerical Inversion of Laplace Transforms," *Comm. ACM*, 1970, Vol. 13, pp. 47-49.

Stehfest, H., "Remarks on Algorithm 368 [D5]: Numerical Inversion of Laplace Transforms," *Comm. ACM*, 1970, Vol. 13, p. 624.

Stewart, G. and Wittmann, M., "Interpretation of the Pressure Response of the Repeat Formation Tester," SPE Paper No. 8362, *54th Annual Fall Technical Conference and Exhibition of the Society of Petroleum Engineers of AIME*, held in Las Vegas, Nevada, Sept. 23-26, 1979.

Thompson, J.F., Warsi, Z.U.A. and Mastin, C.W., *Numerical Grid Generation*, Elsevier Science Publishing, New York, 1985.

Todd, M.R. and Longstaff, W.J., "The Development, Testing and Application of a Numerical Simulator for Predicting Miscible Flood Performance," *Journal of Petroleum Technology*, July 1972, pp. 874-882.

van Dyke, M., *Perturbation Methods in Fluid Mechanics*, Academic Press, New York, 1964.

Villareal, S.G., Ciglenec, R., Stucker, M.J., and Duong, K., "Formation Evaluation While Drilling," United States Patent No. 7,367,394 issued May 6, 2008.

Wang, X. and Economides, M., "Aggressive Fracturing Slashes Turbulence in High-Permeability Gas Wells," *World Oil*, July 2004, pp. 73-79.

Xu, H., Bassiouni, Z., and Desbrandes, R., "Three-Dimensional Finite Difference Modeling of Wireline Formation Tests in Tight Gas Sands," SPE Paper No. 24886, *67th Annual Technical Conference and Exhibition of the Society of Petroleum Engineers*, Washington, DC, Oct. 4-7, 1992.

Zhou, Y., Hao, Z., Feng, Y., Yu, Q. and Chin, W.C., "Formation Testing: New Methods for Rapid Mobility and Pore Pressure Prediction," Paper OTC-24890-MS, 2014 Offshore Technology Conference Asia (OTC Asia), Kuala Lumpur, Malaysia, Mar. 25-28, 2014.

Zhou, Y., Zhao, L., Feng, Y., Yu, Q., and Chin, W.C., "Formation Testing: New Methods for Rapid Mobility and Pore Pressure Prediction," Paper 17214, 7th International Petroleum Technology Conference (IPTC), Doha, Qatar, Jan. 19-22, 2014.

Index

E

F

G

H

I

R

S

T

U

V

W

About the Authors





Yanmin Zhou Yongren Feng Qiang Yu Wilson Chin Jenny Zhuang

Yanmin Zhou received her Ph.D. in Geological Resources Engineering from the University of Petroleum, Beijing, and serves as Geophysics Engineer at CNOOC/COSL. She participated in the Drilling and Reservoir Testing Instrument Development Program, National 863 Project, and acts as Associate Project Leader in national formation testing activities.

Yongren Feng is Chief Mechanical Engineer at CNOOC/COSL with three decades of design experience covering a dozen logging tools. With more than one hundred patents, Feng serves as Project Leader for the 12th National Five Year Plan in formation tester development; he was elected as one of China's National Technology and Innovation Leaders.

Qiang Yu earned his M.Sc. in Measurement Technology and Instrumentation from Xi'an Shiyou University and serves as Senior Control Engineer in formation testing and field operations. He is an Associate Project Leader with CNOOC/COSL in the national formation testing program.

Xiaoying "Jenny" Zhuang, with Stratamagnetic Software, LLC in Beijing, provides English-Chinese language interpretation and facilitation services. She has over ten years of experience in petroleum technology, with her efforts focusing on marketing and technology transfer at oilfield companies COSL, CNPC and Sinopec.

Wilson Chin, who earned his Ph.D. from M.I.T. and M.Sc. from Caltech, heads Stratamagnetic Software, LLC in Houston, which develops mathematical modeling software for formation testing, MWD telemetry, borehole electromagnetics, well logging, reservoir engineering and managed pressure drilling (e.g., visit www.stratamagnetic.com for details). Mr. Chin is the author of thirteen books, more than one hundred papers and over forty patents. He may be contacted at wilsonchin@aol.com or by cell at (832) 483-6899.

Also of Interest

Check out these other related titles from Scrivener Publishing

Books Now Available in the *Advances in Petroleum Engineering* series:
Wave Propagation in Drilling, Well Logging, and Reservoir Applications, by Wilson C. Chin, ISBN 9781118925898. The only book providing validated math models for drillstring vibrations, swab-surge, mud pulse telemetry, seismic ray tracing, ocean wave loading and borehole geophysics, a must for every petroleum engineer, researcher and software developer! *NOW AVAILABLE!*

Other Books From the Same Author:
Measurement While Drilling (MWD) Signal Analysis, Optimization, and Design, by Wilson C. ChinYinao Su, Limin Sheng, Lin Li, Hailong Bian and Rong Shi, ISBN9781118831687. The only book explaining modern MWD technology, to include hardware design, signal processing and telemetry, offering unique approaches to high-data-rate well logging. *NOW AVAILABLE!*

Formation Testing: Pressure Transient and Formation Analysis, by Wilson C. Chin, Yanmin Zhou, Yongren Feng, Qiang Yu, and Lixin Zhao, ISBN 9781118831137. This is the only book available to the reservoir or petroleum engineer covering formation testing algorithms for wireline and LWD reservoir analysis that are developed for transient pressure, contamination modeling, permeability, and pore pressure prediction. *NOW AVAILABLE!*

Electromagnetic Well Logging, by Wilson C. Chin, ISBN 9781118831038. Mathematically rigorous, computationally fast, and easy to use, this new approach to electromagnetic well logging does not bear the limitations of existing methods and gives the reservoir engineer a new dimension to MWD/LWD interpretation and tool design. *NOW AVAILABLE!*

Other Related Titles available from Scrivener Publishing:
Oil Spill Risk Management: Modeling Gulf of Mexico Circulation and Oil Dispersal, By David Dietrich, Malcolm J. Bowman, Konstantin

Korotenko, and Hamish Bowman, ISBN: 9781118290385. This book describes and applies state-of-the-art software designed to help balance cost and profit estimates against risk in the petrochemical industry using oil extracted from ocean bottom deposits. *SEPTEMBER 2014*

Bioremediation of Petroleum and Petroleum Products, by James Speight and Karuna Arjoon, ISBN 9780470938492. With petroleum-related spills, explosions, and health issues in the headlines almost every day, the issue of remediation of petroleum and petroleum products is taking on increasing importance, for the survival of our environment, our planet, and our future. This book is the first of its kind to explore this difficult issue from an engineering and scientific point of view and offer solutions and reasonable courses of action. *NOW AVAILABLE!*

Sustainable Resource Development, by Gary Zatzman, ISBN 9781118290392. Taking a new, fresh look at how the energy industry and we, as a planet, are developing our energy resources, this book looks at what is right and wrong about energy resource development. *NOW AVAILABLE!*

An Introduction to Petroleum Technology, Economics, and Politics, by James Speight, ISBN 9781118012994. The perfect primer for anyone wishing to learn about the petroleum industry, for the layperson or the engineer. *NOW AVAILABLE!*

Ethics in Engineering, by James Speight and Russell Foote, ISBN 9780470626023. Covers the most thought-provoking ethical questions in engineering. *NOW AVAILABLE!*

Fundamentals of the Petrophysics of Oil and Gas Reservoirs, by Buryakovsky, Chilingar, Rieke, and Shin. ISBN 9781118344477. The most comprehensive book ever written on the basics of petrophysics for oil and gas reservoirs. *NOW AVAILABLE!*

Petroleum Accumulation Zones on Continental Margins, by Grigorenko, Chilingar, Sobolev, Andiyeva, and Zhukova. ISBN 9781118385074. Some of the best-known petroleum engineers in the world have come together to produce one of the first comprehensive publications on the detailed (zonal) forecast of offshore petroleum potential, a must-have for any petroleum engineer or engineering student. *NOW AVAILABLE!*

Mechanics of Fluid Flow, by Basniev, Dmitriev, and Chilingar, ISBN 9781118385067. The mechanics of fluid flow is one of the most important fundamental engineering disciplines explaining both natural phenomena and human-induced processes. A group of some of the best-known petroleum engineers in the world give a thorough understanding of this important discipline, central to the operations of the oil and gas industry. *NOW AVAILABLE!*

Zero-Waste Engineering, by Rafiqul Islam, ISBN 9780470626047. In this controversial new volume, the author explores the question of zero-waste engineering and how it can be done, efficiently and profitably. *NOW AVAILABLE!*

Formulas and Calculations for Drilling Engineers, by Robello Samuel, ISBN 9780470625996. The most comprehensive coverage of solutions for daily drilling problems ever published. *NOW AVAILABLE!*

Emergency Response Management for Offshore Oil Spills, by Nicholas P. Cheremisinoff, PhD, and Anton Davletshin, ISBN 9780470927120. The first book to examine the Deepwater Horizon disaster and offer processes for safety and environmental protection. *NOW AVAILABLE!*

Advanced Petroleum Reservoir Simulation, by M.R. Islam, S.H. Mousavizadegan, Shabbir Mustafiz, and Jamal H. Abou-Kassem, ISBN 9780470625811. The state of the art in petroleum reservoir simulation. *NOW AVAILABLE!*

Energy Storage: A New Approach, by Ralph Zito, ISBN 9780470625910. Exploring the potential of reversible concentrations cells, the author of this groundbreaking volume reveals new technologies to solve the global crisis of energy storage. *NOW AVAILABLE!*

WILEY END USER LICENSE AGREEMENT

Go to www.wiley.com/go/eula to access Wiley’s ebook EULA.